Numerical analysis for a combined space-time discretization of air-sea exchanges and their parameterizations

Simon Clément

THÈSE

Pour obtenir le grade de

DOCTEUR DE L'UNIVERSITÉ GRENOBLE ALPES

École doctorale : MSTII - Mathématiques, Sciences et technologies de l'information, Informatique
Spécialité : Mathématiques Appliquées
Unité de recherche : Laboratoire Jean Kuntzmann

Analyse numérique pour la réconciliation en espace et en temps des discrétisations des échanges air-mer et de leur paramétrisation

Numerical analysis for a combined space-time discretization of air-sea exchanges and their parameterizations

Présentée par :

Simon CLEMENT

Direction de thèse :

Eric BLAYO Professeur, Université Grenoble Alpes	Directeur de thèse
Florian LEMARIÉ Chargé de recherche, Inria Grenoble	Co-encadrant de thèse

Rapporteurs :

Pascal OMNES
INGENIEUR HDR, CEA Saclay
Franz CHOULY
PROFESSEUR DES UNIVERSITES, Université de Bourgogne

Thèse soutenue publiquement le **23 novembre 2022**, devant le jury composé de :

Pascal OMNES INGENIEUR HDR, CEA Saclay	Rapporteur
Franz CHOULY PROFESSEUR DES UNIVERSITES, Université de Bourgogne	Rapporteur
Jeffrey CONNORS PROFESSEUR ASSOCIE, University of Connecticut	Examinateur
Eric BLAYO PROFESSEUR DES UNIVERSITES, Université Grenoble Alpes	Directeur de thèse
Martin SCHREIBER PROFESSEUR DES UNIVERSITES, Université Grenoble Alpes	Président
Véronique MARTIN MAITRE DE CONFERENCE, Université de Picardie Jules Verne	Examinatrice

Invités :

Franck DUMAS
INGENIEUR, SHOM Brest
Florian LEMARIÉ
CHARGE DE RECHERCHE, Inria Grenoble

Remerciements

Merci à Pascal Omnes et Franz Chouly, les deux rapporteurs de cette thèse qui ont accordé beaucoup de temps et d'énergie à mon travail.

Merci également aux autres membres du jury : Jeffrey Connors, Véronique Martin, Martin Schreiber et Franck Dumas, qui ont également fait de ma soutenance un moment inoubliable.

Les années passées au LJK auraient été bien moins plaisantes sans l'ensemble des doctorant-es qui ont évolué avec moi. Je remercie donc les membres du bureau 196 : Philomène, Rishabh, Sanal, Manolis, Qiao ainsi que feue la plante de Matthieu. Je suis d'ailleurs reconnaissant envers son propriétaire pour m'avoir fourni une quantité innombrable d'explications ainsi qu'un exemple de rigueur. Le LJK n'étant pas limité à mon bureau : Anatole, Nils, Thibault, Hippolyte, Gilles et toutes celles et ceux que j'ai côtoyé (en particulier les membres de la fine équipe airsea), merci. Je remercie aussi mes prédécesseur-euses Sophie et Charles pour toute l'inspiration et l'aide plus ou moins directe qu'ils m'ont apporté.

Quelques mots sur cette page ne sauraient décrire l'immense gratitude que j'ai pour Éric et Florian, qui m'ont guidé tout au long de ma thèse. Vous avez toujours su rester patients, à l'écoute et j'ai beaucoup apprécié la confiance que vous m'avez accordé. Merci pour tout.

Je n'ai pas cité toutes les personnes qui m'entourent en dehors du contexte académique mais soyez sûrs que votre présence m'est précieuse.

Résumé détaillé

Cette thèse s'intéresse à la représentation numérique des interactions air-mer, notamment au sein du couplage entre un modèle d'océan et un modèle d'atmosphère. Nous étudierons donc conjointement des méthodes de couplage et la représentation numérique de la *couche limite de surface* : une zone cruciale pour le calcul des interactions.

Chapitre 1: Modélisation d'une colonne océan-atmosphère

Le chapitre 1 présente les équations et principes physiques utilisés au sein de cette thèse.

Tout d'abord, le système des *équations primitives* décrivant les écoulements atmosphériques et océaniques est présenté. Une attention particulière est portée à la représentation de la *turbulence*, qui induit une séparation entre des échelles "résolues" et des plus petites échelles dites "turbulentes".

Cette séparation d'échelle est nécessaire d'un point de vue numérique : les échelles résolues correspondent à celles représentées dans les grilles de calcul des schémas numériques (actuellement, de l'ordre de centaines de mètres). Au contraire, les échelles turbulentes *sous-maille* ne peuvent pas être représentées explicitement par les grilles de calcul et doivent être paramétrisées.

Le concept de couche limite de surface (basé sur une hypothèse de flux constants) est ensuite introduit. Celui-ci est au centre du sujet de la thèse : il permet de décrire, à travers un formalisme nommé "loi du mur", le comportement turbulent des écoulements aux abords de la surface.

Dans les modèles d'atmosphère, la couche limite de surface est représentée par les *formulations bulk*, qui permettent de calculer les composantes turbulentes des flux air-mer à partir des données autour de l'interface. La stratification (variation verticale de la densité) joue un rôle important dans la couche limite de surface. Elle affecte la "loi du mur" et est une composante essentielle des formulations bulk.

Cette thèse s'articule autour d'une hiérarchie de modèles présentés au chapitre 1. Ceux-ci décrivent tous l'évolution temporelle d'une colonne d'atmosphère au-dessus d'une colonne d'océan en une seule dimension spatiale (verticale).

1. Le plus bas niveau de la hiérarchie est un couplage de simples équations réaction-diffusion, utilisé aux chapitres 2 et 3 pour étudier et optimiser des méthodes itératives de couplage (dites *méthodes de Schwarz*). Ce modèle ne prend pas en compte les aspects de turbulence sous-maille.

2. Le niveau intermédiaire (utilisé au chapitre 6) est un autre couplage d'équations réaction-diffusion. Cependant, ce couplage utilise des conditions de bord à l'interface décrivant une couche limite de surface.

3. Le plus haut niveau de la hiérarchie est un modèle utilisant une paramétrisation de la turbulence et qui inclut une stratification en température. A l'interface, de véritables formulations bulk sont utilisées (au lieu d'une formulation simplifiée dans le niveau intermédiaire). Ce modèle est utilisé aux chapitres 4 et 5 pour s'intéresser à l'impact des discrétisations de couche limite, notamment dans le couplage océan-atmosphère.

Les objectifs de cette thèse correspondent aux trois niveaux de la hiérarchie :

1. étudier l'effet de la discrétisation sur la vitesse de convergence des méthodes de Schwarz ;

2. étudier la vitesse de convergence des méthodes de Schwarz en présence d'une couche limite de surface (i.e. avec des conditions de transmission non-linéaires) ;

3. développer une discrétisation permettant de représenter au mieux les couches limites de surface, en prenant en compte les paramétrisations au sein de ces couches limites.

Chapitre 2 : Analyse discrète des méthodes de Schwarz avec des équations de réaction-diffusion

Le chapitre 2 a été publié sous la forme de l'article [Clement et al., 2022] dans le journal *SMAI Journal of Computational Mathematics*.

- **Modèle continu et méthode de Schwarz** : Le modèle utilisé dans les deux premiers chapitres est le suivant:

$$\partial_t u_j + (r - \nu_j \partial_x^2) u_j = f_j \qquad (j = o, a) \qquad (x,t) \in \widetilde{\Omega}_j \times]0,T] \tag{1a}$$

$$u_j(x,0) = u_{j,0}(x) \qquad x \in \widetilde{\Omega}_j \tag{1b}$$

$$u_o(0^-,t) = u_a(0^+,t) \qquad t \in [0,T] \tag{1c}$$

$$\nu_o \partial_x u_o(0^-,t) = \nu_a \partial_x u_a(0^+,t) \qquad t \in [0,T] \tag{1d}$$

  où r et ν_j sont les coefficients de réaction et de diffusion. Pour résoudre ce problème couplé, les domaines $\widetilde{\Omega}_o = \mathbb{R}_-$ et et $\widetilde{\Omega}_a = \mathbb{R}_+$ voient leurs équations correspondantes

(1a) être résolues tour à tour dans $\widetilde{\Omega}_j \times [0,T]$ en utilisant les équations (1c) et (1d) en tant que conditions de bord. Cette méthode s'appelle *Relaxation d'onde de Schwarz avec des conditions de transmission Dirichlet-Neumann*. L'étude de la convergence de cette méthode se fait en deux étapes :

  - Les équations (1a) sont résolues dans l'espace de Fourier : la dimension temporelle devient un espace de fréquences. On obtient une formule analytique de la différence entre u_j^k (k note l'itération de Schwarz courante) et la solution couplée, c'est-à-dire de l'évolution de l'erreur en fin des itérations.
  - Les conditions de transmission à l'interface permettent de quantifier l'évolution de cette différence au fur et à mesure des itérations.

  La convergence est *linéaire*, c'est-à-dire que la différence entre u_j^k et la solution couplée est multipliée à chaque itération par un *facteur de convergence* ne dépendant pas de k. Dans le cas continu avec des conditions de transmission Dirichlet-Neumann, le facteur de convergence ne dépend pas non plus de la fréquence ni de r et vaut $\rho_{DN}^{(c,c)} = \sqrt{\frac{\nu_o}{\nu_a}}$.

- **Facteur de convergence semi-discret en temps** : la convergence observée lors de l'implémentation d'une méthode de Schwarz dépend des discrétisations en temps et en espace utilisées. On utilise la transformée en Z au lieu de la transformée de Fourier pour étudier un signal semi-discret en temps. Si le passage du continu au discret est aisé pour les schémas en temps qui ne comportent qu'une étape, les schémas à plusieurs étapes demandent une attention particulière. En effet, les conditions d'interface sont interpolées durant les étapes intermédiaires. Cette interpolation modifie la vitesse de convergence de la méthode de Schwarz, particulièrement dans les hautes fréquences temporelles.

- **Discrétisation en espace** : la convergence des méthodes de Schwarz a été étudiée pour deux discrétisations en espace. La première est une discrétisation de référence utilisant des différences finies (FD) centrées d'ordre 2 ; la deuxième est une discrétisation en volumes finis (FV) basée sur des splines paraboliques. Chaque maille est ainsi caractérisée par un polynôme d'ordre 2 et l'approximation volumes finis est déduite du raccord des polynômes entre les mailles. Retrouver la solution numérique mono-domaine s'avère immédiat lorsque la discrétisation FV est utilisée. Avec la discrétisation FD, utiliser une condition de transmission particulière dans ce but diminue drastiquement la vitesse de convergence.

- **Analyse discrète** : une méthode d'analyse est présentée et appliquée pour les combinaisons de deux discrétisations en temps et en espace. Ces combinaisons sont démontrées stables en étudiant les valeurs propres des matrices à inverser.

Finalement, en utilisant des conditions de transmission contenant des degrés de liberté, la vitesse de convergence des méthodes de Schwarz peut être accélérée en optimisant les

paramètres introduits. Si l'optimisation se fait au niveau continu, les paramètres choisis ne seront en général pas optimaux pour la vitesse de convergence observée numériquement. Au contraire, en optimisant sur le facteur de convergence discret on obtient des vitesses de convergence supérieures dans les expériences numériques.

Le facteur de convergence discret peut cependant s'avérer contraignant à calculer, en particulier pour des discrétisations en temps à plusieurs étapes ou pour des discrétisations en espace d'ordre élevé.

Chapitre 3 : Approximation du facteur de convergence discret des méthodes de Schwarz

L'objet du chapitre 3 est donc de proposer de nouvelles approximations qui rendent le facteur de convergence observé numériquement plus facile à estimer que par une approche d'analyse discrète complète (comme au chapitre 2), tout en étant plus précis que le facteur de convergence continu. La première approximation étudiée est la méthode des *équations modifiées* qui introduit un terme représentant les principaux effets de la discrétisation. La seconde est une combinaison des analyses semi-discrètes pour approcher l'analyse complètement discrète.

Équations modifiées

La méthode des équations modifiées consiste à étudier au niveau continu non pas l'équation différentielle originale mais celle qui est résolue par le schéma numérique. Ces équations modifiées sont obtenues à l'aide d'un développement de Taylor de la discrétisation.

Équations modifiées en temps

Lors du calcul du facteur de convergence, l'utilisation d'équations modifiées en temps se traduit par un changement de la variable fréquentielle ω utilisée dans la transformée de Fourier :

- La complexité de l'étude continue des équations modifiées en temps est similaire à celle semi-discrète des schémas à une étape.

- Les équations modifiées en temps simplifient l'étude de convergence des schémas à deux étapes. Cependant, l'utilisation du développement de Taylor cache l'opération d'interpolation des données de transmission réalisée dans les étapes intermédiaires. Ainsi, lorsque la différence entre les facteurs de convergence continu et semi-discret en temps vient de cette opération d'interpolation, les équations modifiées ne permettent pas d'approcher le facteur de convergence semi-discret.

Équations modifiées en espace

L'utilisation des équations modifiées sur les schémas en espace suscite d'autres observations :

- le développement de Taylor introduit des dérivées d'ordre plus élevé que dans l'équation originale. Pour obtenir le caractère bien posé des équations modifiées, il est donc nécessaire d'ajouter des conditions d'interface. Celles-ci peuvent être judicieusement choisies à partir de la discrétisation en espace proche du bord.
- Il est en général insuffisant de n'étudier que l'effet de la discrétisation de l'équation aux dérivées partielles. En effet, les conditions d'interface et de bord sont elles aussi affectées par la discrétisation et leurs versions discrètes doivent être utilisées dans le calcul du facteur de convergence.
- Dans le cas général, l'utilisation des équations modifiées en espace augmente l'ordre de l'équation aux dérivées partielles et ne rend pas plus aisé le calcul du facteur de convergence par rapport au calcul semi-discret.
- Dans le cas particulier d'une équation ne faisant intervenir qu'une seule différentiation en espace de n'importe quel ordre : une astuce de calcul permet de se ramener au cas où un simple changement de variable fréquentielle suffit pour caractériser l'équation modifiée. L'analyse de la convergence en prenant en compte la discrétisation devient alors similaire à l'analyse continue.

Combinaison des facteurs de convergence

Il est possible de combiner les facteurs de convergence semi-discrets (S-D) et continu pour approcher le facteur de convergence discret selon la formule:

$$\text{DISCRET} \approx \text{S-D EN ESPACE} + \text{S-D EN TEMPS} - \text{CONTINU} \tag{2}$$

Des expériences numériques présentées à la fin du chapitre 3 montrent dans quels cas et dans quelle mesure :

- ces diverses approximations sont efficaces pour approcher le facteur de convergence discret ;
- la convergence peut être accélérée en optimisant ces approximations.

Chapitre 4 : Vers une discrétisation de la couche limite atmosphérique cohérente avec la théorie physique

Dans le chapitre 4, nous étudions une colonne atmosphérique et sa discrétisation. À cause de considérations numériques, la colonne d'atmosphère doit se diviser en deux parties :

1. la couche limite de surface, exclue du domaine de calcul et paramétrisée par une “loi du mur” ;
2. le reste de la colonne, qui réagit plus lentement aux variations des conditions à la surface.

L'objectif de ce chapitre est d'évaluer les discrétisations possibles de cette couche limite.

- Dans une discrétisation FD typique (telle que celle qui sera utilisée au chapitre 6), ce découpage est implicite : l'équation d'évolution est utilisée à partir du premier point de grille et on considère la zone sous ce point comme la couche limite. Les flux turbulents sont calculés à l'aide de la solution au premier point de grille, ce qui correspond donc à l'extrémité supérieure de la couche limite.
- La construction de discrétisations en volumes finis est moins souple dans sa gestion de la couche limite. La solution au premier point de grille correspond alors à une moyenne sur une cellule qui se trouve partagée entre deux zones. Des travaux antérieurs ont montré qu'une gestion de la couche limite calquée sur les méthodes FD conduit à un biais systématique dans l'estimation des flux turbulents.

Ainsi, [Nishizawa and Kitamura, 2018] proposent d'étendre la couche limite de surface à l'entièreté de la première cellule et d'utiliser un algorithme bulk adapté aux données moyennées.

Ce chapitre 4 propose d'implémenter directement dans la discrétisation FV les hypothèses existantes dans les formulations bulk. Pour ce faire, la reconstruction à l'intérieur de la première maille est réalisée à l'aide des fonctions particulières intervenant dans les lois du mur et non seulement avec des polynômes.

Ces reconstructions particulières permettent notamment d'étendre la hauteur de la couche limite au-delà de la première maille. En effet, le *log-layer mismatch*, un problème numérique bien connu dans les simulations à haute résolution (Large Eddies Simulations), provient d'une couche limite trop mince.

En étant capable de choisir l'épaisseur de la couche limite de surface sur des critères physiques et non seulement numériques, la consistance des schémas s'en trouve améliorée. La résolution verticale peut ainsi être raffinée sans pour autant changer les équations continues résolues par la discrétisation.

En utilisant un critère de consistance, les stratégies de gestion de la couche limite sont comparées pour différents types de stratification. Une comparaison de ces stratégies est également effectuée à l'aide d'un couplage avec une colonne océanique.

Chapitre 5 : Discrétisation de la couche limite oceanique

Le chapitre 5 est tourné vers la définition et l'implémentation d'une couche limite de surface océanique.

Il est maintenant bien connu que les algorithmes bulk doivent utiliser des vents relatifs aux courants de surface pour calculer plus précisément les flux turbulents. Des travaux récents [Pelletier et al., 2021] se sont intéressés à la prise en compte des mouvements turbulents dans la description des courants de surface. Par symétrie avec les caractéristiques de la couche limite atmosphérique, les formulations bulk peuvent également intégrer une couche limite océanique.

L'implémentation de cette couche limite peut suivre les mêmes principes que son homologue atmosphérique. Une différence notable est la présence de la pénétration du flux solaire, très importante dans les premiers mètres sous la surface. Ce flux solaire vient contredire la notion de flux constant utilisée dans les lois du mur.

Les stratégies de gestion de la couche limite océanique sont comparées dans des simulations numériques, dans un cas forcé et dans un cas couplé.

Chapitre 6: Méthodes de Schwarz pour le couplage discret océan-atmosphère

Le dernier chapitre de cette thèse met en relation l'étude discrète des méthodes de Schwarz et l'utilisation d'une couche limite de surface.

Comme mentionné précédemment, la hauteur de la couche limite de surface est choisie dans les modèles actuels en fonction de la résolution de la grille. Pour cette raison, étudier la convergence de l'algorithme de Schwarz au niveau semi-discret en espace semble pertinent, puisque les conditions de transmission sont liées au choix de discrétisation.

Le chapitre 6 se concentre sur la discrétisation FD qui a le mérite d'être à la fois simple à manipuler et représentative de l'état de l'art. Les conditions de transmission sont simplifiées : on formule le flux à l'interface comme égal à $C_D|\Delta U|\Delta U$ où ΔU est le saut des solutions à travers l'interface et C_D est une constante (au lieu d'être une fonction non-linéaire de ΔU).

Nous prouvons l'existence et l'unicité d'une solution du problème couplé au voisinage d'un état stationnaire. Cette preuve est réalisée au niveau semi-discret en espace, pour lequel l'état stationnaire est unique pour notre choix de paramètres.

La convergence des méthodes de Schwarz sur une version linéaire du problème (où on pose $\alpha = C_D|\Delta U| = \text{const}$) est tout d'abord discutée. L'optimisation d'un paramètre de relaxation θ introduit dans la condition de transmission donne un paramètre optimal $\theta \approx 1$.

Le problème non-linéaire est ensuite étudié en passant par une linéarisation de la condition de transmission autour de l'état stationnaire. Au contraire de ce qu'on peut trouver habituellement dans les études de convergence (qui utilisent dans l'immense majorité des cas des conditions de transmission linéaires), le facteur de convergence pour une fréquence donnée change d'une itération à une autre. Une optimisation est également réalisée dans ce cas et donne un paramètre optimal $\theta \approx 1.5$.

Finalement, des expériences numériques valident les résultats obtenus analytiquement.

Contents

Introduction

Numerical models are ubiquitous in oceanography, climatology and meteorology. They become more and more accurate as the computational power increases and as we refine our knowledge on both physical phenomena and numerical behaviour. As long as we want to encompass more phenomena in the simulations, both mathematical models and their implementations must be adapted to new scales and new challenges.

The interactions between the ocean and the atmosphere are crucial for climate projections and mid- to long-term weather forecasts. It means that the ocean and atmosphere must be jointly simulated; however, there is no ocean-atmosphere model in a single block to our knowledge. Indeed, the scales and dynamics involved in those two systems are sufficiently different to justify the use of separate models, and there are historically two separate communities behind the models. For those reasons simulations of the air-sea system always rely on the *coupling* between numerical models describing the oceanic and atmospheric circulations.

A numerical implementation does not directly solve the mathematical model (the *continuous* equations) but an approximation of it (the *discrete* equations). There exist many of these approximations (called *discretizations*), the choice of which is not to be taken lightly: a discretization introduces some numerical error, and may also enforce desirable mathematical or physical properties.

A numerical simulation cannot explicitly represent all the scales involved in geophysical phenomena, because of the colossal cost it would induce. In climate simulations, scales smaller than an hour in time and dozens of kilometers in space are only represented through their effects on larger scales. Among the parameterizations of small scales, the *turbulence* accounts for sub-grid chaotic motions.

Moreover, the interface between the models in the case of the ocean-atmosphere coupling contains specific turbulent motions. The discretization of this zone called *surface layer* is a key for a proper coupling.

Because of cost constraints, the ocean-atmosphere coupling algorithms are in practice quite simple and many of them actually correspond to a single step of a *Schwarz method* [Lemarié et al., 2015a]. The latter domain decomposition methods consist in solving iteratively the models (here, the ocean model and the atmosphere model) until the solutions at the interface match. These coupling methods, widely used for number of applications outside the ocean-atmosphere context, are known for being relatively slow. However, the

mismatch at the interface is multiplied at each iteration by a *convergence factor* which can be optimized to accelerate the convergence of the Schwarz method.

[Marti et al., 2021] used several Schwarz iterations instead of a single one to evaluate the loss of precision generated by the coupling within the operational climate model IPSL-CM. A significant difference was found *"after sunrise and before sunset, when the external forcing (insolation at the top of the atmosphere) has the fastest pace of change"* and recent additional ensemble simulations tend to highlight a significant long-term impact of performing iterations. Although it would be unaffordable to use multiple iterations of Schwarz methods in actual climate simulations, this approach is useful to evaluate current methods used in this context. Studying the convergence properties of Schwarz methods is hence of interest, first for the evaluation of present simulations, and then for the reduction of the error in the first iteration[1].

The discretizations interact with the coupling methods: if the study of the convergence factor is pursued at the *continuous* level, the coupling of the *discrete* equations may converge differently than expected. Moreover, if the convergence is optimized at the discrete level, one expects to obtain a faster numerical convergence. Besides, the continuous equations describing the surface layer are actually linked with the numerical implementation. It is hence appropriate to directly study at the *discrete* level the coupling methods when taking into account the surface layer.

In this context, the objectives of this thesis are:

- Improve our knowledge on how the discretization affects the convergence factor of Schwarz methods.
- Discuss the numerical treatment of the surface layer and propose improvements.
- Study the effect of the surface layer within the ocean-atmosphere coupling.

The surface layer

The surface layer contains strong disparities and can be modeled by a so-called *law of the wall*. A review of wall modelling was done by [Larsson et al., 2016], focusing on Large Eddy Simulations (which are simulations for small scales). In particular, it is emphasized that the height of the surface layer should be chosen based on both physical and numerical criteria.

Recent advances in *bulk formulations* (which characterize the law of the wall in the atmosphere models) partially underpin this thesis: one is the introduction by [Pelletier et al., 2021] of an oceanic part of the surface layer in the *bulk formulations*. The other is the discovery of a systematic bias created in some discretizations because the variables are "used as the center point value in the model grid to estimate the surface fluxes even though the

[1]However, note that in the overwhelming majority of convergence studies (including this thesis) the convergence factor of Schwarz methods does not characterize the very first iteration because the initial value is not the solution of the considered differential equation.

variables are volume-averaged values" [Nishizawa and Kitamura, 2018]. In the latter case, the bias can be avoided by adapting the bulk formulations to averaged data.

Moreover, the hypotheses on which the bulk formulations rely are generally not included in the discretization. We propose to reunite the hypotheses in the bulk formulations and in the discretization in order to approximate more rigorously the continuous equations.

From a more theoretical point of view, the modeling of the surface layer leads to non-linearities in the surface fluxes. This raises some questions about the well-posedness of the mathematical problem. The existence and regularity of solutions for the ocean-atmosphere coupling is proved in [Lions et al., 1995] with linear conditions at the interface and a part of the non-linearities inside the computational domains. More recently, a study focused only on the ocean domain [Chacon-Rebollo et al., 2014] shows the existence and unicity of a solution in the neighborhood of a steady state. It is proven on a one-dimensional model that includes a parameterization of the turbulence. We will discuss the well-posedness of the ocean-atmosphere coupling in the presence of a parameterized surface layer.

Schwarz methods

The choice of the coupling methods in the ocean-atmosphere context is not straightforward. In addition to the trade-off between the required computational time and the achieved precision, the coupling methods also face some constraints:

- some quantities must be conserved by the method (e.g. water, energy);
- the atmosphere and ocean models being very sophisticated, the methods should not be intrusive (i.e. they should consider the models as black boxes);
- it is generally unaffordable to call multiple times the ocean and atmosphere models.

With wisely chosen interface conditions, Schwarz methods can satisfy those constraints. In the context of making a very small number of iterations, the acceleration of the convergence can be used to increase the precision of the coupling. Discrete transparent boundary conditions [Zisowsky and Ehrhardt, 2006] allow to converge up to the numerical precision in two iterations. However, those boundary conditions are non-local in time. Schwarz methods can be instead accelerated by an optimization [Gander, 2006] where the boundary conditions at interface are local in time.

This optimization, when carried in a semi-discrete in space [Wu and Al-Khaleel, 2014], in time [Arnoult et al., 2022] or in a fully discrete setting [Wu and Al-Khaleel, 2017] yields a theoretical convergence rate which is closer to the one observed in numerical simulations and generally leads to faster convergence. However, even if they also consider reaction-diffusion equations, [Wu and Al-Khaleel, 2014] and [Wu and Al-Khaleel, 2017] focus on electric circuits where there are overlaps between the domains. [Gander et al., 2018] analyze the presence of an overlap but to our knowledge no previous study stands in the discrete case without

overlap (note that the semi-discrete 2D stationary case was done by [Gerardo-Giorda and Nataf, 2005]). Discrete Schwarz Waveform Relaxation studies with other equations can be found in [Haynes and Mohammad, 2020] together with the finite domain case. In the continuous case, a lot of efforts have been made to study the convergence of Schwarz methods (e.g. [Thery et al., 2021] where the viscosity is varying and is discontinuous at interface or [Häberlein and Halpern, 2014] who give an overview of nonlinear systems).

Outline

This thesis contains six chapters. Chapter 1 focuses on the derivation of the equations driving the ocean-atmosphere coupling. It presents in particular a hierarchy of models which is used in the other chapters: two couplings of reaction-diffusion equations (with linear or nonlinear conditions at interface), and a more sophisticated model using a turbulence parameterization.

[Clement et al., 2022] (Chapter 2) studies the effect of the discretisation in space and time of the linear reaction-diffusion coupling problem without overlap. In particular, it gives a methodology to study the convergence factor of Schwarz methods at the discrete and semi-discrete levels and highlights some features of these convergence factors. It also presents a *Finite Volume* discretization used throughout all the other chapters.

Chapter 3 introduces alternative methods to estimate the convergence speed of the discrete problem with less computations. The ultimate goal would be to obtain the convergence speed of the discrete or semi-discrete optimization with a continuous study. The linear reaction-diffusion coupling is taken as an illustration to show how much the convergence can be accelerated with the proposed approximations and to discuss their correctness.

Using the sophisticated model based on a parameterization of turbulence, Chapter 4 and 5 discuss the discretization of the surface layer. We propose a discretization that is more coherent with the physical theory of the surface layer. Chapter 4 introduces the ideas and discretization for the atmosphere surface layer and Chapter 5 extends the discussion to the ocean surface layer and focuses on handling specific features of the ocean surface layer.

Finally, Chapter 6 treats the nonlinearity due to the presence of the surface layer. The well-posedness of the nonlinear coupling of reaction-diffusion equations is discussed. Nonlinearities at interface were introduced in domain decomposition methods by [Caetano et al., 2011] where they created interface conditions resembling to linear ones specifically to match with the existing studies. We start instead with an existing nonlinear interface and study its convergence properties.

Chapter 1

Ocean-atmosphere vertical column modelling

Table of contents

We present in this chapter the concepts and equations at the continuous level which will be used in the rest of this thesis. In particular, in Section 1.1 the primitive equations describing the large-scale oceanic and atmospheric circulation are derived; then the turbulent features are described in Section 1.2. Finally, the simplified models used in this thesis are summed up in Section 1.3, before discussing Schwarz methods in Section 1.4.

Symbol	Quantity	Unit
ρ	Density	$\mathrm{kg.m^{-3}}$
p	Pressure	$\mathrm{kg.m^{-1}.s^{-2}}$
$\mathbf{U}$	Velocity	$\mathrm{m.s^{-1}}$
θ	Potential temperature	K
$K_{u,\mathrm{mol}}$	Molecular viscosity	$\mathrm{m^{-1}.s^{-2}}$
$\mathbf{g}$	Gravity acceleration	$\mathrm{m.s^{-2}}$
$\mathbf{\Omega}$	Earth angular speed	$\mathrm{rad.s^{-1}}$
∇	Spatial Gradient	$\mathrm{m^{-1}}$
Δ	Spatial Laplacian	$\mathrm{m^{-2}}$

Table 1.1: Symbols used in Section 1.1. Bold letters indicate that the quantity lies in $\mathbb{R}^3$.

1.1 Derivation of the primitive equations

This section aims to present the so-called primitive equations, which are used to model the fluid dynamics in the inner parts of both the atmosphere and ocean. They represent a classical choice for studying climate and weather predictions.

1.1.1 Unaveraged primitive equations

We start from the *Navier-Stokes momentum equation* in a rotating frame which describes the evolution of the momentum $\rho\mathbf{U}$ (the symbols are given in Table 1.1):

$$\rho \underbrace{(\partial_t + \mathbf{U}\cdot\nabla)}_{\text{Material derivative}} \mathbf{U} = \underbrace{-\nabla p}_{\text{Pressure gradient}} + \underbrace{K_{u,\mathrm{mol}}\Delta\mathbf{U}}_{\text{Molecular diffusion}} - \underbrace{\rho\mathbf{g}}_{\text{Gravity}} - \underbrace{2\mathbf{\Omega}\times(\rho\mathbf{U})}_{\text{Coriolis effect}} \tag{1.1}$$

and the *continuity equation* which ensures conservation of mass:

$$\partial_t \rho = -\nabla\cdot(\rho\mathbf{U}) \tag{1.2}$$

In the three components of $\mathbf{U} = \begin{pmatrix} u \\ v \\ w \end{pmatrix}$, u and v correspond to the horizontal velocities (in x and y directions) and w is the vertical velocity (the vertical axis is noted with the letter z). Some common approximations simplify the two equations (1.1) and (1.2):

- *Spherical geoid approximation*: we assume that the earth is spherical and that the gravity acceleration is given by $\mathbf{g} = \begin{pmatrix} 0 \\ 0 \\ g \end{pmatrix}$ where $g \approx 9.81\mathrm{m.s^{-2}}$.

- *Traditional approximation*: We neglect the horizontal terms of the rotation vector $\mathbf{\Omega}$ involved in the Coriolis force: we assume that $\mathbf{\Omega} = \begin{pmatrix} 0 \\ 0 \\ f/2 \end{pmatrix}$ where f depends on the latitude. f is commonly referred to as the Coriolis frequency.
- *Hydrostatic fluid*: the vertical pressure gradient balances the gravity force: $\partial_z p = -\rho g$. The vertical acceleration is neglected compared to pressure and gravity. This approximation is usually done in large-scale simulations when the horizontal space step is larger than the vertical one by several orders of magnitude; it is typically the case in climate simulations.
- *Boussinesq approximation* [Boussinesq, 1903]: the density ρ is close to a constant ρ_0. The variation of density $\widetilde{\rho} = \rho - \rho_0$ is neglected except when it is multiplied by g computing in the pressure gradient $\partial_z p = -\rho g$. The atmosphere models rely on compressibility and do not use this approximation. However, we make the Boussinesq approximation for both domains as we assume that the compressibility effects are small close to the surface and that they can be neglected to study the surface layer.

We hence obtain the *unaveraged* primitive equations:

$$\begin{cases} \nabla \cdot \mathbf{U} & = 0 \\ \partial_t u + \nabla \cdot (\mathbf{U} u) & = -\dfrac{\partial_x p}{\rho_0} + K_{u,\mathrm{mol}} \Delta u + f v \\ \partial_t v + \nabla \cdot (\mathbf{U} v) & = -\dfrac{\partial_y p}{\rho_0} + K_{u,\mathrm{mol}} \Delta v - f u \\ \partial_z p & = -\rho g \end{cases} \tag{1.3}$$

where the vertical component of the velocity w is implicitly represented and can be obtained from $\nabla \cdot \mathbf{U} = 0$.

Stratification ρ is given by an equation of state, which only involves the temperature in our case (in particular, the effect of humidity (in the atmosphere) and salinity (in the ocean) are neglected here). A *neutral* stratification refers to a constant density along the vertical axis. Our focus will eventually be reduced to the vertical axis and we assume for this reason that the density is a constant along all directions. A consequence of the density being constant is that the temperature does not need to be computed to determine the velocity $\mathbf{U}$.

On the contrary, in a *stratified* case the density depends on the potential temperature θ through an equation of state:

$$\rho = \rho_{\mathrm{eos}}(\theta) \tag{1.4}$$

and θ is given by a transport-diffusion equation:

$$\partial_t \theta + \nabla \cdot (\mathbf{U} \theta) = K_{\theta,\mathrm{mol}} \Delta \theta + F_\theta \tag{1.5}$$

where $K_{\theta,\text{mol}}$ and F_θ are the molecular diffusivity and some forcing term. θ must be computed jointly with $\mathbf{U}$ to solve the system (1.3). The coupling between θ and $\mathbf{U}$ is done through the pressure gradient.

1.1.2 Reynolds decomposition

The solution of the system (1.3) contains very small scales which cannot be solved numerically for large domains such as the ocean or the atmosphere. It is hence usual to use the *Reynolds decomposition*, which consists in separating the variables into an "average" part which can be represented by the numerical schemes and a *turbulent* part which will be parameterized with appropriate turbulence closure schemes (detailed later in §1.2.1).

For $X = u, v, w$ or θ, we note

$$X = \underbrace{\langle X \rangle}_{\text{average part}} + \underbrace{X'}_{\text{turbulent part}} \tag{1.6}$$

where $\langle \cdot \rangle$ represents a *statistical* average which satisfies:

$$\begin{aligned} \langle X' \rangle &= 0 \\ \langle \partial_\beta X \rangle &= \partial_\beta \langle X \rangle, \quad \beta = x, y, z, t \\ \langle \langle \cdot \rangle \rangle &= \langle \cdot \rangle \\ \langle \langle X \rangle Y \rangle &= \langle X \rangle \langle Y \rangle \end{aligned} \tag{1.7}$$

Using those properties, the Reynolds decomposition of (1.3) gives a system of equations satisfied by the Reynolds-averaged quantities:

$$\begin{cases} \nabla \cdot \langle \mathbf{U} \rangle & = 0 \\ \partial_t \langle u \rangle + \nabla \cdot (\langle \mathbf{U} \rangle \langle u \rangle) & = -\frac{\partial_x p}{\rho_0} + K_{u,\text{mol}} \Delta \langle u \rangle + f \langle v \rangle - \nabla \cdot \langle \mathbf{U}' u' \rangle \\ \partial_t \langle v \rangle + \nabla \cdot (\langle \mathbf{U} \rangle \langle v \rangle) & = -\frac{\partial_y p}{\rho_0} + K_{u,\text{mol}} \Delta \langle v \rangle - f \langle u \rangle - \nabla \cdot \langle \mathbf{U}' v' \rangle \\ \partial_z p & = -\rho g \\ \partial_t \langle \theta \rangle + \nabla \cdot (\langle \mathbf{U} \rangle \langle \theta \rangle) & = K_{\theta,\text{mol}} \Delta \langle \theta \rangle + F_\theta - \nabla \cdot \langle \mathbf{U}' \theta' \rangle \\ \rho & = \rho_{\text{eos}}(\langle \theta \rangle) \end{cases} \tag{1.8}$$

From now on, this thesis will only focus the vertical terms $\langle w'u' \rangle$, $\langle w'v' \rangle$ and $\langle w'\theta' \rangle$ because the surface layer turbulent features are mainly limited to those terms. For the same reason, we restrict our spatial domain to one dimension: the equations model a vertical column of atmosphere and of ocean. Those are common simplifications to study vertical turbulent mixing problems. Finally, note that (1.8) shoult be completed with initial and boundary conditions: they will be given for our models of interest in §1.2.2.

The non-linear advective terms and the horizontal pressure gradient term absent from the one dimensional model will be taken into account through an external *geostrophic* forcing.

The latter represents the geostrophic equilibrium which is a state of the fluid in which the pressure gradient compensates the Coriolis effect. This geostrophic forcing reduces drastically the complexity of the system and keeps reasonable values for the variables.

The one-dimensional system of equations is the following:

$$\begin{cases} \partial_t\langle u\rangle + \partial_z\langle w'u'\rangle & = K_{u,\mathrm{mol}}\partial_z^2\langle u\rangle + f\left(\langle v\rangle - v_G\right) \\ \partial_t\langle v\rangle + \partial_z\langle w'v'\rangle & = K_{u,\mathrm{mol}}\partial_z^2\langle v\rangle - f\left(\langle u\rangle - u_G\right) \\ \partial_t\langle\theta\rangle + \partial_z\langle w'\theta'\rangle & = K_{\theta,\mathrm{mol}}\partial_z^2\langle\theta\rangle + F_\theta \\ \rho & = \rho_{\mathrm{eos}}(\langle\theta\rangle) \end{cases} \tag{1.9}$$

where u_G, v_G are the geostrophic velocity.

With this decomposition we obtain more unknown than equations because of the introduction of the terms $\langle w'u'\rangle, \langle w'v'\rangle$ and $\langle w'\theta'\rangle$: this is known as the turbulence closure problem. The quantities of interest are the averaged quantities $\langle u\rangle, \langle v\rangle, \langle\theta\rangle$: a *turbulence closure* defines a relation between the turbulent terms $\langle w'u'\rangle, \langle w'v'\rangle, \langle w'\theta'\rangle$ and those averaged quantities. The density ρ is not used explicitly in (1.9) but appear in the turbulence closure.

1.2 The turbulence

To tackle the turbulence closure problem, we now provide additional relations between the turbulent terms and the average quantities. We first detail a common choice of parameterization for the turbulence closure far from the surface and then (in §1.2.2) focus on the surface layer which acts as a bottom boundary condition for (1.9) in the atmosphere. The ocean case is discussed in §1.2.3.

1.2.1 Turbulence closure and kinetic energy

Boussinesq hypothesis From the observation that the turbulent term acts like a diffusion term oriented "down-gradient", the turbulent terms are approximated with the help of a "turbulent viscosity" K_u and a "turbulent diffusivity" K_θ:

$$\langle w'u'\rangle = -K_u\partial_z\langle u\rangle, \quad \langle w'v'\rangle = -K_u\partial_z\langle v\rangle, \quad \langle w'\theta'\rangle = -K_\theta\partial_z\langle\theta\rangle \tag{1.10}$$

This is known as the *Boussinesq hypothesis* ([Boussinesq, 1897], different from the Boussinesq *approximation* neglecting effects of compressibility)

The turbulent viscosity and diffusivity can be defined in a lot of different ways. A typical formulation for K_u, K_θ is

$$K_u = C_m l_m\sqrt{e}, \qquad K_\theta = \frac{C_m}{\mathrm{Pr}} l_m\sqrt{e} = \frac{K_u}{\mathrm{Pr}} \tag{1.11}$$

where C_m is a constant; the turbulent Prandtl number Pr indicates the ratio of the viscosity to the diffusivity; the mixing length l_m is a characteristic length of the turbulent flow and depends on the stratification. e is an important quantity often used in the turbulence models, the Turbulent Kinetic Energy (TKE):

$$e = \frac{1}{2}\left(\langle (u')^2\rangle + \langle (v')^2\rangle + \langle (w')^2\rangle\right) \tag{1.12}$$

The evolution equation for the TKE is

$$\partial_t e \;-\; \underbrace{\partial_z\left(K_e \partial_z e\right)}_{\text{diffusion with } K_e \propto K_u} \;=\; \underbrace{P}_{\substack{\text{source}\\ \text{(shear)}}} \;+\; \underbrace{B}_{\substack{\text{source/sink}\\ \text{(buoyancy)}}} \;-\; \underbrace{\epsilon}_{\text{dissipation rate}} \tag{1.13}$$

where $P > 0$ and B are terms denoting respectively the shear and buoyancy production of kinetic energy; $\epsilon > 0$ is the dissipation rate of TKE into heat.

P corresponds to the energy lost by $\langle u\rangle$ through the *shear* term $\partial_z\left(K_u \partial_z \langle u\rangle\right)$: to compute it, we multiply by $\langle u\rangle$ the equation $\partial_t\langle u\rangle = \partial_z(K_u \partial_z\langle u\rangle)$ and express the result as a function of the energy of the mean velocity $\langle u\rangle^2/2$. This gives (e.g. [Burchard, 2002], where the derivation is done both at the continuous and at the discrete level):

$$\partial_t\left(\frac{\langle u\rangle^2}{2}\right) - \partial_z\left(K_u \partial_z\left(\frac{\langle u\rangle^2}{2}\right)\right) = -K_u\left(\partial_z\langle u\rangle\right)^2 \tag{1.14}$$

where we deduce that $P = K_u\left(\left(\partial_z\langle u\rangle\right)^2 + \left(\partial_z\langle v\rangle\right)^2\right)$ is the energy *produced* by the shear.

A similar treatment with the density (whose diffusion term is multiplied by z instead of $\langle u\rangle$) gives that the potential energy is increased or reduced by $B = -K_\theta N^2$ where $N^2 = -g\partial_z\rho/\rho_0$ is the Brunt-Väisälä frequency. The dissipation rate ϵ can be parameterized by $\epsilon \propto \dfrac{e^{3/2}}{l_\epsilon(z)}$ where l_ϵ is a mixing length similar to l_m. This parameterization of ϵ gives the widely used *Prandtl's one-equation turbulence model*.

Finally, the one-dimensional evolution equation for the TKE is

$$\partial_t e = \underbrace{\partial_z\left(K_e \partial_z e\right)}_{\text{diffusion}} + \underbrace{K_u\left(\left(\partial_z\langle u\rangle\right)^2 + \left(\partial_z\langle v\rangle\right)^2\right)}_{\substack{\text{source}\\ \text{(shear)}}} \;-\; \underbrace{K_\theta N^2}_{\substack{\text{source/sink}\\ \text{(buoyancy)}}} \;-\; \underbrace{c_\epsilon \frac{e^{3/2}}{l_\epsilon(z)}}_{\text{dissipation}} \tag{1.15}$$

The equation (1.15) is used as a model of the turbulent energy: e is jointly integrated in time with $\langle \mathbf{U}\rangle, \langle\theta\rangle$ and is used to characterize the turbulent terms appearing in (1.9). From now on, the operator $\langle\cdot\rangle$ will be omitted and the letters u, v, θ will refer to the averaged variables $\langle u\rangle, \langle v\rangle, \langle\theta\rangle$.

This model is only accurate outside the surface layer. The latter offers boundary conditions for the turbulent terms and is discussed in the next §.

1.2.2 Law of the wall and Monin-Obukhov Similarity Theory

We call *surface layer* the area close to the ocean surface such that it responds to a change at the surface with a "short" timescale[1]. Wall modelling gives us a description of the surface layer and provides the boundary conditions for $\langle w'u' \rangle, \langle w'v' \rangle$ and $\langle w'\theta' \rangle$.

One of the main hypothesis of the wall modelling is that the interface is a rough surface. Indeed, for the atmosphere the ocean surface can be seen as rough: the wind cannot slip on the ocean which means that the velocity of the wind is zero relatively to the surface.

Neutral case We first present the case without stratification: [Kármán, 1930] noticed that the fluids close to rough surfaces present similarities and proposed a universal function based on dimensional analysis. Von Kármán also states that "the characteristic length of the flow pattern is proportional to [the distance to the wall]".

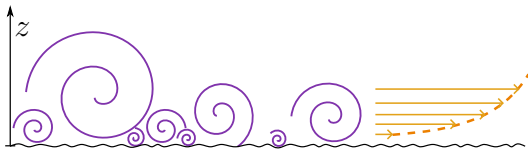

Figure 1.1: The characteristic size of the eddies (in purple) is proportional to the distance to the surface. The link between the size of the eddies and the logarithmic profile (in orange) is the constant flux approximation.

We list below the main features of the surface layer:

- the Coriolis effect and the geostrophic forcing are neglected (we assume that the effect of the proximity to the surface is predominant);
- it is well mixed: the governing equation is quasi-stationary (the surface layer immediately adjusts to the external parameters). As a consequence, the fluxes $\langle w'u' \rangle = -K_u \partial_z u$ and $\langle w'v' \rangle = -K_u \partial_z v$ are constant along the vertical axis.
- The vertical profile of K strongly depends on z. The size of the turbulent eddies at height z is proportional to the distance to the surface z (e.g. [Kawai and Larsson, 2012], see Figure 1.1). As a consequence, the turbulent viscosity linearly scales with $z + z_u$:

$$K_u \propto z + z_u \tag{1.16}$$

where z_u (detailed later) accounts for both the molecular viscosity and the geometry of the surface. In the stratified case we also have for the turbulent diffusivity $K_\theta \propto z + z_\theta$.

[1] In the literature, a boundary layer can also be defined as the region in which the fluid goes from zero velocity to the maximum velocity: this definition is however less adapted to the oceanic surface layer where the currents are driven by the surface wind.

We first assume that it is aligned with the direction of u: since the Coriolis effect is neglected and the turbulence is assumed isotropic, there is no rotation of the fluid inside the surface layer and we can assume without loss of generality that $v = 0$ (with a possible rotation of the axes). We will use the orientation of the wind speed later.

Let us define the *friction scale* $u_\star$ such that[2] $u_\star^2 = |\langle w'u' \rangle|$ and we have that $z_u = z_u(K_{\text{mol}}, u_\star)$ (see e.g. [Schlichting, 1960] for the choice of z_u as a constant of integration).

Finally, the profiles of u can be integrated vertically with the two equations

$$K_u \partial_z u = u_\star^2 \qquad K_u = \kappa u_\star (z + z_u) \tag{1.17}$$

and we obtain the law of the wall which reads:

$$u(z) - u(0) = \frac{u_\star}{\kappa} \ln\left(\frac{z + z_u}{z_u}\right) \qquad \forall z \in [0, \delta_{\text{a}}] \tag{1.18}$$

where $\kappa = 0.4$ is the Von Kármán constant. $\delta_{\text{a}} \approx 10$ m is the height of the atmospheric surface layer.

Remark *Generally, the law of the wall refers to an expression using* $\ln\left(\frac{z}{z_u}\right)$. *By using* $z + z_u$ *instead of* z, *the molecular sub-layer is included inside the law of the wall: we can hence use the profile of* u *for small* z *[Pelletier et al., 2021]. This formulation is not standard but it is appropriate for mathematical analyses and it does not change the results significantly.*

Stratified case The extension of the law of the wall to stratified fluids is called *Monin-Obukhov Similarity Theory*. It is used in all ocean-atmosphere coupled methods to our knowledge. The quasi-stationarity is also assumed for the temperature and $K_u \partial_z u$ and $K_\theta \partial_z \theta$ are both constant along the vertical axis. We can define a friction scale $\theta_\star$ for the potential temperature, such that

$$\langle w'\theta' \rangle = u_\star \theta_\star \tag{1.19}$$

Figure 1.2 summarizes the handling of the turbulent terms in the stratified case. To describe

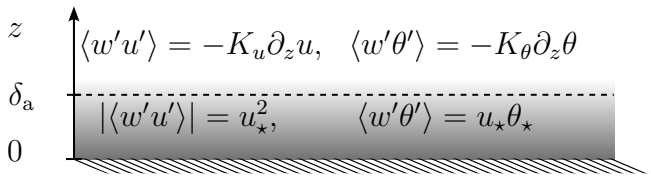

Figure 1.2: Summary of the turbulent term handling

the stratification, the *Obukhov length* is used:

$$L_{MO} = \frac{u_\star^2}{g\kappa \frac{\theta_\star}{\theta(\delta_{\text{a}})}} \tag{1.20}$$

[2] If $v \neq 0$ then the formula reads instead $u_\star^2 = \sqrt{\langle w'u' \rangle^2 + \langle w'v' \rangle^2}$.

which is the only characteristic length describing accurately the effect of the stratification in the surface layer [Obukhov, 1946]. $L_{MO} > 0$ in stable stratifications (where $\theta_\star > 0$) and $L_{MO} < 0$ in unstable stratifications (where $\theta_\star > 0$). The neutral case will be recovered for $L_{MO} \to \infty$, corresponding to $\theta_\star \to 0$.

Note that the potential temperature at the very top of the surface layer $\theta(\delta_\mathrm{a})$ is used. Indeed, the surface layer is usually driven by the values of u, θ computed at δ_a.

The difference with the neutral case is then contained in stability functions ϕ_m, ϕ_h:

$$\begin{aligned} K_u &\propto (z + z_u)\ \phi_m\left(\frac{z}{L_{MO}}\right) \\ K_\theta &\propto (z + z_u)\ \phi_h\left(\frac{z}{L_{MO}}\right) \end{aligned} \tag{1.21}$$

Typical stability functions are plotted in the left panel of Figure 1.3. A stable (resp. unstable)

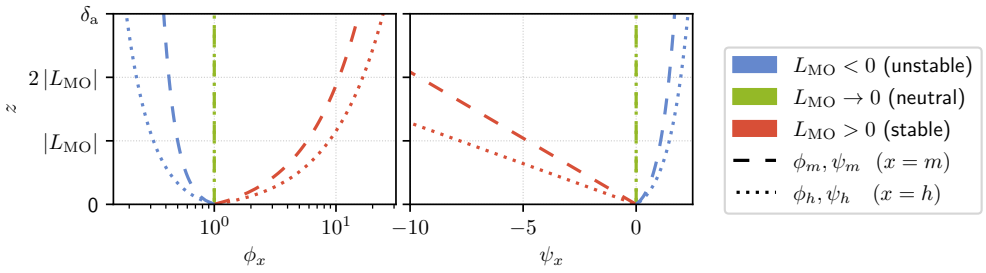

Figure 1.3: Typical profiles of the stability functions (left) and of their integrated form (right) in the surface layer $[0, \delta_\mathrm{a}]$. In the unstable and stable cases, $\frac{\delta_\mathrm{a}}{L_\mathrm{MO}}$ was arbitrarily set to respectively -3 and 3.

stratification leads to a decrease (resp. increase) of K_u, K_θ and $L_{MO} \to \infty$ indeed recovers the neutral case. To obtain the solution profiles, the *integrated forms* of the stability functions ψ_m, ψ_h are defined as

$$\psi_x\left(\frac{z}{L_{MO}}\right) = \int_0^{\frac{z}{L_{MO}}} \frac{1 - \phi_x(\zeta)}{\zeta} d\zeta, \qquad x = m, h \tag{1.22}$$

and we have

$$\begin{aligned} u(z) - u(0) &= \frac{u_\star}{\kappa}\left(\ln\left(1 + \frac{z}{z_u}\right) - \psi_m\left(\frac{z}{L_{MO}}\right)\right) \\ \theta(z) - \theta_s &= \frac{\theta_\star}{\kappa}\left(\ln\left(1 + \frac{z}{z_\theta}\right) - \psi_h\left(\frac{z}{L_{MO}}\right)\right) \end{aligned} \tag{1.23}$$

where θ_s is the surface temperature. Monin-Obukhov Similarity Theory is extensively used (e.g. [Basu and Lacser, 2017]); it is however not universally accepted in particular in very stable stratifications (see [Optis et al., 2014]).

Bulk algorithm Using (1.23) and the values of $u(\delta_a) - u(0)$ and $\theta(\delta_a) - \theta_s$ it is possible to compute the friction scales $u_\star, \theta_\star$. It is however not trivial as L_{MO} and z_u, z_θ depend themselves on $u_\star, \theta_\star$. The so-called "bulk algorithms" are designed for this task: they generally rely on a fixed-point method:

1. input: $u(\delta_a) - u(0)$ and $\theta(\delta_a) - \theta_s$;
2. choose a first guess $u_\star^{n=0}, \theta_\star^{n=0}$;
3. iteratively apply (1.23) (or (1.18) in the neutral case) to compute $u_\star^n, \theta_\star^n$ using $u_\star^{n-1}, \theta_\star^{n-1}$ in the expressions of z_u, z_θ and L_{MO};
4. at convergence i.e. $(u_\star^n, \theta_\star^n) \approx (u_\star^{n-1}, \theta_\star^{n-1})$, return the friction scales $u_\star = u_\star^n, \theta_\star = \theta_\star^n$ (or only $u_\star = u_\star^n$ in the neutral case)

The bulk formulation is generally part of the atmosphere models and is essential to compute the surface boundary conditions given the typical grid resolution in numerical models. The convergence of this fixed point method is discussed in [Thery, 2021].

1.2.3 Two-sided bulk

The ocean and atmosphere have not been distinguished in equations so far. From this point, we will use a subscript "o" for the ocean quantities and "a" for the atmosphere quantities. In Chapter 5 we will also consider the *oceanic surface layer*. In actual numerical models the sea surface temperature and the surface currents are often evaluated taking values below the surface. The common approach is to neglect the difference between the temperature and currents at the surface and typically one meter below. However, [Donlon et al., 2002] show that the difference between the surface temperature and the sub-surface temperature is approximatively constant for medium and strong winds but that it is harder to evaluate in stratified condition corresponding to winds slower than 6 m.s^{-1}). [Ward, 2006] "*show the strong dependency of the SST on air-sea heat flux estimates, with warm-layer errors of almost 60* W.m^{-2} *associated with intense stratification. This indicates the importance of the inclusion of the skin temperature for accurate calculation of latent, sensible, and net longwave heat fluxes*". In [Pelletier et al., 2021] a non-standard bulk formulation which uses Monin-Obukhov Similarity Theory (MOST) in the oceanic surface layer is derived. Figure 1.4 shows the difference between the one-sided and the two-sided bulk formulations. We follow this idea and incorporate to our coupled model an oceanic surface layer which follows the same principles as the surface layer in the atmosphere.

The application of MOST will yield the ocean counterpart of (1.23) with different friction scales. The continuity of the fluxes across the interface

$$\rho_a K_{u,a} \partial_z u_a|_{z=0} = \rho_o K_{u,o} \partial_z u_o|_{z=0}\,, \qquad \rho_a K_{u,a} \partial_z \theta_a|_{z=0} = \rho_o K_{u,o} \partial_z \theta_o|_{z=0} \tag{1.24}$$

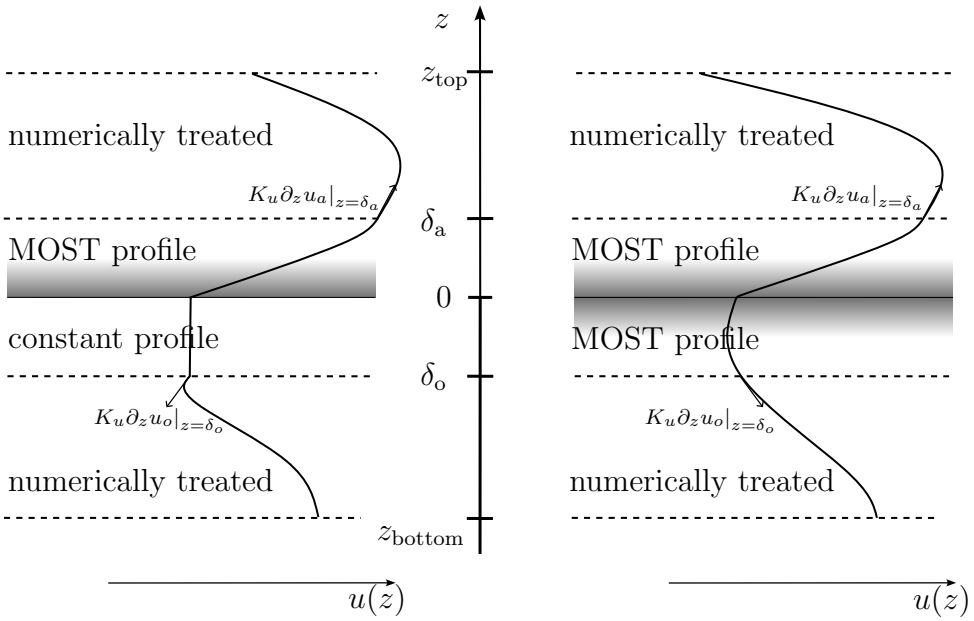

Figure 1.4: Comparison between one-sided (left) and two-sided (right) bulk formulations. The gradient discontinuity at zero comes from the difference in density. Adapted from [Pelletier et al., 2021].

adds the constraint that the friction scales of the ocean are $\sqrt{\frac{\rho_a}{\rho_o}}u_\star$ and $\sqrt{\frac{\rho_a}{\rho_o}\frac{c_a^p}{c_o^p}}\theta_\star$ where c_o^p, c_a^p are the heat capacities of water and air. We hence have for $\delta_o \leq z \leq 0$ (where $\delta_o \leq 0$ is the depth of the surface layer):

$$\begin{aligned} |K_u \partial_z u_o| &= \frac{\rho_a}{\rho_o} u_\star^2 \\ K_\theta \partial_z \theta_o &= \frac{\rho_a c_a^p}{\rho_o c_o^p} \theta_\star u_\star \end{aligned} \tag{1.25}$$

and the reconstruction of u_o, θ_o follow equations similar to (1.23):

$$\begin{aligned} u_o(0) - u_o(z) &= \frac{\rho_a}{\rho_o}\frac{u_\star}{\kappa}\left(\ln\left(1 - \frac{z}{z_u^o}\right) - \psi_m^o\left(-\frac{z}{L_{MO}}\right)\right) \\ \theta_s - \theta_o(z) &= \sqrt{\frac{\rho_a}{\rho_o}\frac{c_a^p}{c_o^p}}\frac{\theta_\star}{\kappa}\left(\ln\left(1 - \frac{z}{z_\theta^o}\right) - \psi_h^o\left(-\frac{z}{L_{MO}}\right)\right) \end{aligned} \tag{1.26}$$

If δ_o is set to zero, then there is no surface layer in the ocean and we call the surface layer *one-sided*. In the other case ($\delta_o < 0$) the surface layer is *two-sided*. The full coupled problem described until here is called "turbulent Ekman problem". It is summed up in §1.3.1.

1.3 A hierarchy of models

The analysis of coupling algorithms applied to the ocean-atmosphere system requires additional simplifications to be performed. These simplifications form a hierarchy of models which will be used in this thesis, from the most sophisticated to the most idealized:

1. **Turbulent Ekman**: described in the previous sections.
2. **Ekman**: additionally, the viscosity is constant in the atmosphere and in the ocean; the bulk formulation is simplified.
3. **Reaction-diffusion**: The surface layer is ignored; the density jump is neglected; the Coriolis term is replaced by a reaction term.

1.3.1 Neutral or Stratified Ekman problem with bulk and turbulent kinetic energy

The **Turbulent Ekman** model is the one described up till now. We restrict ourselves to a vertical column of atmosphere above a vertical column of ocean. For an easier handling, u and v will be represented together in a single complex variable $u^{\mathbb{C}} = u + iv$. The rotation of the Coriolis effect corresponds to a rotation in the complex plane. Indeed, rewriting (1.9) with an operator $\mathcal{L}$ corresponding to everything except the Coriolis term gives:

$$\begin{cases} \mathcal{L}u &= fv \\ \mathcal{L}v &= -fu = (i^2)fu \end{cases} \tag{1.27}$$

which can be written $\mathcal{L}u^{\mathbb{C}} = -ifu^{\mathbb{C}}$. In the following we will drop the $\mathbb{C}$ superscript and use a reaction term ifu for the Coriolis effect. The orientation of u will be noted $e_\tau = \frac{u}{|u|}$. Figure 1.5 gives the equations of the coupled system. In the *stratified* case, the potential temperature θ is jointly computed with the momentum u whereas in the *neutral* case the momentum is the only quantity of interest.

1.3.2 Ekman problem with a friction law

To our knowledge, the discrete analysis of the convergence of Schwarz methods currently exists only with a constant viscosity. This is a very strong assumption which corresponds to a vertical mixing not physically relevant. However, it allows a first attempt to study the effect of the surface layer on the convergence of Schwarz methods. The bulk methods used to parameterize the surface layer use implicitly defined applications which are hard to deal with in a convergence study. For this reason, we parameterize $u_\star$ with

$$u_\star^2 = C_D |U_a(\delta_\mathrm{a}) - U_o(\delta_\mathrm{o})|^2 \tag{1.28}$$

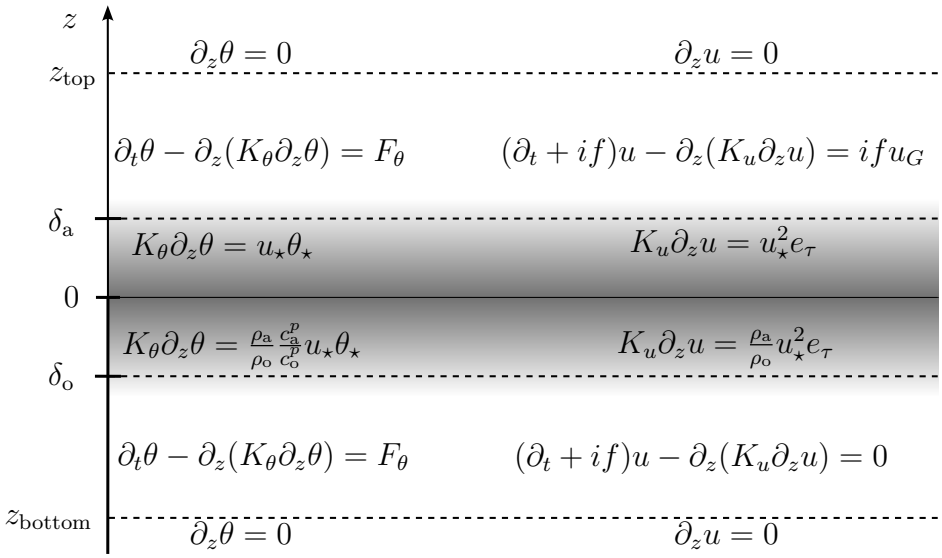

Figure 1.5: Summary of the turbulent ekman problem with a *two-sided* surface layer (where the initial conditions were omitted). The system with a *one-sided* surface layer corresponds to $\delta_o \to 0$.

where C_D is a constant and capital letter U denotes the solution for this non-turbulent Ekman problem. The right-hand side of the boundary condition of the turbulent term hence reads $C_D|U_a(\delta_{\text{a}}) - U_o(\delta_{\text{o}})|(U_a(\delta_{\text{a}}) - U_o(\delta_{\text{o}}))$. It corresponds to actual implementations in atmosphere models, except that C_D usually depends on $u_\star$. The simplifications are hence:

- constant viscosity in each fluid;
- neutral stratification;
- C_D is constant.

The surface layer is excluded from the computational domain and the reaction-diffusion equations are hence solved in $\Omega_{\text{a}} = [\delta_{\text{a}}, H_{\text{a}}]$ and in $\Omega_{\text{o}} = [H_{\text{o}}, \delta_{\text{o}}]$ where $H_{\text{a}} = z_{\text{top}}, H_{\text{o}} = z_{\text{bottom}}$. The model problem (analyzed in Chapter 6) reads:

$$\begin{aligned}
\partial_t U_j + ifU_j - \partial_z\left(\nu_j\partial_z U_j\right) &= g_j, \qquad (j = o, a) && \text{in } \Omega_j \times (0,T)\\
U_j(H_j, t) &= U_j^\infty(t), && t \in (0,T),\\
U_j(z,0) &= U_0(z), && \forall z \text{ in } \Omega_j,\\
\rho_o\nu_o\partial_z U_o(\delta_o,t) = \rho_a\nu_a\partial_z U_a(\delta_a,t) &= \mathcal{F}_{\text{sl}}(U_a(\delta_a,t) - U_o(\delta_o,t)), && t \in (0,T)
\end{aligned} \tag{1.29}$$

Table 1.2 gives the specific notations used for the Ekman problem.

Notations ($j = \mathrm{a}, \mathrm{o}$)	Quantities	Unit
U_j	fluids velocities	$\mathrm{m.s}^{-1}$
ν_j	constant viscosities	$\mathrm{m}^{-1}.\mathrm{s}^{-2}$
g_j	geostrophic forcing terms	$\mathrm{m.s}^{-2}$
U_j^{∞}	boundary values	$\mathrm{m.s}^{-1}$
$H_j(\to \infty)$	size of the domains	m
$T(\to \infty)$	length of the time windows	s
Ω_j	computational domains	-
$\mathcal{F}_{\mathrm{sl}}(\cdot) = \rho_a C_D \lvert\cdot\rvert(\cdot)$	simplified bulk method	-

Table 1.2: Notations used in Chapter 6.

1.3.3 Reaction-diffusion equations coupling with heterogeneous diffusion

To study in details the mechanisms involved in the discrete coupled system, we will also study the very idealized case where

- both viscosities are constant but possibly different;
- the law of the wall is not applied at the interface;
- $u(z,t) \in \mathbb{R}$ and if is replaced by $r \in \mathbb{R}$;
- we do not include the density ratio in the continuity of the flux at interface.

The coupled system is more symmetric and we note u_1, u_2 instead of u_o, u_a in Chapters 2 and 3.

$$\partial_t u_1 + (r - \nu_1 \partial_x^2) u_1 = f_1 \qquad (x,t) \in (-\infty, 0) \times]0, T] \qquad \text{(1.30a)}$$
$$\partial_t u_2 + (r - \nu_2 \partial_x^2) u_2 = f_2 \qquad (x,t) \in (0, +\infty) \times]0, T] \qquad \text{(1.30b)}$$
$$u_1(x,0) = u_{1,0}(x) \qquad x \in (-\infty, 0) \qquad \text{(1.30c)}$$
$$u_2(x,0) = u_{2,0}(x) \qquad x \in (0, +\infty) \qquad \text{(1.30d)}$$
$$u_1(0^-,t) = u_2(0^+,t) \qquad t \in [0,T] \qquad \text{(1.30e)}$$
$$\nu_1 \partial_x u_1(0^-,t) = \nu_2 \partial_x u_2(0^+,t) \qquad t \in [0,T] \qquad \text{(1.30f)}$$

Here, f_1 and f_2 stand for forcing terms and are not linked with the Coriolis effect. $r \in \mathbb{R}$ is a reaction term.

1.4 Schwarz methods for the ocean-atmosphere coupling

The coupled problems presented in Section 1.3 are numerically solved with coupling algorithms. Schwarz methods include a large diversity of coupling strategies relying on iteratively solving the subdomains separately and using boundary conditions as transmission conditions.

1.4.1 Current practices

Many ocean-atmosphere coupling methods are equivalent to performing one iteration of a Schwarz method. They splits the computation time into time windows and use the averaged information at the interface as transmission conditions. The coupling algorithms then iterate (once):

- either in parallel, where both models use information of the previous time windows (e.g. in CNRM [Voldoire et al., 2013] or in IPSL [Marti et al., 2010]);

- or sequentially, where the atmosphere model uses interface data from the previous time windows whereas the ocean uses the updated air-sea fluxes. This is the *atmosphere-first* method described in Figure 1.6 and used in the European Centre for Medium-Range Weather Forecasts [Mogensen et al., 2012] and by Environment and Climate Change Canada [Marti et al., 2021]. In the atmosphere-first method, the models can actually also be run in parallel by using the data of the ocean not of the previous time windows but from the one before.

Performing only one iteration and using the data of the previous time windows induces significant errors in the air-sea interactions [Marti et al., 2021].

1.4.2 Schwarz Waveform Relaxation

There are many Schwarz Waveform Relaxation methods as there are multiple choices for the boundary conditions for the interface. Moreover, the two domains can be run either simultaneously or sequentially. The analyses of convergence are similar and it is generally found that the convergence factor of the parallel version is the square root of the convergence factor of the sequential version. We restrict our study to the latter.

The Schwarz Waveform Relaxation applied to the reaction-diffusion equations coupling consists in solving at iteration k the system (1.30a, 1.30c) , with the *transmission operator* $\mathcal{B}_1$ prescribing the boundary condition with the information obtained at the previous iteration

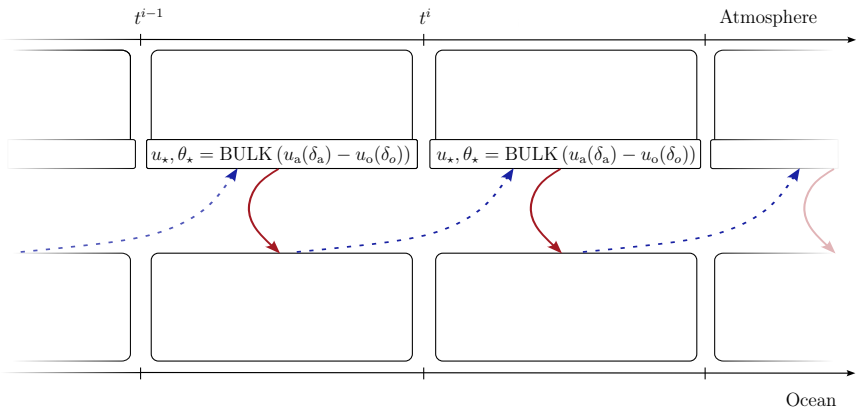

Figure 1.6: Atmosphere-first method: note that the models are integrated on time windows that are composed of a lot of internal time steps. In the stratified case, the BULK function takes $\theta_a(\delta_a) - \theta_o(\delta_o)$ as an additional parameter. The dashed arrows represent the transmission of $u_o(\delta_o)$ and the continuous arrows represent the transmission of the fluxes which depend on $u_\star, \theta_\star$.

$\mathcal{B}_2 u_2^{k-1}(0^+, t)$:

$$\partial_t u_1^k + (r - \nu_1 \partial_x^2) u_1^k = f_1 \qquad (x,t) \in (-\infty, 0) \times]0, T] \qquad (1.31a)$$

$$u_1^k(x, 0) = u_{1,0}(x) \qquad x \in (-\infty, 0) \qquad (1.31b)$$

$$\mathcal{B}_1 u_1^k(0^-, t) = \mathcal{B}_2 u_2^{k-1}(0^+, t) \qquad t \in [0, T] \qquad (1.31c)$$

The iteration is then completed by the resolution of the system in the other subdomain, using another transmission operator $\mathcal{C}_2$:

$$\partial_t u_2^k + (r - \nu_2 \partial_x^2) u_2^k = f_2 \qquad (x,t) \in (0, +\infty) \times]0, T] \qquad (1.32a)$$

$$u_2^k(x, 0) = u_{2,0}(x) \qquad x \in (0, +\infty) \qquad (1.32b)$$

$$\mathcal{C}_2 u_2^k(0^+, t) = \mathcal{C}_1 u_1^k(0^-, t) \qquad t \in [0, T] \qquad (1.32c)$$

The convergence is attained when $\mathcal{B}_1 u_1^k(0^-, t) = \mathcal{B}_2 u_2^k(0^+, t)$ over all the time window. The convergence study of Schwarz methods in the linear case with $T \to \infty$ relies on 3 steps:

1. consider the difference with the coupled solution u_j^∞: $e_j^k = u_j^k - u_j^\infty$. This amounts to set to zero the forcing terms f_j, the initial conditions $u_{j,0}$ and the boundary conditions.

2. Perform a Fourier (or Laplace) transform on all the equations: the convergence will be studied on the transformed variables $\widehat{e}_j^k(x, \omega)$ where ω is the time frequency variable.

3. Use the transmission operators to derive the convergence factor $\rho^{(c,c)}(\omega) = |\frac{\widehat{e}_j^k(0,\omega)}{\widehat{e}_j^{k-1}(0,\omega)}|$.

1.4.3 Schwarz Waveform Relaxation with a surface layer

In the presence of a surface layer, the Schwarz Waveform Relaxation takes a slightly different form. Indeed,

- the surface layer is excluded from the computational domains, creating a sort of "negative overlap": the informations are not transmitted at 0 but at δ_{a} and at δ_{o}.
- There is a nonlinear transmission condition: the bulk formulation. It computes the turbulent fluxes from the jump of u and θ across the interface.

Omitting external boundary conditions and initial conditions, a realistic version of the implementation of Schwarz methods for the ocean-atmosphere coupling in the neutral case would be:

$$(\partial_t + if)u_o^k - \partial_z\left(K_u \partial_z u_o^k\right) = if u_G^{\mathrm{o}} \qquad (z,t) \in \Omega_{\mathrm{o}} \times]0,T] \qquad (1.33a)$$

$$(\partial_t + if)u_a^k - \partial_z\left(K_u \partial_z u_a^k\right) = if u_G^{\mathrm{a}} \qquad (z,t) \in \Omega_{\mathrm{a}} \times]0,T] \qquad (1.33b)$$

$$K_u \partial_z u_o^k(\delta_o) = K_u \frac{\rho_a}{\rho_o} \partial_z u_a^k(\delta_{\mathrm{a}}) \qquad t \in]0,T] \qquad (1.33c)$$

$$|K_u \partial_z u_a^k(\delta_{\mathrm{a}})| = \mathrm{BULK}(u_a^k(\delta_{\mathrm{a}}) - u_o^{k-1}(\delta_o))^2, \qquad t \in]0,T] \qquad (1.33d)$$

In Chapters 4 and 5 the coupling is implemented with (1.33). However the implementation of the nonlinear boundary condition (1.33d) is not straightforward and for the analysis of the discrete version of the Ekman problem in Chapter 6 we use instead of (1.33d) the transmission condition:

$$\nu_a \rho_a \partial_z U_a^k(\delta_{\mathrm{a}}) = C_D \left|U_a^{k-1}(\delta_{\mathrm{a}}) - U_o^{k-1}(\delta_o)\right| \left(U_a^{k-1+\theta}(\delta_{\mathrm{a}}) - U_o^{k-1}(\delta_o)\right) \qquad (1.34)$$

where θ is a relaxation parameter and $U_a^{k-1+\theta} = (1-\theta)U_a^{k-1} + \theta U_a^k$. The implementation of (1.34) is direct: once U_a^{k-1}, U_o^{k-1} are known it is equivalent to a Robin condition.

We focus on *Schwarz Waveform Relaxation* (SWR) methods:

- *Waveform* means that the time domain is split in time intervals;
- *Relaxation* means that there are some parameters in the transmission conditions that can be optimized for a faster convergence. Despite the name suggesting that the parameter is a relaxation parameter this name is used for other types of parameters like the ones in Robin transmission conditions.

A particularity of the surface layer is that the values of $\delta_{\mathrm{a}}, \delta_{\mathrm{o}}$ are set to match the first grid level of the vertical grids. The surface conditions (1.33d) or (1.34) are hence linked with the numerical implementation. Moreover, some nonlinearities in (1.33d) can be simplified (see Chapter 4) through the discretization in time. The analysis of Schwarz methods at the semi-discrete level in space or even at the fully discrete level is hence adapted to (1.33).

Chapter 2

Discrete Analysis of Schwarz methods for a diffusion reaction problem with discontinuous coefficients

Table of contents

As seen in the previous chapter (§1.4.2) the convergence of Schwarz methods is usually studied on the continuous problem. For the inclusion of the surface layer in the convergence study it seems important to switch to the semi-discrete level or even to the fully discrete level. In this chapter the focus is on the effect of the discretization on the convergence speed of Schwarz methods. The reaction-diffusion equations coupling problem presented in Chapter 1 is used: the goal is to present the methodology that can be used to study the convergence of Schwarz methods in a discrete setting.

For this purpose, the article [Clement et al., 2022] was published in *SMAI Journal of Computational Mathematics* and is reported here. This article is built upon the following steps:

- Description of a methodology to study the convergence speed of Schwarz methods.
- Introduction of space and time schemes, notably a Finite Volume discretization based on quadratic spline reconstruction in space and a Diagonally Implicit Runge Kutta scheme in time.
- Numerical experiments and optimization of continuous and discrete convergence factors.

The key points of this chapter are:

- The difference between the discrete convergence factor and the continuous one and the expression of those convergence factors.
- The stability of the discrete schemes considered.
- An operator showing the specificity of multi-stage time schemes within Schwarz methods.
- The interactions between the time and space discretizations.
- The numerical optimization of the convergence factors.

Code availability All the theoretical results were numerically validated: the code used for the experiments in this chapter and all the others is available in a Zenodo archive (https://doi.org/10.5281/zenodo.7092357, [Clement, 2022]).

SMAI Journal of Computational Mathematics
Vol. 8, 99-124 (2022)

Discrete analysis of Schwarz waveform relaxation for a diffusion reaction problem with discontinuous coefficients

Simon Clement [1]
Florian Lemarié [1]
Eric Blayo [1]

[1] Univ. Grenoble Alpes, Inria, CNRS, Grenoble INP, LJK, Grenoble, France
E-mail address: simon.clement@grenoble-inp.org
E-mail address: florian.lemarie@inria.fr
E-mail address: eric.blayo@univ-grenoble-alpes.fr.

Abstract. In this paper, we investigate the effect of the space and time discretisation on the convergence properties of Schwarz Waveform Relaxation (SWR) algorithms. We consider a reaction-diffusion problem with discontinuous coefficients discretised on two non-overlapping domains with several numerical schemes (in space and time). A methodology to determine the rate of convergence of the classical SWR method with standard interface conditions (Dirichlet-Neumann or Robin-Robin) accounting for discretisation errors is presented. We discuss how such convergence rates differ from the ones derived at a continuous level (i.e. assuming an exact discrete representation of the continuous problem). In this work we consider a second-order finite difference scheme and a finite volume scheme based on quadratic spline reconstruction in space, combined with either a simple backward Euler scheme or a two-step "Padé" scheme (resembling a Diagonally Implicit Runge Kutta scheme) in time. We prove those combinations of space-time schemes to be unconditionally stable on bounded domains. We illustrate the relevance of our analysis with specifically designed numerical experiments.

2020 Mathematics Subject Classification. 65B99, 65L12, 65M12.

Keywords. Schwarz methods, Waveform relaxation, Semi-discrete.

1. Introduction

Schwarz Waveform Relaxation (SWR) methods [e.g. 14] are widely used in scientific computing for the parallel resolution of numerical models. These iterative methods have proved to be quite efficient, their performances being closely linked to a proper optimisation of their convergence rate. This convergence speed can indeed be improved thanks to several levers, in particular by designing more or less sophisticated interface conditions and by optimising their associated degrees of freedom (e.g. the weight between the Dirichlet and Neumann components within Robin interface conditions, or a relaxation parameter within Dirichlet-Neumann interface conditions). However the actual performances obtained in numerical experiments may be not as good as expected, and several recent studies [e.g. 1, 17, 31] showed that this can be attributed to the effect of the numerical discretisation. As a matter of fact, working at a continuous level neglects the impact of this discretisation, that may be rather significant. On the other hand, taking into account the discretised form of the equations for the optimisation of the convergence obviously reduces the scope of the results and their generality.

In the present paper, we address this optimisation of SWR methods at the discrete level in the context of 1-D diffusion-reaction equations. Such equations are relevant in many fields of application. For example (this was our initial motivation), they can be seen as a simplified formulation of the oceanic and atmospheric thermodynamics in the vicinity of the air-sea interface [e.g. 19], hence as a

This work was supported by the French national research agency through the ANR project "COCOA" (COmprehensive Coupling approach for the Ocean and the Atmosphere), grant ANR-16-CE01-0007. Florian Lemarié appreciates the funding from the SHOM/DGA under grant agreement No 19CP07.

toy model for ocean-atmosphere coupling. But more generally, these equations are also relevant for applications in porous media, electrochemistry, biology, electrical circuit simulations, etc [7, 26].

The diffusion-reaction equations have been widely studied in the context of Schwarz domain decomposition methods (e.g. [8, 11, 13, 24]). However the discrete optimisation of SWR method for these equations has been few addressed yet to our knowledge: the specific case of discrete duality finite volumes with backward Euler time discretisation has been investigated in [5] and [6], while complementary results are presented in the stationary case in [12, 15]. [29] addressed the semi-discrete (i.e. continuous in time) optimisation problem for second-order central and fourth-order compact finite differences, and [30] extended this work to the discrete case with a θ-scheme in time combined with second-order central finite differences in space. However, the analysis excludes a multi-physics setting and the optimisation requires overlapping domains.

Our aim here is to complement those preceding papers by studying the case of several discretisation schemes commonly used in the context of ocean-atmosphere modelling, and trying to take a step back to be fairly general in our methodology and conclusions. Section 2 presents our model problem, and briefly recalls about the SWR algorithm and its convergence rate computed from the continuous equations. Section 3 introduces the two time schemes (backward Euler and Diagonally Implicit Runge Kutta - DIRK) and the two space schemes (second-order central finite difference, and a finite volume scheme based on quadratic spline reconstruction) that we consider. The analytical expression of the semi-discrete convergence rate is computed for Dirichlet-Neumann and for Robin-Robin interface conditions. In Section 4, we prove the stability of the discrete schemes, and study the discrete convergence rate and the interactions between the discretisations in time and space. Then (Section 5), the theoretical speeds of convergence predicted by these continuous, semi-discrete and discrete analyses are compared in actual numerical experiments. We will see that significant differences may appear and emphasize the peculiar role of a centering operator involved in multi-step time schemes.

2. Model problem and Schwarz waveform relaxation algorithm

2.1. Model problem

As indicated previously, the model problem that will be considered in this paper is a reaction-diffusion problem, that reads:

$$\partial_t u_1 + (r - \nu_1 \partial_x^2) u_1 = f_1 \qquad (x,t) \in (-\infty, 0) \times]0, T] \tag{2.1a}$$

$$\partial_t u_2 + (r - \nu_2 \partial_x^2) u_2 = f_2 \qquad (x,t) \in (0, +\infty) \times]0, T] \tag{2.1b}$$

$$u_1(x,0) = u_{1,0}(x) \qquad x \in (-\infty, 0) \tag{2.1c}$$

$$u_2(x,0) = u_{2,0}(x) \qquad x \in (0, +\infty) \tag{2.1d}$$

$$u_1(0^-,t) = u_2(0^+,t) \qquad t \in [0,T] \tag{2.1e}$$

$$\nu_1 \partial_x u_1(0^-,t) = \nu_2 \partial_x u_2(0^+,t) \qquad t \in [0,T] \tag{2.1f}$$

where ν_1, ν_2, r are given positive constants. For the sake of simplicity we consider the same damping rate r in the two subdomains, but it is straightforward to extend our results to the case with two different values.

2.2. Schwarz waveform relaxation algorithm

To solve the coupled problem (2.1), a Schwarz waveform relaxation (SWR) algorithm can be set. Such algorithms are well-known and widely used in scientific computing, at least for domain decomposition problems [e.g. 23]. They are also particularly well-suited for coupled problems, since they

can naturally handle differences in the continuous formulations of the models to be coupled (dimensions, equations...) as well as in their discrete formulations (discretisation techniques, space and time steps...). A SWR algorithm applied to (2.1) reads

$$\partial_t u_1^k + (r - \nu_1 \partial_x^2) u_1^k = f_1 \qquad (x,t) \in (-\infty, 0)\times]0,T] \tag{2.2a}$$
$$u_1^k(x,0) = u_{1,0}(x) \qquad x \in (-\infty, 0) \tag{2.2b}$$
$$\mathcal{B}_1 u_1^k(0^-,t) = \mathcal{B}_2 u_2^{k-1}(0^+,t) \qquad t \in [0,T] \tag{2.2c}$$

then

$$\partial_t u_2^k + (r - \nu_2 \partial_x^2) u_2^k = f_2 \qquad (x,t) \in (0, +\infty)\times]0,T] \tag{2.3a}$$
$$u_2^k(x,0) = u_{2,0}(x) \qquad x \in (0, +\infty) \tag{2.3b}$$
$$\mathcal{C}_2 u_2^k(0^+,t) = \mathcal{C}_1 u_1^k(0^-,t) \qquad t \in [0,T] \tag{2.3c}$$

where $k \geq 1$ is an iteration index, and where $u_2^0(0^+,t)$ is chosen arbitrarily, or using previous calculations. This iteration loop is repeated until convergence of the sequences $(u_1^k)_k$ and $(u_2^k)_k$. The interface operators $\mathcal{B}_j$ and $\mathcal{C}_j$ $(j = 1, 2)$ are chosen such that (2.2) and (2.3) are well-posed, and that satisfying both relations $\mathcal{B}_1 u_1(0^-,t) = \mathcal{B}_2 u_2(0^+,t)$ and $\mathcal{C}_2 u_2(0^+,t) = \mathcal{C}_1 u_1(0^-,t)$ is equivalent to (2.1e) and (2.1f). This ensures that the converged solution satisfies the desired Dirichlet-Neumann interface conditions and thus is the solution of the initial coupled system (2.1).
This algorithm is said to be "multiplicative", while replacing u_1^k by u_1^{k-1} in (2.3c) would lead to a so-called "parallel" version which requires more iterations to converge but allows for a simultaneous resolution of (2.2) and (2.3) when implemented numerically.

2.3. General form of the continuous convergence rate

In order to study the convergence of the preceding SWR algorithm (2.2)-(2.3), let us introduce the errors $\mathfrak{e}_j^k(x,t) = u_j^k(x,t) - u_j(x,t)$ where $u_j(x,t)$ is the solution on domain j of (2.1).. Assuming that the operators $\mathcal{B}_j$ and $\mathcal{C}_j$ are linear, these errors satisfy:

$$\partial_t \mathfrak{e}_1^k + (r - \nu_1 \partial_x^2) \mathfrak{e}_1^k = 0 \qquad (x,t) \in (-\infty, 0)\times]0,T]$$
$$\mathfrak{e}_1^k(x,0) = 0 \qquad x \in (-\infty, 0)$$
$$\mathcal{B}_1 \mathfrak{e}_1^k(0^-,t) = \mathcal{B}_2 \mathfrak{e}_2^{k-1}(0^+,t) \qquad t \in [0,T]$$

and

$$\partial_t \mathfrak{e}_2^k + (r - \nu_2 \partial_x^2) \mathfrak{e}_2^k = 0 \qquad (x,t) \in (0, +\infty)\times]0,T]$$
$$\mathfrak{e}_2^k(x,0) = 0 \qquad x \in (0, +\infty)$$
$$\mathcal{C}_2 \mathfrak{e}_2^k(0^+,t) = \mathcal{C}_1 \mathfrak{e}_1^k(0^-,t) \qquad t \in [0,T].$$

A time Fourier transform can be performed, assuming that $T \to +\infty$ and extending $\mathfrak{e}_j$ to zero for $t < 0$. This leads to the following ordinary differential equations for the errors $\widehat{\mathfrak{e}}_j$ in Fourier space:

$$(i\omega + r)\, \widehat{\mathfrak{e}}_1^k - \nu_1\, \partial_x^2 \widehat{\mathfrak{e}}_1^k = 0 \qquad (x,\omega) \in (-\infty, 0) \times \mathbb{R} \tag{2.4a}$$
$$\mathcal{B}_1 \widehat{\mathfrak{e}}_1^k(0^-,\omega) = \mathcal{B}_2 \widehat{\mathfrak{e}}_2^{k-1}(0^+,\omega) \qquad \omega \in \mathbb{R} \tag{2.4b}$$

and

$$(i\omega + r)\, \widehat{\mathfrak{e}}_2^k - \nu_2\, \partial_x^2 \widehat{\mathfrak{e}}_2^k = 0 \qquad (x,\omega) \in (0, +\infty) \times \mathbb{R} \tag{2.5a}$$
$$\mathcal{C}_2 \widehat{\mathfrak{e}}_2^k(0^+,\omega) = \mathcal{C}_1 \widehat{\mathfrak{e}}_1^k(0^-,\omega) \qquad \omega \in \mathbb{R} \tag{2.5b}$$

where ω is the Fourier frequency. Hence the analytic expressions:

$$\widehat{\mathfrak{e}}_1^k(x,\omega) = A_k\, e^{\mu_1 x} \qquad \text{and} \qquad \widehat{\mathfrak{e}}_2^k(x,\omega) = B_k\, \mathfrak{e}^{-\mu_2 x} \tag{2.6}$$

where μ_j is the square root of $(r+i\omega)/\nu_j$ with positive real part (since $\mathfrak{e}_1(x) \to 0$ for $x \to -\infty$ and $\mathfrak{e}_2(x) \to 0$ for $x \to +\infty$).
Convergence factors can thus be defined, equal to $\widehat{\mathfrak{e}}_j^k/\widehat{\mathfrak{e}}_j^{k-1}$, i.e. A_k/A_{k-1} or B_k/B_{k-1}. The convergence rate of the SWR algorithm is thus equal to the module of these convergence factors. The link between (A_k, B_k) and (A_{k-1}, B_{k-1}) is provided by the interface conditions (2.4b) and (2.5b). In the particular case of Dirichlet-Neumann conditions $\mathfrak{e}_1^k(0^-,t) = \mathfrak{e}_2^{k-1}(0^+,t)$ and $\nu_2\,\partial_x\mathfrak{e}_2^k(0^+,t) = \nu_1\,\partial_x\mathfrak{e}_1^k(0^-,t)$, one gets $A_k = B_{k-1}$ and $-\nu_2\mu_2 B_k = \nu_1\mu_1 A_k$, which leads to $A_k/A_{k-1} = B_k/B_{k-1} = -(\nu_1\mu_1)/(\nu_2\mu_2) = -\sqrt{\nu_1/\nu_2}$. The convergence rate for infinite domains [1] is thus

$$\rho_{\mathrm{DN}}^{(\mathrm{c,c})} = \sqrt{\frac{\nu_1}{\nu_2}}. \tag{2.7}$$

The exponent (c, c) means that both the time and space dimensions have been treated in a continuous way to derive (2.7) whereas in the following we will study semi-discrete and fully discrete cases. Similarly, for so-called two-sided Robin interface conditions $\nu_1\,\partial_x\mathfrak{e}_1^k(0^-,t) + p_1\,\mathfrak{e}_1^k(0^-,t) = \nu_2\,\partial_x\mathfrak{e}_2^{k-1}(0^+,t) + p_1\,\mathfrak{e}_2^{k-1}(0^+,t)$ and $\nu_2\,\partial_x\mathfrak{e}_2^k(0^+,t) + p_2\,\mathfrak{e}_2^k(0^+,t) = \nu_1\,\partial_x\mathfrak{e}_1^k(0^-,t) + p_2\,\mathfrak{e}_1^k(0^-,t)$, the convergence rate reads:

$$\rho_{\mathrm{RR}}^{(\mathrm{c,c})} = \left| \frac{p_1 - \sqrt{\nu_2}\sqrt{i\omega + r}}{p_1 + \sqrt{\nu_1}\sqrt{i\omega + r}} \; \frac{p_2 + \sqrt{\nu_1}\sqrt{i\omega + r}}{p_2 - \sqrt{\nu_2}\sqrt{i\omega + r}} \right|.$$

3. Semi-discrete and discrete convergence rates

The discretisation in time (resp. space) uses a step Δt (resp. h) constant across subdomains $j = 1$ and $j = 2$. Time index is noted with the letter n whereas grid points are localised through the index m. The letter k denotes the Schwarz iterate.

From the analysis conducted in this section, we can derive several discrete and semi-discrete convergence rates. In the following, to characterize those convergence rates, we will use the unified notation $\rho_{\text{interface}}^{(\text{time,space})}$ where "interface" can be either "DN" for Dirichlet-Neumann or "RR" for Robin-Robin, "time" can be "c" for continuous, "BE" for backward Euler or "P2" for the second-order Padé scheme, and "space" is either "c" for continuous, or "FD" for finite difference or "FV" for finite volume. In this section we give the expression of ρ for various combinations of time and space discretisations and interface conditions.

Choosing the discretisation of a continuous problem requires to focus on some desirable properties (e.g. simplicity, accuracy, discrete conservation laws). Two properties arise when using Schwarz methods: the speed of convergence (characterized by ρ) and the difference between the converged solution and a so-called monolithic solution, which solves the problem discretised over the full domain $\Omega_1 \cup \Omega_2$ without any domain decomposition method. The latter difference should not exceed the order of accuracy w.r.t. the continuous problem; apart from that, it may be desirable for additional discrete properties to recover the monolithic solution at convergence up to the precision set to stop the iterations.

3.1. Time discretisation

In this subsection, the objective is to incorporate in the convergence analysis the impact of the time discretisation. The error in time will now be interpreted as a discrete signal $\{e(n)\}_{n=0}^{\infty}$ with constant

[1] For finite domains of size H, [27] gives $\rho_{DN}^{(\mathrm{c,c})} = \sqrt{\frac{\nu_1}{\nu_2}}\left|\coth\left(-H\sqrt{\frac{r+i\omega}{\nu_1}}\right)\tanh\left(H\sqrt{\frac{r+i\omega}{\nu_2}}\right)\right|$. With our numerical parameters the relative difference with (2.7) is smaller than 1% for $\omega \geq 10^{-3}\ s^{-1}$ without reaction and for all ω if $r \geq 10^{-3}\ s^{-1}$.

sampling Δt ($\Delta t > 0$) such that $e(n)$ approximates the continuous signal $\mathfrak{e}(t = n\Delta t)$. To play the role of a discrete equivalent of the Fourier transform used in the continuous analysis (see Sec. 2.3), we use the one-sided $\mathcal{Z}$-transform [e.g. 4] which is defined as

$$\widehat{e}(z) = \mathcal{Z}\left\{e(n)\right\} = \sum_{n=0}^{\infty} e(n) z^{-n}$$

where $z = \exp(s\Delta t)$ with Δt the sampling period and s a complex frequency. In the following we extensively use the property

$$\mathcal{Z}\left\{e(n+1)\right\} = z\left(\mathcal{Z}\left\{e(n)\right\} - e(0)\right) \tag{3.1}$$

knowing that $e(0) = 0$ in our context (the error is initially zero).

3.1.1. *One-step time schemes: a change of frequency variable*

Time discretisation of our model problem (2.1a)-(2.1b) applied to the errors (i.e. with $f_j = 0$) with a backward Euler scheme gives

$$\frac{e(n+1) - e(n)}{\Delta t} + (r - \nu\partial_x^2) e(n+1) = 0. \tag{3.2}$$

After a $\mathcal{Z}$-transform and using property (3.1), the semi-discrete equation (3.2) becomes

$$\left(\frac{z-1}{z\Delta t}\right) \widehat{e}(z) + (r - \nu\partial_x^2)\widehat{e}(z) = 0. \tag{3.3}$$

For one-step time schemes, using a $\mathcal{Z}$-transform instead of a Fourier transform is equivalent to performing a change of variable: the Fourier variable $s = i\omega$ is approximated in the $\mathcal{Z}$-domain by a s_d^{time}. For the backward Euler scheme it is obvious from (3.3) that $s_d^{\text{BE}}(z) = \dfrac{z-1}{z\Delta t}$. Once the approximation s_d associated to the temporal discretisation of interest has been found, the rest of the convergence analysis follows the same steps as the one in the continuous case and convergence rates accounting for the time discretisation can be derived. However this methodology only works for one-step time schemes using two time levels like Euler (forward or backward) or Crank-Nicholson, and for one-step time schemes using more time levels like Leapfrog. For more advanced time integration methods, for example used for realistic simulations of geophysical flows [e.g. 20, 28], the determination of convergence rates in the semi-discrete case is significantly more complicated, as shown in the next subsection.

3.1.2. *A two-step time scheme*

The analyses of two-step time schemes feature higher-order $\mathcal{Z}$-transformed differential equations. Another specificity of multiple-step time schemes is the time interpolation operator providing boundary and interface conditions to the intermediate steps. A similar temporal operator also appears when considering differing time steps [22], and has a significant impact on the convergence rate of Schwarz iterations.

Determination of the semi-discrete errors. We now consider the "Padé" two-step (P2) scheme proposed in [21] and [28] which, when applied to our model problem for the errors and reformulated, reads

$$\left(1 + \beta\Delta t\left(r - \nu\partial_x^2\right)\right) e^\star = \left(1 - (1-2\beta)\,\Delta t\left(r - \nu\partial_x^2\right)\right) e(n) \tag{3.4a}$$

$$\left(1 + \beta\Delta t\left(r - \nu\partial_x^2\right)\right) e(n+1) = e^\star \tag{3.4b}$$

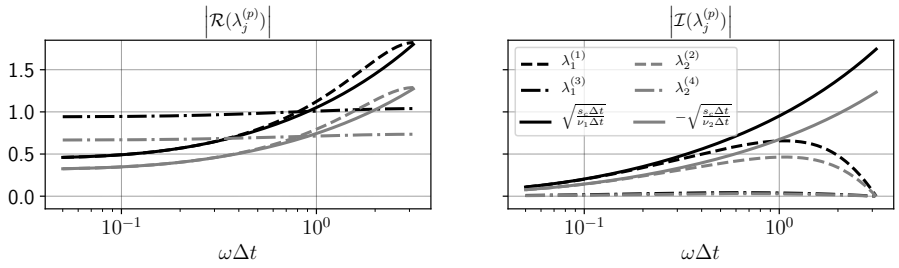

Figure 3.1. Absolute value of the real (left) and imaginary (right) parts of the four complex roots of the characteristic equation associated with the Padé time scheme with respect to $\omega\Delta t$. The non-dimensional frequency variable $\omega\Delta t$ naturally appears when dealing with time discretisations. The roots in the continuous case are also reported (solid lines). Parameter values are $\nu_1\Delta t = 0.5\ \mathrm{m}^2, \nu_2\Delta t = 1\ \mathrm{m}^2, r\Delta t = 0.1$ and $\omega\Delta t \leq \pi$.

with $\beta = 1 + 1/\sqrt{2}$. This scheme, implemented in the atmospheric model of the European Centre for Medium-Range Weather Forecasts (ECMWF), has the property to be second-order accurate, unconditionally stable and "monotonic damping" (i.e. shortest resolved scales are always more damped than the larger ones). This last property is not satisfied by a Crank-Nicolson scheme, which explains why this scheme is seldom used in "real-world" simulations. In a multiple step scheme like (3.4), a discrete frequency $s_d \in \mathbb{C}$ does not naturally appear. Indeed, combining the $\mathcal{Z}$-transforms of (3.4a) and (3.4b), we obtain

$$\left(z\left(1+\beta\Delta t\left(r-\nu\partial_x^2\right)\right)^2-\left(1-(1-2\beta)\,\Delta t\left(r-\nu\partial_x^2\right)\right)\right)\widehat{e}(x)=0 \tag{3.5}$$

where, unlike (3.3), derivatives with orders higher than that of the original equation are present. By analogy with the one-step case, we can rearrange (3.5) as $\left(s_d^{\mathrm{P2}}+r-\nu\partial_x^2\right)\widehat{e}=0$ to find that s_d^{P2} corresponds to the following differential operator:

$$s_d^{\mathrm{P2}} = s_d^{\mathrm{BE}} + \Delta t(r-\nu\partial_x^2)\left((2\beta-1)\,s_d^{\mathrm{BE}}+\beta^2(r-\nu\partial_x^2)\right)$$

where $s_d^{\mathrm{BE}} = \dfrac{z-1}{z\Delta t}$ is defined in §3.1.1. In multiple-step schemes, even if s_d takes the form of a differential operator and not of a complex scalar, a discrete analysis can nevertheless be pursued. However having no representation of the time discretisation as a simple change of variable means that the temporal scheme contribution to the convergence factor cannot be separated from the space scheme contribution. In the continuous-in-space case, we solve the fourth-order ordinary differential equation (3.5) whose solutions have general form $\widehat{e}(x) = \sum_{p=1}^{4} c^{(p)} \exp(\lambda^{(p)} x)$ with $\lambda^{(p)}$ the complex roots of the associated characteristic equation. If we note $\lambda^{(1)}, \lambda^{(2)}, \lambda^{(3)}, \lambda^{(4)}$ respectively $\lambda_{(+,-)}, \lambda_{(-,-)}, \lambda_{(+,+)}, \lambda_{(-,+)}$, the $\lambda^{(p)}$'s are

$$\lambda_{(\pm,\pm)} = \pm\frac{1}{\beta\sqrt{2\Delta t\nu}}\sqrt{z^{-1}+2\beta\Delta t s_d^{\mathrm{BE}}+2\beta^2\Delta t r \pm \sqrt{z^{-1}}\sqrt{z^{-1}+4\beta\,(1-\beta)\,\Delta t s_d^{\mathrm{BE}}}}$$

and the semi-discrete form of the errors is obtained. Two of the roots ($\lambda^{(2)}$ and $\lambda^{(4)}$) have a negative real part and the two others ($\lambda^{(1)}$ and $\lambda^{(3)}$) have a positive real part. The evolution of $\lambda^{(p)}$ with respect to $\omega\Delta t$ is plotted in Figure 3.1.

3.1.3. *Semi-Discrete convergence rates*

In the following we use the subscript j to distinguish the two subdomains. The boundary conditions at infinity lead to $c_1^{(2)} = c_1^{(4)} = 0$ and $c_2^{(1)} = c_2^{(3)} = 0$ and thus

$$\begin{aligned} \widehat{e}_1(x) &= c_1^{(1)} \exp(\lambda_1^{(1)} x) + c_1^{(3)} \exp(\lambda_1^{(3)} x), \qquad x \in \Omega_1 \\ \widehat{e}_2(x) &= c_2^{(2)} \exp(\lambda_2^{(2)} x) + c_2^{(4)} \exp(\lambda_2^{(4)} x), \qquad x \in \Omega_2 \end{aligned} \tag{3.6}$$

where $\Omega_1 = \mathbb{R}_-$ and $\Omega_2 = \mathbb{R}_+$. At this point we have four coefficients to set but only two relations provided by the transmission conditions (either Dirichlet-Neumann or Robin-Robin).

To close this system, it is necessary to provide interface conditions to $e^\star$ in (3.4). In the time domain and in the Dirichlet-Neumann case, those interface conditions are $e_1^\star(x=0) = e_2(t=t^\star, x=0)$ (with $t^\star = (n+1-\beta)\Delta t = (n-1/\sqrt{2})\Delta t$) for subdomain $j=1$ and $\nu_2 \partial_x e_2^\star(x=0) = \nu_1 \partial_x e_1(t=t^\star, x=0)$ for subdomain $j=2$. We note γ the frequency operator used to center the appropriate values at time $t^\star$. This interpolation or extrapolation operator γ will impact the convergence rate: the choice of γ is discussed below in the present subsection. Considering Dirichlet-Neumann interface conditions, the remaining coefficients in (3.6) are thus determined using the following conditions

$$\widehat{e}_1^k(x=0,z) = \widehat{e}_2^{k-1}(x=0,z) \tag{3.7a}$$

$$\nu_2 \partial_x \widehat{e}_2^k(x=0,z) = \nu_1 \partial_x \widehat{e}_1^k(x=0,z) \tag{3.7b}$$

$$\left(1 + \Delta t \beta (r - \nu_1 \partial_x^2)\right) z \widehat{e}_1^k(x=0,z) = \gamma(z)\, \widehat{e}_2^{k-1}(x=0,z) \tag{3.7c}$$

$$\nu_2 \left(1 + \Delta t \beta (r - \nu_2 \partial_x^2)\right) z \partial_x \widehat{e}_2^k(x=0,z) = \gamma(z)\, \nu_1 \partial_x \widehat{e}_1^k(x=0,z) \tag{3.7d}$$

where (3.4b) was used to treat the term $e_j^\star(x=0)$. Combining (3.7) and (3.6), we get after some algebra:

$$\begin{aligned} c_{1,k}^{(1)} &= (1-\tilde{\gamma}) \left(c_{2,k}^{(2)} + c_{2,k}^{(4)}\right) \\ c_{1,k}^{(3)} &= \tilde{\gamma} \left(c_{2,k}^{(2)} + c_{2,k}^{(4)}\right) \\ \nu_2 c_{2,k}^{(2)} \lambda_2^{(2)} &= (1-\tilde{\gamma})\, \nu_1 \left(c_{1,k-1}^{(1)} \lambda_1^{(1)} + c_{1,k-1}^{(3)} \lambda_1^{(3)}\right) \\ \nu_2 c_{2,k}^{(4)} \lambda_2^{(4)} &= \tilde{\gamma} \nu_1 \left(c_{1,k-1}^{(1)} \lambda_1^{(1)} + c_{1,k-1}^{(3)} \lambda_1^{(3)}\right) \end{aligned} \tag{3.8}$$

where

$$\tilde{\gamma} = \frac{z\left(1 + \beta \Delta t \left(r - \nu_1 \left(\lambda_1^{(1)}\right)^2\right)\right) - \gamma}{(1/\beta)\sqrt{1 + 4\beta(1-\beta)(z-1)}} = \frac{z\left(1 + \beta \Delta t \left(r - \nu_2 \left(\lambda_2^{(2)}\right)^2\right)\right) - \gamma}{(1/\beta)\sqrt{1 + 4\beta(1-\beta)(z-1)}}$$

$\tilde{\gamma}$ represents a weighted difference between two ways to estimate $e_j(x=0, t=t^\star)$: either via a time interpolation/extrapolation (by operator γ) or via the second step of the time scheme (3.4), represented by $z\left(1 + \beta \Delta t \left(r - \nu_j \lambda_j^2\right)\right)$. From (3.8) we can deduce a convergence rate defined here as $\rho_{\mathrm{DN}}^{(\mathrm{P2,c})} = \left|\varrho_{\mathrm{DN}}^{(\mathrm{P2,c})}\right| = \left|\dfrac{\nu_1 \partial_x \widehat{e}_1^k}{\nu_1 \partial_x \widehat{e}_1^{k-1}}\right|$ with

$$\varrho_{\mathrm{DN}}^{(\mathrm{P2,c})} = \frac{c_{1,k}^{(1)} \lambda_1^{(1)} + c_{1,k}^{(3)} \lambda_1^{(3)}}{c_{1,k-1}^{(1)} \lambda_1^{(1)} + c_{1,k-1}^{(3)} \lambda_1^{(3)}} = \varrho_{\mathrm{DN}}^{(\mathrm{c,c})} \sqrt{\frac{\nu_1}{\nu_2}} \left(\lambda_1^{(1)}(1-\tilde{\gamma}) + \lambda_1^{(3)} \tilde{\gamma}\right) \left(\frac{1-\tilde{\gamma}}{\lambda_2^{(2)}} + \frac{\tilde{\gamma}}{\lambda_2^{(4)}}\right).$$

Choosing γ for multi-step time schemes. When implementing a Schwarz method with multi-step time scheme, a special attention should be paid to the choice of the operator of projection onto the intermediate steps. In the case of the Padé time scheme, a first-order extrapolation from the current times ($\gamma_{\text{extr}} = z(1-\beta)+\beta$, which corresponds to the weights $1-\beta$ at t^{n+1} and β at t^n) suffices to guarantee a second-order accuracy of the solution.

Once the desired order of accuracy is attained, one may want to recover the monolithic solution (i.e. the solution that would have been obtained by discretising the problem directly on $\Omega_1 \cup \Omega_2$) to obtain additional discrete properties. This solution can only be obtained if γ perfectly matches the second step of the scheme, resulting in $\tilde{\gamma} = 0$. In such an ideal case, the analysis would be similar to a one-step scheme with the change of variable $s_d^{P2,\tilde{\gamma}=0} = \frac{1}{2\beta^2 \Delta t}\left(2\beta + (1-2\beta)\, z^{-1} - \sqrt{z^{-1}}\sqrt{z^{-1} + 4\beta\,(1-\beta)\,\Delta t s_d^{\text{BE}}}\right)$ and the operator of projection would be $\gamma^{\tilde{\gamma}=0}(z) = 1 - \frac{1}{2\beta}\left(1 - \sqrt{1 + 4\beta\,(1-\beta)\,(z-1)}\right)$.

However this operator $\gamma^{\tilde{\gamma}=0}(z)$ is non-local in time: indeed γ is a sum of $z^{\pm p}$ with z^0 representing the current time t_n and $z^{\pm p}$ the time $t_{n\pm p}$. If $\gamma(z)$ is not of this form, then its time counterpart is not local-in-time.

To ensure a small $\tilde{\gamma}$ and a local-in-time γ, a second-order Taylor development of $\gamma^{\tilde{\gamma}=0}(z)$ at $z=1$ can be made: $\gamma_{\text{imit}}(z) = z - \beta(z-1) - \beta\,(\beta-1)^2\,(z-1)^2$. This development is not in general a second-order accurate extrapolation. Indeed, instead of precisely computing the interface condition at $t = t^\star$, γ needs to mimic the second step of the time scheme (3.4). A more precise interpolation/extrapolation of $e(t = t^\star)$ would thus not give a smaller $\tilde{\gamma}$ because of the error committed by the second step of (3.4).

The choice of γ is crucial for the convergence speed, as can be seen in Figure 3.2 which compares the first-order extrapolation to the Taylor expansion of $\gamma^{\tilde{\gamma}=0}(z)$. This operator is a specific feature of the intermediate steps of multi-step time schemes.

Equivalence with DIRK scheme. The analysed Padé two-step time scheme is equivalent to a Diagonally Implicit Runge-Kutta scheme (DIRK) for space-periodic problems. However, in DIRK schemes as defined in [2]:

$$\left(1 + \beta\Delta t\left(r - \nu\partial_x^2\right)\right) e^{\star\star} = e(n)$$
$$\left(1 + \beta\Delta t\left(r - \nu\partial_x^2\right)\right) e(n+1) = e(n) + (1-\beta)\Delta t\left(r - \nu\partial_x^2\right) e^{\star\star}$$

the intermediate step is not performed in the same way. Consequently, $t^{\star\star}$ is not $\Delta t\,(n+1-\beta)$ but is $t^{\star\star} = \Delta t\,(n+\beta)$. When considering problems that are non-periodic in space, a Dirichlet interface condition on this $e^{\star\star}$ yields instead of (3.7c):

$$\widehat{e}_1^k(x=0,z) = \gamma(z)\left(1 + \beta\Delta t(r - \nu_1\partial_x^2)\right)\widehat{e}_2^{k-1}(x=0,z)$$

$\tilde{\gamma}$ and γ hence depend on the intermediate step and the convergence rate may differ from the P2 scheme. However canceling $\tilde{\gamma}$ never leads to a local-in-time $\gamma^{\tilde{\gamma}=0}(z)$ and the above discussion is extendable to other multi-step schemes as long as the steps involve space differentiation.

3.2. **Space discretisation**

We now consider the semi-discretisation in space at a given location $x = (m+l)h$ of the partial differential equation satisfied by the errors on subdomain Ω_j

$$\left(\partial_t + r\right) e_{m+l,j} - \nu_j \partial_x^2 e_j\Big|_{x=x_{m+l}} = 0$$

where we formulate the second-order derivative as a general flux divergence:

$$\nu_j \partial_x^2 e_j\Big|_{x=x_{m+l}} = \frac{\nu_j}{h}\left(\phi_{m+l+\frac{1}{2},j} - \phi_{m+l-\frac{1}{2},j}\right), \qquad \text{with } \phi_{m+l+\frac{1}{2},j} \approx \partial_x e_j|_{x=x_{m+l+\frac{1}{2}}} \tag{3.10}$$

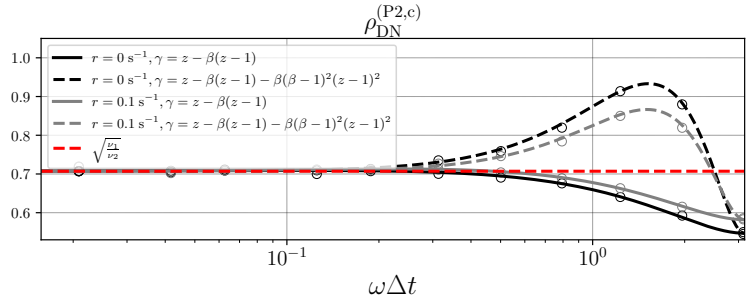

Figure 3.2. Convergence rate $\rho_{\mathrm{DN}}^{(\mathrm{P2,c})}$ with respect to $\omega\Delta t$ for different choices of the extrapolation function $\gamma(z)$ and different values of the reaction coefficient. Other parameter values are $\nu_1 = 0.5\,\mathrm{m}^2\,\mathrm{s}^{-1}, \nu_2 = 1\,\mathrm{m}^2\,\mathrm{s}^{-1}, \Delta t = 1\,\mathrm{s}$ and $\omega\Delta t \leq \pi$. The Finite Differences numerical experiment (circles) uses 10^4 vertical levels with a space step $h = 10^{-2}m$ and 300 time steps are performed.

where $l = 0$ or $l = \frac{1}{2}$ depending on the discretisation scheme (see Figure 3.3). In the following we introduce a second-order centered finite difference scheme for which $l = 0$ and a finite volume scheme based on quadratic splines reconstruction for which $l = \frac{1}{2}$. For both schemes we provide the form of the semi-discretised in space error in Fourier space for various interface conditions. Note that the domains are assumed of infinite size ($m \in \mathbb{Z}$) and the numerical experiments that will be presented later will also use a domain large enough for this approximation to be valid.

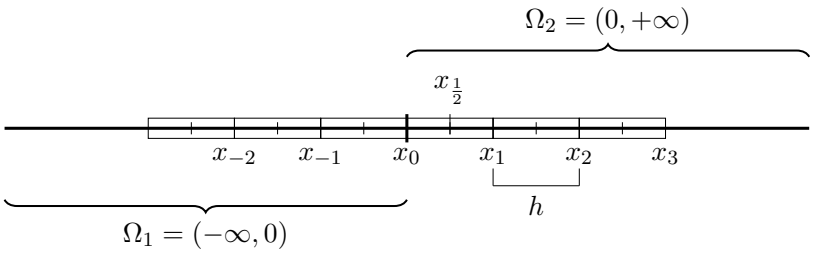

Figure 3.3. Computational grid in space for the discretisation in subdomains Ω_1 and Ω_2 with a common interface located at $x = x_0$. For the finite difference scheme presented in Sec. 3.2.1 the solution is computed at integer indices x_m ($m \in \mathbb{Z}$) and fluxes at half indices while for the finite volume scheme in Sec. 3.2.2 control volumes are centered on half indices, i.e. at $x_{m+1/2}$ ($m \in \mathbb{Z}$).

3.2.1. *Standard finite difference scheme*

We first consider a standard second-order finite difference space scheme for which the approximation of derivatives at cell interfaces is

$$\phi^{\mathrm{FD}}_{m+\frac{1}{2},j} = \frac{e_{m+1,j} - e_{m,j}}{h}.$$

Using (3.10), we easily find that the error at $x = x_m$ satisfies the differential equation

$$(\partial_t + r)e_{m,j} - \frac{\nu_j}{h^2}\left(e_{m+1,j} - 2e_{m,j} + e_{m,j}\right) = 0.$$

Denoting $\widehat{e}_{m,j}(s)$ the Fourier transform[2] of $e_{m,j}(t)$ with $s \in \mathbb{C}$, the error in the frequency domain satisfies

$$(\chi_j + 2)\,\widehat{e}_{m,j} - (\widehat{e}_{m-1,j} + \widehat{e}_{m+1,j}) = 0, \qquad \text{with } \chi_j = \frac{h^2(r+s)}{\nu_j}. \tag{3.11}$$

The general form of the semi-discretised error arising from a finite-difference spatial discretisation is

$$\widehat{e}^k_{m,1} = \alpha_k(s)\left(\sigma_1^+\right)^m + \gamma_k(s)\left(\sigma_1^-\right)^m$$
$$\widehat{e}^k_{m,2} = \beta_k(s)\left(\sigma_2^-\right)^m + \varsigma_k(s)\left(\sigma_2^+\right)^m$$

where $\sigma_j^{\pm} = \frac{1}{2}\left(2 + \chi_j \pm \sqrt{\chi_j\,(\chi_j+4)}\right)$. The α_k, γ_k, β_k, and ς_k coefficients are determined using the boundary conditions. The infinite domain assumption leads to $\gamma_k = \varsigma_k = 0$ and thus

$$\widehat{e}^k_{m,1} = \alpha_k(s)\left(\sigma_1^+\right)^m, \qquad \widehat{e}^k_{m,2} = \beta_k(s)\left(\sigma_2^-\right)^m. \tag{3.12}$$

3.2.2. *A finite volume scheme based on quadratic spline reconstruction*

A finite volume alternative to the standard finite difference scheme is derived in appendix A. This scheme offers the advantage to naturally handle the transmission conditions between the two non-overlapping domains and to guarantee that the converged solution is similar to the monolithic solution of the problem. Among others, [13] also uses a finite volume scheme for the same reasons. This scheme, denoted FV, corresponds to solving the tridiagonal system

$$\frac{1}{6}\phi^{\mathrm{FV}}_{m-1} + \frac{2}{3}\phi^{\mathrm{FV}}_{m} + \frac{1}{6}\phi^{\mathrm{FV}}_{m+1} = \frac{\bar{u}_{m+\frac{1}{2}} - \bar{u}_{m-\frac{1}{2}}}{h} \tag{3.13}$$

to get ϕ^{FV}_m, and to deduce the second-order derivative via (3.10). In (3.13), $\bar{u}_{m+\frac{1}{2}}$ is defined in a finite-volume sense as $\bar{u}_{m+\frac{1}{2}} = \dfrac{1}{h}\displaystyle\int_{x_m}^{x_{m+1}} u(x)\,dx$ with $h = x_{m+1} - x_m$. We then find that the error at $x = x_m$ satisfies the differential equation

$$(\partial_t + r)\left(\frac{1}{6}\phi^{\mathrm{FV}}_{m-1,j} + \frac{2}{3}\phi^{\mathrm{FV}}_{m,j} + \frac{1}{6}\phi^{\mathrm{FV}}_{m+1,j}\right) - \frac{\nu_j}{h^2}\left(\phi^{\mathrm{FV}}_{m+1,j} - 2\phi^{\mathrm{FV}}_{m,j} + \phi^{\mathrm{FV}}_{m-1,j}\right) = 0 \tag{3.14}$$

where using coefficients $(\frac{1}{12}, \frac{5}{6})$ instead of $(\frac{1}{6}, \frac{2}{3})$ would give a fourth-order accurate compact scheme [e.g. 18]. For convenience we will formulate here the convergence rate in terms of derivatives $\phi^{\mathrm{FV}}_{m,j}$ instead of the errors $\bar{e}_{m+\frac{1}{2},j}$ themselves. It is straightforward to show that both approaches lead to equivalent results. Unlike in the finite difference case where we applied a Fourier transform on $e_{m,j}(t)$, we apply it here on $\phi^{\mathrm{FV}}_{m,j}(t)$ in (3.14) to obtain the tridiagonal system

$$\left(\frac{\chi_j}{6} - 1\right)\widehat{\phi}^{\mathrm{FV}}_{m-1,j} + \left(\frac{2\chi_j}{3} + 2\right)\widehat{\phi}^{\mathrm{FV}}_{m,j} + \left(\frac{\chi_j}{6} - 1\right)\widehat{\phi}^{\mathrm{FV}}_{m+1,j} = 0 \tag{3.15}$$

where χ_j is defined in (3.11). The roots of the characteristic equation associated to (3.15) are $\lambda_j^{\pm} = \dfrac{1}{\frac{1}{\chi_j} - \frac{1}{6}}\left(\dfrac{1}{\chi_j} + \dfrac{1}{3} \pm \sqrt{\dfrac{1}{\chi_j} + \dfrac{1}{12}}\right)$ whose Taylor expansion gives

$$\lambda_j^{\pm} = 1 \pm \sqrt{\frac{r+s}{\nu_j}}h + \frac{h^2}{2}\left(\frac{r+s}{\nu_j}\right) + \mathscr{O}(h^3)$$

[2]When the time axis is continuous, it should be noted $\widehat{\mathfrak{e}}$. However we use the discrete notation $\widehat{e}$ because s can be either the continuous frequency variable or a one-step time scheme change of variable.

showing that $\lambda_j^{\pm}$ is an approximation of $e^{\pm\sqrt{\frac{r+s}{\nu_j}}h}$. The infinite domain assumption thus leads to

$$\left(\widehat{\phi}_{m,1}^{\mathrm{FV}}\right)^k = \upsilon_k(s)\left(\lambda_1^+\right)^m, \qquad \left(\widehat{\phi}_{m,2}^{\mathrm{FV}}\right)^k = \tau_k(s)\left(\lambda_2^-\right)^m \tag{3.16}$$

where $\upsilon_k(s) = \sqrt{\frac{s+r}{\nu_1}}\alpha_k(s)$ and $\tau_k(s) = -\sqrt{\frac{s+r}{\nu_2}}\beta_k(s)$ will be determined using the interface conditions.

3.2.3. *Interface conditions*

The discretisation of the interface conditions will allow to determine the semi-discrete errors in (3.12) and (3.16). In the following we will consider the discretisations of Dirichlet and Neumann interface conditions which also straightforwardly provide the discretisation of Robin interface conditions. We define $\eta_{j,\mathrm{operator}}$ to represent the boundary operator on domain j where "operator" can either be "dir" for a Dirichlet condition or "neu" for a Neumann condition. In a continuous setting, application of the Dirichlet-Neumann interface conditions would lead to

$$\eta_{1,\mathrm{dir}}\alpha_k(s) = \widehat{e}_1^k(0,s)\ \eta_{2,\mathrm{dir}}\beta_k(s) = \widehat{e}_2^k(0,s)$$
$$\eta_{1,\mathrm{neu}}\alpha_k(s) = \nu_1\partial_x\widehat{e}_1^k(0,s)\ \eta_{2,\mathrm{neu}}\beta_k(s) = \nu_2\partial_x\widehat{e}_2^k(0,s)$$

with $\eta_{1,\mathrm{dir}} = \eta_{2,\mathrm{dir}} = 1$, $\eta_{1,\mathrm{neu}} = \sqrt{\nu_1(s+r)}$, and $\eta_{2,\mathrm{neu}} = -\sqrt{\nu_2(s+r)}$. We now derive the discrete counterpart for $\eta_{j,\mathrm{operator}}$ in the finite difference and finite volume cases. In case we work on fluxes $\widehat{\phi}_j^k = \partial_x\widehat{e}_j^k$ rather than directly on the error $\widehat{e}_j^k$, we would simply have

$$\eta_{1,\mathrm{dir}}\alpha_k(s) = \sqrt{\frac{\nu_1}{s+r}}\,\widehat{\phi}_1^k(0,s)\ \eta_{2,\mathrm{dir}}\beta_k(s) = -\sqrt{\frac{\nu_2}{s+r}}\,\widehat{\phi}_2^k(0,s)$$
$$\eta_{1,\mathrm{neu}}\alpha_k(s) = \nu_1\widehat{\phi}_1^k(0,s)\ \eta_{2,\mathrm{neu}}\beta_k(s) = \nu_2\widehat{\phi}_2^k(0,s).$$

Finite differences interface conditions. Due to the grid arrangement we used (see Figure 3.3), the discretisation of the Dirichlet boundary condition in the finite difference case is trivial since a grid point is located on the interface at $x = x_0$. We thus obtain in (3.12) $\widehat{e}_{0,1}^k = \alpha_k(s)$ and therefore $\eta_{1,\mathrm{dir}}^{\mathrm{FD}} = 1$ which corresponds to the continuous case (same applies for subdomain 2). As far as the Neumann boundary condition is concerned, derivatives are naturally located at cell interfaces i.e. a half grid cell inside the domain and the finite difference discretisation requires a specific care. We propose two possible discretisations for the Neumann boundary condition:

- **Strategy #1 (naive discretisation)**: assume a Dirichlet-Neumann algorithm with Dirichlet on Ω_1 and Neumann on Ω_2. For the grid points at $x = x_1$ and $x = x_{-1}$ we have

$$\nu_1\partial_x^2 e_1\Big|_{x=x_{-1}} = \frac{\nu_1}{h}\left(\widetilde{\phi}_{-\frac{1}{2},1}^{\mathrm{FD}} - \phi_{-\frac{3}{2},1}^{\mathrm{FD}}\right)$$
$$\nu_2\partial_x^2 e_2\Big|_{x=x_1} = \frac{\nu_2}{h}\left(\phi_{\frac{3}{2},2}^{\mathrm{FD}} - \widetilde{\phi}_{\frac{1}{2},2}^{\mathrm{FD}}\right)$$

  where the $\widetilde{\cdot}$ fluxes are influenced by interface conditions. On Ω_1 we receive a Dirichlet condition $e_{m=0,1} = e_{\mathrm{int}}$ such that

$$\widetilde{\phi}_{-\frac{1}{2},1}^{\mathrm{FD}} = \frac{e_{\mathrm{int}} - e_{m=-1,1}}{h}$$

  and $\nu_1\phi_{-\frac{1}{2},1}^{\mathrm{FD}}$ is sent to subdomain 2 and used as a Neumann condition.

  On Ω_2 we have

$$\nu_2\widetilde{\phi}_{\frac{1}{2},2}^{\mathrm{FD}} = \nu_1\widetilde{\phi}_{-\frac{1}{2},1}^{\mathrm{FD}} \tag{3.17}$$

and the Dirichlet condition e_{int} for subdomain Ω_1 is computed as

$$e_{\text{int}} = e_{m=1,2} - h\widetilde{\phi}^{\text{FD}}_{\frac{1}{2},2}.$$

- **Strategy #2 (corrected discretisation)**: the previous interface discretisation has the drawback to be less accurate than inside the domains. We now derive a second-order accurate discretisation with the additional property of recovering the monolithic solution at convergence of the Schwarz iterations. Starting from the discretisation we would have at $x = x_0$ in the monolithic case:

$$(\partial_t + r)\, e|_{x=x_0} - \frac{1}{h}\left(\nu_2 \phi^{\text{FD}}_{\frac{1}{2},2} - \nu_1 \phi^{\text{FD}}_{-\frac{1}{2},1}\right) = 0$$

and considering that $e|_{x=x_0} = \frac{1}{2}\left(e_{m=0,j=1} + e_{m=0,j=2}\right)$ we end up with

$$\nu_1 \phi^{\text{FD}}_{-\frac{1}{2},1} + \frac{h}{2}(\partial_t + r)\, e_{0,1} = \nu_2 \phi^{\text{FD}}_{\frac{1}{2},2} - \frac{h}{2}(\partial_t + r)\, e_{0,2} \tag{3.18}$$

as a substitute for (3.17) in the naive case. It is similar to a so-called ghost-point method, but the time derivative in (3.18) will have a significant effect on the convergence. Using the reaction-diffusion equation to replace the time derivative would require to know in a given subdomain the diffusivity used in the other subdomain, which is not always practical.

To obtain unified notations between the naive and the corrected cases, we introduce a parameter κ_c in front of the $\frac{h}{2}$ coefficient in (3.18) such that for $\kappa_c = 0$ we recover the naive Neumann condition (3.17) and for $\kappa_c = 1$ we get the corrected discretisation (3.18).

Now going back to the determination of the $\eta_{j,\text{neu}}$ we apply a Fourier transform on the discretisations (3.17) and (3.18) and use (3.12) to obtain

$$\nu_1\, \partial_x \widehat{e}^k_1\Big|_{x=x_0} = \nu_1 \frac{\widehat{e}^k_{0,1} - \widehat{e}^k_{-1,1}}{h} + \kappa_c \frac{h}{2}(s+r)\widehat{e}^k_{0,1} = \alpha^k(s) \underbrace{\frac{\nu_1}{h}\left(1 - \frac{1}{\sigma_1^+} + \frac{\kappa_c}{2}\chi_1\right)}_{\eta^{\text{FD}}_{1,\text{neu}}}$$

$$\nu_2\, \partial_x \widehat{e}^k_2\Big|_{x=x_0} = \nu_2 \frac{\widehat{e}^k_{1,2} - \widehat{e}^k_{0,2}}{h} - \kappa_c \frac{h}{2}(s+r)\widehat{e}^k_{0,2} = \beta^k(s) \underbrace{\frac{\nu_2}{h}\left(\sigma_2^- - 1 - \frac{\kappa_c}{2}\chi_2\right)}_{\eta^{\text{FD}}_{2,\text{neu}}}.$$

Finite volume discretisation of interface conditions. In the case of the finite volume discretisation (3.13), the interface conditions are much easier and natural to discretise. Using the notations introduced in appendix A, the error at the interface reads as follows

$$e_1(x=0,t) = \mathscr{S}_{-\frac{1}{2}}(h/2) = \bar{e}_{-\frac{1}{2},1} + \frac{h}{6}\left(\phi^{\text{FV}}_{-1,1} + 2\phi^{\text{FV}}_{0,1}\right)$$
$$e_2(x=0,t) = \mathscr{S}_{\frac{1}{2}}(-h/2) = \bar{e}_{\frac{1}{2},2} - \frac{h}{6}\left(\phi^{\text{FV}}_{1,2} + 2\phi^{\text{FV}}_{0,2}\right)$$

where $\mathscr{S}$ is defined in (A.1) as the spline reconstruction of the solution. Considering the Fourier transform of (A.4) for $m = 0$ and $j = 1$, we obtain the expression of $\widehat{\bar{e}}_{-\frac{1}{2},1}$, and similarly, using (A.3)

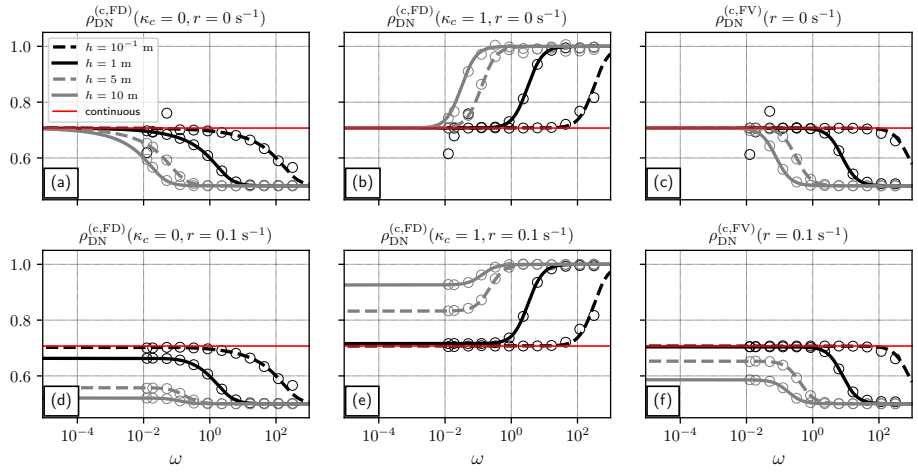

Figure 3.4. Convergence rates with Dirichlet-Neumann interface conditions with respect to ω for $s = i\omega$, $\nu_1 = 0.5$ m^2 s^{-1}, $\nu_2 = 1$ m^2 s^{-1}. The convergence rates represented correspond to (a) $\rho_{\mathrm{DN}}^{(\mathrm{c,FD})}$ for $\kappa_c = 0$ and $r = 0$ s^{-1}, (b) $\rho_{\mathrm{DN}}^{(\mathrm{c,FD})}$ for $\kappa_c = 1$ and $r = 0$ s^{-1}, (c) $\rho_{\mathrm{DN}}^{(\mathrm{c,FV})}$ for $r = 0$ s^{-1} (d),(e) and (f) are the same as (a),(b) and (c) but for $r = 0.1$ s^{-1}. Results are shown for different values of h: $h = 0.1$ m (black dashed lines), $h = 1$ m (black solid lines), $h = 5$ m (grey dashed lines), and $h = 10$ m (grey solid lines). The convergence rate in the continuous case is represented with red solid lines.

for $m = 0$ and $j = 2$, we obtain $\widehat{\widehat{e}}_{\frac{1}{2},2}$. We end up with:

$$\widehat{e}_1^k(0,s) = \left\{ \left(\frac{h}{3} + \frac{h}{\chi_1}\right) \left(\widehat{\phi}_{0,1}^{\mathrm{FV}}\right)^k + \left(\frac{h}{6} - \frac{h}{\chi_1}\right) \left(\widehat{\phi}_{-1,1}^{\mathrm{FV}}\right)^k \right\} = \alpha_k(s) \underbrace{\sqrt{\chi_1} \left[\left(\frac{1}{3} + \frac{1}{\chi_1}\right) + \left(\frac{1}{6} - \frac{1}{\chi_1}\right) \frac{1}{\lambda_1^+} \right]}_{\eta_{1,\mathrm{Dir}}^{\mathrm{FV}}}$$

$$\widehat{e}_2^k(0,s) = \left\{ \left(\frac{h}{\chi_2} - \frac{h}{6}\right) \left(\widehat{\phi}_{1,2}^{\mathrm{FV}}\right)^k - \left(\frac{h}{\chi_2} + \frac{h}{3}\right) \left(\widehat{\phi}_{0,2}^{\mathrm{FV}}\right)^k \right\} = \beta_k(s) \underbrace{\sqrt{\chi_2} \left[\left(\frac{1}{\chi_2} + \frac{1}{3}\right) - \left(\frac{1}{\chi_2} - \frac{1}{6}\right) \lambda_2^- \right]}_{\eta_{2,\mathrm{Dir}}^{\mathrm{FV}}}.$$

The expressions for $\eta_{j,\mathrm{Dir}}^{\mathrm{FV}}$ thus obtained can be further simplified and are such that $\eta_{j,\mathrm{Dir}}^{\mathrm{FV}} = \sqrt{1 + \frac{\chi_j}{12}}$. As far as the Neumann boundary condition is concerned, since we have constructed the scheme under the constraints $\partial_\xi \mathscr{S}_{1/2}(-h/2) = \phi_{0,2}^{\mathrm{FV}}$ and $\partial_\xi \mathscr{S}_{-1/2}(h/2) = \phi_{0,1}^{\mathrm{FV}}$ (see appendix A) we easily obtain $\eta_{1,\mathrm{neu}} = \sqrt{(s+r)\nu_1} = \dfrac{\nu_1\sqrt{\chi_1}}{h}$ and $\eta_{2,\mathrm{neu}} = -\sqrt{(s+r)\nu_2} = -\dfrac{\nu_2\sqrt{\chi_2}}{h}$ (i.e. the ones from the continuous case). As mentioned earlier our finite volume discretisation allows to recover at convergence the solution that would have been obtained by a numerical simulation over the union of the two subdomains up to the precision set to stop the iterations.

Table 3.1. Summary of the formulation of the $\eta_{j,\text{dir}}$ and $\eta_{j,\text{neu}}$ quantities which characterise the space discretisation through the interface operators. $\kappa_c = 1$ for the corrected FD case and $\kappa_c = 0$ in the naive FD case.

Space setting	$\eta_{1,\text{dir}}$	$\eta_{2,\text{dir}}$	$\eta_{1,\text{neu}}$	$\eta_{2,\text{neu}}$
Finite Volume	$\sqrt{1+\frac{\chi_1}{12}}$	$\sqrt{1+\frac{\chi_2}{12}}$	$\frac{\nu_1}{h}\sqrt{\chi_1}$	$-\frac{\nu_2}{h}\sqrt{\chi_2}$
Finite Difference	1	1	$\frac{\nu_1}{2h}\left(\chi_1(\kappa_c-1)+\sqrt{\chi_1(4+\chi_1)}\right)$	$\frac{\nu_2}{2h}\left(\chi_2(1-\kappa_c)-\sqrt{\chi_2(4+\chi_2)}\right)$
Continuous	1	1	$\frac{\nu_1}{h}\sqrt{\chi_1}$	$-\frac{\nu_2}{h}\sqrt{\chi_2}$

Table 3.2. Frequency variables s, which characterise the time discretisation. z can be replaced by $e^{i\omega\Delta t}$. Using a change of variable for a multi-step time scheme would neglect the projection operator γ (see section 3.1.3).

Time setting	s
Backward Euler	$s_d^{\text{BE}} = \frac{z-1}{z\Delta t}$
Padé scheme	$s_d^{\text{P2}} = \frac{z-1}{z\Delta t} - \Delta t\left((2\beta-1)\frac{z-1}{z\Delta t}\nu\left(\partial_x^2 - r\right) - \beta^2\nu^2\left(\partial_x^2 - r\right)^2\right)$
Continuous	$s_c = i\omega$

3.2.4. *Semi-Discrete convergence rates*

We study the semi-discrete in space case where the determination of $\alpha_k(s)$ and $\beta_k(s)$ in (3.12) can be easily done via the $\eta_{j,\text{dir}}$ and $\eta_{j,\text{neu}}$ expressions derived in previous subsection. In the Dirichlet-Neumann case, the transmission conditions lead to

$$\eta_{1,\text{dir}}^{\text{FD}}\alpha_k(s) = \eta_{2,\text{dir}}^{\text{FD}}\beta_k(s) \tag{3.19}$$

$$\eta_{2,\text{neu}}^{\text{FD}}\beta_k(s) = \eta_{1,\text{neu}}^{\text{FD}}\alpha_{k-1}(s) \tag{3.20}$$

and using the specific form of the η_j functions given in Tab. 3.1 we obtain the convergence rate (corresponding here to $|\alpha_k/\alpha_{k-1}|$)

$$\rho_{\text{DN}}^{(\text{c,FD})} = \left|\frac{\eta_{2,\text{dir}}^{\text{FD}}\eta_{1,\text{neu}}^{\text{FD}}}{\eta_{1,\text{dir}}^{\text{FD}}\eta_{2,\text{neu}}^{\text{FD}}}\right| = \left|\varrho_{\text{DN}}^{(\text{c,FD})}\right|, \qquad \varrho_{\text{DN}}^{(\text{c,FD})} = \frac{\nu_1}{\nu_2}\left(\frac{\chi_1(\kappa_c-1)+\sqrt{\chi_1(\chi_1+4)}}{\chi_2(1-\kappa_c)-\sqrt{\chi_2(\chi_2+4)}}\right)$$

where we recall that $\chi_j = h^2(s+r)/\nu_j$. For $h \to 0$ we have

$$\varrho_{\text{DN}}^{(\text{c,FD})} = \sqrt{\frac{\nu_1}{\nu_2}} + (\kappa_c - 1)\frac{h}{2}\left(\sqrt{\frac{\nu_1}{\nu_2}} - 1\right)\sqrt{\frac{s+r}{\nu_2}} + \mathscr{O}(h^2)$$

and thus $\rho_{\text{DN}}^{(\text{c,FD})}$ is a first-order (resp. second-order) approximation of the convergence rate $\rho_{\text{DN}}^{(\text{c,c})}$ in the continuous case for $\kappa_c = 0$ (resp. $\kappa_c = 1$). The Taylor expansion of $\varrho_{\text{DN}}^{(\text{c,FD})}$ suggests that the impact of numerical errors is small when ν_1 is close to ν_2 and ν_2 is large because the leading order term is scaled by $\dfrac{\sqrt{\nu_1}-\sqrt{\nu_2}}{\nu_2}$. In other situations the numerical results may deviate significantly from the continuous analysis as shown in Figure 3.4. Moreover, whatever the parameter values, $\lim\limits_{\omega\to\infty}\varrho_{\text{DN}}^{(\text{c,FD})}\Big|_{\kappa_c=1} = 1$ (with $\omega = \text{Im}(s)$) such that we can anticipate poor performances with finite differences for high temporal

frequencies. Figure 3.4 illustrates this aspect. On the other hand, $\lim_{\omega\to\infty} \varrho_{\mathrm{DN}}^{(\mathrm{c,FD})}\big|_{\kappa_c=0} = \dfrac{\nu_1}{\nu_2}$ which means that the algorithm converges faster (if $\nu_1 < \nu_2$) for high frequencies.

In the continuous analysis, the reaction coefficient r does not appear in the convergence factor which depends only on the diffusion coefficients ν_j $(j = 1, 2)$, see (2.7). However in the semi-discretised in space case with finite difference, the following asymptotes for low frequencies can be found:

$$\lim_{\omega\to 0} \varrho_{\mathrm{DN}}^{(\mathrm{c,FD})}\big|_{\kappa_c=1} = \sqrt{\frac{\nu_1}{\nu_2}}\left(\frac{1+\frac{rh^2}{4\nu_1}}{1+\frac{rh^2}{4\nu_2}}\right), \qquad \lim_{\omega\to 0} \varrho_{\mathrm{DN}}^{(\mathrm{c,FD})}\big|_{\kappa_c=0} = \sqrt{\frac{\nu_1}{\nu_2}}\frac{\sqrt{1+\frac{rh^2}{4\nu_1}}-\sqrt{\frac{rh^2}{4\nu_1}}}{\sqrt{1+\frac{rh^2}{4\nu_2}}-\sqrt{\frac{rh^2}{4\nu_2}}}$$

meaning that the discretisation affects the convergence factor even at lower frequencies compared to the continuous case. In particular, assuming that $\nu_1 < \nu_2$ we have $\left(\frac{1+\frac{rh^2}{4\nu_1}}{1+\frac{rh^2}{4\nu_2}}\right) > 1$. The convergence is thus slower and increasing r slows it down with the corrected FD discretisation. With the naive FD discretisation, the convergence is faster than predicted by the continuous analysis since $\frac{\sqrt{1+\frac{rh^2}{4\nu_1}}-\sqrt{\frac{rh^2}{4\nu_1}}}{\sqrt{1+\frac{rh^2}{4\nu_2}}-\sqrt{\frac{rh^2}{4\nu_2}}} < 1$, and increasing r accelerates the convergence. The impact of the reaction coefficient on the convergence rate is illustrated in Figure 3.4.

In the finite volume case, (3.19) and (3.20) also apply, and

$$\rho_{\mathrm{DN}}^{(\mathrm{c,FV})} = \left|\frac{\eta_{1,\mathrm{neu}}^{\mathrm{FV}}\eta_{2,\mathrm{dir}}^{\mathrm{FV}}}{\eta_{2,\mathrm{neu}}^{\mathrm{FV}}\eta_{1,\mathrm{dir}}^{\mathrm{FD}}}\right| = \left|\varrho_{\mathrm{DN}}^{(\mathrm{c,FV})}\right|, \qquad \varrho_{\mathrm{DN}}^{(\mathrm{c,FV})} = \frac{\nu_1\sqrt{\frac{\chi_1}{12+\chi_1}}}{\nu_2\sqrt{\frac{\chi_2}{12+\chi_2}}}.$$

$\varrho_{\mathrm{DN}}^{(\mathrm{c,FV})}$ is a second-order approximation of $\sqrt{\nu_1/\nu_2}$, since

$$\varrho_{\mathrm{DN}}^{(\mathrm{c,FV})} = \sqrt{\frac{\nu_1}{\nu_2}} + \frac{h^2}{24}\left(\frac{\nu_1-\nu_2}{\sqrt{\nu_1\nu_2}}\right)\left(\frac{s+r}{\nu_2}\right) + \mathscr{O}(h^4).$$

Just like in the finite difference case, the order of magnitude of the leading error term in the Taylor expansion for $h \to 0$ depends on the parameter values for ν_1 and ν_2. This is also the case for large values of ω since $\lim_{\omega\to\infty} \varrho_{\mathrm{DN}}^{(\mathrm{c,FV})} = \dfrac{\nu_1}{\nu_2}$. Like in the naive FD case, in the FV case the algorithm for $\nu_1 < \nu_2$ will be more efficient for high temporal frequencies than for low frequencies. This is confirmed by Figure 3.4.

The reaction coefficient does not affect the asymptote for large values of ω. However for small values of ω we have

$$\lim_{\omega\to 0} \varrho_{\mathrm{DN}}^{(\mathrm{c,FV})} = \sqrt{\frac{\nu_1}{\nu_2}}\sqrt{\frac{1+\frac{h^2 r}{12\nu_2}}{1+\frac{h^2 r}{12\nu_1}}}$$

which is systematically smaller than $\sqrt{\nu_1/\nu_2}$ for $\nu_1 < \nu_2$ as seen in Figure 3.4. Moreover, with both discretisations $\varrho_{\mathrm{DN}}^{(\mathrm{c,c})}$ is obtained when $\chi_j \to 0$. Consequently if $s + r \to 0$ the continuous convergence rate is recovered even when using a large h.

4. **Discrete case**

4.1. **Stability analysis**

In the following, we investigate the stability of the various combinations between the space and time discretisations. To this aim, we consider a Dirichlet condition on the external boundaries of the individual subproblems and Robin conditions at interface. It will thus be straightforward to extend the

results to a Dirichlet or a Neumann interface condition. The subscript j is omitted as the stability does not depend on it. To describe the space discretisations, we introduce two tridiagonal matrices $\boldsymbol{Y}^{\{\mathrm{FD,FV}\}}$ and two tridiagonal matrices $\boldsymbol{D}^{\{\mathrm{FD,FV}\}}$ such that both discretisations read in matrix form

$$\left((\partial_t + r)\boldsymbol{Y} - \frac{\nu}{h^2}\boldsymbol{D}\right)\boldsymbol{x} = \boldsymbol{c}$$

where $\boldsymbol{x}$ represents the variable u with the finite difference discretisation and the variable ϕ when using finite volumes. $\boldsymbol{c}$ has no effect on the stability, and consists of the possible forcing and contributions from the boundary and interface conditions.

$$\boldsymbol{Y}^{\mathrm{FD}} = \begin{pmatrix} \frac{1}{2}\kappa_c & & & & \\ & 1 & & 0 & \\ & & \ddots & & \\ & 0 & & 1 & \\ & & & & 0 \end{pmatrix}, \boldsymbol{D}^{\mathrm{FD}} = \begin{pmatrix} -(\frac{h}{\nu}\tilde{p}+1) & 1 & & & \\ 1 & -2 & 1 & & 0 \\ & \ddots & \ddots & \ddots & \\ 0 & & & -2 & 1 \\ & & & 0 & -1 \end{pmatrix} \tag{4.1}$$

and

$$\boldsymbol{Y}^{\mathrm{FV}} = \frac{1}{6}\begin{pmatrix} 2(3+\frac{h}{\nu}\tilde{p}) & \frac{h}{\nu}\tilde{p} & & & & \\ 1 & 4 & 1 & & & 0 \\ & \ddots & \ddots & \ddots & & \\ 0 & & 1 & 4 & 1 & \\ & & & 1 & 2 & \end{pmatrix}, \boldsymbol{D}^{\mathrm{FV}} = \begin{pmatrix} -\frac{h\tilde{p}}{\nu} & \frac{h\tilde{p}}{\nu} & & & & \\ 1 & -2 & 1 & & & 0 \\ & \ddots & \ddots & \ddots & & \\ 0 & & 1 & -2 & 1 & \\ & & & 1 & -1 & \end{pmatrix}. \tag{4.2}$$

$\tilde{p}$ is p_1 in the domain Ω_1 or $-p_2$ in the domain Ω_2.

4.1.1. *Theoretical tools for analysis*

The proof of stability relies on the hypothesis that $\tilde{p} \geq 0$ to obtain diagonally dominant matrices. The following propositions will help us proving the stability of both time schemes by providing the sign of the eigenvalues of $(\boldsymbol{D}^{\mathrm{FD}})^{-1}\boldsymbol{Y}^{\mathrm{FD}}$ and $(\boldsymbol{Y}^{\mathrm{FV}})^{-1}\boldsymbol{D}^{\mathrm{FV}}$.

Proposition 4.1. *For any $l \in \mathbb{C}$ such as $\Re(l) > 0$, $\det(\boldsymbol{D} - l\boldsymbol{Y}) \neq 0$ (i.e. $\det(\boldsymbol{D}^{\mathrm{FV}} - l\boldsymbol{Y}^{\mathrm{FV}}) \neq 0$ and $\det(\boldsymbol{D}^{\mathrm{FD}} - l\boldsymbol{Y}^{\mathrm{FD}}) \neq 0$).*

Proof. Using the hypotheses $\widetilde{p} \geq 0$ and $\Re(l) > 0$, we get:

- $\boldsymbol{D}^{\mathrm{FV}} - l\boldsymbol{Y}^{\mathrm{FV}}$ is strictly diagonally dominant and is hence non-singular.
- If $\kappa_c = 1$ or $\tilde{p} > 0$, $\boldsymbol{D}^{\mathrm{FD}} - l\boldsymbol{Y}^{\mathrm{FD}}$ is also strictly diagonally dominant.
- If $\kappa_c = 0$ and $\tilde{p} = 0$, the first row of $\boldsymbol{D}^{\mathrm{FD}} - l\boldsymbol{Y}^{\mathrm{FD}}$ is only weakly diagonally dominant. However the matrix is *weakly chained diagonally dominant* (see e.g. [3]) thus non-singular.

■

Proposition 4.2. *$\boldsymbol{D}^{\mathrm{FD}}$ and $\boldsymbol{Y}^{FV}$ are non-singular.*

Proof. $\boldsymbol{Y}^{FV}$ is strictly diagonally dominant and $\boldsymbol{D}^{FD}$ is weakly chained diagonally dominant. Hence both are non-singular. ■

From now on, the superscript FD or FV will be omitted when a sentence stands for both discretisations.

4.1.2. *Stability of the Backward Euler scheme*

The Backward Euler scheme corresponds to the operation $\boldsymbol{A}\boldsymbol{x}^{n+1} = \boldsymbol{Y}\boldsymbol{x}^n + \Delta t\boldsymbol{c}$ where $\boldsymbol{A} = ((1 + r\Delta t)\boldsymbol{Y} - \Gamma\boldsymbol{D})$ and Γ is the parabolic Courant number.

Proposition 4.3. *The Backward Euler scheme is unconditionally stable with FD and FV on a bounded domain with Dirichlet-Robin boundary conditions.*

Proof. It is easy to see that $\boldsymbol{A}$ is non-singular for $\tilde{p} \geq 0$. Let $\sigma \in \mathbb{C}^*$ be a non-zero eigenvalue of $\boldsymbol{A}^{-1}\boldsymbol{Y}$ and $\boldsymbol{v}$ the associated eigenvector. Then $\sigma\boldsymbol{A}\boldsymbol{v} = \boldsymbol{Y}\boldsymbol{v}$, i.e. $(\sigma(1 + r\Delta t) - 1)\boldsymbol{Y}\boldsymbol{v} = \sigma\Gamma\boldsymbol{D}\boldsymbol{v}$. Then:

- $\boldsymbol{v}$ is an eigenvector of $(\boldsymbol{Y}^{\mathrm{FV}})^{-1}\boldsymbol{D}^{\mathrm{FV}}$, with eigenvalue $\lambda = \frac{\sigma(1+r\Delta t)-1}{\Gamma\sigma}$.
- $\boldsymbol{v}$ is an eigenvector of $(\boldsymbol{D}^{\mathrm{FD}})^{-1}\boldsymbol{Y}^{\mathrm{FD}}$, with eigenvalue $1/\lambda$.

We assumed that $\sigma \neq 0$. By definition of λ, $\det(\boldsymbol{D} - \lambda\boldsymbol{Y}) = 0$. From proposition 4.1 we get that $\Re(\lambda) \leq 0$, and since $\sigma = \frac{1}{1+r\Delta t-\Gamma\lambda}$, we conclude that $|\sigma| \leq 1$. The moduli of all eigenvalues of $A^{-1}Y$ are therefore smaller or equal to 1: the Backward Euler scheme is unconditionally stable for finite differences and for finite volumes (for variable ϕ).
Special attention must be paid to the finite volume scheme if $r = 0$: $\overline{u}^n_{m+1/2} = \overline{u}^0_{m+1/2} + \frac{\nu}{h}\sum_{i=1}^n(\phi^i_{m+1} - \phi^i_m + \overline{f}^i_{m+1/2})$. To prove stability we need this serie to be bounded when $\overline{f} = 0$ and the eigenvalues should hence be of modulus strictly smaller than 1 in order to have geometric convergence. However the eigenspace associated to 1 is the kernel of $\boldsymbol{D}^{FV}$. In this eigenspace, $\phi_{m+1} - \phi_m = 0$. We hence conclude that the Backward Euler scheme is unconditionally stable also for the variable $\overline{u}$ of finite volumes. ∎

4.1.3. *Stability of the "Padé" two-step scheme*

The "Padé" two-step time scheme studied in this paper reads:

$$(\widetilde{\boldsymbol{Y}}_\beta - \beta\Gamma\boldsymbol{D})\boldsymbol{x}^\star = \left(\widetilde{\boldsymbol{Y}}_{2\beta-1} - (2\beta-1)\Gamma\boldsymbol{D}\right)\boldsymbol{x}^n + \beta\Delta t\boldsymbol{c}^\star - (2\beta-1)\Delta t\boldsymbol{c}^n$$
$$(\widetilde{\boldsymbol{Y}}_\beta - \beta\Gamma\boldsymbol{D})\boldsymbol{x}^{n+1} = \boldsymbol{Y}\boldsymbol{x}^\star + \beta\Delta t\boldsymbol{c}^{n+1}$$

where $\widetilde{\boldsymbol{Y}}_X = (1 + Xr\Delta t)\boldsymbol{Y}$ and $\Gamma = \frac{\nu\Delta t}{h^2}$.

Proposition 4.4. *The "Padé" two-step scheme is unconditionally stable with FD and FV on a bounded domain with Dirichlet-Robin boundary conditions.*

Proof. We study the eigenvalues of the matrix

$$\boldsymbol{A}_P = \left(\widetilde{\boldsymbol{Y}}_\beta - \beta\Gamma\boldsymbol{D}\right)^{-1}\boldsymbol{Y}\left(\widetilde{\boldsymbol{Y}}_\beta - \beta\Gamma\boldsymbol{D}\right)^{-1}\left(\widetilde{\boldsymbol{Y}}_{2\beta-1} - (2\beta-1)\Gamma\boldsymbol{D}\right).$$

From proposition 4.1:

- we get that all eigenvalues $\lambda \in \mathbb{C}$ of $(\boldsymbol{Y}^{\mathrm{FV}})^{-1}\boldsymbol{D}^{\mathrm{FV}}$ are such that $\Re(\lambda) \leq 0$.
- All non-zero eigenvalues $1/\lambda \in \mathbb{C}$ of $(\boldsymbol{D}^{\mathrm{FD}})^{-1}\boldsymbol{Y}^{\mathrm{FD}}$ are such that $\Re(\lambda) \leq 0$.

Let $\lambda \in \mathbb{C}$ defined as in one of the two cases above. The associated eigenvector is also an eigenvector of $\boldsymbol{A}_P$, with eigenvalue σ given by:

$$\sigma = \frac{1 + (2\beta-1)(r\Delta t - \Gamma\lambda)}{(1 + \beta(r\Delta t - \Gamma\lambda))^2}. \tag{4.3}$$

All the eigenvalues of $\boldsymbol{A}_P$ correspond to a λ in (4.3) or correspond to the zero eigenvalue of $(\boldsymbol{D}^{FD})^{-1}\boldsymbol{Y}^{FD}$. In the latter case, the eigenvectors correspond to the zero eigenvalue of $\boldsymbol{A}_P$.
Since Γ and $r\Delta t$ are strictly positive, we can restrain our study to the function $\tilde{\lambda} \mapsto \left|\frac{1+(2\beta-1)\tilde{\lambda}}{(1+\beta\tilde{\lambda})^2}\right|$, where $\tilde{\lambda} = r\Delta t - \Gamma\lambda$ belongs to the right half of the complex plane. A routine calculation returns that for $\beta = 1 + 1/\sqrt{2}$, this function is always strictly smaller than 1, except in $\tilde{\lambda} = 0$.
As for the Backward Euler scheme, the eigenspace associated to $\sigma = 1$ for finite volumes scheme is the kernel of $\boldsymbol{D}^{FV}$ and we can draw the same conclusion: the Padé two-step time scheme is unconditionally stable. ■

4.2. **Convergence rates**

In previous subsections we have derived the semi-discrete (either in time or in space) convergence rates of SWR algorithm. Now that we have checked that the various combinations of space and time discretisations are unconditionally stable for bounded domains, the discrete convergence rates can be studied.

In Section 3.1 we mentioned that adding the time-discretisation in the analysis amounts to a change of variable for one-step time schemes (i.e. s in the continuous case is replaced by $s_d(z)$ in the discretised case). We also showed that for a multiple-step time scheme, the convergence factor $\varrho_{\mathrm{DN}}^{(\mathrm{P2,space})}$ requires solving a characteristic equation which is fourth order. Because of the lengthy computations involved in the derivation of $\rho_{\mathrm{DN}}^{(\mathrm{P2,FD})}$ and $\rho_{\mathrm{DN}}^{(\mathrm{P2,FV})}$ we do not provide their analytical expressions.

4.2.1. *Dirichlet-Neumann boundary conditions*

The convergence with Dirichlet-Neumann operators does not directly depend on the discretisation in time itself. Indeed $\rho_{\mathrm{DN}}^{(\mathrm{BE,c})} = \rho_{\mathrm{DN}}^{(\mathrm{c,c})}$ and $\rho_{\mathrm{DN}}^{(\mathrm{P2,c})} = \rho_{\mathrm{DN}}^{(\mathrm{c,c})}$ (provided that $\tilde{\gamma} = 0$). With those transmission operators, changing the value of Δt in a semi-discrete in time convergence rate has no effect, whereas changing it in a fully-discrete case shows the effect of the time scheme on the semi-discrete in space convergence rate.

Figure 4.1 shows the fully-discrete convergence rate for several values of the parabolic Courant number $\Gamma = \nu\Delta t/h^2$. The convergence rate is not much affected by Backward Euler scheme (a, b, c). This is not surprising as the semi-discrete in time and the continuous convergence rates are identical. On the other hand, the Padé time scheme (d, e, f) interacts with the Finite Difference scheme differently when changing the operator γ. In the right column, the reaction coefficient r accelerates the convergence in low frequencies and damps the space-time interactions. We see that leaving aside the operator γ which plays an important role in high frequencies, the discretisation in time modifies only slightly the effect of the semi-discrete analysis in space.

4.2.2. *Robin-Robin boundary conditions*

Now considering the two-sided Robin-Robin case for one-step time schemes, we obtain the following general expression of the interface conditions:

$$p_1\eta_{1,\mathrm{dir}}\alpha_k(s) + \eta_{1,\mathrm{neu}}\alpha_k(s) = p_1\eta_{2,\mathrm{dir}}\beta_k(s) + \eta_{2,\mathrm{neu}}\beta_k(s)$$
$$p_2\eta_{2,\mathrm{dir}}\beta_k(s) + \eta_{2,\mathrm{neu}}\beta_k(s) = p_2\eta_{1,\mathrm{dir}}\alpha_{k-1}(s) + \eta_{1,\mathrm{neu}}\alpha_{k-1}(s).$$

The convergence rate thus reads:

$$\rho_{\mathrm{RR}} = \left|\frac{(p_2\eta_{1,\mathrm{dir}} + \eta_{1,\mathrm{neu}})\,(p_1\eta_{2,\mathrm{dir}} + \eta_{2,\mathrm{neu}})}{(p_2\eta_{2,\mathrm{dir}} + \eta_{2,\mathrm{neu}})\,(p_1\eta_{1,\mathrm{dir}} + \eta_{1,\mathrm{neu}})}\right|.$$

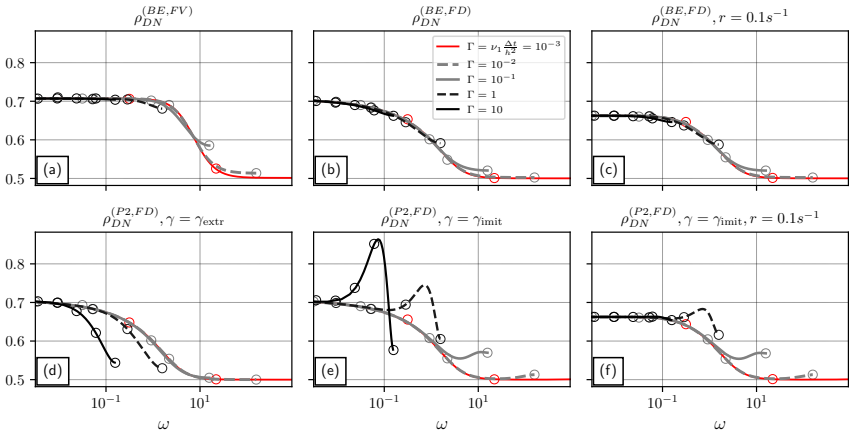

Figure 4.1. Interactions between space and time discretisations with Dirichlet-Neumann transmission operators. The relative importance of time and space schemes are characterised by the parabolic Courant number $\Gamma = \nu_1 \frac{\Delta t}{h^2}$: as $\Gamma \to 0$ (in red), the semi-discrete in space case is recovered, whereas the convergence rate gets closer to the semi-discrete in time setting when $\Gamma \to \infty$.

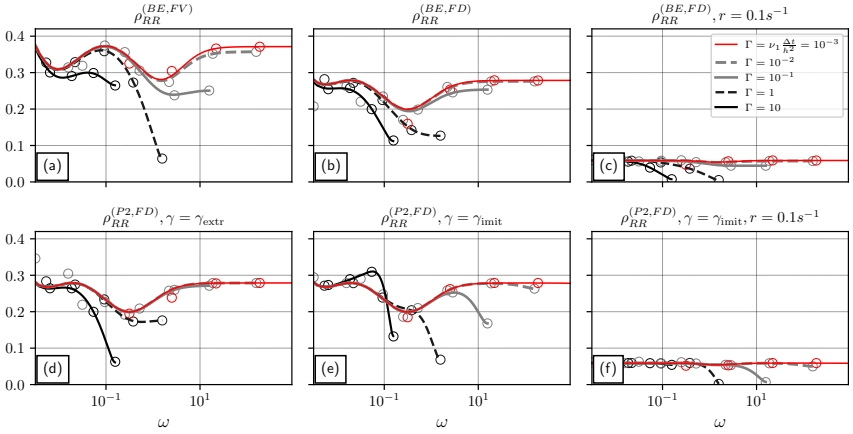

Figure 4.2. Convergence factor for different combinations of space and time discretisation schemes, with Robin *two-sided* transmission operators optimised in the semi-discrete in space setting (see Section 5.2). Several values of $\Gamma = \nu_1 \frac{\Delta t}{h^2}$ are compared. The reference red curve corresponds to the very small value $\Gamma = 10^{-3}$ (i.e. almost semi-discrete in space). The reaction coefficient r is set to 0, except in the right column ($r = 0.1$). The extrapolation is $\gamma_{\text{extr}} = z - \beta(z-1)$ whereas the imitation of the scheme is $\gamma_{\text{imit}} = \gamma_{\text{extr}} - \beta\,(\beta-1)^2\,(z-1)^2$.

The operators η, which depend on the space discretisation, are given in Table 3.1, and the frequency variables are given in Table 3.2. A semi-discrete or fully-discrete setting is thus characterized by a particular interface operator η_j^{Space} and frequency variable s_d^{Time}. Using s_d^{P2} here amounts to neglecting the operator γ. We instead use for $\rho_{\text{RR}}^{(\text{P2},\cdot)}$ an other expression based on subsection 3.1.3.

Section 5.2 will detail the optimisation of the convergence rate with Robin two-sided interface conditions and compare the discrete and semi-discrete cases. First results are shown in Figure 4.2 which presents the discrete convergence rates with several discretisations, reaction coefficients r and parabolic Courant number Γ. For each discretisation and reaction coefficient, Robin parameters are fixed as the optimal parameters for a semi-discrete in space setting, in order to focus on the effect of changing Γ. It is seen on this figure that the convergence speed is accelerated by Backward Euler (a,b,c) when Γ increases. When using Padé time scheme (d, e, f) the interaction with the finite difference scheme drastically depends on γ. In the right column, the presence of a reaction coefficient $r > 0$ accelerates the convergence.

The operator of projection γ becomes more important as Γ increases. However, unlike with Dirichlet-Neumann boundary conditions, the convergence is not slowed down by γ.

5. Numerical examples and optimisation of convergence rates

5.1. Comparison between numerical and theoretical convergence rates

Figures 3.2, 3.4, 4.1, 4.2 include circles that represent frequencies obtained in numerical simulations [3]. It is seen that the numerical simulation fits the theoretical convergence rates. In Figure 3.4 for $r = 0\ s^{-1}$ there are significant differences between the theoretical prediction with $h = 10^{-1}\ m$ with FD and FV. For lower frequencies, this comes from the limited size of the space domains (100 vertical levels are used in each Ω_j: the domains are smaller if h is smaller) In the highest frequencies, the difference comes from the time discretisation. Figure 3.4 uses $\Delta t = 10^{-2}\ s$ and 10^5 time steps to be close to a semi-discrete in space setting. In Figures 4.1 and 4.2 there are 10^4 time steps and 100 vertical levels are used in each Ω_j. The differences between the theoretical analysis and the numerical simulation come from the size of the time window. Other parameters are given in legend of Figure 5.1.

Note that for all the numerical experiments (including those in next section) we tried to obtain a robust estimation of the convergence rate by performing 10 simulations, each one being initialized with $e^{k=0}$ as a white noise. Schwarz algorithm is applied to each of these 10 simulations. The convergence rate is then computed as the rate of reduction of the standard deviation of the quantity $|p_1\widehat{e}_2^k + \nu_2\widehat{\phi}_2^k|$ over the 10 instances.

5.2. Optimisation of the two-sided Robin interface conditions

Having an accurate description of the discrete convergence rate is useful to maximize the convergence speed. One way to do so stems from the optimised Schwarz methods framework [e.g. 14]. In the present study we consider an optimisation based on the two-sided Robin interface conditions defined in §2.3. Those interface conditions introduce two free parameters p_1, p_2 which can be chosen to minimise the convergence rate:

$$(p_1, p_2) = \underset{(q_1,q_2)\in\mathbb{R}^2}{\operatorname{argmin}} \max_{\omega_{\min}\leq\omega\leq\omega_{\max}} \rho_{RR}^{(\cdot,\cdot)}(\omega; q_1, q_2). \tag{5.1}$$

Depending on which $\rho_{RR}^{(\cdot,\cdot)}$ is used, the optimal (p_1, p_2) may differ.

Figure 5.1 compares the solutions of (5.1) with convergence rates obtained through continuous, semi-discrete in time and discrete analyses. It illustrates how taking a discretisation into account in (5.1) affects the convergence speed of Schwarz algorithms. Several comments can be drawn (theoretical $\rho^{(\cdot,\cdot)}$ are referred to as "prediction" in the following sentences):

[3] The code used is available in the Zenodo archive (https://doi.org/10.5281/zenodo.6324930, [9])

Table 5.1. Ratio of the L2 norms between consecutive iterations ($k = 1, 2$) in cases shown in Figure 5.1. Left (resp. right) parts of the cells correspond to the BE (resp. P2) implementation and to the left (resp. right) of Figure 5.1. The first three lines of this Table are obtained with the FV implementation.

Optimised $\rho_{\mathrm{RR}}^{(\cdot,\cdot)}$ (left | right)	$\frac{\|\|p_1 e_2^{k=2}+\phi_2^{k=2}\|\|_2}{\|\|p_1 e_2^{k=1}+\phi_2^{k=1}\|\|_2}$ (with BE | P2)	Figure 5.1 color
$\rho_{\mathrm{RR}}^{(\mathrm{c,c})}$ | $\rho_{\mathrm{RR}}^{(\mathrm{c,c})}$	0.32 | 0.32	green
$\rho_{\mathrm{RR}}^{(\mathrm{BE,c})}$ | $\rho_{\mathrm{RR}}^{(\mathrm{P2,c})}$	0.28 | 0.29	red
$\rho_{\mathrm{RR}}^{(\mathrm{BE,FV})}$ | $\rho_{\mathrm{RR}}^{(\mathrm{P2,FV})}$	0.28 | 0.30	black
$\rho_{\mathrm{RR}}^{(\mathrm{BE,FD})}$ | $\rho_{\mathrm{RR}}^{(\mathrm{P2,FD})}$	0.23 | 0.23 (FD)	blue

- The first thing to notice is that predictions (triangles) are close to corresponding observed values (solid lines of the same color): they accurately fit, except for high frequencies in the continuous or semi-discrete cases.

- For high frequencies, the convergence rate predicted by the continuous analysis significantly differs from the actual convergence rate, which is here smaller than the prediction. For lower frequencies, the discretisations accurately describe the continuous equations. Similarly to Figure 4.1, changing the time step would shift the frequencies for which the continuous equation is well represented. As in the upper part of Figure 3.4 decreasing the space step would reduce the range of frequencies for which the continuous and semi-discrete in space convergence rate differ since r is small.

- The discrete analysis provides a better convergence (the maximum attained by the curves "Discrete" are smaller than the maximum attained by the other analyses) and Robin parameters change significantly between the discrete and continuous cases.

- The optimised convergence is faster for finite differences with $k_c = 0$ than for finite volumes. It is also the case for Dirichlet-Neumann in Figure 4.1 and Figure 3.4 indicates that this comes from the discretisation of the flux.

- The optimal Robin parameters minimise a 3-point equi-oscillation. If the prediction differs from the observed convergence at one of the equi-oscillation points then the minimisation can be refined.

- Table 5.1 gives the convergence rate of the L^2 norm in the time domain for each simulation of Figure 5.1. The maximum of $\rho_{RR}^{(\cdot,\cdot)}$ is an upper bound of the L^2 convergence rate and it is seen that the discrete analysis provides as well a better convergence in the time domain. It was checked that the convergence is linear for our choice of time window. For shorter time windows, the convergence is superlinear as shown in the case of SWR with Dirichlet boundary conditions in [10].

The choice was made here to illustrate the use of discrete analysis on Robin *two sided* transmission operators, but an optimisation could of course also be performed on a relaxation parameter within Dirichlet-Neumann interface conditions [e.g. 16, 22]. We quantitatively checked (not shown) that for values of ν_1, ν_2 varying in a range from 10^{-2} to 2 the results obtained are consistent with the one shown in Figure 5.1 for particular values of ν_1, ν_2. Our results hence seem quite robust to the values of these parameters.

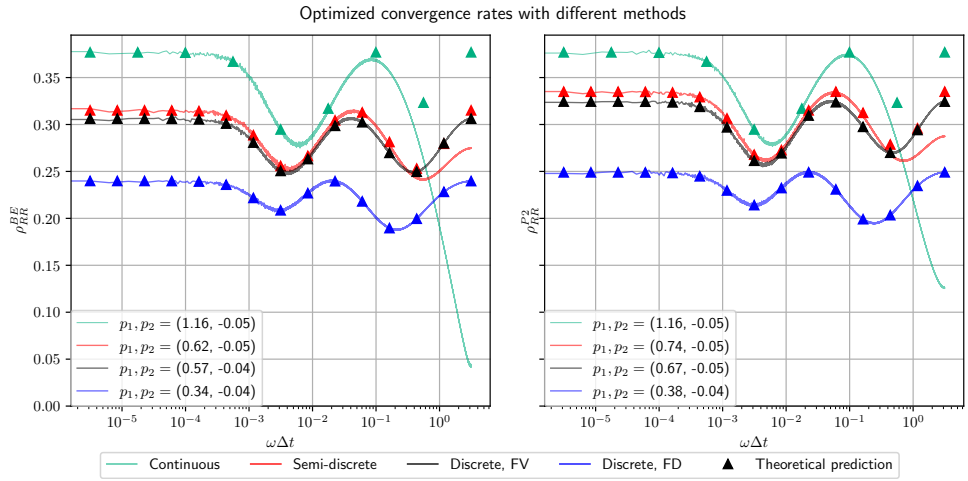

Figure 5.1. Comparison of theoretical (triangles) and observed (solid lines) convergence rates with Robin-Robin interface conditions. Theoretical values correspond to $\rho_{RR}^{(\mathrm{c,c})}(p_1,p_2)$ (green), $\rho_{RR}^{(\mathrm{Time,c})}(p_1,p_2)$ (red), $\rho_{RR}^{(\mathrm{Time,FV})}(p_1,p_2)$ (black) and $\rho_{RR}^{(\mathrm{Time,FD})}(p_1,p_2)$ (blue), with "Time" being BE (left panel) or P2 (right panel). The actual values of p_1, p_2 are chosen to solve the min-max optimisation problem of the corresponding convergence rate. Solid lines are Fourier-transformed observed convergence rates obtained by implementing SWR in a numerical code, with the finite difference scheme ($\kappa_c = 0$) for the blue line and the finite volume scheme in the other cases. Parameter values are $\nu_1 = 0.5$ m^{2}s^{-1}, $\nu_2 = 1$ m^{2}s^{-1}, $h = 1$ m, $r = 10^{-3}$ s^{-1}, $\Delta t = 1$ s and $\omega\Delta t \leq \pi$. For Padé time scheme, $\gamma = \gamma_{\mathrm{extr}}$. There are 100 space levels in each domain and 10^6 time steps.

6. Conclusion

In this paper, we studied an iterative Schwarz method defined for non-overlapping diffusion-reaction problems with discontinuous coefficients. We analytically examined the behavior of the discrete convergence rates of the iterative process for different spatial and temporal discretisations of the problem and compared it to the ones obtained in the conventional continuous case. In particular we showed that the discretisation of the interface conditions has a significant impact on the efficiency of the method. For example the standard ghost-point method used for the finite difference discretisation of Neumann conditions significantly slows down the convergence speed for high frequencies. As far as the time dimension is concerned, when a simple one-step time-stepping scheme is used the impact of the temporal discretisation on the convergence can be easily obtained from the continuous analysis via a change of frequency variable. However for more advanced multi-step schemes the algebra is more tedious because higher-order differential equations must be considered to determine the convergence rate. In this case we also showed that the projection operator required to provide the boundary data at the intermediate steps must be carefully chosen not to compromise the convergence speed. This aspect has been discussed for a diagonally implicit Runge-Kutta scheme and a two-step "Padé" scheme.

A discrete analysis provides a convergence rate more representative of the behavior observed in actual numerical experiments. Knowledge of the discrete convergence rate is thus advantageous for techniques aimed at optimising the speed of convergence either through approximation of the absorbing conditions or through a relaxation parameter weighting two or more successive iterates. We have

illustrated this aspect in the particular case of zeroth-order approximation of the absorbing conditions (i.e. using two-sided Robin-Robin interface conditions).

In future work the methodology developed in the present paper will be applied to problems with more complex interface conditions (e.g. in the presence of turbulent boundary layers) like the ones arising from wall laws in fluid dynamics. With applications to multi-physics settings in mind the approach presented in this paper can also be used to analyse the case of different time and space discretisations in each subdomain.

Appendix A. A finite volume scheme based on quadratic spline reconstruction

We present here a finite volume alternative to the standard finite difference scheme introduced in section 3.2.1. We construct a scheme based on quadratic splines. This scheme offers the advantage to naturally handle the transmission conditions between the two non-overlapping domains and to guarantee that the converged solution is similar to the monolithic solution of the problem. In this appendix we drop the j subscript to denote subdomains for the sake of clarity. As described in Figure 3.3, we consider control volumes delimited by x_m and x_{m+1} such that $h = x_{m+1} - x_m$ and the solution $\bar{u}_{m+\frac{1}{2}}$ has to be interpreted in a finite volume sense, i.e. $\bar{u}_{m+\frac{1}{2}} = \dfrac{1}{h}\displaystyle\int_{x_m}^{x_{m+1}} u(x)\,\mathrm{d}x$.

We suppose here that the subgrid reconstruction $u(x)$ on a volume centered at $x = x_{m+\frac{1}{2}}$ is given by a quadratic polynomial:

$$u(x) = \mathscr{S}_{m+\frac{1}{2}}(x - x_{m+\frac{1}{2}}) \quad \text{with } x - x_{m+\frac{1}{2}} \in \left[-\frac{h}{2}; \frac{h}{2}\right]$$
$$\mathscr{S}_{m+\frac{1}{2}}(\xi) = r_{m+\frac{1}{2},2}\xi^2 + r_{m+\frac{1}{2},1}\xi + r_{m+\frac{1}{2},0}.$$

Consistent with (3.10) in section 3.2, we note ϕ_m^{FV} the approximation of the derivative of u at the interface between volumes $m - \frac{1}{2}$ and $m + \frac{1}{2}$. The coefficients $r_{m+\frac{1}{2},p}$ in $\mathscr{S}_{m+\frac{1}{2}}(\xi)$ are chosen to satisfy the following constraints:

(1) $\dfrac{1}{h}\displaystyle\int_{-h/2}^{h/2} \mathscr{S}_{m+\frac{1}{2}}(\xi)\, d\xi = \bar{u}_{m+\frac{1}{2}}$

(2) $\partial_\xi \mathscr{S}_{m+\frac{1}{2}}(-h/2) = \phi_m^{\mathrm{FV}}$

(3) $\partial_\xi \mathscr{S}_{m+\frac{1}{2}}(h/2) = \phi_{m+1}^{\mathrm{FV}}$.

Those constraints, imposing the continuity of ϕ between two neighboring volumes and the consistency with $\bar{u}_{m+\frac{1}{2}}$, provide $r_{m+\frac{1}{2},p}$ coefficients such that:

$$\mathscr{S}_{m+\frac{1}{2}}(\xi) = \bar{u}_{m+\frac{1}{2}} + \frac{\phi_{m+1}^{\mathrm{FV}} + \phi_m^{\mathrm{FV}}}{2}\xi + \frac{\phi_{m+1}^{\mathrm{FV}} - \phi_m^{\mathrm{FV}}}{2h}\left(\xi^2 - \frac{h^2}{12}\right). \tag{A.1}$$

The last step amounts to impose the continuity of the solution at cell interfaces, i.e. $\mathscr{S}_{m-\frac{1}{2}}\left(\frac{h}{2}\right) = \mathscr{S}_{m+\frac{1}{2}}\left(-\frac{h}{2}\right)$, to obtain

$$\frac{1}{6}\phi_{m-1}^{\mathrm{FV}} + \frac{2}{3}\phi_m^{\mathrm{FV}} + \frac{1}{6}\phi_{m+1}^{\mathrm{FV}} = \frac{\bar{u}_{m+\frac{1}{2}} - \bar{u}_{m-\frac{1}{2}}}{h} \tag{A.2}$$

which corresponds to a tridiagonal problem to solve to get ϕ_m^{FV} and then the second-order derivative via (3.10). This scheme was also used for example in [25] to discretise vertical advection in an oceanic

model. Note that using coefficients $\frac{1}{12}$ instead of $\frac{1}{6}$ and $\frac{5}{6}$ instead of $\frac{2}{3}$ in (A.2) would lead to a fourth-order accurate compact scheme [e.g. 18].

Now that we have presented the numerical scheme of interest, we apply it to the equation satisfied by the error. Considering (3.10) and the equations satisfied by the errors $\bar{e}_m$ interpreted in a finite volume sense we end up with

$$(\partial_t + r)\bar{e}_{m+\frac{1}{2}} = \frac{\nu}{h}\left(\phi_m^{\mathrm{FV}} - \phi_{m-1}^{\mathrm{FV}}\right) \tag{A.3}$$

$$(\partial_t + r)\bar{e}_{m-\frac{1}{2}} = \frac{\nu}{h}\left(\phi_{m+1}^{\mathrm{FV}} - \phi_m^{\mathrm{FV}}\right) \tag{A.4}$$

which, when combined with (A.2), leads to

$$(\partial_t + r)\left(\frac{1}{6}\phi_{m-1}^{\mathrm{FV}} + \frac{2}{3}\phi_m^{\mathrm{FV}} + \frac{1}{6}\phi_{m+1}^{\mathrm{FV}}\right) - \frac{\nu}{h^2}\left(\phi_{m+1}^{\mathrm{FV}} - 2\phi_m^{\mathrm{FV}} + \phi_{m-1}^{\mathrm{FV}}\right) = 0.$$

Acknowledgement

We thank the two anonymous reviewers whose suggestions helped improve and clarify this manuscript.

Code availability

The code used to generate Figures and Table 5.1 is available in a Zenodo archive (https://doi.org/10.5281/zenodo.6324930, [9]).

References

[1] M. D. Al-Khaleel and S.-L. Wu. Quasi-overlapping Semi-discrete Schwarz Waveform Relaxation Algorithms: The Hyperbolic Problem. *Comput. Methods Appl. Math.*, 20(3):397–417, 2020.

[2] R. Alexander. Diagonally Implicit Runge–Kutta Methods for Stiff O.D.E.'s. *SIAM J. Numer. Anal.*, 14(6):1006–1021, 1977.

[3] P. Azimzadeh and P. A. Forsyth. Weakly Chained Matrices, Policy Iteration, and Impulse Control. *SIAM J. Numer. Anal.*, 54(3):1341–1364, 2016.

[4] R. J. Beerends, H. G. ter Morsche, J. C. van den Berg, and E. M. van de Vrie. *Fourier and Laplace Transforms*. Cambridge University Press, 2003.

[5] P.-M. Berthe. *Méthodes de décomposition de domaine de type relaxation d'ondes optimisées pour l'équation de convection-diffusion instationnaire discrétisée par volumes finis*. PhD thesis, Paris 13, 2013. Thèse de doctorat dirigée par Omnes, P. et Japhet, C. Mathématiques appliquées Paris 13 2013.

[6] P.-M. Berthe, C. Japhet, and P. Omnes. Space–Time Domain Decomposition with Finite Volumes for Porous Media Applications. In *Domain Decomposition Methods in Science and Engineering XXI*, pages 567–575. Springer, 2014.

[7] N. F. Britton et al. *Reaction-diffusion equations and their applications to biology.* Academic Press Inc., 1986.

[8] F. Caetano, M. J. Gander, L. Halpern, and J. Szeftel. Schwarz waveform relaxation algorithms for semilinear reaction-diffusion equations. *Netw. Heterog. Media*, 5(3):487–505, 2010.

[9] Simon Clement. Code for Discrete analysis of SWR for a diffusion reaction problem with discontinuous coefficients, 2022. `https://zenodo.org/record/6324930`.

[10] M. J. Gander. A waveform relaxation algorithm with overlapping splitting for reaction diffusion equations. *Numer. Linear Algebra Appl.*, 6(2):125–145, 1999.

[11] M. J. Gander and L. Halpern. Optimized Schwarz Waveform Relaxation Methods for Advection Reaction Diffusion Problems. *SIAM J. Numer. Anal.*, 45(2):666–697, 2007.

[12] M. J. Gander, L. Halpern, F. Hubert, and S. Krell. Optimized Overlapping DDFV Schwarz Algorithms. In *Finite Volumes for Complex Applications IX - Methods, Theoretical Aspects, Examples*, pages 365–373. Springer, 2020.

[13] M. J. Gander, L. Halpern, and M. Kern. A Schwarz Waveform Relaxation Method for Advection—Diffusion—Reaction Problems with Discontinuous Coefficients and Non-matching Grids. In *Domain Decomposition Methods in Science and Engineering XVI*, pages 283–290. Springer, 2007.

[14] M. J. Gander, L. Halpern, and F. Nataf. Optimal Schwarz waveform relaxation for the one dimensional wave equation. *SIAM J. Numer. Anal.*, 41(5):1643–1681, 2003.

[15] M. J. Gander, F. Hubert, and S. Krell. Optimized Schwarz Algorithms in the Framework of DDFV Schemes. In *Domain Decomposition Methods in Science and Engineering XXI*, pages 457–466. Springer, 2014.

[16] M. J. Gander, F. Kwok, and B. C. Mandal. Dirichlet–Neumann waveform relaxation methods for parabolic and hyperbolic problems in multiple subdomains. *BIT Numer. Math.*, 61(1):173–207, 2021.

[17] R. D. Haynes and K. Mohammad. Fully Discrete Schwarz Waveform Relaxation on Two Bounded Overlapping Subdomains. In *Domain Decomposition Methods in Science and Engineering XXV*, pages 159–166. Springer, 2020.

[18] M. H. Kobayashi. On a Class of Padé Finite Volume Methods. *J. Comput. Phys.*, 156(1):137–180, 1999.

[19] F. Lemarié. *Algorithmes de Schwarz et couplage océan-atmosphère.* Theses, Université Joseph-Fourier - Grenoble I, 2008.

[20] F. Lemarié, L. Debreu, G. Madec, J. Demange, J. M. Molines, and M. Honnorat. Stability constraints for oceanic numerical models: implications for the formulation of time and space discretizations. *Ocean Modelling*, 92:124–148, 2015.

[21] G. Manfredi and M. Ottaviani. Finite-difference schemes for the diffusion equation. In *Dynamical Systems, Plasmas and Gravitation*, pages 82–92. Springer, 1999.

[22] A. Monge and P. Birken. A Multirate Neumann–Neumann Waveform Relaxation Method for Heterogeneous Coupled Heat Equations. *SIAM J. Sci. Comput.*, 41(5):S86–S105, 2019.

[23] F. Nataf. Recent Developments on Optimized Schwarz Methods. In *Domain Decomposition Methods in Science and Engineering XVI*, pages 115–125. Springer, 2007.

[24] E. Nourtier-Mazauric and E. Blayo. Towards efficient interface conditions for a Schwarz domain decomposition algorithm for an advection equation with biharmonic diffusion. *Appl. Numer. Math.*, 60(1):83–93, 2010.

[25] A. F. Shchepetkin. An adaptive, Courant-number-dependent implicit scheme for vertical advection in oceanic modeling. *Ocean Modelling*, 91:38–69, 2015.

[26] J. Smoller. *Shock waves and reaction-diffusion equations*, volume 258 of *Grundlehren der Mathematischen Wissenschaften*. Springer, 1983.

[27] S. Thery, C. Pelletier, F. Lemarié, and E. Blayo. Analysis of Schwarz waveform relaxation for the coupled Ekman boundary layer problem with continuously variable coefficients. *Numer. Algorithms*, 2021.

[28] N. Wood, M. Diamantakis, and A. Staniforth. A monotonically-damping second-order-accurate unconditionally-stable numerical scheme for diffusion. *Quarterly Journal of the Royal Meteorological Society*, 133(627):1559–1573, 2007.

[29] S.-L. Wu and M. D. Al-Khaleel. Semi-discrete Schwarz waveform relaxation algorithms for reaction diffusion equations. *BIT Numer. Math.*, 54(3):831–866, 2014.

[30] S.-L. Wu and M. D. Al-Khaleel. Optimized waveform relaxation methods for RC circuits: discrete case. *ESAIM: M2AN*, 51(1):209–223, 2017.

[31] A. Zisowsky and M. Ehrhardt. Discrete transparent boundary conditions for parabolic systems. *Math. Comput. Modelling*, 43(3):294–309, 2006.

Chapter 3

Approximations of the discrete convergence factor of Schwarz methods

Table of contents

In Chapter 2 the semi-discrete and discrete convergence factors of Schwarz methods were studied. As the complexity of the discretizations increase, it becomes tedious to compute those convergence factors. The goal of this chapter is to ease the computations with approximations. An article in preparation is reported here: it discusses two different methods to approximate the discrete or semi-discrete convergence factor without actually having to compute them.

- The first method approximates a semi-discrete (in space or time) convergence factor by using *modified equations*.
- The second method combines the semi-discrete convergence factors and the continuous

one to get an approximation of the discrete in space and time convergence factor.

Those two methods are then used in the optimization of the convergence to evaluate the potential of these approximations in the acceleration of Schwarz methods.

The main results of this chapter are listed below.

- The convergence study with modified equations includes the main features of the semi-discrete schemes for low-frequencies.
- Using the modified equations technique on a multi-step time scheme amounts to ignoring the presence of the intermediate step. We conclude that this technique should not be used for the approximation of the semi-discrete in time convergence factor.
- For space schemes, using the modified equations simplifies the analysis of the convergence factor (compared to the semi-discrete level) only for a particular type of differential equations.
- The combination of the semi-discrete analyses can provide a good approximation of the discrete convergence factor. For a large range of the problem parameters, the optimization performs better on the *combined* convergence than on the continuous one. However, this improvement is not systematic and using this method on other problems without further investigations would be uncertain.

Approximations of the discrete convergence factor of Schwarz methods

Simon Clement [1]
Florian Lemarié [2]
Eric Blayo [3]

[1] Univ. Grenoble Alpes, Inria, CNRS, Grenoble INP, LJK, Grenoble, France
Email address: simon.clement@grenoble-inp.org
[2] Univ. Grenoble Alpes, Inria, CNRS, Grenoble INP, LJK, Grenoble, France
Email address: florian.lemarie@inria.fr
[3] Univ. Grenoble Alpes, Inria, CNRS, Grenoble INP, LJK, Grenoble, France
Email address: Eric.Blayo@univ-grenoble-alpes.fr.

Abstract. This paper discusses two methods to estimate the discrete and semi-discrete convergence speed of Schwarz coupling algorithms without having to carry out the full calculations. A first method is based on the modified equations technique to approximate the semi-discrete convergence factor. A second method whose purpose is to estimate the discrete convergence factor by combinations between continuous and semi-discrete analyses is also introduced. Both methods are illustrated with a heterogeneous coupling of two 1-D reaction-diffusion equations, discretised with second-order schemes in time (diagonally implicit Runge Kutta) and space (finite differences). We consider Dirichlet-Neumann Waveform Relaxation and two-sided Robin-Robin coupling algorithms which both offer the possibility of optimising the convergence speed. We compare the performance of such algorithms when the optimisation is done on the exact discrete convergence factor and on approximate forms of it. Interestingly it appears that the modified equations are not applicable in time and are of limited interest in space. On the other hand, optimising the combination of the semi-discrete and the continuous analyses can accelerate significantly the convergence speed, especially in the Robin two-sided case.

Keywords. Schwarz methods, Semi-discrete, Discrete.
2020 Mathematics Subject Classification. 65M12; 65M55; 65L20.

1. Introduction

Schwarz iterative methods are widely used for efficiently computing the solution of PDEs on parallel computers, and/or solving coupled problems. Their factor of convergence often depends on some free parameters that are present in the interface conditions. It is therefore important to assess the expression of the convergence factor a priori as accurately as possible, in order to determine values of the free parameters that allow an efficient convergence. This is done usually by considering the continuous form of the PDEs, often using Fourier and/or Laplace transform to get an analytical expression of the convergence factor in the spectral space (see [8] for a review).
However actual numerical simulations use discretised versions of the PDEs rather than the continuous one, which may lead to significant differences in the convergence factor. That is why several recent works focused on the determination of this factor starting directly from the discretised equations (listed in [12]). But such calculations often appear to be difficult and tedious, especially as the space stencil size in finite differences methods and the number of stages in the time-integration increase. In this context, this paper presents two possible alternative methods to approximate the actual discrete

This work was supported by the French national research agency through the ANR project "COCOA" (COmprehensive Coupling approach for the Ocean and the Atmosphere), grant ANR-16-CE01-0007. Florian Lemarié appreciates the funding from the SHOM/DGA under grant agreement No 19CP07.

convergence factor of Schwarz algorithms while avoiding the corresponding fully discrete calculations. The first method (for multistage time schemes or finite differences space schemes), described in Section 3, is to use the so-called *modified* equations, that represent the "actual partial differential equations which are solved numerically" [16]. The second method presented in Section 4 combines semi-discrete and continuous analyses to get an approximation of the fully discrete convergence factor. Section 5 discusses whether the methodologies described in Sections 3 and 4 provide an improvement compared to the continuous analysis in the case of an optimisation process on free parameters arising from a relaxation step or Robin interface conditions. Note that for sake of clarity the technical details of the computation of continous, semi-discrete and discrete convergence factors are grouped in Appendices A and B.

2. Discretisation and Schwarz methods studied

We consider in this paper the use of an iterative Schwarz algorithm for solving the evolution equation $\partial_t u - \mathcal{L}u = F$ on a domain Ω with some given boundary conditions, where $\mathcal{L}$ is a linear operator. In order to design the Schwarz method, Ω is divided into two subdomains Ω_1 and Ω_2. Let $\mathcal{L}_j$ denote the restriction of $\mathcal{L}$ to Ω_j. If $\mathcal{L}_1 = \mathcal{L}_2$ then one gets a domain decomposition problem and Ω_1 and Ω_2 may partially overlap, otherwise it is a coupling problem and Ω_1 and Ω_2 cannot overlap. We focus on the latter case in our examples but the methods discussed in the following can be applied in broader context.
Schwarz methods correspond to a sequence of resolutions of $\partial_t u_j^k - \mathcal{L}_j u_j^k = F_j$ with boundary conditions on $\partial\Omega$ and additional conditions at the interface between Ω_1 and Ω_2. $j = 1, 2$ denotes the space domain and k is the iteration index. The convergence of the Schwarz methods can be investigated by considering the error $e_j^k = u_j^k - u$ and we define the convergence factor as the ratio of the Fourier transforms (denoted by a hat) at the interface $\varrho = \frac{\hat{e}_1^k\big|_{\text{int}}}{\hat{e}_1^{k-1}\big|_{\text{int}}}$. $\mathcal{L}_j$ being linear, e_j^k satisfies the corresponding homogeneous equations. We will thus focus throughout this paper on the equations:

$$\partial_t u_j^k = \mathcal{L}_j u_j^k, \qquad u_j^k(t=0) = 0, \qquad j = 1, 2 \tag{2.1}$$

For our illustrations and numerical examples, we will use 1-D reaction-diffusion operators $\mathcal{L}_j = \nu_j \partial_{xx} - r$, with an interface $\{x = 0\}$. Two variants of Schwarz methods are presented in this study:

- Dirichlet-Neumann Waveform Relaxation (*DNWR*, [9]), whose interface conditions are

$$u_1^k(0^-, t) = (1-\theta) u_2^{k-1}(0^+, t) + \theta u_1^{k-1}(0^-, t) \tag{2.2a}$$

$$\nu_2 \partial_x u_2^k(0^+, t) = \nu_1 \partial_x u_1^k(0^-, t) \tag{2.2b}$$

- Robin-Robin Schwarz methods (*RR*, [7]), whose interface conditions are

$$(p_1 + \nu_1 \partial_x) u_1^k(0^+, t) = (p_1 + \nu_2 \partial_x) u_2^{k-1}(0^-, t) \tag{2.3a}$$

$$(p_2 + \nu_2 \partial_x) u_2^k(0^+, t) = (p_2 + \nu_1 \partial_x) u_1^k(0^-, t) \tag{2.3b}$$

θ is called the relaxation parameter and p_1, p_2 are called the Robin parameters.

The discretisation in space used for ullustrative purposes is a simple centered second-order finite difference (FD) scheme. The Neumann interface condition is approximated with the help of a ghost point:

$$\nu_2 \partial_x u_2^k(x_0) \approx \nu_2 \frac{u_2^k(x_1) - u_2^k(x_0)}{h} - \frac{h}{2}(\partial_t + r) u_2^k(x_0) \tag{2.4}$$

which is the simplest non-intrusive second-order discretisation of the transmission condition allowing to recover the monolithic semi-discrete in space solution at convergence [e.g. see 5]. x_0 stands here for

APPROXIMATING DISCRETE CONVERGENCE FACTOR OF SCHWARZ METHODS

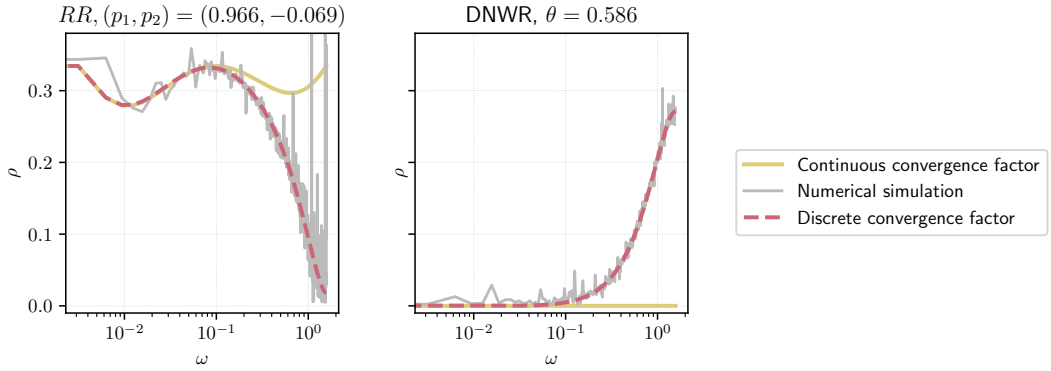

Figure 1. Comparison between the convergence factors modulus predicted with the continuous analyses (yellow), the convergence factors predicted by the discrete analyses (red dashed), and the convergence factors observed through numerical simulations (grey). x-axis: ω is the time frequency. The Robin parameters p_1, p_2 and the relaxation parameter θ are chosen in each setting to minimise the min-max problem on continuous equations described in Section 5. The numerical experiments are described in 5.3. The convergence factor is computed with the ratio of the discrete Fourier transform of the first two errors.

the interface point and x_1 the first point inside the domain. We use a Diagonally Implicit Runge-Kutta (DIRK, [1]) two-stage time scheme, in order to illustrate the methods for multistage time schemes:

$$\frac{u_j^\star - u_j^n}{\Delta t} = b\mathcal{L}(u_j^\star) - a\mathcal{L}(u_j^n) \tag{2.5a}$$

$$\frac{u_j^{n+1} - u_j^\star}{\Delta t} = b\mathcal{L}(u_j^{n+1}) \tag{2.5b}$$

where $b = 1 + 1/\sqrt{2}$ and $a = 2b - 1 = 1 + \sqrt{2}$ guarantee that it is a second-order scheme which monotonically damps the frequencies [14]. The superscript k (Schwarz iteration index) was omitted and n stands for the time index. A linear combination between times t^n and t^{n+1} is used to provide the boundary and interface conditions for $u_j^\star$ when solving (2.5a). Let γ be the discrete Fourier transform of this operation (see e.g. (A.8)). An analysis of the effect of γ on the convergence of Schwarz methods can be found in [5]. In the following we will return several times to the particular role played by the operator γ in our study.

The usual domain decomposition procedure with Schwarz methods is to derive a convergence factor from the continuous problem and choose parameters independently from the discretisation [e.g. 7, 9]. However, as seen in Figure 1, the convergence factor derived with the continuous equations can significantly differ from the convergence factor observed in the numerical simulation because of the discretisation. Semi-discrete and discrete analyses of Schwarz methods (e.g. [12] for the heat equation) better anticipate the behaviour of numerical simulations.

The semi-discrete in space, semi-discrete in time and discrete analyses of the convergence factor are given in appendices for the case study presented here. Figure 1 shows that the discrete convergence factor fits the numerical simulation for our set of parameters. However the semi-discrete computations become tedious as the size of the stencil (in space) and as the number of stages (in time) increase. The fully discrete analyses generally combine the difficulty of both schemes and it can become challenging to derive the exact convergence factor. We hence introduce two alternative methods for estimating the discrete or semi-discrete convergence factor and discuss their validity.

In Section 3 an intermediate convergence factor is used: "Continuous with Discrete Transmission Operators" (CDTO). Appendix A.1 presents this convergence factor that takes into account the discretisation of the boundary condition (2.4) while keeping the continuous equation inside the domains. Figure 2 shows that in our case this convergence factor is close to the semi-discrete in space convergence factor (which takes into account the spatial discretisation also in the inner domains). The importance of the discretisation of the transmission operators is discussed in [5].

3. Semi-discrete convergence factor from the modified equation technique

It is shown in Appendix A that switching from the continuous to the semi-discrete case affects the derivation of the convergence factor in the following ways:

- With one-stage time schemes, a change of variable is sufficient to switch from the continuous analysis to the discrete one. Conversely, for time schemes with multiple stages the nature of the differential equation to be considered is fundamentally different from the one in the continuous case which makes the study more challenging.
- Space schemes change the way of computing the solutions in the frequency domain $\widehat{u}^k$. Instead of solving a differential equation, $\widehat{u}^k$ is obtained by finding roots of a characteristic polynomial. The order of the characteristic polynomial increases with the stencil of the space scheme under consideration.

The analysis of convergence of Schwarz methods is hence specific to the space and time discretisations. In the same spirit as [3] where a modified viscosity is used to include the impact of an off-centered (a.k.a. upwind) advection scheme in a continuous analysis, we will use modified equations associated to the discretisations considered so far. We thereby introduce a new approach to estimate the convergence factor of a discretised Schwarz algorithm through the modified equations technique. An advantage of such an approach is that it takes into account the main features of the discrete schemes for low frequencies while keeping the simplicity of the continuous analysis. By analysing a continuous problem closer to the one actually solved by the numerical scheme, the discrete convergence factor could be better approximated.

3.1. Derivation of the modified convergence factor

When numerically solving a differential equation using structured grids, a way to analyse the discretisation error is to interpret an error term as a differential operator. By solving the *modified* differential equation, the effect of the discretisation on the solution can be quantified [16, 4].

We propose to add the main error terms of the discretisation in the derivation of the *continuous* convergence factor. It leads to a *modified* convergence factor, more accurate in well-resolved frequencies than the *continuous* one. Modified equations were also used to analyse the convergence speed of successive overrelaxation in [10].

3.1.1. *Time scheme*

We assume that the discrete operator $\mathcal{D}_t$ which approximates ∂_t can be developed into a sum of differential operators through a Taylor expansion:

$$\mathcal{D}_t u = \left(\partial_t + d_1^t\, \Delta t \partial_{tt} + d_2^t\, \Delta t^2 \partial_{ttt}\right) u + o(\Delta t^2)$$

where $d_1^t = 0$ for second-order time schemes and $d_1^t = d_2^t = 0$ for higher-order time schemes (for which higher-order expansions are therefore needed). Instead of equation (2.1), the following *modified*

equation is considered:

$$\begin{cases} \left(\partial_t + d_1^t\, \Delta t \partial_{tt}\right) u = \mathcal{L}u \text{ if } d_1^t \neq 0 \\ \left(\partial_t + d_2^t\, \Delta t^2 \partial_{ttt}\right) u = \mathcal{L}u \text{ otherwise} \end{cases} \tag{3.1}$$

For instance, for the DIRK scheme (2.5) $d_1^t = 0$ and $d_2^t = \frac{2}{3} + \frac{\sqrt{2}}{2}$.

Let $s^{(c,c)} = i\omega$ and $s_m^{(\text{Time},c)} = i\omega + d_1^t \Delta t (i\omega)^2$ (or $s_m^{(\text{Time},c)} = i\omega + d_2^t \Delta t^2 (i\omega)^3$ if $d_1^t = 0$) be the symbols of respectively ∂_t and the left-hand side of (3.1). The effect of the time discretisation can be studied by replacing $s^{(c,c)}$ by $s_m^{(\text{Time},c)}$ in the continuous analysis.

Recall that similarly to the previous method the semi-discrete analysis of a single stage time scheme (for instance Euler or Crank-Nicolson methods) can already be done by a simple change of frequency variable [5]. Hence, in those single-stage cases there is no point using modified equations. We thus restrain our study to the multistage time schemes, for which we will show in Section 3.2 that modified equations are not helpful because of the projection in time operator γ used for interface conditions.

Note on well-posedness. Since our initial condition is limited to $u_j(t_0)$, additional initial conditions are necessary for (3.1) to be well-posed as soon as $d_1^t \neq 0$ or $d_2^t \neq 0$. Assuming u regular enough, $\mathcal{L}$ a linear space differential operator and $\partial_t^p u(t_0) = 0$ for some $p \geq 0$, recursively differentiating (2.1) in time and reversing the order of differentiation gives $\partial_t^{p+1} u(t_0) = \mathcal{L}\partial_t^p u(t_0) = 0$. The number of homogeneous initial boundary conditions can thus be sufficient to allow the well-posedness. [11] states that modified *problems* should be used instead of modified *equations*. In example (C) of [11] an initial condition prevents modified problems to attain third order of correctness. Similarly to this example there is no modified problem of third order that takes into account γ.

3.1.2. *Finite Differences space scheme*

The discussion in subsection 3.1.1 can be applied to FD space schemes as well, or other methods that have a FD interpretation. For instance the modified equation in space of the centered second-order FD scheme is

$$(\partial_t + r)u - \nu\partial_{xx}u - \frac{h^2}{12}\nu\partial_{xxxx}u = 0 \tag{3.2}$$

with the homogeneous initial condition $u(x, t_0) = 0$. At the interface, the modified equation satisfies the RR or DNWR condition given in Section 2. An additional interface condition is needed to ensure unicity of the modified solution (see the paragraph on well-posedness below). To keep the order of accuracy, a Taylor expansion up to $o(h^2)$ of the discrete evolution equation at the first inner point $(\partial_t + r)u(x_1) = \frac{\nu}{h^2}(u(x_2) - 2u(x_1) + u(x_0))$ gives in Ω_2:

$$\left(1 + h\partial_x + \frac{h^2}{2}\partial_{xx}\right)\left(\partial_t + r - \nu\partial_{xx} - \frac{h^2}{12}\nu\partial_{xxxx}\right)u(0) = 0. \tag{3.3}$$

Using the modified equations in space may not be simpler than using the semi-discrete equations: indeed the order of the modified ODE that needs to be solved (the Fourier transform of (3.2) is a fourth-order ODE) is higher than the degree of the characteristic polynomial of the semi-discrete case (the order being 2 for the second-order FD scheme, as mentioned in Appendix A). The modified equations generally lead to a derivation which is more tedious than the semi-discrete analysis that they aim to approximate. However in the particular case of $\mathcal{L}$ having exactly one differentiation operator of any order, a transformation can be pursued: the space differentiation can then be treated like time derivatives. Taking the example of the reaction-diffusion equation, the modified equation is

$(\partial_t + r)u_j = \nu_j \left(\partial_{xx} + d_1^x h^2 \partial_{xxxx}\right) u_j$. We use the approximation $\nu_j \partial_{xx} \approx \partial_t + r$ and get this *modified-in-space* equation:

$$\left(\partial_t + r - d_1^x \frac{\Delta t}{\Gamma_j}(\partial_t + r)^2\right) u_j - \nu_j \partial_{xx} u_j = 0$$

where $\Gamma_j = \nu_j \frac{\Delta t}{h^2}$ is the parabolic Courant number. A similar derivation is done in [16] to interpret the error in time as dissipative or dispersive operators in space. Here we do the opposite, transforming space derivatives into time derivatives so that a simple change of variable can be used: after a Fourier transform in time, the modified equation indeed becomes $(s_m^{(\mathrm{c,Space})} + r)\widehat{u}_j = \nu_j \partial_{xx} \widehat{u}_j$ where

$$s_m^{(\mathrm{c,Space})} = s_m^{(\mathrm{c,c})} - d_1^x \frac{\Delta t}{\Gamma_j}(s_m^{(\mathrm{c,c})} + r)^2$$

is an approximation of the symbol of ∂_t modified by the discretisation of $\mathcal{L}$. This transformation requires to have a single differentiation in space: for instance, the error term of an advection-diffusion equation would generally fail to be expressed only as a combination of time derivatives. Note that s_m depends on the domain j; it does not however make the continuous derivation much more tedious.

As mentioned in [11], the modified equations need to be analysed with the discrete boundary conditions (or an approximation of them). This also stands in the case of Schwarz convergence analysis: we will hence use the discrete interface transmission operators when comparing modified-in-space and continuous convergence factors, the latter being referred as "Continuous with Discrete Transmission Operators" (CDTO, see Appendix A.1) in the figures.

Note on well-posedness. The well-posedness of (3.2) together with boundary conditions can be easily proven following Appendix C of [6] with the simplification coming from the homogeneous initial condition and the semi-infinite domain in space. For given h, ν, r, it then suffices to show that the interface conditions are not redundant in the Laplace domain.

3.2. Frequency range of validity for the modified equation technique

Figures 2 and 3 illustrate the approximation made by using modified equations respectively in space and time when estimating the semi-discrete convergence factors. Figure 2 shows that the use of modified-in-space equations results in a gain of accuracy once the discrete transmission operators are used. This improvement is notable on an intermediate range of frequencies for which the continuous prediction deviates from the discrete convergence factor. In Figure 3, the estimation of the semi-discrete in time convergence factor leads to less positive results: as mentioned in Section A.3, the convergence factor of the DIRK time scheme is highly dependent of the projection in time operator γ used for interface conditions. The convergence factor of any multistage time scheme depends on a time interpolation/extrapolation of boundary data and is thus likely to contain a term $f_j(\gamma)$ (see equation (A.10) where $f_j(\gamma)$ is independent of j and noted $\tilde{\gamma}$). The Robin-Robin convergence factor of a two-stage time scheme should be similar to (A.20):

$$\varrho_{\mathrm{RR}}^{(\mathrm{DIRK,c})} = \left(\frac{p_1 + \nu_2\sigma_2}{p_2 + \nu_2\sigma_2}(1 - \tilde{\gamma}) + \frac{p_1 + \nu_2\sigma_4}{p_2 + \nu_2\sigma_4}\tilde{\gamma}\right)\left(\frac{p_2 + \nu_1\sigma_1}{p_1 + \nu_1\sigma_1}(1 - \tilde{\gamma}) + \frac{p_2 + \nu_1\sigma_3}{p_1 + \nu_1\sigma_3}\tilde{\gamma}\right). \tag{3.4}$$

where $\tilde{\gamma}$ contains the dependency in γ. The definition of σ_i is in (A.6). The modified equation technique yields an approximation of $\frac{p_1+\nu_2\sigma_2}{p_2+\nu_2\sigma_2}\frac{p_2+\nu_1\sigma_1}{p_1+\nu_1\sigma_1}$ and can thus only approximate the ratios multiplied by $(1 - \tilde{\gamma})$ in (3.4). Consequently using modified equations is effective only if this $\tilde{\gamma}$ is sufficiently small. In the particular case of Dirichlet-Neumann transmission operators (right panel in Figure 3), the difference between analyses in the continuous case and in the semi-discrete in time case comes only from γ (see (A.15) in Appendix). Hence, in this case the use of modified equations has no effect on the theoretical prediction of the convergence. Since γ is usually not chosen to diminish $f_j(\gamma)$

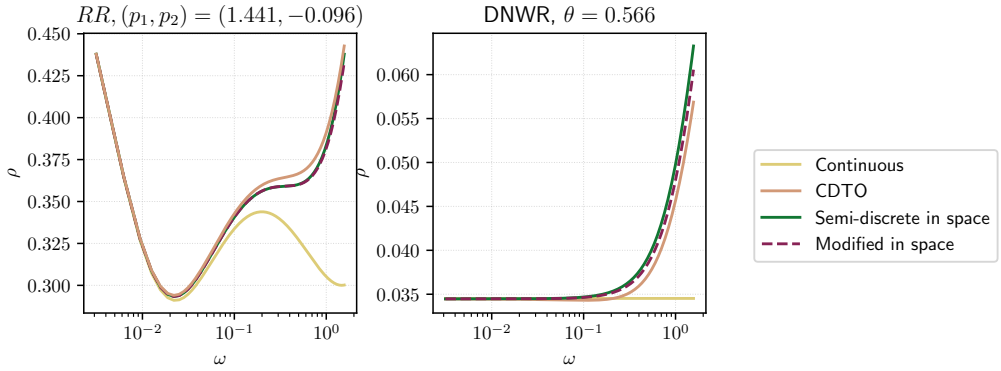

Figure 2. Comparison of the convergence factors obtained with the continuous with discrete transmission operators (brown), semi-discrete in space (green) and modified-in-space (dashed red) analyses. The modified-in-space convergence factors are computed with discrete interface operators. The Robin parameters p_1, p_2 and the relaxation parameter θ are chosen in each setting to minimise the min-max problem on the semi-discrete in space convergence factor. Fully continuous case (yellow) is shown for reference.

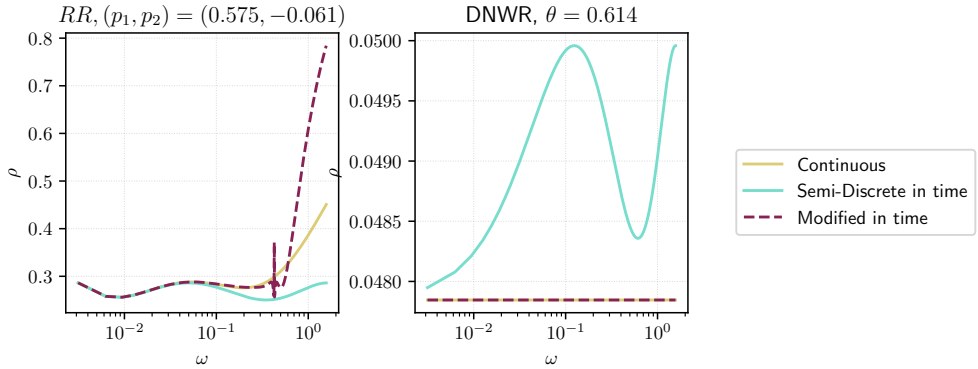

Figure 3. Comparison of the convergence factors obtained with the continuous (in yellow), semi-discrete in time (in blue) and modified-in-time (in dashed red) analyses. The Robin parameters p_1, p_2 and the relaxation parameter θ are chosen in each setting to minimise the min-max problem on the semi-discrete in time convergence factor.

when designing the scheme, we advise not to use modified-in-time equations for the study of Schwarz methods' convergence and we do not present them in Section 5. In the figures, the operator γ is defined as a linear interpolation[1] operator.

4. Combining semi-discrete analyses

We have seen that the applicability of the method presented in Section 3 is limited to the inner equations of semi-discrete schemes in space with exactly one differentiation in space. We now introduce an other approach in order to approximate the fully discrete convergence factor $\varrho_{\mathrm{RR}}^{(\mathrm{DIRK,FD})}$ whose

[1]We chose $\gamma = (1-b)z + b$ which corresponds to $u^\star \approx (1-b)u^{n+1} + bu^n$

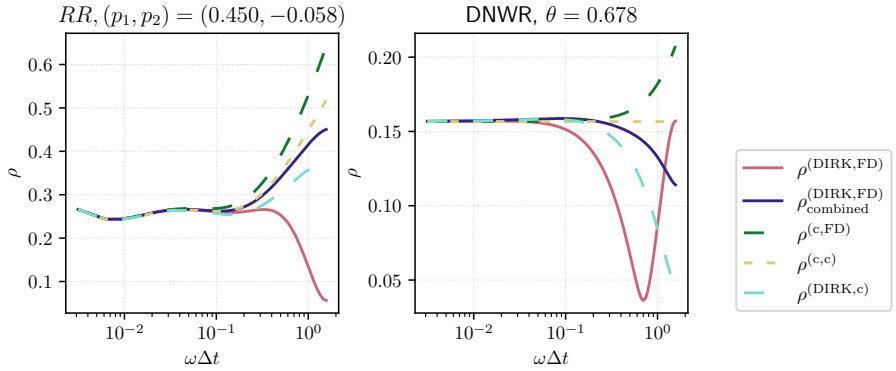

Figure 4. Comparison of the convergence factors for the continuous analyses (dashed yellow), combined analyses (purple), semi-discrete in space (dashed green) and in time (dashed blue) analyses. The fully discrete analyses are plotted in pink. The Robin parameters p_1, p_2 and the relaxation parameter θ are chosen in each setting to minimise the min-max problem on the fully discrete convergence factor.

derivation is presented in Appendix B. This derivation is specific to the given selection of space and time schemes and becomes lengthy as the schemes are more and more sophisticated. In this section we propose an approximation of the fully discrete convergence factor, based on the continuous, semi-discrete in time and semi-discrete in space derivations.

We first observe (e.g. in Appendix A) that the semi-discrete convergence factors varies smoothly when the step size is changed. For a given frequency ω, the discrete convergence factor asymptotically equals the continuous case when the step sizes tend to zero:

$$\varrho^{(\text{Time,Space})} \xrightarrow[\Delta t\to 0]{} \varrho^{(\text{c,Space})} \xrightarrow[h\to 0]{} \varrho^{(\text{c,c})} \text{ and } \varrho^{(\text{Time,Space})} \xrightarrow[h\to 0]{} \varrho^{(\text{Time,c})} \xrightarrow[\Delta t\to 0]{} \varrho^{(\text{c,c})} \tag{4.1}$$

where $\varrho^{(\text{c,c})}$, $\varrho^{(\text{Time,c})}$, $\varrho^{(\text{c,Space})}$ and $\varrho^{(\text{Time,Space})}$ are respectively the continuous, semi-discrete in time, semi-discrete in space and fully discrete convergence factors. Assuming that the space and time schemes have at least a first order accuracy, we combine Taylor expansions with regards to h and Δt of the convergence factors appearing in (4.1) and get:

$$\varrho^{(\text{c,Space})} + \varrho^{(\text{Time,c})} - \varrho^{(\text{c,c})} = \varrho^{(\text{Time,Space})} - h\,\Delta t\,\frac{\partial^2 \varrho^{(\text{Time,Space})}}{\partial \Delta t\,\partial h} + o(h\Delta t) = \varrho^{(\text{Time,Space})}_{\text{combined}} \tag{4.2}$$

This *combined* convergence factor is a second-order approximation of the fully discrete convergence factor, and tends to the semi-discrete factor in time as $h \to 0$ and to the semi-discrete convergence factor in space as $\Delta t \to 0$. It therefore captures the main effects of both schemes on the convergence factor, and combines them accurately as long as they don't interact too much with each other (the interactions are represented by the term $h\Delta t\frac{\partial^2 \varrho^{(\text{Time,Space})}}{\partial \Delta t \partial h}$). We considered here constant h and Δt but the combination could be made with variable time and space steps (if the semi-discrete analysis is available). Note that this method can be applied in a wide variety of situations.

Figure 4 shows that the combined factor $\rho^{(\text{DIRK,FD})}_{\text{combined}} = \left|\varrho^{(\text{DIRK,FD})}_{\text{combined}}\right|$ is accurate (i.e. close to $\rho^{(\text{DIRK,FD})}$) in low frequencies. However it should be used carefully in the high frequencies where it is often that the interactions $\frac{\partial^2 \varrho^{(\text{Time,Space})}}{\partial \Delta t\,\partial h}$ play an important role. Although the *combined* convergence factor is not more accurate than the continuous one on Figure 4, Section 5 exhibits parameter ranges for which the combined analysis is better than the continuous one.

APPROXIMATING DISCRETE CONVERGENCE FACTOR OF SCHWARZ METHODS

5. Effect on the optimisation on free parameters

The accurate estimation of the convergence factor of a Schwarz method is motivated by the possibility to optimise the convergence speed of the algorithm via the free parameters brought by the interface conditions (2.2) or (2.3). The corresponding optimisation problem takes the form of a min-max problem $\min_{\theta}\left(\max_{\omega\in(\omega_{\min},\omega_{\max})}\rho^{(.,.)}_{DNWR}(\omega,\theta)\right)$ or $\min_{(p_1,p_2)}\left(\max_{\omega\in(\omega_{\min},\omega_{\max})}\rho^{(.,.)}_{RR}(\omega,p_1,p_2)\right)$ which is solved numerically for a given ρ. We note $\theta^\star, p_1^\star, p_2^\star$ the solutions of those optimisation problems. Our objective is here to answer the following questions:

- Can we accelerate the convergence speed of Schwarz methods when the optimisation is done on the convergence factor obtained from the modified equations technique compared to the Continuous analysis with Discrete Transmission Operators (CDTO)?
- Is the optimised convergence speed obtained with the combined analysis presented in Section 4 faster compared to that obtained with the semi-discrete in space or time and continuous analyses ?

As it is shown in Figure 2 the transmission operators account in our case for the greatest part of the difference between the continuous and semi-discrete in space convergence factors. Moreover, the modified equations only aim to take into account the discretisation inside the domains. This is why CDTO (rather than the standard continuous analysis) is compared to modified equations in the first question.

Numerical experiments. In all the figures, unless otherwise specified, $\nu_1 = 0.5$ m^{2}s^{-1}, $\nu_2 = 1$ m^{2}s^{-1}, $r = 10^{-3}$ s^{-1}, h$= 1$ m. The time step is $\Delta t = 2s$ and the number of steps is $N = 10^3$. Frequencies of interest are $(\omega_{\min}, \omega_{\max}) = (\frac{\pi}{N\Delta t}, \frac{\pi}{\Delta t})$. The results shown in Figures 1 and 8 are obtained from numerical simulations initialised with a white noise and discretised using 100 space points in each domain. The space domains are assumed infinite in the theoretical convergence factors. [15] gives an analysis of the effect of bounded domains and it is found that in our case this assumption is justified for the parameter values considered here.

5.1. One-parameter optimisation

Figure 5 and 6 compare the maximum (over the range of time frequencies) of the convergence factors obtained with the different analyses, for a range of the free parameters p_1 ($= -p_2$) and θ. The optimised convergence factor with a single parameter presents an equi-oscillation between the lowest $\omega_{\min}$ and highest $\omega_{\max}$ frequencies (not seen in the figures). The maximum of the convergence factor is attained in low frequencies for the largest values of θ and p_1, and it is attained at the highest frequency for small θ and p_1 (for instance in Figure 1, θ is smaller than the optimum $\theta^\star$: the discrete convergence factor is larger in high frequencies than in low frequencies). Since the proposed approximation methods are mostly valid for low frequencies, the maxima of the convergence factors obtained from continuous and modified equations are close to the corresponding maximum of the discrete case on the right sides of the plots (i.e. for the largest values of θ and p_1). Conversely, for small values of the optimised parameter p_1 or θ, the effect of the discretisation is more visible since high frequencies influence the convergence speed.

5.1.1. *Modified equations*

Is the optimised convergence speed obtained with the modified equations technique faster compared to the one obtained from a continuous analysis? Recall that the modified equations aim to approximate

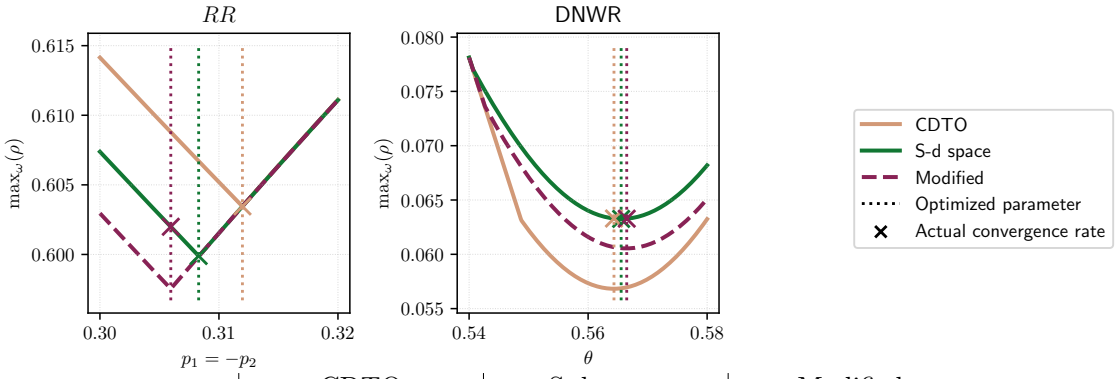

	CDTO	S-d space	Modified
RR	0.603 ($p_1^\star = 0.312$)	0.600 ($p_1^\star = 0.308$)	0.602 ($p_1^\star = 0.306$)
DNWR	0.063 ($\theta^\star = 0.564$)	0.063 ($\theta^\star = 0.566$)	0.063 ($\theta^\star = 0.566$)

Figure 5. Maximum of the convergence factor, derived in the continuous (with Discrete Transmission Operators, CDTO), semi-discrete (S-d) in space and modified-in-space cases for $\omega \in (\omega_{\min}, \omega_{\max})$. Robin transmission condition is chosen to be one-sided ($p_1 = -p_2$) for easier representation. See Figure 7 for the two-sided Robin operators. We aim to approximate the semi-discrete in space convergence factor: the "actual convergence rate" indicated in the table is to be read on the green curves ("×" markers). The vertical dotted lines highlight the parameters chosen with each convergence factor.

the semi-discrete case which is the reference in this paragraph. In Figure 5, the use of the *modified-in-space* setting is compared to the CDTO and semi-discrete in space convergence factors. For each convergence factor, the parameter chosen by the optimisation procedure is shown with a vertical dotted line. The performance of parameters obtained with the optimisation procedure can be read on the table or on the green curve. The parameter obtained with modified equations does not significantly outperforms the CDTO parameter. As seen in Figure 2, in our case the discrete transmission operators stand for most of the effect of the space discretisation. It is confirmed in Figure 5 where the semi-discrete optimised parameter is close to its CDTO counterpart. Since the modified-in-time equation approach was not found to improve the approximation of the convergence factor compared to the continuous case in Figure 3, the time scheme equivalent to Figure 5 is not presented.

5.1.2. *Combined analyses*

Is the optimised convergence speed obtained with the combined analysis faster compared to the one obtained with semi-discrete in space or time and continuous analyses? Figure 6 compares combined, continuous, semi-discrete and fully discrete analyses; the actual convergence factor maximum is to be read on the discrete case to compare parameters.

- It is seen that the discrete parameter outperforms every other parameters.
- The combined parameter gives a faster convergence than the continuous one.
- The semi-discrete analysis brings the parameter in the wrong direction compared to the continuous analysis. This can be explained by the particular choice of transmission operators (2.4) discussed in [5]. The effect of (2.4) on the convergence factor in high frequencies is weakened by the time discretisation. Hence, the semi-discrete in space parameter choice compensates for an effect that vanishes in the discrete case.

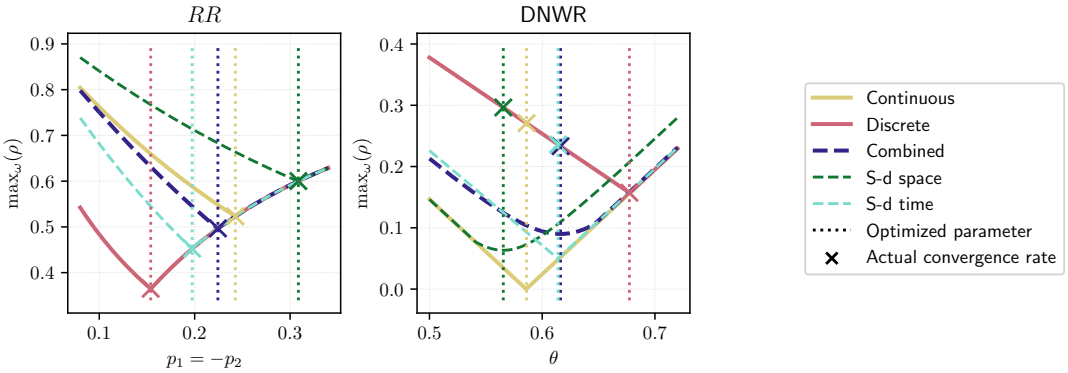

	Continuous	Discrete	Combined	S-d space	S-d time
RR	0.523 ($p_1^\star = 0.243$)	0.365 ($p_1^\star = 0.154$)	0.496 ($p_1^\star = 0.224$)	0.600 ($p_1^\star = 0.309$)	0.452 ($p_1^\star = 0.197$)
DNWR	0.271 ($\theta^\star = 0.586$)	0.157 ($\theta^\star = 0.677$)	0.233 ($\theta^\star = 0.616$)	0.296 ($\theta^\star = 0.566$)	0.236 ($\theta^\star = 0.614$)

Figure 6. Same as Figure 5 but for the continuous, discrete, combined and semi-discrete cases.

- The combined parameter is close but not better than the one chosen with the semi-discrete in time analysis. The interactions between space and time discretisations (e.g. weakening of the effect of (2.4)) prevents the combined analysis to fit the discrete one.

5.2. **Robin two-sided optimisation**

Figure 7 presents the optimised Robin-Robin *two-sided* parameters (i.e. $p_1 \neq -p_2$) for the modified-in-space equations and for the combined method.The convergence factors with Robin *two-sided* transmission conditions often have two local minima: at $(p_1, p_2) \approx (1, -0.05)$ and $(p_1, p_2) \approx (0.05, -1)$. The optimisation routine selects the best output of two local optimisations starting from the previous values.

The conclusions of Section 5.1 are confirmed by Figure 7. The parameters chosen with the proposed alternative approaches are getting closer to the discrete optimal than the parameters chosen with the continuous approaches, and lead to a faster convergence than the continuous analyses in both cases. The alternative methods can hence accelerate the convergence when combined with an optimisation of the free parameters.

5.3. **Robustness**

Figure 8 shows the evolution of the L^2 norm of the error across iterations for RR and DNWR. In both cases, optimising with the combined convergence factor accelerates the convergence speed compared to the continuous case. Unsurprisingly it is seen that a smaller convergence factor in the frequency domain leads to a faster convergence with the L^2 norm. The modified case is not presented because the differences of convergence speed are negligible.

Figure 9 shows how much the alternative methods accelerate the theoretical convergence depending on the problem's parameters. Although the parameters space is not fully covered, the following conjectures can be made:

- The "Combined" method is efficient for large ν_1, ν_2 and for a small r;

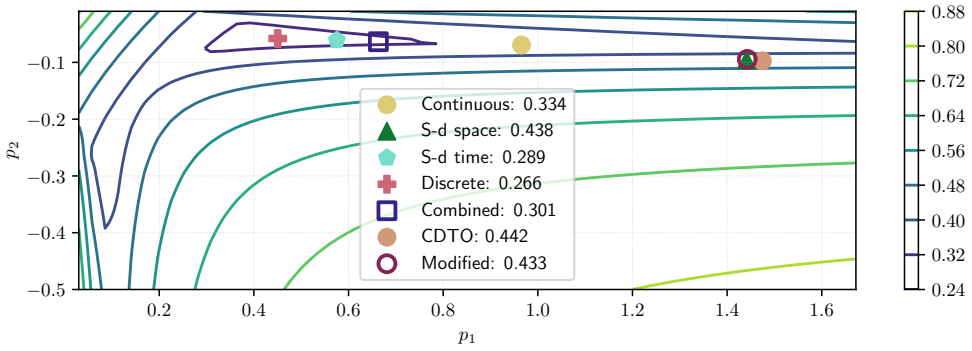

Figure 7. Comparison of the optimised parameters yielded by the Robin *two-sided* analyses. The contour lines are those of maximum of the discrete convergence factor. The value of the latter function for the parameters of each analysis is given in the legend.

- The "Modified" method does not significantly improve the convergence speed and the dependency on the parameters is not easy to interpret. For DNWR, the zero line for $\nu_1 = \nu_2$ is coherent with the optimal relaxation parameter being $\theta^\star = \frac{1}{2}$ in the continuous, semi-discrete in space and modified cases.

- A non-negligible part of the parameter space is filled with negative values which means that the proposed approaches can occasionally degrade the performance of the algorithm compared to the continuous case.

- For both methods the convergence speed accelerates with Δt. Indeed, for larger Δt (or equivalently for lower frequencies) the proposed approximations are more accurate.

- For both methods the convergence speed accelerates as h becomes smaller since in this case the Taylor expansion is more and more accurate.

6. Conclusion

In this paper we have investigated different ways of taking into account discretisation errors when studying the convergence speed of Schwarz iterative methods. Given the complexity of a discrete analysis for multi-stage time-stepping schemes and high-order spatial discretisations, our objective was to find ways to obtain accurate approximations of the discrete convergence factor. Considering either separately or jointly the impact of the discretization of the interface conditions and of the equations in the inner domains, different approximation methods have been introduced. The proposed methods have been applied to a reaction-diffusion problem discretized using a second-order Finite Differences discretisation in space and a diagonally implicit Runge-Kutta multi-stage scheme in time.

We first investigated the possibility to use the modified equations technique to account for the main error term of the discretisation in the convergence analysis. An advantage of such an approach is that it takes into account the main features of the discrete schemes for low-frequencies. We discussed the relevance of using such an approach with a general linear differential equation, and focused on the particular case with exactly one differentiation in space of any order. In this case, we derived the modified-in-space method which turned out to provide relatively modest improvements compared to

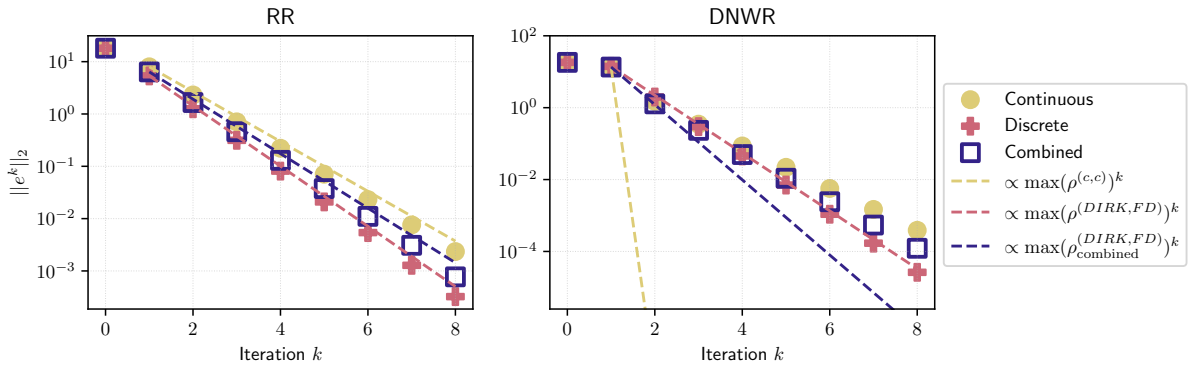

Figure 8. L^2 norm of the error in the time domain across iterations for RR (left) and DNWR (right). The dashed lines show the upper bound on the convergence obtained with the theoretical convergence factor. It is expected that the yellow and purple dashed lines do not really bound the L^2 norm since the discretisation is not perfectly taken into account.

the standard continuous analysis. This result suggests that the discretization in the inner domains does not have much influence on the convergence speed for reaction-diffusion equations. This statement is supported by the fact that keeping the continuous formulation in the inner domain and accounting only for the discretization of the interface conditions leads to a similar approximation of the discrete convergence factor. The modified equations in time could easily be used but we have pointed out that they do not simplify the discrete analysis for one-stage schemes and are not accurate for multi-stage schemes.

We then introduced a second method whose principle is to combine the semi-discrete in time, semi-discrete in space, and continuous analyses to approximate the fully discrete convergence factor. Even though this approach neglects the interactions between the time and space discretisations, the *combined* analysis can provide a good approximation of the discrete convergence factor.

To illustrate the benefits of the proposed methods, we examined the gain of performance obtained when optimising the convergence factor taking advantage of the free parameters provided either by Dirichlet-Neumann (with relaxation parameter) or Robin-Robin (one-sided and two-sided) interface conditions. Optimising on a better approximation of the discrete convergence factor leads to a faster numerical convergence. When the optimisation is done on the convergence factor obtained from the modified equations approach, the convergence speed is not significantly improved compared to a continuous analysis. The *combined* method provides much better results especially for large diffusion coefficients and small reaction parameter, and seems quite robust by nature. As a future work, theses findings should generalized to other types of PDEs. Moreover, each of the two methods can be further developed. By following [13] the modified equations can be derived *around any wave number*. The idea of combining semi-discrete analyses can be extended to other aspects (e.g. variable diffusivity, particular shape of the domains) to take into account specific problems one by one.

References

[1] R. Alexander. Diagonally Implicit Runge–Kutta Methods for Stiff O.D.E.'s. *SIAM Journal on Numerical Analysis*, 14(6):1006–1021, 1977.

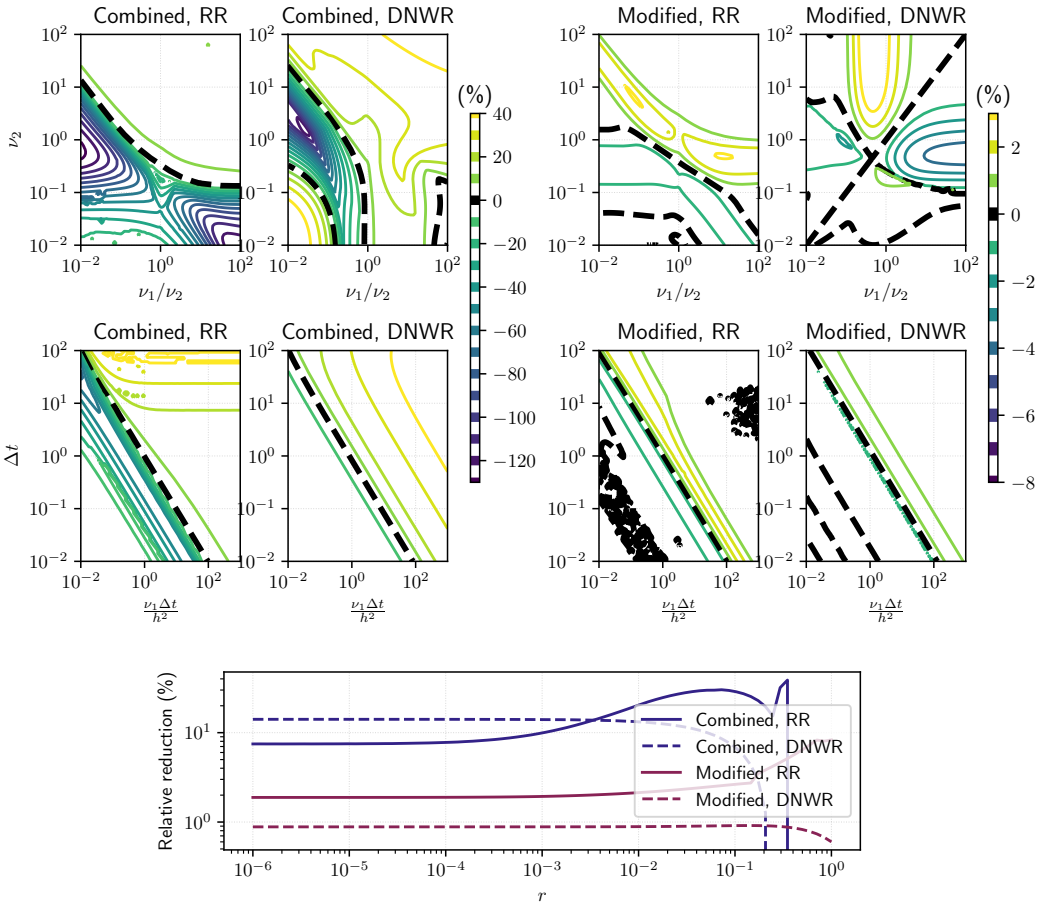

Figure 9. Relative reduction of the convergence factor of the "combined" and "modified" methods depending on parameters ν_1, ν_2 (top), $\Delta t, h$ (middle) and r (bottom). Relative reduction is defined as $1 - \frac{\widetilde{\rho}_{\text{Combined}}}{\widetilde{\rho}_{\text{Continuous}}}$ or $1 - \frac{\widetilde{\rho}_{\text{Modified}}}{\widetilde{\rho}_{\text{Continuous}}}$ where $\widetilde{\rho}_{(\cdot)} = \max_{\omega \in [\omega_{\min}, \omega_{\max}]} |\varrho^{(\text{DIRK,FD})}|$ with the relaxation or Robin parameters optimised using the method subscripted ("Combined", "Modified" or "Continuous"). The dashed black lines stand for the zero. ν_1 is constant in the Courant parabolic number $\frac{\nu_1 \Delta t}{h^2}$.

[2] R. J. Beerends, H. G. ter Morsche, J. C. van den Berg, and E. M. van de Vrie. *Fourier and Laplace Transforms*. Cambridge University Press, Cambridge, 2003.

[3] P.-M. Berthe. *Méthodes de décomposition de domaine de type relaxation d'ondes optimisées pour l'équation de convection-diffusion instationnaire discrétisée par volumes finis*. PhD Thesis, Paris 13, 2013.

[4] R. Carpentier, A. de La Bourdonnaye, and B. Larrouturou. On the derivation of the modified equation for the analysis of linear numerical methods. *ESAIM: Mathematical Modelling and Numerical Analysis*, 31(4):459–470, 1997.

[5] S. Clement, F. Lemarié, and E. Blayo. Discrete analysis of Schwarz waveform relaxation for a diffusion reaction problem with discontinuous coefficients. *SMAI J. Comput. Math.*, 2022. in press.

[6] A. S. Fokas and B. Pelloni. A transform method for linear evolution PDEs on a finite interval. *IMA journal of applied mathematics*, 70(4):564–587, 2005.

[7] M. J. Gander. Optimized Schwarz methods. *SIAM Journal on Numerical Analysis*, 44(2):699–731, 2006.

[8] M. J. Gander. Schwarz methods over the course of time. *Electronic transactions on numerical analysis*, 31:228–255, 2008.

[9] M. J. Gander, F. Kwok, and B. Mandal. Dirichlet-Neumann and Neumann-Neumann Waveform Relaxation algorithms for parabolic problems. *Electronic transactions on numerical analysis*, 45, 2013.

[10] P. Garabedian. Estimation of the relaxation factor for small mesh size. *Mathematical Tables and other Aids to Computation*, 10(56):183–185, 1956.

[11] D. F. Griffiths and J. M. Sanz-Serna. On the scope of the method of modified equations. *SIAM Journal on Scientific and Statistical Computing*, 7(3):994–1008, 1986.

[12] R. D. Haynes and K. Mohammad. Fully Discrete Schwarz Waveform Relaxation on Two Bounded Overlapping Subdomains. In *Domain Decomposition Methods in Science and Engineering XXV*, pages 159–166, Cham, 2020. Springer International Publishing.

[13] J. Li and Z. Yang. The Von Neumann analysis and modified equation approach for finite difference schemes. *Applied Mathematics and Computation*, 225:610–621, 2013.

[14] G. Manfredi and M. Ottaviani. Finite-difference schemes for the diffusion equation. In *Dynamical Systems, Plasmas and Gravitation*, pages 82–92, Berlin, Heidelberg, 1999. Springer Berlin Heidelberg.

[15] S. Thery, C. Pelletier, F. Lemarié, and E. Blayo. Analysis of Schwarz waveform relaxation for the coupled Ekman boundary layer problem with continuously variable coefficients. *Numerical Algorithms*, 2021.

[16] R. F. Warming and B. J. Hyett. The modified equation approach to the stability and accuracy analysis of finite-difference methods. *Journal of Computational Physics*, 14(2):159 – 179, 1974.

[17] S.-L. Wu and M. D. Al-Khaleel. Semi-discrete Schwarz waveform relaxation algorithms for reaction diffusion equations. *BIT Numerical Mathematics*, 54(3):831–866, 2014.

Appendix A. Semi-discrete convergence analysis

This Appendix presents the method to derive the convergence factor in the semi-discrete cases, through the example of the reaction-diffusion equation in two 1D non-overlapping subdomains with different diffusivities. The Schwarz iteration index is noted k. The solution u_j^k of the homogeneous equation (2.1) studied here is to be understood as the error of a coupling problem with respect to the converged solution.

A.1. **Continuous with Discrete Transmission Operators (CDTO)**

We examine the convergence factor with semi-discrete in space transmission operators defined by (2.4). This convergence factor is referred by "Continuous with Discrete Transmission Operators" in this study because we keep the continuous equations in the inner domains. The Fourier transform of the equation (2.1) with $\mathcal{L} = \nu\partial_{xx} - r$ together with the assumption that the spatial domains are of infinite size yield $\widehat{u}_1^k = A_k \exp(x\sqrt{\frac{i\omega+r}{\nu_1}})$ and $\widehat{u}_2^k = B_k \exp(-x\sqrt{\frac{i\omega+r}{\nu_2}})$. The DNWR transmission operators (2.2) discretised with (2.4) give

$$A_k = (1-\theta)B_{k-1} + \theta A_{k-1},\ B_k = \frac{\eta_1}{\eta_2}A_k \tag{A.1}$$

where $\eta_1 = \nu_1\left(\frac{1-\exp(x_{-1}\sqrt{\frac{i\omega+r}{\nu_1}})}{h} + h\frac{i\omega+r}{2}\right)$ and $\eta_2 = \nu_2\left(\frac{\exp(-x_1\sqrt{\frac{i\omega+r}{\nu_2}})-1}{h} - h\frac{i\omega+r}{2}\right)$. The convergence factor $\varrho_{\text{DNWR}}^{(\text{c,CDTO})} = \frac{\widehat{u}_1^k(x=0)}{\widehat{u}_1^{k-1}(x=0)}$ with discrete transmission operator is $\frac{A_k}{A_{k-1}} = (1-\theta)\frac{\eta_1}{\eta_2} + \theta$. For Robin-Robin transmission conditions, keeping the same η_1, η_2 (2.3) discretised with (2.4) give

$$(p_1+\eta_1)A_k = (p_1+\eta_2)B_{k-1},\ (p_2+\eta_2)B_k = (p_2+\eta_1)A_k. \tag{A.2}$$

The convergence factor $\varrho_{\text{RR}}^{(\text{c,CDTO})}$ with discrete transmission operator is hence $\frac{A_k}{A_{k-1}} = \frac{(p_1+\eta_2)(p_2+\eta_1)}{(p_1+\eta_1)(p_2+\eta_2)}$.

A.2. **Semi-discrete in space**

When applying a second-order FD centered scheme to $\mathcal{L} = \nu\partial_{xx} - r$, the PDE is transformed into a set of ODEs, which can be solved through Fourier transform together with the ansatz $\widehat{u}_1^k(x_{-m}) = A_k(\lambda_1+1)^m$ and $\widehat{u}_2^k(x_m) = B_k(\lambda_2+1)^m$ where $m \in \mathbb{N}$ is the space index, x_0 is the location of the interface and x_m is the m-th collocation point. λ_j $(j = 1, 2)$ is the root with negative real part of a second-order polynomial: $\lambda_j = \chi_j - \sqrt{\chi_j}\sqrt{\chi_j+2}$ with $\chi_j = \frac{(i\omega+r)h^2}{2\nu_j}$ (see [17] for a more detailed derivation). The convergence factor then depends on the Schwarz method used (in both cases, the transmission operator (2.4) is treated with a ghost point):

- DNWR: A discretised Neumann transmission condition in the Fourier domain simplifies to $B_k = -\sqrt{\frac{\nu_1}{\nu_2}}\sqrt{\frac{\chi_1+2}{\chi_2+2}}A_k$ and the Dirichlet transmission condition together with the relaxation step yield a convergence factor equal to $\varrho_{\text{DNWR}}^{(\text{c,FD})} = \frac{\widehat{u}_1^k(0)}{\widehat{u}_1^{k-1}(0)} = \frac{A_k}{A_{k-1}} = -\theta\sqrt{\frac{\nu_1}{\nu_2}}\sqrt{\frac{\chi_1+2}{\chi_2+2}} + (1-\theta)$.
- RR: The discretised Robin conditions yield $B_k = \frac{p_2h-\nu_1(\lambda_1-\chi_1)}{p_2h+\nu_2(\lambda_2-\chi_2)}A_k$ and $A_k = \frac{p_1h+\nu_2(\lambda_2-\chi_2)}{p_1h-\nu_1(\lambda_1-\chi_1)}B_{k-1}$. Hence the convergence factor $\varrho_{\text{RR}}^{(\text{c,FD})} = \frac{A_k}{A_{k-1}} = \frac{p_1h+\nu_2(\lambda_2-\chi_2)}{p_1h-\nu_1(\lambda_1-\chi_1)}\frac{p_2h-\nu_1(\lambda_1-\chi_1)}{p_2h+\nu_2(\lambda_2-\chi_2)}$.

A.3. **Semi-discrete in time**

Instead of the Fourier transform, the discretisation in time requires using the z-transform (e.g. [2, 12]). In the simple case of the Backward-Euler scheme, a semi-discrete frequency $s^{BE} = \frac{z-1}{z\Delta t}$ appears and replaces the symbol $i\omega$ appearing in a continuous in time case. For one-stage time schemes, the semi-discrete analysis of the convergence of Schwarz methods only requires a change of frequency variable.

Let us now consider the multi-stage time scheme (2.5). The convergence factor of Schwarz Waveform Relaxation with Dirichlet-Neumann condition is given in [5]. Once a z-transform is applied to both stages, a fourth-order differential equation is obtained:

$$\left(z\left(1 + r\Delta t\, b - \Delta t\, b\, \nu\, \partial_x^2\right)^2 - 1 - r\Delta t\, a + \Delta t\, a\, \nu\, \partial_x^2\right)\widehat{u}_j^k = 0 \tag{A.3}$$

APPROXIMATING DISCRETE CONVERGENCE FACTOR OF SCHWARZ METHODS

Using $2b = 1 + a$ and the frequency variable $s^{BE} = \frac{z-1}{z\Delta t}$, it becomes:

$$\left(s^{BE} - (1 + a\Delta t s^{BE})\left(\nu\partial_x^2 - r\right) + b^2\Delta t\left(\nu\partial_x^2 - r\right)^2\right)\widehat{u}_j^k = 0 \tag{A.4}$$

The solution of this fourth-order ODE is:

$$\begin{aligned}\widehat{u}_1^k &= A_k e^{x\sigma_1} + A'_k e^{x\sigma_3} + C_k e^{-x\sigma_1} + C'_k e^{-x\sigma_3}\\ \widehat{u}_2^k &= B_k e^{x\sigma_2} + B'_k e^{x\sigma_4} + D_k e^{-x\sigma_2} + D'_k e^{-x\sigma_4}\end{aligned} \tag{A.5}$$

where

$$\sigma_{\{1,2,3,4\}} = \pm\frac{1}{a\sqrt{\Delta t\nu_j}}\sqrt{1 + a\tilde{s} + a^2\Delta t r \pm \sqrt{1-\tilde{s}}\sqrt{1-a^2\tilde{s}}} \tag{A.6}$$

with $\tilde{s} = \Delta t\, s^{\mathrm{BE}}$, where $\sigma_{\{1,3\}}$ use ν_1 and $\sigma_{\{2,4\}}$ use ν_2. σ_1 and σ_3 (resp. σ_2 and σ_4) have positive (resp. negative) real parts and have a $+$ (resp. $-$) sign in place of the first $\pm$ in (A.6). The second $\pm$ is a $-$ sign for σ_1, σ_2 and a $+$ sign for σ_3, σ_4. We will look at the evolution of $\widehat{u}_j^k$, where $C_k = C'_k = D_k = D'_k = 0$ because of the infinite domain assumption together with the real parts signs.

$$\begin{aligned}\widehat{u}_1^k &= A_k e^{x\sigma_1} + A'_k e^{x\sigma_3}\\ \widehat{u}_2^k &= B_k e^{x\sigma_2} + B'_k e^{x\sigma_4}\end{aligned} \tag{A.7}$$

A.3.1. *Neumann conditions*

We now apply the preceding expressions of $\widehat{u}_j^k$ in the following system:

$$\begin{aligned}\nu_2\,\partial_x\widehat{u}_2^{\star k}(x_0) &= \gamma(z)\,\nu_1\,\partial_x\widehat{u}_1^{k-1}(x_0)\\ \nu_2\,\partial_x\widehat{u}_2^{k}(x_0) &= \nu_1\,\partial_x\widehat{u}_1^{k-1}(x_0)\end{aligned} \tag{A.8}$$

where $\gamma(z)$ is the discrete Fourier image of the projection operator in the frequency domain that uses the interface values of u_1 and returns a projection to the interface condition of the intermediate step $u_2^\star$. Let $\mu_i = z(1 + r\Delta t\, b - \Delta t\, b\,\nu_j\sigma_i^2)$ be the frequencies characterising the second stage of the time scheme (for all the variables indexed by i, the domain $j = 1$ for $i = 1, 3$ and $j = 2$ for $i = 2, 4$). The intermediate values then read $\widehat{u}_1^{\star k} = A_k\,\mu_1 e^{x\sigma_1} + A'_k\,\mu_3 e^{x\sigma_3}$ and $\widehat{u}_2^{\star k} = B_k\,\mu_2 e^{x\sigma_2} + B'_k\,\mu_4 e^{x\sigma_4}$. (A.8) implies:

$$\begin{aligned}\mu_2 B_k\sigma_2 + \mu_4 B'_k\sigma_4 &= \gamma\frac{\nu_1}{\nu_2}\left(A_{k-1}\sigma_1 + A'_{k-1}\sigma_3\right)\\ B_k\sigma_2 + B'_k\sigma_4 &= \frac{\nu_1}{\nu_2}\left(A_{k-1}\sigma_1 + A'_{k-1}\sigma_3\right)\end{aligned} \tag{A.9}$$

Calculating B_k, B'_k as a function of A_{k-1}, A'_{k-1} leads to the part of the convergence factor driven by the Neumann transmission operator:

$$\begin{aligned}B_k &= (1-\tilde{\gamma})\,\frac{1}{\sigma_2}\frac{F_{k-1}}{\nu_2} \quad ,\ \tilde{\gamma} = \frac{\mu_2 - \gamma}{\mu_2 - \mu_4}\\ B'_k &= \tilde{\gamma}\frac{1}{\sigma_4}\frac{F_{k-1}}{\nu_2}\\ F_{k-1} &= \nu_1\left(A_{k-1}\sigma_1 + A'_{k-1}\sigma_3\right)\end{aligned} \tag{A.10}$$

where F_k is the surface flux applied to subdomain Ω_1 at iteration k.

Remark A.1. $\tilde{\gamma}_j$ represents a weighted difference between two ways to determine $u(t^\star)$: either via a time extrapolation (with the operator γ), or via the second stage of the time scheme, represented by μ_i.

- $\tilde{\gamma}_j = 0$ gives a convergence factor similar to one-stage time schemes, because the time scheme performs (through μ_i) an interpolation identical to γ. This implies that the semi-discrete in time solutions of the coupling problem and the monolithic one of the full domain are identical. However $\tilde{\gamma}_j = 0$ also implies that γ is nonlocal in time.

- As $\tilde{\gamma}_j$ increases, the impact of using a two-stage scheme on the convergence factor is increasingly important. When γ is different from μ_i the coupled solution differs from the monolithic solution. For the DIRK scheme considered here, a linear extrapolation suffices to guarantee that the scheme is second order accurate.

A.3.2. *Dirichlet conditions and DNWR convergence factor*

We now apply the different equalities linking A_k, A'_k, B_k and B'_k to the following system arising from the DNWR interface conditions:

$$\begin{aligned} \widehat{u}_1^{\star k}(x_0) &= \gamma\left(\theta \widehat{u}_2^{k}(x_0) + (1-\theta)\widehat{u}_1^{k-1}(x_0)\right) \\ \widehat{u}_1^{k}(x_0) &= \theta \widehat{u}_2^{k-1}(x_0) + (1-\theta)\widehat{u}_1^{k-1}(x_0). \end{aligned} \tag{A.11}$$

Note that the intermediate step $\widehat{u}_1^{\star}$ used in the relaxation is projected using γ. We assume here that the data $\widehat{u}^{\star}$ is not stored for the relaxation step. Using μ_1 and μ_3 to express $\widehat{u}_1^{\star}$, we obtain

$$\begin{aligned} \mu_1 A_k + \mu_3 A'_k &= \gamma\left(\theta(B_k + B'_k) + (1-\theta)(A_{k-1} + A'_{k-1})\right) \\ A_k + A'_k &= \quad \theta(B_k + B'_k) + (1-\theta)(A_{k-1} + A'_{k-1}) \end{aligned} \tag{A.12}$$

which is equivalent to:

$$\begin{aligned} \mu_1 A_k + \mu_3 A'_k &= \gamma\left(\theta\left(\frac{1-\tilde{\gamma}}{\sigma_2} + \frac{\tilde{\gamma}}{\sigma_4}\right)\frac{F_{k-1}}{\nu_2} + (1-\theta)(A_{k-1} + A'_{k-1})\right) \\ A_k + A'_k &= \quad \theta\left(\frac{1-\tilde{\gamma}}{\sigma_2} + \frac{\tilde{\gamma}}{\sigma_4}\right)\frac{F_{k-1}}{\nu_2} + (1-\theta)(A_{k-1} + A'_{k-1}). \end{aligned} \tag{A.13}$$

The evolution of A_k, A'_k is given by

$$\begin{aligned} \mu_1 A_k + \mu_3 A'_k &= \gamma\left(\xi_1 A_{k-1} + \xi_3 A'_{k-1}\right) \\ A_k + A'_k &= \quad \xi_1 A_{k-1} + \xi_3 A'_{k-1} \end{aligned} \tag{A.14}$$

where $\xi_i = \theta\left(\frac{1-\tilde{\gamma}}{\sigma_2} + \frac{\tilde{\gamma}}{\sigma_4}\right)\frac{\nu_1}{\nu_2}\sigma_i + (1-\theta)$. We define the convergence factor as the non-zero eigenvalue of the transition matrix between A_{k-1}, A'_{k-1} and A_k, A'_k, which is equal to $\frac{\xi_1 A_k + \xi_3 A'_k}{\xi_1 A_{k-1} + \xi_3 A'_{k-1}} = \xi_1(1-\tilde{\gamma}) + \xi_3\tilde{\gamma}$, easily computed with (A.14) with the identity $\tilde{\gamma} = \frac{\mu_1 - \gamma}{\mu_1 - \mu_3}$. Finally we get

$$\varrho_{\mathrm{DNWR}}^{(\mathrm{DIRK,c})} = \theta\left(\frac{1-\tilde{\gamma}}{\sigma_2} + \frac{\tilde{\gamma}}{\sigma_4}\right)\frac{\nu_1}{\nu_2}\left(\sigma_1(1-\tilde{\gamma}) + \sigma_3\tilde{\gamma}\right) + (1-\theta) \tag{A.15}$$

Note that while the semi-discrete in space analysis tells us that for identical diffusivities $\nu_1 = \nu_2$, the optimal relaxation parameter θ is 1/2, here setting $\nu_1 = \nu_2$ may lead to a different conclusion, depending on the projection γ.

APPROXIMATING DISCRETE CONVERGENCE FACTOR OF SCHWARZ METHODS

A.3.3. *Robin two-sided case*

In the Robin case, the transmission conditions are

$$\begin{aligned} z(1+r\Delta t\, b-\Delta t\, b\,\nu_2\partial_x^2)(\nu_2\partial_x+p_2)\widehat{u}_2^k(x_0) &= \gamma(\nu_1\partial_x+p_2)\widehat{u}_1^{k-1}(x_0)\\ (\nu_2\partial_x+p_2)\widehat{u}_2^k(x_0) &= (\nu_1\partial_x+p_2)\widehat{u}_1^{k-1}(x_0)\\ z(1+r\Delta t\, b-\Delta t\, b\,\nu_1\partial_x^2)(\nu_1\partial_x+p_1)\widehat{u}_1^k(x_0) &= \gamma(\nu_2\partial_x+p_1)\widehat{u}_2^k(x_0)\\ (\nu_1\partial_x+p_1)\widehat{u}_1^k(x_0) &= (\nu_2\partial_x+p_1)\widehat{u}_2^k(x_0) \end{aligned} \tag{A.16}$$

By defining the same μ_i as in (A.9), in subdomain 2 we end up with:

$$\begin{aligned} \mu_2 B_k\left(p_2+\nu_2\sigma_2\right)+\mu_4 B_k'\left(p_2+\nu_2\sigma_4\right) &= \gamma\left(A_{k-1}\left(p_2+\nu_1\sigma_1\right)+A_{k-1}'\left(p_2+\nu_1\sigma_3\right)\right)\\ B_k\left(p_2+\nu_2\sigma_2\right)+B_k'\left(p_2+\nu_2\sigma_4\right) &= A_{k-1}\left(p_2+\nu_1\sigma_1\right)+A_{k-1}'\left(p_2+\nu_1\sigma_3\right) \end{aligned} \tag{A.17}$$

and on subdomain 1:

$$\begin{aligned} \mu_1 A_k\left(p_1+\nu_1\sigma_1\right)+\mu_3 A_k'\left(p_1+\nu_1\sigma_3\right) &= \gamma\left(B_k\left(p_1+\nu_2\sigma_2\right)+B_k'\left(p_1+\nu_2\sigma_4\right)\right)\\ A_k\left(p_1+\nu_1\sigma_1\right)+A_k'\left(p_1+\nu_1\sigma_3\right) &= B_k\left(p_1+\nu_2\sigma_2\right)+B_k'\left(p_1+\nu_2\sigma_4\right) \end{aligned} \tag{A.18}$$

Using $\tilde{\gamma}=\frac{\mu_2-\gamma}{\mu_2-\mu_4}=\frac{\mu_1-\gamma}{\mu_1-\mu_3}$ previously introduced in the Dirichlet-Neumann analysis, we obtain

$$\begin{aligned} B_k\left(p_2+\nu_2\sigma_2\right) &= \left(A_{k-1}\left(p_2+\nu_1\sigma_1\right)+A_{k-1}'\left(p_2+\nu_1\sigma_3\right)\right)\left(1-\tilde{\gamma}\right)\\ B_k'\left(p_2+\nu_2\sigma_4\right) &= \left(A_{k-1}\left(p_2+\nu_1\sigma_1\right)+A_{k-1}'\left(p_2+\nu_1\sigma_3\right)\right)\tilde{\gamma}\\ A_k\left(p_1+\nu_1\sigma_1\right) &= \left(B_k\left(p_1+\nu_2\sigma_2\right)+B_k'\left(p_1+\nu_2\sigma_4\right)\right)\left(1-\tilde{\gamma}\right)\\ A_k'\left(p_1+\nu_1\sigma_3\right) &= \left(B_k\left(p_1+\nu_2\sigma_2\right)+B_k'\left(p_1+\nu_2\sigma_4\right)\right)\tilde{\gamma} \end{aligned} \tag{A.19}$$

By defining $R_k=A_k\left(p_2+\nu_1\sigma_1\right)+A_k'\left(p_2+\nu_1\sigma_3\right)$, the non-zero eigenvalue of the transition matrix between A_{k-1},A_{k-1}' and A_k,A_k' is $\frac{R_k}{R_{k-1}}$:

$$\varrho_{\mathrm{RR}}^{(\mathrm{DIRK,c})}=\frac{R_k}{R_{k-1}}=\left(\frac{p_1+\nu_2\sigma_2}{p_2+\nu_2\sigma_2}\left(1-\tilde{\gamma}\right)+\frac{p_1+\nu_2\sigma_4}{p_2+\nu_2\sigma_4}\tilde{\gamma}\right)\left(\frac{p_2+\nu_1\sigma_1}{p_1+\nu_1\sigma_1}\left(1-\tilde{\gamma}\right)+\frac{p_2+\nu_1\sigma_3}{p_1+\nu_1\sigma_3}\tilde{\gamma}\right) \tag{A.20}$$

Appendix B. Analysis for discrete space and time: DIRK and Finite Differences

This Appendix presents the analysis of the convergence in the fully discrete case for a reaction-diffusion problem.

B.1. Resolution of the ODEs

We consider a simple centered second-order FD as described in Section 2. In particular, the discrete representation of the flux at interface is $\nu_2\partial_x u_2(x_0)\approx\nu_2\frac{u_2(x_1)-u_2(x_0)}{h}-\frac{h}{2}(\partial_t+r)u_2(x_0)$ for domain 2 and $\nu_1\partial_x u_1(x_0)\approx\nu_1\frac{u_1(x_0)-u_1(x_{-1})}{h}+\frac{h}{2}(\partial_t+r)u_1(x_0)$ for domain 1. For the sake of readability, we introduce $\delta_x^2\phi=\phi_{m-1}-2\phi_m+\phi_{m+1}$ such that the semi-discrete problem reads:

$$(\partial_t+r)u_j^k-\frac{\nu_j}{h^2}\delta_x^2 u_j^k=0 \tag{B.1}$$

Now considering the DIRK scheme to discretise the time derivative, we obtain (k exponents were omitted)

$$\begin{aligned} \left(1+rb\Delta t-b\Delta t\frac{\nu_j}{h^2}\delta_x^2\right)u_j^\star &= \left(1+ra\Delta t-a\Delta t\frac{\nu_j}{h^2}\delta_x^2\right)u_j^n\\ \left(1+rb\Delta t-b\Delta t\frac{\nu_j}{h^2}\delta_x^2\right)u_j^{n+1} &= u_j^\star \end{aligned} \tag{B.2}$$

By substitution of $u^\star$, we find:

$$\left(z\left(1+rb\Delta t-\Gamma_b\delta_x^2\right)^2-\left(1+ra\Delta t-\Gamma_a\delta_x^2\right)\right)\widehat{u}_j^k=0 \tag{B.3}$$

with $\Gamma_b=b\Delta t\frac{\nu_j}{h^2}$. The ansatz $\widehat{u}^k_{m,j=1}=\sum_i A_k^i(\tilde{\lambda}_{ij})^{-m}$ and $\widehat{u}^k_{m,j=2}=\sum_i B_k^i(\tilde{\lambda}_{ij})^m$, $m\in\mathbb{Z}$, leads to

$$\left(z\left(1+br\Delta t\right)^2-1-ar\Delta t\right)\tilde{\lambda}_{ij}^2+\left(\Gamma_a-2z\Gamma_b\left(1+rb\Delta t\right)\right)\tilde{\lambda}_{ij}\left(\tilde{\lambda}_{ij}-1\right)^2+z\Gamma_b^2\left(\tilde{\lambda}_{ij}-1\right)^4=0 \tag{B.4}$$

The 4 roots of this polynomial are noted $\tilde{\lambda}_{ij}=e^{h\tilde{\sigma}_i}$. The index j is omitted in $\tilde{\sigma}_i$ as $i=1,3$ corresponds to $j=1$ and $i=2,4$ corresponds to $j=2$. $\tilde{\sigma}_i$ is the discrete in space counterpart of σ_i: when $h\to 0$, $\tilde{\sigma}_i\to\sigma_i$. The evolution of $\widehat{u}_j$ is given by

$$\begin{aligned}\widehat{u}^k_{m,1}&=A_ke^{-mh\tilde{\sigma}_1}+A'_ke^{-mh\tilde{\sigma}_3}\\ \widehat{u}^k_{m,2}&=B_ke^{mh\tilde{\sigma}_2}+B'_ke^{mh\tilde{\sigma}_4}\end{aligned} \tag{B.5}$$

where, as in the semi-discrete in time case, two roots have a positive real part $(\tilde{\sigma}_1,\tilde{\sigma}_3)$ and $\tilde{\sigma}_2,\tilde{\sigma}_4$ have negative real parts: the infinite domain assumption allows to consider only the roots of one side of the complex plane.

The previous ansatz will also be useful to express $\widehat{u}_j^{\star k}$. Introducing $\tilde{\mu}_i=z\left(1+r\Delta tb-\Gamma_b\left(\tilde{\lambda}_i-2+\frac{1}{\tilde{\lambda}_i}\right)\right)$, we obtain

$$\begin{aligned}\widehat{u}^{\star k}_{m,1}&=\tilde{\mu}_1A_ke^{-mh\tilde{\sigma}_1}+\tilde{\mu}_3A'_ke^{-mh\tilde{\sigma}_3}\\ \widehat{u}^{\star k}_{m,2}&=\tilde{\mu}_2B_ke^{mh\tilde{\sigma}_2}+\tilde{\mu}_4B'_ke^{mh\tilde{\sigma}_4}\end{aligned} \tag{B.6}$$

B.2. **Boundary conditions**

B.2.1. *Neumann conditions*

In the case of the DNWR algorithm, we have two Neumann conditions: one is prescribed to $u^\star$ and the other is applied to $\widehat{u}$. This leads to (k exponents were omitted)

$$\begin{aligned}\beta\nu_2\frac{u_2^\star(x_1)-u_2^\star(x_0)}{h}-a\nu_2\frac{u_2^n(x_1)-u_2^n(x_0)}{h}-\frac{h}{2}\left(\frac{u_2^\star(x_0)-u_2^n(x_0)}{\Delta t}+\beta ru_2^\star(x_0)-aru_2^n(x_0)\right)&=(\beta\gamma-a)g_{DN}^n\\ \nu_2\frac{u_2^{n+1}(x_1)-u_2^{n+1}(x_0)}{h}-\frac{h}{2}\left(\frac{u_2^{n+1}(x_0)-u_2^\star(x_0)}{\beta\Delta t}-ru_2^{n+1}(x_0)\right)&=g_{DN}^{n+1}\end{aligned}$$

where $g_{DN}^n=\nu_1\frac{u_1^n(x_0)-u_1^n(x_{-1})}{h}+\frac{h}{4\Delta t}(u_1^{n+1}(x_0)-u_1^{n-1}(x_0))+\frac{h}{2}ru_1^n(x_0)$. In the frequency domain, $\widehat{g}_{DN}^k=\left(\frac{\nu_1}{h}+h\frac{z^2+2zr\Delta t-1}{4z\Delta t}\right)(A_k+A'_k)-\frac{\nu_1}{h}\left(A_ke^{-h\tilde{\sigma}_1}+A'_ke^{-h\tilde{\sigma}_3}\right)$ and

$$\eta_2^\star B_k+\eta_4^\star B'_k=(\beta\gamma-a)\,\widehat{g}_{DN}^{k-1},\qquad\text{with}\qquad\eta_i^\star=(\beta\tilde{\mu}_i-a)(\nu_2\frac{e^{h\tilde{\sigma}_i}-1}{h}-\frac{h}{2}r)-h\frac{\tilde{\mu}_i-1}{2\Delta t} \tag{B.7}$$

$$\eta_2B_k+\eta_4B'_k=\widehat{g}_{DN}^{k-1},\qquad\text{with}\qquad\eta_i=\nu_2\frac{e^{h\tilde{\sigma}_i}-1}{h}-\frac{h}{2}r-h\frac{1-\mu_i/z}{2\beta\Delta t} \tag{B.8}$$

From those two equalities we get

$$B_k+B'_k=\frac{\eta_4^\star-\eta_2^\star-(\eta_4-\eta_2)(\beta\gamma-a)}{\eta_2\eta_4^\star-\eta_2^\star\eta_4}\widehat{g}_{DN}^{k-1} \tag{B.9}$$

APPROXIMATING DISCRETE CONVERGENCE FACTOR OF SCHWARZ METHODS

B.2.2. *Dirichlet conditions and DNWR convergence factor*

We now consider the Dirichlet conditions with relaxation parameter θ. In practice, we have two Dirichlet conditions: one is applied on $\widehat{u}^\star$ and the other is applied on $\widehat{u}$.

$$\begin{aligned}\widehat{u}_1^{\star k}(x_0) &= \gamma\left(\theta\widehat{u}_2^k(x_0) + (1-\theta)\widehat{u}_1{}^{k-1}(x_0)\right)\\ \widehat{u}_1^k(x_0) &= \theta\widehat{u}_2^{k-1}(x_0) + (1-\theta)\widehat{u}_1^{k-1}(x_0).\end{aligned} \tag{B.10}$$

It is very similar to the Dirichlet conditions of the semi-discrete in time case (A.12) :

$$\begin{aligned}\tilde{\mu_1}A_k + \tilde{\mu_3}A'_k &= \gamma\left(\theta(B_k+B'_k) + (1-\theta)(A_{k-1}+A'_{k-1})\right)\\ A_k + A'_k &= \theta(B_k+B'_k) + (1-\theta)(A_{k-1}+A'_{k-1})\end{aligned} \tag{B.11}$$

where $B_k + B'_k$ can be expressed as A_k, A'_k using (B.9):

$$\begin{aligned}\tilde{\mu_1}A_k + \tilde{\mu_3}A'_k &= \gamma\left(\tilde{\xi}_1 A_{k-1} + \tilde{\xi}_3 A'_{k-1}\right)\\ A_k + A'_k &= \tilde{\xi}_1 A_{k-1} + \tilde{\xi}_3 A'_{k-1}\end{aligned} \tag{B.12}$$

where $\tilde{\xi}_i = 1-\theta+\theta\frac{\eta_4^\star-\eta_2^\star-(\eta_4-\eta_2)(\beta\gamma-a)}{\eta_2\eta_4^\star-\eta_2^\star\eta_4}\left(\nu_1\frac{1-e^{-h\tilde{\sigma}_i}}{h} + h\frac{z^2+2zr\Delta t-1}{4z\Delta t}\right)$. We define the convergence factor as the non-zero eigenvalue of the transition matrix between A_{k-1}, A'_{k-1} and A_k, A'_k, which is equal to $\frac{\xi_1 A_k+\xi_3 A'_k}{\xi_1 A_{k-1}+\xi_3 A'_{k-1}} = \tilde{\xi}_1(1-\tilde{\gamma}_1) + \tilde{\xi}_3\tilde{\gamma}_1$, obtained with (B.12). Finally,

$$\varrho_{\text{DNWR}}^{(\text{DIRK,FD})} = 1-\theta+\theta\frac{\eta_4^\star-\eta_2^\star-(\eta_4-\eta_2)(\beta\gamma-a)}{\eta_2\eta_4^\star-\eta_2^\star\eta_4}\left(\nu_1\frac{1-(1-\tilde{\gamma_1})e^{-h\tilde{\sigma}_1}-e^{-h\tilde{\sigma}_3}\tilde{\gamma_1}}{h} + h\frac{z^2+2zr\Delta t-1}{4z\Delta t}\right) \tag{B.13}$$

B.3. **Robin two-sided case**

In the Robin two-sided case, transmission conditions are similar to the Dirichlet-Neumann conditions: we define $\widehat{\boldsymbol{g}}_1$ such that $\widehat{\boldsymbol{g}}_1\cdot(A_k, A'_k)^T = \widehat{g}_{DN}^k + p_2(A_k+A'_k)$ and $\widehat{\boldsymbol{g}}_2$ the corresponding value in the domain $j=2$, using the Robin parameter p_1:

$$\widehat{\boldsymbol{g}}_2 = \left(\nu_2\frac{e^{h\tilde{\sigma}_2}-1}{h} - h\frac{z^2-1}{4z\Delta t} - \frac{h}{2}r + p_1, \qquad \nu_2\frac{e^{h\tilde{\sigma}_4}-1}{h} - h\frac{z^2-1}{4z\Delta t} - \frac{h}{2}r + p_1\right) \tag{B.14}$$

We note δ_x/h the approximation of the first-order space differentiation and our discrete Robin transmission conditions read

$$\begin{aligned}\left((\nu_2\frac{\delta_x}{h} + p_2 - \frac{h}{2}r)(\beta\mu-a) - \frac{h}{2}\frac{\mu-1}{\Delta t}\right)\widehat{u}_2^k(x_0) &= (\beta\gamma-a)\,\widehat{\boldsymbol{g}}_1\cdot(A_{k-1}, A'_{k-1})^T\\ (\nu_2\frac{\delta_x}{h} + p_2 - \frac{h}{2}\frac{1+r\beta\Delta t-\mu/z}{\beta\Delta t})\widehat{u}_2^k(x_0) &= \widehat{\boldsymbol{g}}_1\cdot(A_{k-1}, A'_{k-1})^T\\ \left((\nu_1\frac{\delta_x}{h} + p_1 + \frac{h}{2}r)(\beta\mu-a) + \frac{h}{2}(\frac{\mu-1}{\Delta t})\right)\widehat{u}_1^k(x_0) &= (\beta\gamma-a)\,\widehat{\boldsymbol{g}}_2\cdot(B_k, B'_k)^T\\ (\nu_1\frac{\delta_x}{h} + p_1 + \frac{h}{2}\frac{1+r\beta\Delta t-\mu/z}{\beta\Delta t})\widehat{u}_1^k(x_0) &= \widehat{\boldsymbol{g}}_2\cdot(B_k, B'_k)^T\end{aligned} \tag{B.15}$$

Noting $\varsigma_i^\star = (\nu_2\frac{e^{h\tilde{\sigma}_i}-1}{h} + p_2 - \frac{h}{2}r)(\beta\mu_i-a) - h\frac{\mu_i-1}{2\Delta t}$ for $i=2,4$ and $\varsigma_i^\star = (\nu_1\frac{1-e^{-h\tilde{\sigma}_i}}{h} + p_1 + \frac{h}{2}r)(\beta\mu_i - a) + h\frac{\mu_i-1}{2\Delta t}$ for $i=1,3$, $\frac{\varsigma_i^\star}{\beta\mu_i-a}$ asymptotically equals the semi-discrete in time $\nu_j\sigma_i+p_j$ when $h\to 0$. We also define $\varsigma_i = \nu_2\frac{e^{h\tilde{\sigma}_i}-1}{h} + p_2 - \frac{h}{2}\frac{1+r\beta\Delta t-\tilde{\mu}_i/z}{\beta\Delta t}$ for $i=2,4$ and $\varsigma_i = \nu_1\frac{1-e^{-h\tilde{\sigma}_i}}{h} + p_1 + \frac{h}{2}\frac{1+r\beta\Delta t-\tilde{\mu}_i/z}{\beta\Delta t}$ for $i=1,3$, which are asymptotically equal to $\nu_j\sigma_i+p_j$ when $h\to 0$.

We get the evolution of A_k, A'_k, B_k, B'_k:

$$\begin{aligned}
\varsigma_2^\star B_k + \varsigma_4^\star B'_k &= (\beta\gamma - a)\widehat{\boldsymbol{g}}_1 \cdot (A_{k-1}, A'_{k-1})^T \\
\varsigma_2 B_k + \varsigma_4 B'_k &= \widehat{\boldsymbol{g}}_1 \cdot (A_{k-1}, A'_{k-1})^T \\
\varsigma_1^\star A_k + \varsigma_3^\star A'_k &= (\beta\gamma - a)\widehat{\boldsymbol{g}}_2 \cdot (B_k, B'_k)^T \\
\varsigma_1 A_k + \varsigma_3 A'_k &= \widehat{\boldsymbol{g}}_2 \cdot (B_k, B'_k)^T
\end{aligned} \tag{B.16}$$

The convergence factor is then $\frac{\widehat{\boldsymbol{g}}_1 \cdot (A_k, A'_k)^T}{\widehat{\boldsymbol{g}}_1 \cdot (A_{k-1}, A'_{k-1})^T}$ which is equal to

$$\varrho_{RR}^{(\mathrm{DIRK,FD})} = \widehat{\boldsymbol{g}}_1 \cdot \left(\frac{\varsigma_3^\star - \varsigma_3(\beta\gamma - a)}{\varsigma_3^\star \varsigma_1 - \varsigma_1^\star \varsigma_3}, \ \frac{\varsigma_1(\beta\gamma - a) - \varsigma_1}{\varsigma_3^\star \varsigma_1 - \varsigma_1^\star \varsigma_3} \right)^T \times \widehat{\boldsymbol{g}}_2 \cdot \left(\frac{\varsigma_4^\star - \varsigma_4(\beta\gamma - a)}{\varsigma_4^\star \varsigma_2 - \varsigma_2^\star \varsigma_4}, \ \frac{\varsigma_2(\beta\gamma - a) - \varsigma_2}{\varsigma_4^\star \varsigma_2 - \varsigma_2^\star \varsigma_4} \right)^T \tag{B.17}$$

Chapter 4

Toward a discretisation of atmospheric surface layer coherent with the physical theory

Table of contents

4.1 Introduction

Schwarz methods have been studied in Chapters 2 and 3; we now focus on the discretisation of the atmospheric surface layer. The dynamics presented in Chapter 1 are recalled in §4.1.1

and the specific problem of the treatment of the surface layer is raised in §4.1.2.

4.1.1 Physical considerations

We consider in this chapter the turbulent Ekman model presented in Chapter 1. This 1D vertical model includes the Coriolis effect and a vertical turbulent term (the stratification will be introduced later in §4.3):

$$\partial_t u + ifu + \partial_z \langle w'u' \rangle = ifu_G \tag{4.1}$$

Remark *As it was detailed in §1.3.1 u is considered to be a complex-valued function for an easier representation of the Coriolis effect. The vector norm $||\cdot||$ is equivalent to the modulus $|\cdot|$.*

In (4.1), the Boussinesq hypothesis is applied on the turbulent flux $\langle w'u' \rangle = -K_u \partial_z u$ where K_u is the turbulent viscosity. In this chapter we focus on this flux and its bottom boundary expression.

We present a continuous model which describes the atmosphere column as the coupling of two regions:

- the surface layer which responds to surface forcing with a short timescale [LeMone et al., 2019];
- the remainder of the atmosphere which is not directly driven by the surface forcing.

In fluid dynamics, the presence of a rough surface makes strong gradients appear: due to the no-slip boundary condition the scales of motion close to the surface are much smaller than elsewhere in the domain and it is numerically intractable in most applications to refine the mesh enough for those small scales. The models hence exclude from the computational domain a part of the surface layer, using an adapted boundary condition. [Mohammadi et al., 1998] show that bulk boundary conditions can be derived with domain decomposition arguments; the computational domain is split into two parts: the surface layer $(0, \delta_a)$ and the remainder of the atmosphere column, $(\delta_a, +\infty)$ (see Figure 4.1).

The surface layer has two main characteristics:

- it is well mixed. The governing equation is usually stationary because the surface layer immediately adjusts to the external parameters. As a consequence (and because the Coriolis effect and the geostrophic forcing are neglected), the flux $K\partial_z u$ is a constant along the vertical axis.
- The vertical profile of K strongly depends on z.

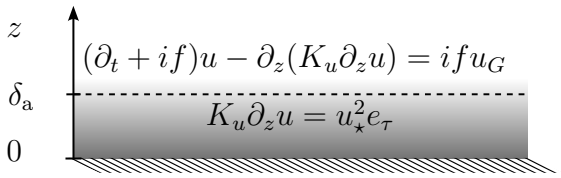

Figure 4.1: Continuous equations where the surface layer is excluded from the computational domain.

The equations in the atmosphere column are hence (see Figure 4.1):

$$(\partial_t + if)u - \partial_z(K_u \partial_z u) = if u_G, \qquad z \geq \delta_a \tag{4.2a}$$

$$K_u \partial_z u = u_\star^2 e_\tau, \qquad z < \delta_a \tag{4.2b}$$

where u_G is a constant value representing the geostrophic guide and f is the Coriolis parameter. The orientation of $\partial_z u$ is contained in $e_\tau = \frac{u(\delta_a) - u(0)}{||u(\delta_a) - u(0)||}$ where the surface current $u(0,t)$ is set to 0 or given by the ocean model in a coupled situation. In the neutral case (without stratification) we assume $u(0,t) = 0$ to shorten the expressions[1]. The initial and top boundary conditions are

$$u|_{t=0} = u_G \tag{4.3a}$$

$$\partial_z u|_{z=z_{\text{top}}} = 0 \tag{4.3b}$$

The viscosity in the surface layer is $K_u(z \leq \delta_a) = \kappa u_\star (z + z_u)$ where $z_u = z_u(K_{\text{mol}}, u_\star)$ depends on the geometry of the space domain; $\kappa = 0.40$ is the Von Kármán constant and K_{mol} is the molecular viscosity. It follows from (4.2b) that

$$||u(z,t)|| = \frac{u_\star}{\kappa} \ln\left(1 + \frac{z}{z_u}\right) \tag{4.4}$$

which is called *logarithmic profile* (or in the stratified case *MOST profile*). The expression *wall law* can refer to either the logarithmic profile, the surface layer viscosity $K_u(z \leq \delta_a)$ and the boundary condition (4.2b).

BULK routines The routine used to compute the friction velocity $u_\star$ is called BULK. It takes as parameters:

- the (relative) wind speed $u(\delta_a)$;
- the height of the surface layer δ_a;

[1]Setting $u(0,t) = 0$ amounts to consider the "absolute" wind speed rather than the "relative" wind w.r.t. the surface currents: the implementation of current feedbacks in ocean-atmosphere coupled models is discussed in [Renault et al., 2019].

- the temperature difference $\theta(\delta_a) - \theta(0)$ (for the stratified case);

In the neutral case, it starts with a first guess of z_u then uses (4.4) to compute iteratively $u_\star$ and $z_u(K_{\text{mol}}, u_\star)$ (see [Fairall et al., 2003] for more precisions).

Bottom boundary condition A typical integration in time from $u(z, t^n)$ to $u(z, t^{n+1})$ is:

1. Neutral Bulk: Use (4.4) to compute $u_\star = \text{BULK}(u(\delta_a, t^n)) := \dfrac{\kappa||u(\delta_a, t^n)||}{\ln\left(1 + \frac{\delta_a}{z_u}\right)}$

2. Integrate in time (4.2a) using (4.2b) as a boundary condition either explicitly:

$$K_u \partial_z u|_{z \leq \delta_a, t^{n+1}} = u_\star^2 \frac{u(\delta_a, t^n)}{||u(\delta_a, t^n)||} \tag{4.5}$$

   or implicitly:

$$K_u \partial_z u|_{z \leq \delta_a, t^{n+1}} = u_\star^2 \frac{u(\delta_a, t^{n+1})}{||u(\delta_a, t^n)||} \tag{4.6}$$

   [Lemarié et al., 2015b] showed that the explicit numerical interface condition is not necessarily stable: we choose to use the implicit condition and note $u_\star^2 e_\tau$ the right-hand side of (4.6). This implicit implementation is used for instance in the ECMWF model (see Section 3.5 of [ECMWF, 2020]). Other more sophisticated possibilities can also guarantee better numerical properties [Connors et al., 2012].

4.1.2 Treatment of the surface layer

The exclusion of the surface layer from the computational domain is justified by the lack of numerical resolution close to the surface: the continuous model (4.2) is split according to the numerical ressources. The height of the surface layer δ_a is hence generally chosen as the first grid level. However, in present numerical models, the evolution equation (4.2a) is also solved inside the surface layer which contradicts the quasi-stationary hypothesis. In order to improve the treatment of the surface layer, we can identify three issues (subjectively in decreasing order of importance and ease of correction):

1. δ_a is too small compared to the space steps. This issue is well-known in the LES community and is called *log-layer mismatch*. Since the scales of motion in the surface layer are proportional to the distance to the surface, it should not be assumed that we solve correctly the mechanisms in the first levels of a finite difference classical approach. [Kawai and Larsson, 2012] propose to use other levels than the first one to parameterize the wall law in the neutral case. [Maronga et al., 2020] give an improved boundary condition for stratified Large-Eddy Simulations which consists in using as the bulk input horizontally averaged values at δ_a chosen for physical and numerical

reasons (within the surface layer, above the roughness sub-layer and in a region where flows are well-resolved).

2. The quasi-stationary hypothesis of the wall law is not compatible with treating the first cell like the other ones. [Nishizawa and Kitamura, 2018] have shown that a bias is created in some Finite Volume models because the average of the first cell is considered to be the value in its center.

$$K_u \partial_z u|_{z\leq\delta_a} = u_\star^2 e_\tau \Rightarrow \begin{cases} (\partial_t + if)u - \partial_z(K_u \partial_z u) \neq if u_G, & z < \delta_a \\ \frac{1}{z_1}\int_0^{z_1} u(z)dz \neq u(z_{\frac{1}{2}}) \end{cases} \tag{4.7}$$

The discretization should take into account the surface layer and adapt to the wall law.

3. It is expected from most discretizations to be *consistent*: the continuous model should be recovered when the space step tends to zero. In particular, the surface layer should still be parametrized with the same wall law which is not the case when δ_a is chosen as the first grid level.

$$\lim_{h\to 0} K_u \partial_z u|_{z\leq\delta_a} = u_\star^2 e_\tau \tag{4.8}$$

[Basu and Lacser, 2017] warn that in several recent LES studies the space step is so small that the Monin-Obukhov hypotheses (that the height of the roughness elements is small: $z_u \ll \delta_a$) do not apply: the consistency problem is not only a theoretical consideration.

This chapter aims to study the treatment of the surface layer and to address those issues. In Section 4.2, the Finite Volume discretisation used in Chapter 2 is recalled and we introduce several strategies to treat the surface layer. In particular, one of the strategies ("FV free") enforces the wall law in the surface layer and does not assume a specific δ_a. The discussion is extended to a stratified case in Section 4.3 then the strategies are compared in Section 4.4.

4.2 Neutral case

This section introduces a method to discretize properly the surface layer of a simplified atmosphere column model. First in §4.2.1, the Finite Volume discretization using spline reconstruction is recalled. §4.2.2 is an overview of several strategies used to deal with the coupling of the two zones mentioned previously. When it makes sense, the strategies are applied with a Finite Volume discretization so that they can be compared with each other. Finally §4.2.3 introduces a new strategy to handle the surface flux scheme, based on a logarithmic reconstruction of the profiles within the surface layer.

In this section 4.2, we assume that the stratification is neutral. As it was explained in Chapter 1, there is no effect of the stratification on the turbulent viscosity so the wind speed $u(z,t)$ can be integrated in time without the temperature and humidity profiles.

4.2.1 Space discretization of (4.2a) with Finite Volumes

We recall here the Finite Volume discretization used throughout this chapter. We focus on the space discretisation and the time dependency of $u(z,t)$ is hence omitted.

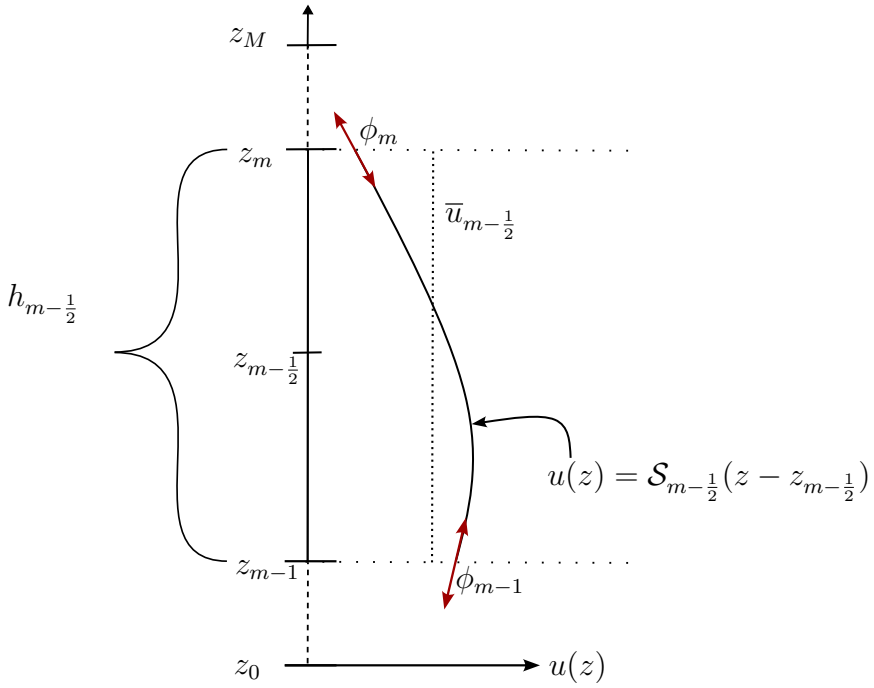

Figure 4.2: Summary of the notations related to the discretisation.

As already mentioned in chapter 3 the space domain is divided into M cells delimited by heights $(z_0 = 0, .., z_m, .., z_M)$. The size of the m-th cell is $h_{m-\frac{1}{2}} = z_m - z_{m-1}$ and the average of $u(z)$ over this cell is noted $\overline{u}_{m-\frac{1}{2}} = \frac{1}{h_{m-\frac{1}{2}}} \int_{z_{m-1}}^{z_m} u(z)dz$. The space derivative of u at z_m is noted ϕ_m. Figure 4.2 summarized the notations used related to the discretisation. Averaging (4.2a) over a cell gives the semi-discrete equation

$$(\partial_t + if)\overline{u}_{m+\frac{1}{2}} - \frac{K_{u,m+1}\phi_{m+1} - K_{u,m}\phi_m}{h_{m+\frac{1}{2}}} = if u_G \tag{4.9}$$

The reconstruction of $u(z) = \mathcal{S}_{m+\frac{1}{2}}(z - z_{m+\frac{1}{2}})$ inside a cell must be chosen to pursue the derivation of the scheme. A simple choice is a quadratic polynomial, $\mathcal{S}_{m+\frac{1}{2}}(\xi) = r_0 + r_1\xi + r_2\xi^2$

where $-\frac{h_{m+1/2}}{2} \leq \xi \leq \frac{h_{m+1/2}}{2}$. Averaging $\mathcal{S}_{m+\frac{1}{2}}$ over the cell and prescribing its space derivative at z_m and z_{m+1} lead to the following system:

$$\begin{aligned}
\overline{u}_{m+1/2} &= \frac{1}{h_{m+1/2}} \int_{-\frac{h_{m+1/2}}{2}}^{\frac{h_{m+1/2}}{2}} \mathcal{S}_{m+\frac{1}{2}}(\xi) d\xi \\
\phi_m &= \partial_z \mathcal{S}_{m+\frac{1}{2}} \left(-\frac{h_{m+1/2}}{2} \right) \\
\phi_{m+1} &= \partial_z \mathcal{S}_{m+\frac{1}{2}} \left(\frac{h_{m+1/2}}{2} \right)
\end{aligned} \tag{4.10}$$

In matrix form, we obtain a system that can be inverted to compute r_0, r_1, r_2:

$$\begin{pmatrix} \overline{u}_{m+1/2} \\ h_{m+\frac{1}{2}} \phi_m \\ h_{m+\frac{1}{2}} \phi_{m+1} \end{pmatrix} = \begin{pmatrix} 1 & 0 & \frac{1}{12} \\ 0 & 1 & -1 \\ 0 & 1 & 1 \end{pmatrix} \begin{pmatrix} r_0 \\ r_1 h_{m+\frac{1}{2}} \\ r_2 h_{m+\frac{1}{2}}^2 \end{pmatrix} \tag{4.11}$$

The reconstruction of $u(z)$ between z_m and z_{m+1} is then

$$\mathcal{S}_{m+\frac{1}{2}}(\xi) = \bar{u}_{m+\frac{1}{2}} + \frac{\phi_{m+1} + \phi_m}{2} \xi + \frac{\phi_{m+1} - \phi_m}{2 h_{m+1/2}} \left(\xi^2 - \frac{h_{m+1/2}^2}{12} \right) \tag{4.12}$$

The continuity of the solution at cell interfaces ($\mathcal{S}_{m-\frac{1}{2}} \left(\frac{h_{m-1/2}}{2} \right) = \mathcal{S}_{m+\frac{1}{2}} \left(-\frac{h_{m+1/2}}{2} \right)$) is then equivalent to

$$\frac{h_{m-1/2}}{6} \phi_{m-1} + \frac{2 \frac{h_{m+1/2} + h_{m-1/2}}{2}}{3} \phi_m + \frac{h_{m+1/2}}{6} \phi_{m+1} = \bar{u}_{m+\frac{1}{2}} - \bar{u}_{m-\frac{1}{2}} \tag{4.13}$$

Combining (4.9) and (4.13) finally gives the prognostic equation to integrate $\partial_z u$ in time:

$$\begin{aligned}
(\partial_t + if) &\left(\frac{h_{m-\frac{1}{2}}}{6} \phi_{m-1} + \frac{h_{m-\frac{1}{2}} + h_{m+\frac{1}{2}}}{3} \phi_m + \frac{h_{m+\frac{1}{2}}}{6} \phi_{m+1} \right) \\
&- \left(\frac{K_{u,m+1} \phi_{m+1} - K_{u,m} \phi_m}{h_{m+\frac{1}{2}}} - \frac{K_{u,m} \phi_m - K_{u,m-1} \phi_{m-1}}{h_{m-\frac{1}{2}}} \right) = 0
\end{aligned} \tag{4.14}$$

To reconstruct the solution, $\overline{u}$ should also be integrated in time with (4.9). (4.14) and (4.9) are hence the two equations defining our finite volume discretization. Note that we arrive naturally on fourth-order compact schemes for the first derivative $\partial_z u$ (eq (4.13)) and second-order for $\partial_z^2 u$ (see e.g. [Piller and Stalio, 2004]), but with a different approach of imposing a spline reconstruction. This approach lets us better control the vertical profiles than the usual compact methods and facilitates the derivation of the boundary conditions.

Remark: fourth-order compact scheme To get a more accurate scheme for the second-order derivative, a fourth degree polynomial could also be used. if $\frac{1}{12}, \frac{5}{6}$ are used in (4.14) instead of $\frac{1}{6}, \frac{2}{3}$, a fourth-order compact scheme is obtained. This scheme is studied in the Finite Difference sense in [Adam, 1977] and was also used by [Piller and Stalio, 2004] in a Finite Volume framework close to the one we are using. If one assumes that the reconstruction is the fourth degree polynomial $\mathcal{S}^4_{m+\frac{1}{2}}(\xi) = r^4_0 + r^4_1\xi + r^4_2\xi^2 + r^4_3\xi^3 + r^4_4\xi^4$, the two additional degrees of freedom r^4_3, r^4_4 need to be constrained. To recover the fourth-order compact scheme through the continuity constraint as in (4.13) one must put as constraints that the reconstruction on the boundaries of the cell is $\mathcal{S}^4_{m+\frac{1}{2}}\left(\frac{h_{m+\frac{1}{2}}}{2}\right) = \overline{u}_{m+\frac{1}{2}} + \frac{h_{m+\frac{1}{2}}}{12}(\phi_m + 5\phi_{m+1})$ and $\mathcal{S}^4_{m+\frac{1}{2}}\left(-\frac{h_{m+\frac{1}{2}}}{2}\right) = \overline{u}_{m+\frac{1}{2}} - \frac{h_{m+\frac{1}{2}}}{12}(5\phi_m + \phi_{m+1})$. Then the reconstruction is given by

$$\begin{pmatrix} r^4_0 \\ r^4_1 h_{m+\frac{1}{2}} \\ r^4_2 h^2_{m+\frac{1}{2}} \\ r^4_3 h^3_{m+\frac{1}{2}} \\ r^4_4 h^4_{m+\frac{1}{2}} \end{pmatrix} = \begin{pmatrix} 1 & 0 & \frac{1}{12} & 0 & \frac{1}{80} \\ 0 & 1 & -1 & \frac{3}{4} & -\frac{1}{2} \\ 0 & 1 & 1 & \frac{3}{4} & \frac{1}{2} \\ 1 & -\frac{1}{2} & \frac{1}{4} & -\frac{1}{8} & \frac{1}{16} \\ 1 & \frac{1}{2} & \frac{1}{4} & \frac{1}{8} & \frac{1}{16} \end{pmatrix}^{-1} \begin{pmatrix} \overline{u}_{m+1/2} \\ h_{m+\frac{1}{2}}\phi_m \\ h_{m+\frac{1}{2}}\phi_{m+1} \\ \overline{u} - \frac{5}{12}h_{m+\frac{1}{2}}\phi_m - \frac{1}{12}h_{m+\frac{1}{2}}\phi_{m+1} \\ \overline{u} + \frac{1}{12}h_{m+\frac{1}{2}}\phi_m + \frac{5}{12}h_{m+\frac{1}{2}}\phi_{m+1} \end{pmatrix} \tag{4.15}$$

and one obtains a subgrid reconstruction corresponding to the fourth-order [2] compact scheme considered. However this representation is heavier than using the quadratic splines: the fourth-order compact scheme will not be used in the following.

4.2.2 State-of-the-art surface flux schemes

We present in this subsection several strategies to derive the discretization of the surface layer (the corresponding equation is (4.2b)). A surface layer discretization consists in two parts, corresponding to the two steps of the integration in time presented in Section 4.1.1:

- how $u_\star$ is computed. For instance, with Finite Differences $u(\delta_a, t^n)$ is used as an input of the bulk routine to get the value of $u_\star = BULK(u(\delta_a, t^n))$.
- How (4.2b) is implemented as a boundary condition: in particular, the height at which the flux is prescribed. The space discretisation of $u(\delta_a, \cdot)$ is the same in the bulk routine and in $e_\tau = \frac{u(\delta_a, t^{n+1})}{||u(\delta_a, t^n)||}$.

[Nishizawa and Kitamura, 2018] investigated the effect of the first part of the discretization and showed that there is a negative bias in conventional surface flux schemes. This bias

[2] On the domain boundaries there is no continuity constraint. $\mathcal{S}^4_{\frac{1}{2}}\left(-\frac{h_{\frac{1}{2}}}{2}\right)$ can be constrained by a special treatment (see [Piller and Stalio, 2004]) to keep the fourth-order accuracy on Dirichlet boundaries.

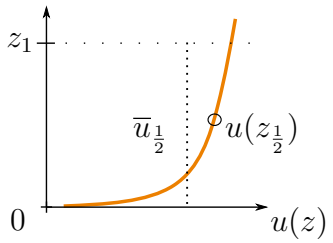

Figure 4.3: The averaged value of the wall law is systematically smaller that the value at the center of the cell.

comes from the fact that these schemes assume that the volume-averaged variables are equal to the value in the center of the volume. However the prognostic variables in the surface layer follow a logarithmic profile as shown in (4.4): the concavity of this profile thus creates a systematic error when assuming that the average and the value at the center of the cell are equal (see Figure 4.3). Finally, [Nishizawa and Kitamura, 2018] propose an alternative bulk formulation which uses the averaged variable in the surface layer instead of its value at the top.

Remark *The scheme* (4.14) *relies on quadratic spline reconstruction; the value at the center of the first cell is*

$$\mathcal{S}_{1/2}(0) = \overline{u}_{1/2} + \frac{h_{1/2}}{24}(\phi_0 - \phi_1) \tag{4.16}$$

If ϕ_0 *and* ϕ_1 *are aligned with* $e_\tau = 1 + 0i$ *then* $\phi_0 > \phi_1$ *implies that* $u(z)$ *is concave (it is parabolic) and that* $\overline{u}_{1/2} < \mathcal{S}_{1/2}(0)$*. However, as it will be discussed in §4.2.3 ("On the value of* $K_{u,0}$*") the wall law cannot be followed. The modification of* $K_{u,0}$ *used in §4.2.3 reduces the difference between* $\overline{u}_{1/2}$ *and* $\mathcal{S}_{1/2}(0)$*. In the following, the difference between "FV pure" and "FV1" will be small for this reason.*

Our objective is to compare the surface flux scheme corresponding to the alternative bulk formulation with the conventional ones and to introduce another surface flux scheme that is more coherent with respect to the continuous model of Section 4.1.1. We now present the strategies that are representative of what is done in actual models. The strategies are applied to the Finite Volume scheme presented in Section 4.2.1 and are summarized in Figure 4.4.

- With Finite Differences: it is assumed that $\delta_{\mathrm{a}} = z_{\frac{1}{2}}$. A standard Finite Difference approximation applied to the evolution equation states that $(\partial_t + if)u_{\frac{1}{2}} = \frac{1}{h_{\frac{1}{2}}}(K_1\phi_1 - K_0\phi_0) + if u_G$. The input value of the bulk is $u(\delta_{\mathrm{a}}) = u_{1/2}$ and the boundary condition is simply applied on the surface flux:

$$\underbrace{K_{u,0}\phi_0^{n+1}}_{\text{Surface flux}} = u_\star^2 e_\tau, \qquad u_\star = \mathrm{BULK}(\underbrace{u_{\frac{1}{2}}^n}_{\text{FD value at } z_{\frac{1}{2}}}) \tag{4.17}$$

Note that using another point further from the surface (e.g. $u^n_{\frac{7}{2}}$) instead of $u^n_{\frac{1}{2}}$ is the idea of the method given by [Kawai and Larsson, 2012] to eliminate log-layer mismatch in LES models. We do not consider this method here as we focus on Finite Volume discretisation.

- "FV pure": it is assumed again that $\delta_{\mathrm{a}} = z_{\frac{1}{2}}$. The scheme is similar to the Finite Difference one. The reconstruction of $u(z)$ inside the first grid cell is used to get $u(z_{\frac{1}{2}})$. The first cell is treated like the others: (4.2a) is applied inside the surface layer. The bottom boundary condition is

$$\underbrace{K_{u,0}\phi_0^{n+1}}_{\text{Surface flux}} = u_\star^2 e_\tau, \qquad u_\star = \mathrm{BULK}\Big(\underbrace{\mathcal{S}^n_{1/2}(\xi = 0)}_{\text{Reconstruction at } z_{\frac{1}{2}}} \Big) \tag{4.18}$$

  Note that $\xi = 0$ corresponds here to $z = z_{\frac{1}{2}} \neq 0$.

- "FV1": it is assumed again that $\delta_{\mathrm{a}} = z_{\frac{1}{2}}$. In state-of-the-art models using finite volumes, $u_\star$ is often computed using the volume-averaged value $u(\delta_{\mathrm{a}}) = \overline{u}_{\frac{1}{2}}$. (4.2a) is also applied inside the surface layer. The corresponding bottom boundary condition is

$$\underbrace{K_{u,0}\phi_0^{n+1}}_{\text{Surface flux}} = u_\star^2 e_\tau, \qquad u_\star = \mathrm{BULK}\Big(\underbrace{\overline{u}^n_{\frac{1}{2}}}_{\text{Average around } z_{\frac{1}{2}}} \Big) \tag{4.19}$$

We present now two additional strategies corresponding to the treatment of the surface layer in [Nishizawa and Kitamura, 2018].

- "FV Nishizawa": unlike the other strategies, it is assumed that the first cell is entirely inside the surface layer: $\delta_{\mathrm{a}} = z_1$. We mentioned previously that [Nishizawa and Kitamura, 2018] show that the "FV1" strategy systematically underestimates $u(\delta_{\mathrm{a}})$ because of the concavity of the logarithmic profile. An alternative bulk algorithm is hence derived by averaging (4.4) in the first cell:

$$||\overline{u}_{\frac{1}{2}}|| = \frac{u_\star}{\kappa}\left(1+\frac{z_u}{\delta_{\mathrm{a}}}\right)\left(\ln\left(1+\frac{z}{z_u}\right)-1\right) \tag{4.20}$$

  However, the equation (4.2a) and the spline reconstruction are left unchanged in the surface layer:

$$\underbrace{K_{u,0}\phi_0^{n+1}}_{\text{Surface flux}} = u_\star^2 e_\tau, \qquad u_\star = \underbrace{\overline{\mathrm{BULK}}}_{\text{Adapted for averages}}\Big(\overline{u}^n_{\frac{1}{2}} \Big) \tag{4.21}$$

- "FV2": the "FV Nishizawa" scheme is not adapted to spline reconstruction. We extend it to our Finite Volume discretisation with the assumption that the spline

reconstruction $u(z)$ inside the surface layer is given by the wall law. The surface layer *is* the first cell: the equation (4.2a) is not integrated in time in this cell and we use instead the wall law (4.4) between 0 and $\delta_a = z_1$. Since the profile of u is given by the wall law in the first cell, using $\overline{u}_{\frac{1}{2}}$ as input of the alternative bulk algorithm of "FV Nishizawa" becomes rigorously equivalent to using the classical bulk formulation with $u(z_1)$ as input. We hence use the reconstruction $u^n(\delta_a) = \mathcal{S}^n_{\frac{3}{2}}(-\frac{h_{3/2}}{2})$ and the boundary condition at z_1 is

$$\underbrace{K_{u,1}\phi_1^{n+1}}_{\text{Flux at } z_1} = u_\star^2 e_\tau, \qquad u_\star = \underbrace{\overline{\text{BULK}}(\overline{u}^n_{\frac{1}{2}})}_{\text{Averaged bulk}} = \text{BULK}(\underbrace{\mathcal{S}^n_{3/2}(\xi = -\frac{h_{\frac{3}{2}}}{2})}_{\text{Reconstruction at } z_1}) \tag{4.22}$$

The first cell is inactive with this method: the numerical computation domain matches with the continuous one (Figure 4.1).

The different strategies are summarized in Table 4.1 together with the "FV free" scheme which will be presented in §4.2.3. Let us draw some comments and comparisons on the surface flux schemes:

- "FV1" relies on the assumption that $\overline{u}_{\frac{1}{2}} = u(z_{\frac{1}{2}})$; as it will be seen on Figure 4.7 the induced difference with "FV pure" is not important in our case where the spline profile are less concave than the logarithmic profile. We will thus only consider "FV pure" to reduce the number of cases.

- Some of the strategies assume (4.2a) inside the surface layer; it is not satisfactory because it is incompatible with the wall law (4.2b). Note that this is not the case with Finite Differences: (4.2a) is only assumed at $z_{1/2}$.

- With our spline reconstruction, when we assume (4.2a) a spline profile (that is incompatible with the logarithmic profile) is also assumed.

As shown in Table 4.1 the "FV2" surface flux scheme solves those problems. However for this scheme and all the others presented here, changing the space step also changes the height of the surface layer δ_a. This behaviour is not satisfactory: although the choice of δ_a is mainly related to numerical reasons we aim to approximate the continuous equations (4.2). [Basu and Lacser, 2017] warns that using a small space step while keeping the same treatment in LES goes against the range of validity of the MOST profiles. That is why in the following, we derive a surface flux scheme that keeps the advantages of the "FV2" scheme, but with a free δ_a.

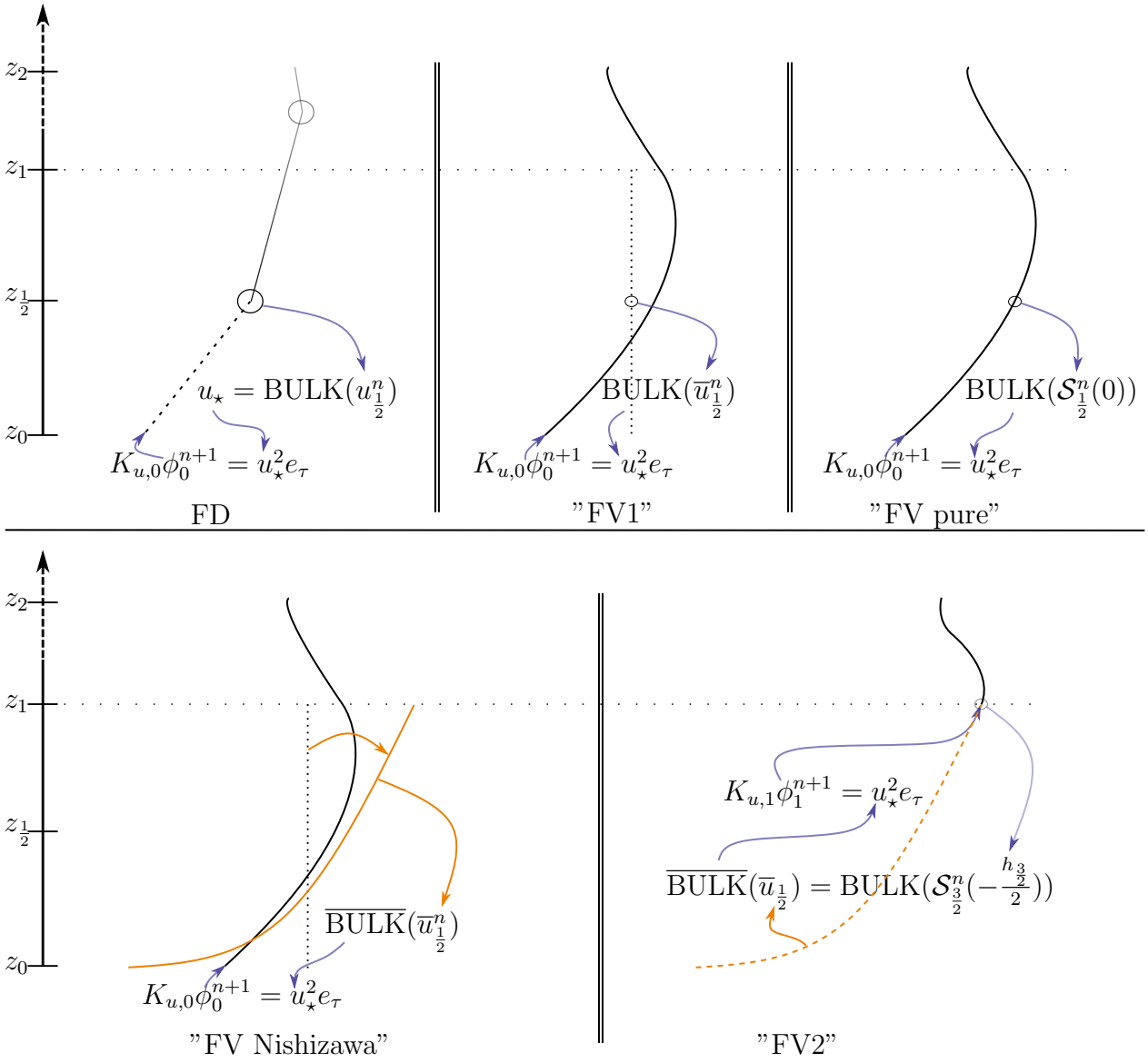

Figure 4.4: Summary of the surface flux schemes. Averaged values are noted with vertical dotted lines; Values considered in the Finite Difference sense are encircled; implicit parts of the schemes are represented as dashed lines; orange profiles follow the wall law. With "FV Nishizawa", the average is *interpreted* as the average of a wall law and is used in the $\overline{\mathrm{BULK}}$ routine.

Scheme	SL flux	$u_\star$	δ_a	(4.2b) in SL?
FD	$K_{u,0}\phi_0$	$\mathrm{BULK}(u_{\frac{1}{2}})$	$z_{\frac{1}{2}}$	✓
"FV pure"	$K_{u,0}\phi_0$	$\mathrm{BULK}(\mathcal{S}^n_{1/2}(\xi=0))$	$z_{\frac{1}{2}}$	×
"FV1"	$K_{u,0}\phi_0$	$\mathrm{BULK}(\overline{u}_{\frac{1}{2}})$	$z_{\frac{1}{2}}$	×
"FV Nishizawa"	$K_{u,0}\phi_0$	$\overline{\mathrm{BULK}}(\overline{u}_{\frac{1}{2}})$	z_1	×
"FV2"	$K_{u,1}\phi_1$	$\mathrm{BULK}(\mathcal{S}_{\frac{3}{2}}(-\frac{h_{3/2}}{2}))$	z_1	✓
"FV free"	$K_{u,\delta}\phi_\delta$	$\mathrm{BULK}(u(\delta_\mathrm{a}))$	δ_a	✓

Table 4.1: Summary of the surface flux schemes presented in Section 4.2

4.2.3 A surface flux scheme with a free δ_a

We now construct a boundary condition that is coherent with the continuous model presented in §4.1.1 with a free δ_a, named "FV free" in Table 4.1:

$$\underbrace{K_{u,\delta}\phi_\delta^{n+1}}_{\text{Flux at } \delta_\mathrm{a}} = u_\star^2 e_\tau, \qquad u_\star = \mathrm{BULK}\Big(\underbrace{u^n(\delta_\mathrm{a})}_{\text{Reconstruction at } \delta_\mathrm{a}} \Big) \tag{4.23}$$

We first assume that $\delta_\mathrm{a} < z_1$ and will then relax this hypothesis. In the first grid cell, we assume that (4.4) applies for $z < \delta_\mathrm{a}$ and we separate the first volume into two parts: the surface layer $[0, \delta_\mathrm{a}]$ and the "sub-cell" $[\delta_\mathrm{a}, z_1]$. This split corresponds to the change of governing equations in the continuous case (4.2). Let $\widetilde{h} = z_1 - \delta_\mathrm{a}$ be the size of the upper sub-cell $[\delta_\mathrm{a}, z_1]$ and $\widetilde{u} = \frac{1}{\widetilde{h}}\int_{\delta_\mathrm{a}}^{z_1} u(z)dz$ be the averaged value of u on this interval. The following subgrid reconstruction is used:

$$u(z) = \begin{cases} \mathcal{S}_{1/2}\left(z - \dfrac{z_1+\delta_\mathrm{a}}{2}\right), & z \geq \delta_\mathrm{a} \\ \dfrac{u_\star}{\kappa}\ln\left(1+\dfrac{z}{z_u}\right)e_\tau, & z < \delta_\mathrm{a} \end{cases} \tag{4.24}$$

The quadratic spline $\mathcal{S}_{1/2}$ used for reconstruction is computed with the averaged value $\widetilde{u}$, the size of the sub-cell $\widetilde{h}$ and the fluxes at the extremities ϕ_δ and ϕ_1: a similar equation to (4.12) is obtained: $\mathcal{S}_{1/2}(\xi) = \widetilde{u} + \frac{\phi_1+\phi_\delta}{2}\xi + \frac{\phi_1-\phi_\delta}{2\widetilde{h}}\left(\xi^2 - \frac{\widetilde{h}^2}{12}\right)$. The notations are summed up in Figure 4.5.

Remark *The flux $K_u\phi$ is constant in the surface layer. Hence $K_{u,\delta}\phi_\delta = K_{u,0}\phi_0$ and since the viscosity at $z=0$ is the molecular viscosity we get $\phi_\delta = \frac{K_{mol}}{K_{u,\delta}}\phi_0$. The implementation uses ϕ_δ as a prognostic variable instead of ϕ_0: this surface flux scheme is hence exactly equivalent to using the "FV2" scheme with grid levels $\{0, \delta_\mathrm{a}, z_1, z_2, ..., z_M\}$.*

We now rewrite the reconstruction (4.24) in terms of the prognostic variables $\overline{u}_{1/2}$, ϕ_δ, ϕ_1. The relation between $\overline{u}_{1/2}$ and $\widetilde{u}$ is given by the Chasles' relation $\int_{\delta_\mathrm{a}}^{z_1} u dz = \int_{z_0}^{z_1} u dz - \int_{z_0}^{\delta_\mathrm{a}} u dz$,

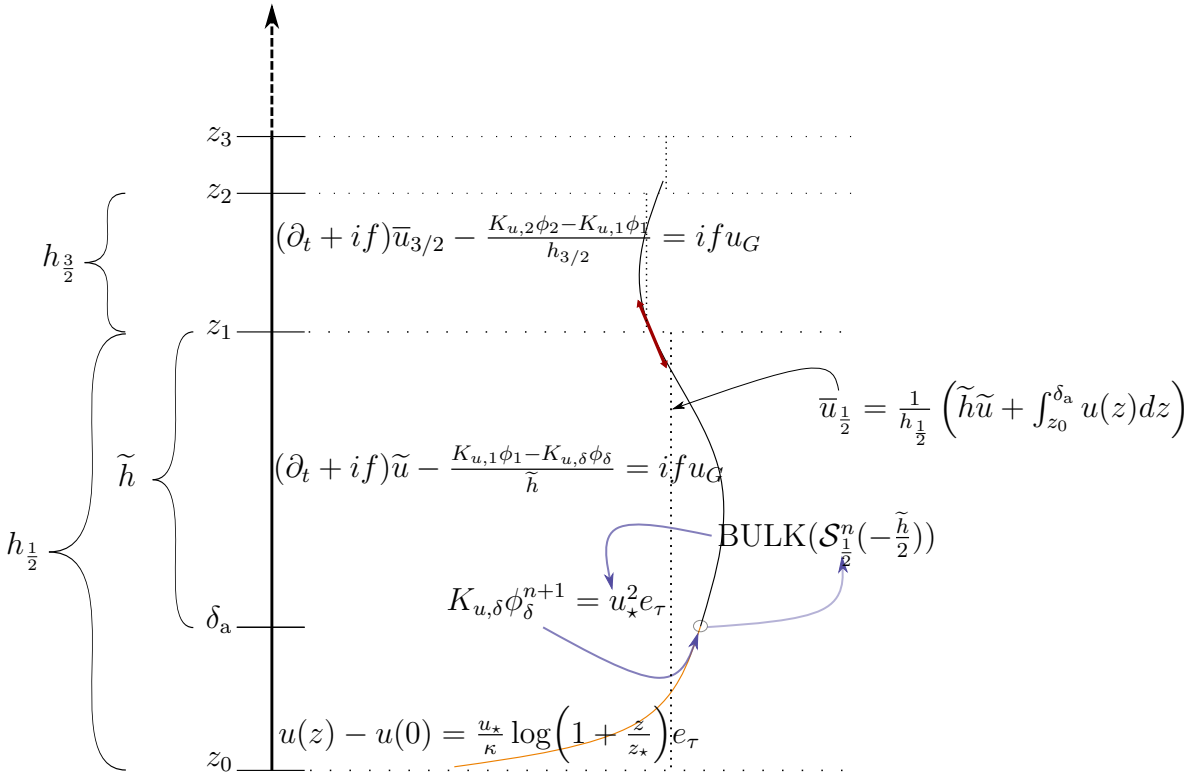

Figure 4.5: Surface layer scheme "FV free".

which can be written as

$$\widetilde{h}\widetilde{u} = h_{1/2}\overline{u}_{1/2} - e_\tau \frac{u_\star}{\kappa}\int_{z_0}^{\delta_\mathrm{a}} \ln\left(1+\frac{z}{z_u}\right)dz \tag{4.25}$$

where the time indices in $e_\tau = \frac{u^{n+1}(\delta_\mathrm{a})}{||u^n(\delta_\mathrm{a})||}$ must be the same as in the bottom boundary condition (4.23). Let us inject the reconstruction of $u(\delta_\mathrm{a}) = \widetilde{u} - \widetilde{h}(\phi_\delta/3 + \phi_1/6)$ (obtained from (4.24)) and the wall law $||u^n(\delta_\mathrm{a})|| = \frac{u_\star}{\kappa}\ln\left(1+\frac{\delta_\mathrm{a}}{z_u}\right)$ in (4.25). One then gets:

$$\widetilde{u}\,\alpha_{sl} = \overline{u}_{\frac{1}{2}} + \widetilde{h}\left(\frac{\phi_\delta}{3}+\frac{\phi_1}{6}\right)\left(\alpha_{sl} - \frac{\widetilde{h}}{h_{\frac{1}{2}}}\right) \tag{4.26}$$

with

$$\alpha_{sl} = \frac{\widetilde{h}}{h_{1/2}} + \frac{1}{h_{1/2}}\int_{z_0}^{\delta_{sl}} \frac{\ln\left(1+\frac{z}{z_u}\right)}{\ln\left(1+\frac{\delta_\mathrm{a}}{z_u}\right)}dz = \frac{(h_{1/2}+z_u)\ln\left(1+\frac{\delta_\mathrm{a}}{z_u}\right) - \delta_\mathrm{a}}{h_{1/2}\ln\left(1+\frac{\delta_\mathrm{a}}{z_u}\right)} \tag{4.27}$$

a non-dimensional number $0 < \alpha_{sl} \leq 1$ which depends on the wall law and on the values of $\widetilde{h}, h_{1/2}$. Finally, note that

$$\alpha_\mathrm{sl} = 1 \iff \widetilde{h} = h_{1/2} \tag{4.28}$$

and in this case (4.26) is equivalent to $\widetilde{u} = \overline{u}_{1/2}$. Figure 4.6 shows the profile of α_{sl} where we see that it decreases when increasing δ_a/z_1 or z_u.

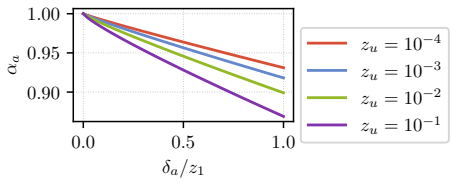

Figure 4.6: Value of α_{sl} for several values of z_u with $z_1 = 20$ m.

Remark α_sl *is a not constant as it depends on* $z_u(u_\star)$ *which will vary. On the other hand, we assume that* δ_a *does not change over time. Indeed, it would be challenging to decrease* δ_a *during the integration in time because a part of the wall law would need to be treated as a spline. It would be however desirable to be able to vary* δ_a *as a physical parameter and we leave this improvement for future work.*

In the reconstruction (4.24) $\widetilde{u}$ can be expressed in terms of the prognostic variables with (4.26) and we obtain $u(\delta_\mathrm{a})$ which is used as input of the bulk routine and in the computation of e_τ:

$$u(\delta_\mathrm{a}) = \frac{\overline{u}_{1/2} - \frac{\widetilde{h}^2}{h_{1/2}}\left(\frac{\phi_\delta}{3}+\frac{\phi_1}{6}\right)}{\alpha_\mathrm{sl}} \tag{4.29}$$

The boundary condition (4.23) is hence formulated as:

$$\underbrace{K_{u,\delta}\phi_\delta^{n+1}}_{\text{Flux at } \delta_a} = u_\star^2 \underbrace{\frac{\overline{u}_{1/2} - \frac{\widetilde{h}^2}{h_{1/2}}\left(\frac{\phi_\delta}{3} + \frac{\phi_1}{6}\right)}{\alpha_{\text{sl}}||u^n(\delta_a)||}}_{e_\tau \text{ using reconstruction at } \delta_a} \tag{4.30}$$

and the evolution equation in the upper part of the first grid level $(\partial_t + if)\widetilde{u} = \frac{K_{u,1}\phi_1 - K_{u,\delta}\phi_\delta}{\widetilde{h}}$ becomes

$$(\partial_t + if)\left(\frac{1}{\alpha_{\text{sl}}(t)}\left(\overline{u}_{1/2} + \widetilde{h}\left(\frac{\phi_\delta}{3} + \frac{\phi_1}{6}\right)\left(\alpha_{sl} - \frac{\widetilde{h}}{h_{\frac{1}{2}}}\right)\right)\right) = \frac{K_{u,1}\phi_1 - K_{u,\delta}\phi_\delta}{\widetilde{h}} \tag{4.31}$$

The prognostic equation (4.13) used to integrate ϕ in time is also changed for $m = 1$: $h_{m-1/2}$ is replaced with $\widetilde{h}$ and $K_{u,m-1}\phi_{m-1}$ is replaced by $K_{u,\delta}\phi_\delta$.

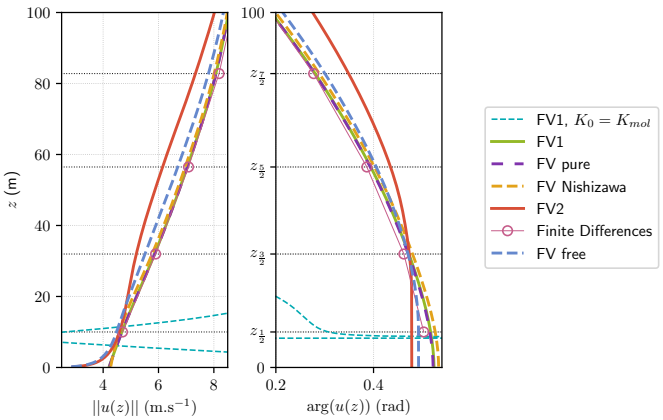

Figure 4.7: Vertical profiles of $||u||$ (left) and $\arg(u)$ (right) for the various surface flux schemes presented after one day of integration in time in neutral conditions. The time step is $\Delta t = 30$ s and the vertical levels are taken on the ECMWF website[3] as the 25 first of the 137 levels configuration of IFS.

Figure 4.7 is a snapshot of the vertical profiles of $|u|$ and $\arg(u)$ close to the surface for the surface flux schemes presented. The profiles are obtained after 24 hours of integration in neutral conditions and with $u(0) = 0$. One can see that the profiles of $|u|$ with the "FV free" and "FV2" follow a wall law. The "FV1" and "FV pure" discretizations present identical profiles that are close to the "FV Nishizawa" and Finite Difference discretizations. However, it is the case only when K_0 is replaced by K_δ in those discretizations (see the paragraph "On

[3] https://confluence.ecmwf.int/display/OIFS/4.4+OpenIFS%3A+Vertical+Resolution+and+Configurations

the value of $K_{u,0}$" below). The profile of $\arg(u)$ is significantly affected by the surface flux scheme: this is not surprising as the Coriolis effect is not taken into account in the surface layer for the "FV2" and "FV free" parameterizations. The differences between "FV2" and "FV free" only come from the choice of δ_{a}: by choosing $\delta_{\mathrm{a}} = z_1$, both profiles would have been rigorously identical (see the paragraph "in the general case where $\delta_{\mathrm{a}} \geq z_1$" below).

On the value of $K_{u,0}$ According to the wall law $K_{u,0}$ should be equal to K_{mol}. However, the boundary condition $K_{u,0}\phi_0 = u_\star^2 e_\tau$ does not behave the same way with Finite Differences and Finite Volumes.

- **Finite Differences**: Injecting the boundary condition at the first grid level gives

$$(\partial_t + if)u_{1/2} = \frac{1}{h_{1/2}}\left(K_{u,1}\frac{u_{3/2} - u_{1/2}}{h_1} - u_\star^2 e_\tau\right) \tag{4.32}$$

  The value of K_0 does not intervene in the equation.

- **Finite Volumes** ("FV pure", "FV1" and "FV Nishizawa"): Combining the equation (4.14) and the reconstruction (4.12) in the second cell $u(z_1) = \mathcal{S}_{\frac{3}{2}}\left(-\frac{h_{\frac{3}{2}}}{2}\right)$ the discretisations "FV pure", "FV1" and "FV Nishizawa" implicitly use that

$$(\partial_t + if)u(z_1) = \frac{K_{u,1}\phi_1 - u_\star^2 e_\tau}{h_{1/2}} + (\partial_t + if)\left(\frac{\phi_1}{3} + \frac{u_\star^2 e_\tau}{6K_{u,0}}\right)h_{1/2} \tag{4.33}$$

  The (small) value of $K_{u,0}$ directly appears when we assume the parabolic profile inside the first grid cell. As a result, $u(z_1)$ scales with $\frac{1}{K_0}$ and as it is seen in Figure 4.7 exhibits unreasonable values. To obtain physically plausible profiles, by mimicking the relation $\phi_\delta = \frac{K_{mol}}{K_{u,\delta}}\phi_0$ of the "FV free" scheme, we choose to multiply the surface viscosity by $\frac{K_{u,\delta}}{K_{mol}}$. As a consequence, the wall law is denied and $(\partial_z u)(z_0)$ is multiplied by $\frac{K_{mol}}{K_{u,\delta}}$. Note that this problem is specific to schemes where $\frac{\phi_0}{K_{u,0}}$ is involved, and is not characteristic of Finite Volume schemes.

In the general case where $\delta_{\mathrm{a}} \geq z_k$. Let k be such that $z_k \leq \delta_{\mathrm{a}} < z_{k+1}$. The surface layer scheme "FV free" is identical to the case $k = 0$, except that

- the sub-cell of average $\widetilde{u}$ and of size $\widetilde{h}$ is $[\delta_{\mathrm{a}}, z_{k+1}]$: k is added to the indices in (4.30) and (4.31);

- $\alpha_{sl} = \frac{\widetilde{h}}{h_{k+\frac{1}{2}}} + \frac{1}{h_{k+\frac{1}{2}}}\int_{z_k}^{\delta_{\mathrm{a}}} \frac{\ln\left(1+\frac{z}{z_u}\right)}{\ln\left(1+\frac{\delta_{\mathrm{a}}}{z_u}\right)}dz$;

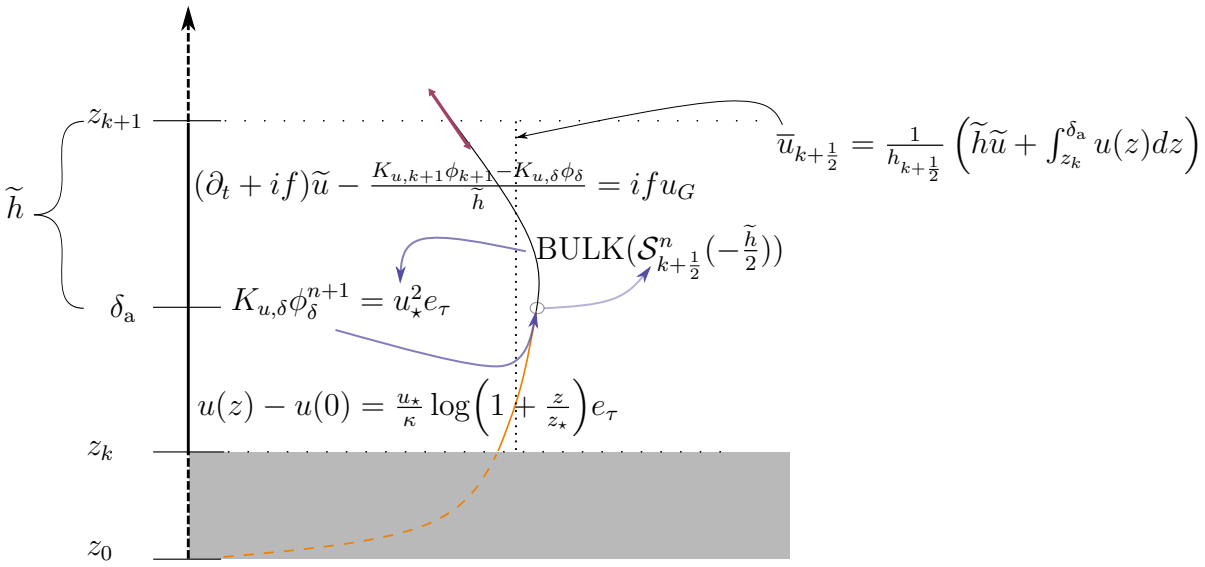

Figure 4.8: Surface layer scheme "FV free" with $\delta_a \geq z_k$.

- for $m < k$, the cell $[z_m, z_{m+1}]$ is filled with $K_{u,m}\phi_m = K_{u,k}\phi_k = {u_\star}^2 e_\tau$ and the average $\overline{u}_{m+1/2}$ is computed with the integrated wall law between z_m and z_{m+1}. The subgrid reconstruction in those cells is directly the wall law.

It is straightforward to check that for $\delta_a = z_1$ the "FV2" scheme is rigorously recovered. The derivation for any $\delta_a \geq 0$ is detailed for the stratified case in Section 4.3.2. Figure 4.8 shows how the surface layer is handled in this case: the part in gray is neutralized for the prognostic equation and is filled afterward with the help of the wall law.

4.3 Stratified case

Now that all the ideas have been presented in the neutral case, we extend the discussion to the case of a stratified column. A stratified fluid has layers of different densities. We assume for simplicity that the atmosphere is dry and that the density variation is proportional to the variation of the temperature:

$$\partial_z \rho \propto -\partial_z \theta \tag{4.34}$$

The stratification is hence given by a temperature profile: if the temperature increases with z, the column is said to be stable and the vertical mixing is reduced. This is typically the case above sea ice or during the night. On the contrary an unstable stratification comes from a decreasing temperature with z: it happens during daytime of diurnal cycles and enhance the vertical mixing. Finally, if the temperature is a constant, the neutral case is recovered.

In this section, we first discuss the continuous and semi-discrete in space equations, then extend the previous discussion on the wall law to Monin-Obukhov Similarity Theory

(MOST). Finally, Section 4.3.3 derives the profile of viscosities depending on the Turbulent Kinetic Energy (TKE).

4.3.1 Continuous model and Finite Volume discretization

The stratification in the column is given by the potential temperature: it will be integrated in time together with u. The continuous equations are given in §4.3.1.1 and their discretisation is detailed in §4.3.1.2. The stratification affects u in two ways:

- As explained in Chapter 1 the bulk routine in the stratified case also gives a friction scale $\theta_\star$ for the potential temperature:

$$u_\star, \theta_\star = \text{BULK}(\theta(\delta_\text{a}), u(\delta_\text{a})) \tag{4.35}$$

  where we omitted the BULK dependency on $u(0)$ and on the surface temperature θ_s. The bulk routine is based on equations (4.37) of §4.3.1.1.

- The TKE (detailed in §4.3.3.1) has a buoyancy term which involves the Brunt-Väisälä frequency $N^2 = -\frac{g\partial_z \rho}{\rho_0}$. With the assumption (4.34) that $\partial_z \rho \propto -\partial_z \theta$ we use instead that $N^2 = -\frac{g\partial_z \theta}{\theta_\text{ref}}$ where $\theta_\text{ref} = 283K$.

4.3.1.1 Continuous model

The continuous equations remain the same for u (see (4.2)), except that the turbulent viscosity and the friction scale $u_\star$ depend on the potential temperature θ, which is governed by:

$$\partial_t \theta - \partial_z (K_\theta \partial_z \theta) = F_\theta, \qquad z \geq \delta_\text{a} \tag{4.36a}$$

$$K_\theta \partial_z \theta|_{z \leq \delta_\text{a}} = \theta_\star u_\star = C_H ||u(\delta_\text{a}) - u(0)|| \left(\theta(\delta_\text{a}) - \theta_s\right), \quad z < \delta_\text{a} \tag{4.36b}$$

The viscosities K_u, K_θ will be detailed with the discretization of the turbulent kinetic energy in section 4.3.3. In the surface layer, Monin-Obukhov Similarity Theory (MOST) profiles for u and θ are

$$\begin{aligned} ||u(z) - u(0)|| &= \frac{u_\star}{\kappa}\left(\ln\left(1 + \frac{z}{z_u}\right) - \psi_u\left(\frac{z}{L_{MO}}\right)\right) \\ \theta(z) - \theta_s &= \frac{\theta_\star}{\kappa}\left(\ln\left(1 + \frac{z}{z_\theta}\right) - \psi_\theta\left(\frac{z}{L_{MO}}\right)\right) \end{aligned} \tag{4.37}$$

where z_θ typically depends on $u_\star$, K_mol and $L_{MO} = \frac{\theta(\delta_\text{a})u_\star^2}{\theta_\star \kappa g}$. Similarly to the neutral case, the semi-discrete in time boundary condition is not explicit: $C_H^n ||u^n(\delta_\text{a}) - u^n(0)||$ is computed with the values at the current time step whereas the temperature variation is taken at time t^{n+1}: the boundary condition for temperature is

$$K_\theta \partial_z \theta = C_H^n ||u^n(\delta_\text{a}) - u^n(0)|| (\theta^{n+1}(\delta_\text{a}) - \theta_s^{n+1}), \qquad z < \delta_\text{a} \tag{4.38}$$

4.3.1.2 Finite Volume discretization

The discretization of u is exactly the same as in the neutral case ((4.9) and (4.14)) and the discretization of the potential temperature is very similar: the average potential temperature $\overline{\theta}_{m+1/2}$ evolves with

$$\partial_t \overline{\theta}_{m+1/2} - \frac{K_{\theta,m+1}(\partial_z\theta)_{m+1} - K_{\theta,m}(\partial_z\theta)_m}{h_{m+1/2}} = \overline{F}_{\theta,m+1/2} \tag{4.39}$$

And the derivative of temperature at z_{m-1}, z_m, z_{m+1} solves

$$\begin{aligned}\partial_t \left(\frac{h_{m-1/2}}{6}(\partial_z\theta)_{m-1} + \frac{h_{m-1/2}+h_{m+1/2}}{3}(\partial_z\theta)_m + \frac{h_{m+1/2}}{6}(\partial_z\theta)_{m+1} \right) \\ - \left(\frac{K_{\theta,m+1}}{h_{m+1/2}}(\partial_z\theta)_{m+1} - \frac{(h_{m-1/2}+h_{m+1/2})K_{\theta,m}}{h_{m-1/2}h_{m+1/2}}(\partial_z\theta)_m + \frac{K_{\theta,m-1}}{h_{m-1/2}}(\partial_z\theta)_{m-1} \right) \\ = \overline{F}_{\theta,m+1/2} - \overline{F}_{\theta,m-1/2}\end{aligned} \tag{4.40}$$

Identically to the reconstruction of $u(z)$, inside the m-th cell $\theta(z) = \mathcal{T}_{m-\frac{1}{2}}(z - z_{m-\frac{1}{2}})$ where (4.12) gives $\mathcal{T}$ by replacing $\overline{u}, \phi$ with $\overline{\theta}, \partial_z\theta$. We also extend the surface flux scheme strategies for the temperature: the ideas of those strategies remain the same (see Figure 4.4) and we only need to introduce the bottom boundary condition for θ.

- With Finite Differences the evolution equation is solved at $z_{\frac{1}{2}}$ with the surface flux:

$$\underbrace{K_\theta \partial_z \theta_0^{n+1}}_{\text{Surface flux}} = C_H|\Delta u|(\theta_{\frac{1}{2}}^{n+1} - \theta_s), \quad \text{using BULK}(\underbrace{\theta_{\frac{1}{2}}^n, u_{\frac{1}{2}}^n}_{\text{FD values at } z_{\frac{1}{2}}}) \tag{4.41}$$

  where $C_H|\Delta u| = C_H||u^n(\delta_a) - u^n(0)|| = \frac{u_\star \kappa}{\ln\left(1+\frac{z}{z_u}\right) - \psi_\theta\left(\frac{z}{L_{MO}}\right)}$.

- With "FV pure" the evolution equation is solved in the whole first grid cell with the reconstructed value $\theta(\delta_a) = \mathcal{T}_{1/2}(0)$:

$$\underbrace{K_\theta \partial_z \theta_0^{n+1}}_{\text{Surface flux}} = C_H|\Delta u|(\mathcal{T}_{1/2}^{n+1}(0) - \theta_s), \quad \text{using BULK}(\underbrace{\mathcal{T}_{1/2}^n(0), \mathcal{S}_{1/2}^n(0)}_{\text{Reconstructions at } z_{\frac{1}{2}}}) \tag{4.42}$$

- With "FV Nishizawa" the evolution equation is solved in the whole first grid cell and the adapted bulk for averaged values is used:

$$\underbrace{K_\theta \partial_z \theta_0^{n+1}}_{\text{Surface flux}} = C_H|\Delta u|(\overline{\theta}_{\frac{1}{2}}^{n+1} - \theta_s), \quad \text{using } \overline{\text{BULK}}(\underbrace{\overline{\theta}_{\frac{1}{2}}^n, \overline{u}_{\frac{1}{2}}^n}_{\text{Averages around } z_{\frac{1}{2}}}) \tag{4.43}$$

The adapted bulk routines read

$$\begin{aligned} ||\overline{u}_{\frac{1}{2}} - u(0)|| &= \frac{u_\star}{\kappa}\left(1+\frac{z_u}{\delta_{\mathrm{a}}}\right)\left(\ln\left(1+\frac{z}{z_u}\right)-1\right) - \Psi_u\left(\frac{z_1}{L_{MO}}\right) \\ \overline{\theta}_{\frac{1}{2}} - \theta_s &= \frac{\theta_\star}{\kappa}\left(1+\frac{z_\theta}{\delta_{\mathrm{a}}}\right)\left(\ln\left(1+\frac{z}{z_\theta}\right)-1\right) - \Psi_\theta\left(\frac{z_1}{L_{MO}}\right) \end{aligned} \tag{4.44}$$

where $\Psi_x(z) = \int_0^z (\psi_x(z'))dz'$ for $x = u, \theta$.

- With "FV2" in the first grid cell the MOST profile for θ is assumed as in [Nishizawa and Kitamura, 2018]. The boundary condition is the flux at the top of the surface layer $\delta_{\mathrm{a}} = z_1$, using the reconstructed solution at z_1:

$$\underbrace{K_\theta \partial_z \theta_1^{n+1}}_{\text{Flux at } z_1} = C_H|\Delta u|\left(\mathcal{T}_{3/2}^{n+1}\left(-\frac{h_{\frac{3}{2}}}{2}\right) - \theta_s\right), \quad \text{using BULK}\left(\underbrace{\mathcal{T}_{3/2}^{n}\left(-\frac{h_{\frac{3}{2}}}{2}\right), \mathcal{S}_{3/2}^{n}\left(-\frac{h_{\frac{3}{2}}}{2}\right)}_{\text{Reconstructions at } z_1}\right) \tag{4.45}$$

The limitations of the strategies shown in the neutral case are the same for the temperature: the "FV pure" and "FV Nishizawa" schemes assume that the evolution equation stands in the surface layer and approximate a MOST profile with a quadratic spline. The value of K_θ at z_0 cannot be set to the molecular diffusivity in those cases for the same reason as the viscosity $K_{u,0}$ in the neutral case. Moreover, the discretizations force δ_{a} to the first grid level $z_{\frac{1}{2}}$ (or z_1 in the case of "FV2" and "FV Nishizawa"). We now derive the stratified version of the "FV free" surface scheme to eliminate those limitations.

4.3.2 FV free

In this §4.3.2 we follow step by step the derivation of the neutral "FV free" scheme and apply it to this stratified case. The stratification adds no complexity: we hence present directly the derivation directly for any $\delta_{\mathrm{a}} \geq 0$. Let k such that $z_k \leq \delta_{\mathrm{a}} < z_{k+1}$. As in the neutral case, the cell $[z_k, z_{k+1}]$ is split into two parts for the "FV free" surface flux scheme. The first part $[z_k, \delta_{\mathrm{a}}]$ is contained in the surface layer where the temperature and wind follow (4.37). The second part is the "sub-cell" $[\delta_{\mathrm{a}}, z_{k+1}]$ of size $\widetilde{h}$, of averages $\widetilde{u}, \widetilde{\theta}$ and of sub-grid reconstructions

$$\begin{aligned} \mathcal{S}_{k+1/2}(\xi) &= \widetilde{u} + \frac{\phi_{k+1}+\phi_\delta}{2}\xi + \frac{\phi_{k+1}-\phi_\delta}{2\widetilde{h}}\left(\xi^2 - \frac{\widetilde{h}^2}{12}\right) \\ \mathcal{T}_{k+1/2}(\xi) &= \widetilde{\theta} + \frac{(\partial_z\theta)_{k+1}+(\partial_z\theta)_\delta}{2}\xi + \frac{(\partial_z\theta)_{k+1}-(\partial_z\theta)_\delta}{2\widetilde{h}}\left(\xi^2 - \frac{\widetilde{h}^2}{12}\right) \end{aligned} \tag{4.46}$$

where $\xi = z - (z_{k+1} - \frac{\widetilde{h}}{2})$ is defined for $\delta_a < z < z_{k+1}$. The relation between $\overline{u}_{k+1/2}, \overline{\theta}_{k+1/2}$ and $\widetilde{u}, \widetilde{\theta}$ is, similarly to the neutral case:

$$\begin{aligned}(\widetilde{u} - u(0))\,\alpha_{sl,u} &= \overline{u}_{k+1/2} - u(0) + \widetilde{h}\left(\frac{\phi_\delta}{3} + \frac{\phi_{k+1}}{6}\right)\left(\alpha_{sl,u} - \frac{\widetilde{h}}{h_{k+\frac{1}{2}}}\right)\\ \left(\widetilde{\theta} - \theta_s\right)\alpha_{sl,\theta} &= \overline{\theta}_{k+1/2} - \theta_s + \widetilde{h}\left(\frac{(\partial_z\theta)_\delta}{3} + \frac{(\partial_z\theta)_{k+1}}{6}\right)\left(\alpha_{sl,u} - \frac{\widetilde{h}}{h_{k+\frac{1}{2}}}\right)\end{aligned} \tag{4.47}$$

where the non-dimensional numbers $\alpha_{sl,u}, \alpha_{sl,\theta}$ depend on the stratification. For $x = u, \theta$,

$$\begin{aligned}\alpha_{sl,x} &= \frac{\widetilde{h}}{h_{k+\frac{1}{2}}} + \frac{\frac{1}{h_{k+\frac{1}{2}}}\int_{z_k}^{\delta_a}\left(\ln\left(1+\frac{z}{z_x}\right) - \psi_x\left(\frac{z}{L_{MO}}\right)\right)dz}{\ln\left(1+\frac{\delta_a}{z_x}\right) - \psi_x\left(\frac{\delta_a}{L_{MO}}\right)}\\ &= \frac{\widetilde{h}}{h_{k+\frac{1}{2}}} + \frac{\frac{1}{h_{k+\frac{1}{2}}}\left[(z+z_x)\ln\left(1+\frac{z}{z_x}\right) - z + z\Psi_x\left(\frac{z}{L_{MO}}\right)\right]_{z_k}^{\delta_a}}{\ln\left(1+\frac{\delta_a}{z_x}\right) - \psi_x\left(\frac{\delta_a}{L_{MO}}\right)}\end{aligned} \tag{4.48}$$

Note that, instead of ψ_x, we used Ψ_x, the averaged form of the universal profile stability functions defined in [Nishizawa and Kitamura, 2018]. Since $\ln\left(1+\frac{z}{z_x}\right) - \psi_x(\frac{z}{L_{MO}})$ is non-negative and increases with z even in strongly unstable situations, $0 < \alpha_{sl,x} \leq 1$ and as in the neutral case $\alpha_{sl,x} = 1 \iff \widetilde{h} = h_{k+1/2}$. This lets us retrieve the "FV2" surface flux scheme by setting the height of the surface layer to exactly z_1.

Finally, equations (4.30) and (4.31) of the neutral case can be used for u and the equations for θ are similar: the boundary condition of "FV free" is

$$\underbrace{K_{\theta,\delta}(\partial_z\theta)_\delta}_{\text{Flux at } \delta_a} = C_H|\Delta u|\underbrace{\frac{\overline{\theta}_{k+1/2} - \frac{\widetilde{h}^2}{h_{k+1/2}}\left(\frac{(\partial_z\theta)_k}{3} + \frac{(\partial_z\theta)_{k+1}}{6}\right) - \theta_s}{\alpha_{sl,\theta}}}_{\text{Reconstruction at } \delta_a} \tag{4.49}$$

and the evolution equation in the first active grid cell is

$$\partial_t\left(\frac{1}{\alpha_{sl,\theta}(t)}\left(\overline{\theta}_{k+\frac{1}{2}} + \widetilde{h}\left(\frac{(\partial_z\theta)_\delta}{3} + \frac{(\partial_z\theta)_{k+1}}{6}\right)\left(\alpha_{sl,\theta} - \frac{\widetilde{h}}{h_{k+\frac{1}{2}}}\right) - (1-\alpha_{sl,\theta})\theta_s\right)\right) = \frac{K_{\theta,k+1}(\partial_z\theta)_{k+1} - K_{\theta,\delta}(\partial_z\theta)_\delta}{\widetilde{h}} + \overline{F}_{\theta,k+1/2} \tag{4.50}$$

The prognostic equation (4.40) for $\partial_z\theta$ is also adjusted for the first cell to replace $h_{k+1/2}$ by $\widetilde{h}$.

4.3.3 Turbulent viscosities and diffusivities

As it was explained in Chapter 1 the viscosity K_u and diffusivity K_θ follow the Monin-Obukhov theory in the surface layer and are parameterized above the surface layer by the Turbulent Kinetic Energy (TKE) with a one-equation closure. The objective of this section is to derive the discretised turbulence closure:

1. The vertical profiles of u and θ depend strongly on the discretisation of the Turbulent Kinetic Energy and of the mixing lengths. Those discretisations are detailed in §4.3.3.1.

2. To obtain smooth solutions, the viscosity and the diffusivity must also be smooth. At the top of the surface layer, the parameterization of K_u, K_θ with the TKE should follow Monin-Obukhov similarity theory: the link is done through the mixing lengths in §4.3.3.2.

4.3.3.1 Finite Volume discretization of TKE equation

The Turbulent Kinetic Energy (TKE) evolves with the equation

$$\partial_t e = \underbrace{\partial_z\left(K_e \partial_z e\right)}_{\text{diffusion}} + \underbrace{K_u ||\partial_z u||^2}_{\text{shear}} - \underbrace{K_\theta N^2}_{\text{buoyancy}} - \underbrace{c_\epsilon \frac{e^{3/2}}{l_\epsilon(z)}}_{\text{dissipation}} \tag{4.51}$$

The turbulent viscosities K_u, K_θ and K_e are computed with constants C_m, C_s, C_e such that $(K_u, K_\theta, K_e) = (C_m, C_s\phi_z(z), C_e) l_m(z)\sqrt{e(z)}$. The value ϕ_z is proportional to the inverse of the so-called turbulent Prandtl number and is bounded by $\phi_z^{\max} = 2.2$ [Lemarié et al., 2021].

$$\phi_z = \frac{1}{1 + \max\left(-0.5455, 0.143 \times \frac{l_m l_\epsilon N^2}{e}\right)} \tag{4.52}$$

Mixing lengths The mixing lengths $l_m(z) = \min\left(l_{\text{up}}(z), l_{\text{down}}(z)\right)$ and $l_\epsilon(z) = \sqrt{l_{\text{up}}(z) l_{\text{down}}(z)}$ (introduced in [Bougeault and Lacarrere, 1989]) are obtained with the method named $l^\star_{\text{D80}}$ described in [Lemarié et al., 2021] that we explain here:

1. Define
$$l^\star_{\text{D80}} = \frac{2\sqrt{e}}{c_0 ||\partial_z u|| + \sqrt{c_0^2 ||\partial_z u||^2 + 2N^2}}, \quad \text{with } c_0 = 0.2 \tag{4.53}$$

2. initialize l_{up} and l_{down} to $l^\star_{\text{D80}}$;

3. limit l_{up} by the distance to the top and to a strongly stratified area of the air column: this is done by ensuring $-\partial_z l_{\text{up}} < 1$ and $l_{\text{up}}(z_{\text{top}}) \approx 0$.

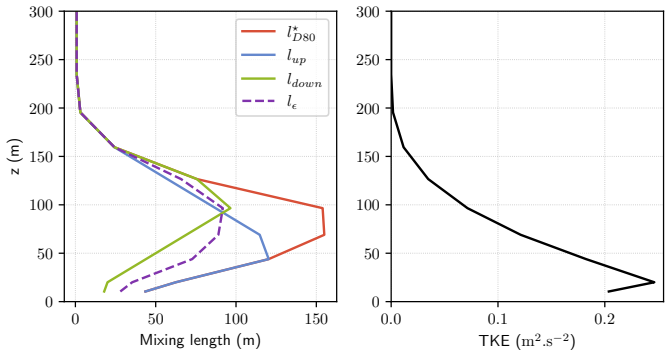

Figure 4.9: Typical vertical profiles of the mixing lengths (left) reported with the corresponding TKE (right). It is seen that $\partial_z l_{\text{up}}$ is limited by -1 for $z \in (50\text{ m}, 150\text{ m})$ whereas $\partial_z l_{\text{down}}$ is limited by 1 for $z < 100$ m. The surface flux scheme used is "FV free" which is why the profiles start at $\delta_{\text{a}} = 10$ m.

4. limit l_{down} by the distance to the surface and to a strongly stratified area of the air column: this is done by ensuring $\partial_z l_{\text{down}} < 1$ and an appropriate surface layer value. The value here is not zero, so that the surface layer links correctly with the computational domain.

Steps 3 and 4 are implemented by applying sequentially from top (for l_{up}) and bottom (for l_{down}):

$$\begin{aligned} l_{\text{up}}(z_m) &= \min\left(l^\star_{D80}(z_m), \quad l_{\text{up}}(z_{m+1}) + h_{m+\frac{1}{2}}\right) \\ l_{\text{down}}(z_m) &= \min\left(l^\star_{D80}(z_m), \; l_{\text{down}}(z_{m-1}) + h_{m-\frac{1}{2}}\right) \end{aligned} \tag{4.54}$$

Figure 4.9 shows vertical profiles of $l_{\text{up}}, l_{\text{down}}, l_m, l^\star_{D80}$. The value of l_{down} in the surface layer is detailed in §4.3.3.2 to link the Monin-Obukhov similarity theory to the turbulent parameterization based on the TKE.

Turbulent Kinetic Energy in the computational domain The discretisation of the turbulent kinetic energy requires some care. Instead of choosing the Finite Volume scheme used for u and θ, we prefer a Finite Difference method which has a positivity preserving property. The energy e and the lengths scales l_m, l_ϵ are evaluated at the interfaces z_m between the cells:

$$\left(\frac{c_\epsilon\sqrt{e^n_m}}{l_\epsilon} + \partial_t\right) e_m = \frac{(K_e\partial_z e)_{m+1/2} - (K_e\partial_z e)_{m-1/2}}{z_{m+1/2} - z_{m-1/2}} + K_u||\partial_z u||^2 - K_\theta N^2 \tag{4.55}$$

The discretisation of the dissipation term $\frac{c_\epsilon\sqrt{e^n_m}e^{n+1}_m}{l_\epsilon}$ ensures the preservation of the positivity of e, as long as $K_u||\partial_z u||^2 - K_\theta N^2$ is positive. Indeed, ignoring the diffusion term a backward-

Euler discretisation of (4.55) gives

$$e^{n+1} = \frac{e^n + (K_u||\partial_z u||^2 - K_\theta N^2)}{1 + \Delta t \frac{c_\epsilon \sqrt{e^n}}{l_\epsilon}} \tag{4.56}$$

which is non-negative if e^n is non-negative. In the cells where the buoyancy is stronger than the shear, $K_\theta N^2$ is multiplied by $\frac{e^{n+1}}{e^n}$ to keep the positivity preserving property. This multiplication is known as the "Patankar's trick" [Lemarié et al., 2021].

Boundary conditions In the surface layer, because of the strong mixing, e is quasi-stationary ($\partial_t e = 0$). The energy is given by an equilibrium between shear, buoyancy and dissipation:

$$e(z < \delta_\mathrm{a}) = \left(\frac{l_\epsilon}{c_\epsilon} (K_u||\partial_z u||^2 - K_\theta N^2) \right)^{2/3} \tag{4.57}$$

where $K_u||\partial_z u||^2$ and $K_\theta N^2$ are given by MOST. A homogeneous Neumann boundary condition is used at the top: $\partial_z e(z_\mathrm{top}) = 0$

4.3.3.2 Matching viscosities at the surface layer

In order to obtain a regular solution from the "FV free" discretization, we derive here the constraints on mixing length and on TKE inside the surface layer. A sub-grid model that suits both surface layer and free turbulence was proposed by [Redelsperger et al., 2001], physically justified by measurements. In the neutral case, this sub-grid model leads to linear mixing lengths l_m, l_ϵ in the surface layer; with stratified fluids, the formulation is more sophisticated and depends strongly on the Obukhov length. The link between the surface layer and the regions further away from the surface is ensured with a linear combination between the two regimes.

Instead of following the latter method, we aim to keep the mixing lengths (4.53) of the computational domain and to set a particular boundary condition for l_down to satisfy the Monin-Obukhov Similarity Theory. Assuming that

$$K_m = C_m l_m \sqrt{e} \quad \text{and} \quad K_\theta = C_s l_m \phi_z \sqrt{e} \tag{4.58}$$

inside the SL, we have for $z \leq \delta_\mathrm{a}$

1. Monin-Obukhov viscosity profiles in the surface layer:

$$K_m = \kappa u_\star \frac{z + z_u}{\phi_m(z/L_{MO})} \quad \text{and} \quad K_\theta = \kappa u_\star \frac{z + z_u}{\phi_h(z/L_{MO})} \tag{4.59}$$

   (4.58) together with (4.59) put a constraint on ϕ_z in the surface layer: $\phi_z = \frac{C_m \phi_m(z/L_{MO})}{C_s \phi_h(z/L_{MO})} \forall z \leq \delta_\mathrm{a}$.

2. Quasi-equilibrium of the TKE equation:

$$c_\epsilon \frac{e^{3/2}}{l_\epsilon} = K_m ||\partial_z u||^2 - \frac{g}{\theta_{ref}} K_\theta \partial_z \theta \tag{4.60}$$

We assume that l_ϵ in (4.60) is taken at time index n, so that the energy can be integrated in time with a proper boundary condition before computing the mixing length. The characteristic length l_{up} (resp. l_{down}) indicates how much the turbulent mixing is acting upwards (resp. downward). In the surface layer, it is hence natural to follow the procedure (4.53) for l_{up}, using the MOST profiles for the shear and buoyancy. We derive the surface value of l_{down} to link Monin-Obukhov Similarity Theory with the turbulence closure used here.

Rewriting (4.60) with MOST and $l_{\text{up}}, l_{\text{down}}$ gives:

$$e = (l_{\text{up}} l_{\text{down}})^{\frac{1}{3}} \left(\frac{u_\star}{c_\epsilon} \left(u_\star^2 \frac{\phi_m(z/L_{MO})}{\kappa(z+z_u)} - \frac{g}{\theta_{\text{ref}}} \theta_\star \right) \right)^{\frac{2}{3}} \tag{4.61}$$

which is the bottom boundary condition of the TKE (4.57). Now, (4.59) gives

$$\min(l_{\text{down}}^2, l_{\text{up}}^2) = \frac{1}{e} \left(\frac{\kappa u_\star}{C_m} \frac{z+z_u}{\phi_m(z/L_{MO})} \right)^2 \tag{4.62}$$

l_{down} is limited by the distance to the bottom only in the free-turbulence zone. In the SL, it is given by (4.62) so that (4.59) is verified. We inject (4.61) into the previous equation and get

$$\begin{cases} l_{\text{down}}^{7/3} = \frac{1}{l_{\text{up}}^{1/3}} \frac{u_\star^{4/3} \left(\frac{\kappa}{C_m} \frac{z+z_u}{\phi_m(z/L_{MO})} \right)^2}{\left(u_\star^2 \frac{\phi_m(z/L_{MO})}{c_\epsilon \kappa (z+z_u)} - \frac{g}{\theta_{\text{ref}} c_\epsilon} \theta_\star \right)^{2/3}} & \text{if} \quad l_{\text{down}} < l_{\text{up}} \\ l_{\text{down}}^{1/3} = \frac{1}{l_{\text{up}}^{7/3}} \frac{u_\star^{4/3} \left(\frac{\kappa}{C_m} \frac{z+z_u}{\phi_m(z/L_{MO})} \right)^2}{\left(u_\star^2 \frac{\phi_m(z/L_{MO})}{c_\epsilon \kappa (z+z_u)} - \frac{g}{\theta_{\text{ref}} c_\epsilon} \theta_\star \right)^{2/3}} & \text{otherwise} \end{cases} \tag{4.63}$$

It is actually sufficient to use (4.62) with the assumption $l_{\text{down}} < l_{\text{up}}$ to compute l_{down} explicitly. It also guarantees that the MOST viscosity and the MOST diffusivity numerically scale with $l_m \sqrt{e}$. However, using (4.62) with the surface condition for the TKE (4.57) amounts to solving iteratively (4.61- 4.62); using (4.63) directly solves the system (4.61-4.62).

4.4 Consistency study

In this section, we investigate the consistency of the discretisation depending on the strategy used to treat the surface layer. In particular, a special attention is paid to the effect of changing δ_{a}. Let δ_1,δ_2 two different heights of surface layer such that $\delta_1 < \delta_2$; let u_1, u_2 be solutions of (4.2) using respectively δ_1, δ_2 for δ_{a}. The main direct changes between u_1 and u_2 are:

- the Coriolis effect and the large-scale forcing are taken into account in $[\delta_1, \delta_2]$ only by u_1;
- the viscosity $K_u(z)$ for $z \in [\delta_1, \delta_2]$ is forced by the wall law to compute u_2 and not to compute u_1.

There are also indirect effects due to the non-linearity of the problem:

- If the bulk algorithm is well designed it does not need the very top of the surface layer. Any height $z < \delta_a$ within the wall law can be used to obtain the friction scales $u_\star$, $\theta_\star$: changing δ_a does not *directly* change the friction scales. However, the changes between u_1 and u_2 mentioned above indirectly change the output of the bulk algorithm. The friction scales $u_{\star,1}$ and $u_{\star,2}$ are hence different.

4.4.1 Study of the consistency: neutral case

Figure 4.10 shows three vertical profiles of u obtained with $\delta_a = 5, 10$ and 20 m. As expected, the angle $\mathrm{Arg}(u)$ is constant in the surface layer because the Coriolis effect is not taken into account: changing δ_a has an effect on the orientation of the wind. Moreover, the vertical profile of $||u||$ above the surface layer does not follow the wall law. Consequently, the profile of $||u||$ depends strongly on the choice of δ_a.

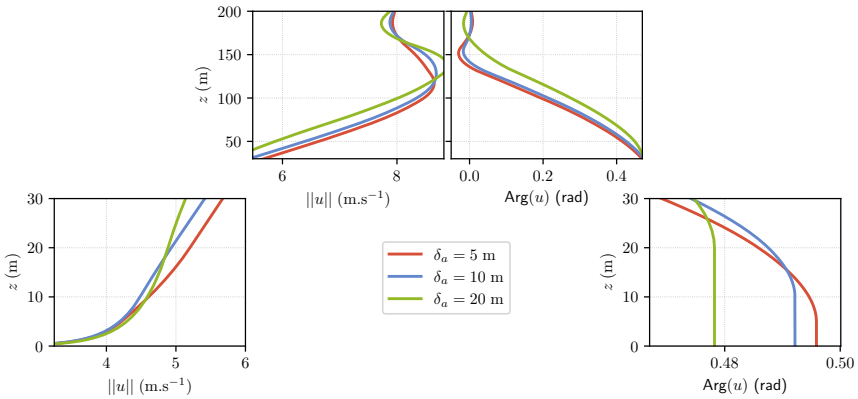

Figure 4.10: Typical profiles of $||u||$ and $\mathrm{Arg}(u)$ for several choices of δ_a, obtained with the "FV free" discretisation. Notice the changes of horizontal and vertical scales between the bottom and top panels.

4.4.1.1 Analytical study of the sensitivity to δ_a

In this subsection we study the sensitivity to δ_a of the continuous solution of (4.2). We will assume that the viscosity K_u and the roughness length z_u are the same for both u_1 and u_2.

In Figure 4.10 the value of z_u for $\delta_a = 5$ m, 10 m, 20 m is respectively $z_u = 3.8 \times 10^{-5}$ m, 3.8×10^{-5} m and 3.6×10^{-5} m. It seems reasonable to assume that z_u do not depend on δ_a for this analytical study of the sensitivity to δ_a.

First, note that inside the surface layer for u_2, since $u_2(z) = \frac{u_\star}{\kappa} \ln\left(1 + \frac{z}{z_u}\right) \frac{u_2(\delta_2)}{||u_2(\delta_2)||}$, assuming $||u_2(z)||$ follows the same wall low (it only works when the problem is continuous in time), we have:

$$(\partial_t + if)u_2(z) = \frac{\ln\left(1 + \frac{z}{z_u}\right)}{\ln\left(1 + \frac{\delta_2}{z_u}\right)} (\partial_t + if)u_2(\delta_2), \quad \forall z \leq \delta_2 \tag{4.64}$$

Let us assume that $K\partial_z u_2$ is continuously differentiable at δ_2; then $\partial_z(K\partial_z u_2) = 0$ in all the interval $(0, \delta_2)$ and the evolution equation of u_2 in (δ_1, δ_2) is

$$(\partial_t + if)u_2(z) = \frac{\ln\left(1 + \frac{z}{z_u}\right)}{\ln\left(1 + \frac{\delta_2}{z_u}\right)} if u_G, \quad \forall z \in (\delta_1, \delta_2) \tag{4.65}$$

The difference between u_1 and u_2 is governed by the difference of treatment of this interval: subtracting the two evolution equations gives

$$(\partial_t + if)(u_2 - u_1) = \left(\frac{\ln\left(1 + \frac{z}{z_u}\right)}{\ln\left(1 + \frac{\delta_2}{z_u}\right)} - 1 \right) if u_G - \partial_z(K\partial_z u_1), \quad \forall z \in (\delta_1, \delta_2) \tag{4.66}$$

We see in the right hand side of the latter equation the two items of the beginning of the section: the large-scale forcing with the Coriolis effect, and the diffusion term of u_1 which is actually $\partial_z(K\partial_z u_1) = \partial_z(K\partial_z u_1 - K\partial_z u_2)$

Let $w = u_2 - u_1$. If we assume that K is the viscosity for both u_2 and u_1 then

$$\begin{cases} (\partial_t + if)w = \partial_z(K\partial_z w), & \forall z > \delta_2 \\ (\partial_t + if)w = \partial_z(K\partial_z w) + \left(\frac{\ln\left(1+\frac{z}{z_u}\right)}{\ln\left(1+\frac{\delta_2}{z_u}\right)} - 1 \right) if u_G, & \forall z \in (\delta_1, \delta_2) \\ K\partial_z w = \frac{\kappa}{\ln\left(1+\frac{\delta_1}{z_u}\right)} \left(u_{\star,2} u_2(\delta_1) - u_{\star,1} u_1(\delta_1) \right), & \forall z \leq \delta_1 \end{cases} \tag{4.67}$$

Apart from the bulk sensitivity in the surface condition, the difference comes hence from the forcing $\left(\frac{\ln\left(1+\frac{z}{z_u}\right)}{\ln\left(1+\frac{\delta_2}{z_u}\right)} - 1 \right) if u_G$. This forcing is more important when $\frac{\delta}{z_u}$ is small. As it can be seen on Figure 4.10 the effect of changing δ_a is not limited to the surface: the differences between the profiles are seen up to 150 meters.

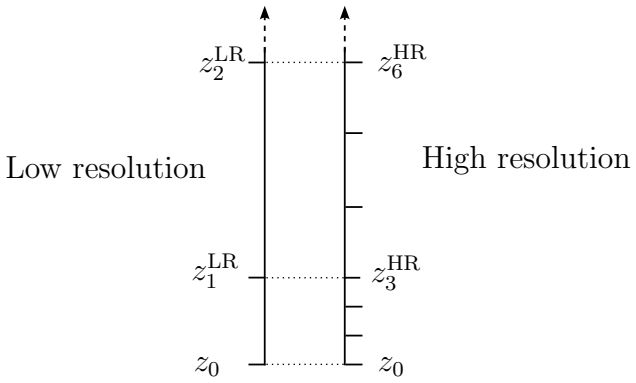

Figure 4.11: The "High resolution" has two additional grid levels between each "Low resolution" levels.

4.4.1.2 Study of the consistency: neutral case

We now compare the profiles of a high resolution simulation with the profiles of a simulation with lower resolution. To create the high resolution grid, two additional grid levels are added between each grid levels (see Figure 4.11). After the simulation ($\Delta t = 30$ s, one day of integration in time) the high resolution ("HR") simulation is projected onto the low resolution ("LR") grid and the relative difference $\frac{||u^{\mathrm{HR}}(z)-u^{\mathrm{LR}}(z)||}{||u^{\mathrm{LR}}(z)||}$ is computed. For each surface flux scheme, Figure 4.12 shows the profile of $||u||$, the relative u difference and the relative $u_\star$ difference between low and high resolutions. One can see that the difference between low and high resolution of the "FV free" scheme is small in low altitude. Two factors reduce the difference between low and high resolution for "FV free":

- $\delta_{\mathrm{a}} = z_{\frac{1}{2}}^{LR}$ is the same for both low and high resolution whereas for the other surface flux schemes the continuous equations changes with δ_{a}.
- In the relative $u_\star$ difference, one can see that the initial relative difference for $u_\star$ is already smaller than with the other schemes. This is a consequence of the imposed wall law: at initialization, there is already a logarithm profile in the surface layer.

Figure 4.12 shows that the Finite Difference discretisation is not very sensitive to the increase of the space step. We show in §4.4.1.3 that the boundary condition is robust with regard to δ_{a}.

4.4.1.3 Semi-Discrete sensitivity to δ_{a} (Finite Differences)

We put aside the sensitivity of the bulk procedure by assuming as in §4.4.1.1 that z_u is a constant. The approach used in Finite Difference schemes consists in assuming $\delta_{\mathrm{a}} = z_{1/2}$ and to use the flux at z_0 in the integration in time $K_0\phi_0 = u_\star^2 \frac{u(\delta_{\mathrm{a}})}{||u(\delta_{\mathrm{a}})||}$ (we assume that $u(0) = 0$

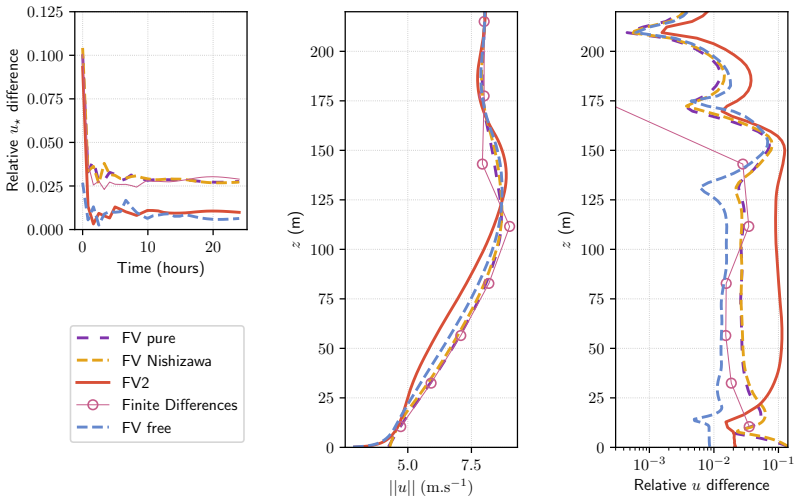

Figure 4.12: Evolution of $u_\star$, vertical profiles of $||u||$ and relative difference of u between low and high resolutions. Above 200m, the profiles are those of the initial condition. In all the numerical experiments the bulk routine is based on $z_u = z_\theta = \frac{K_{u,\mathrm{mol}}}{\kappa u_\star}$.

for simplicity). We generalize the usual approach with $\delta_\mathrm{a} = z_{1/2} - \epsilon$ with $\epsilon < \frac{h_{\frac{1}{2}}}{2}$. The value $u(\delta_\mathrm{a})$ can be approximated by $u_{1/2} - (\partial_z u)(\delta_\mathrm{a})\epsilon$. The implementation of such a boundary condition would be

$$K_0\phi_0 = \kappa^2 ||u_{1/2} - (\partial_z u)(\delta_\mathrm{a})\epsilon|| \frac{u_{1/2} - (\partial_z u)(\delta_\mathrm{a})\epsilon}{\ln\left(1 + \frac{\delta_\mathrm{a}}{z_u}\right)^2} \tag{4.68}$$

and it becomes convenient to compute the difference between $\delta_\mathrm{a} = z_{1/2}$ and $\delta'_\mathrm{a} = z_{1/2} - \epsilon$. Indeed, $|u - (\partial_z u)\epsilon| = |u| - \epsilon\frac{\Re(\overline{u}\partial_z u)}{|u|} + O(\epsilon^2)$ so $|u - (\partial_z u)\epsilon|(u - (\partial_z u)\epsilon) = |u|u - \epsilon\left(u\frac{\Re(\overline{u}\partial_z u)}{|u|} + |u|\partial_z u\right) + O(\epsilon^2)$. Using the wall law $\partial_z u = \frac{u(\delta_\mathrm{a})}{(\delta_\mathrm{a}+z_u)\ln\left(1+\frac{\delta_\mathrm{a}}{z_u}\right)}$ we obtain

$$|u - (\partial_z u)\epsilon|(u - (\partial_z u)\epsilon) - |u|u = -\epsilon\left(\frac{2|u_{1/2}|u_{1/2}}{(\delta_\mathrm{a} + z_u)\ln\left(1 + \frac{\delta_\mathrm{a}}{z_u}\right)}\right) + O(\epsilon^2) \tag{4.69}$$

Combining with the derivative of $\frac{\kappa^2}{\ln\left(1+\frac{\delta_\mathrm{a}}{z_u}\right)}$, we find the derivative of the right-hand side of (4.68) with respect to δ_a to be equal to zero. In conclusion, if z_u does not depend on u and if the evolution equation is integrated in time at $z_{\frac{1}{2}}$, then for the Finite Difference scheme

$$\partial_{\delta_\mathrm{a}}(K_0\phi_0) = 0 \tag{4.70}$$

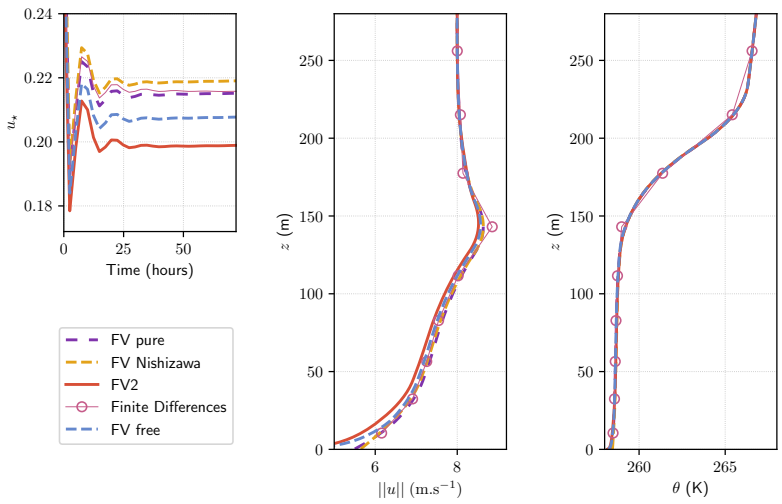

Figure 4.13: Evolution of $u_\star$ and vertical profiles of $||u||$ and $\arg(u)$ for several surface flux schemes. Above 200m, the profiles are those of the initial condition.

This result is expected since in the boundary condition $K_0\phi_0 = u_\star^2 e_\tau$ the orientation e_τ is not changed by the use of the wall law for $\partial_z u$ and the friction scale $u_\star$ is not affected because $u(z_{\frac{1}{2}} - \epsilon)$ is given by the wall law.

4.4.2 Study of the consistency: stable case

We study numerically in a stable case the consistency of the discretisations: how does the change of the space step affect the solution of the discrete equations ?

Description of the test case We intend to obtain a strongly stratified profile: the temperature is hence increasing with the height at the initialization and the surface temperature decreases with time. The initial temperature is 265 K in the first 100 meters of the atmosphere and then gains 1 degree every 100 meters; the surface temperature starts at 265 K and loses 1 degree every ten hours. The geostrophic wind is $u_G = 8$ m.s^{-1}, the time step is $\Delta t = 30$ s. The profiles obtained after 72 hours of integration are shown in Figure 4.13. It is seen that the temperature and wind profiles are all similar. Two simulations are done: the first one ("Low resolution") uses 15 grid points in the 400m column and the second one ("High resolution") uses 45 grid points (see Figure 4.11) and is then projected onto the first grid for the comparison.

Results The differences between the two simulations are shown in Figure 4.14. The difference between the high resolution and the low resolution does not significantly change with the surface flux schemes. The difference in $u_\star$ is especially high for the "FV2" scheme. Note

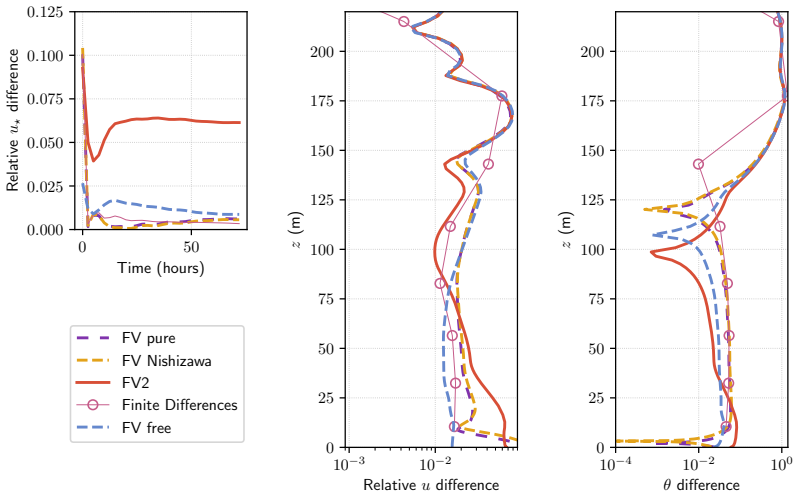

Figure 4.14: Differences in $u_\star$, $||u||$ and $\arg(u)$ between a high resolution and a low resolution of the surface flux schemes presented in a stable stratification.

that the initialization for FV free and FV2 is particular: to ensure the continuity of the solution, the initial profile is already adjusted for the MO theory. This is why the relative $u_\star$ difference is zero at initialization whereas it is very high for the other surface flux schemes. The "FV2" scheme is not very consistent because it follows the continuous model with δ_a changing together with the space step. The Finite Difference or the "FV pure" methods suffer less from this problem because even if δ_a changes, it is assumed that the evolution equation is integrated inside the surface layer. [Maronga et al., 2020] also find that the sensitivity of their LES model to the grid spacing is "*more likely related to under-resolved near-surface gradients and turbulent mixing at the boundary-layer top, to the [sub-grid scale] model formulation, and/or to numerical issues, and not to deficiencies due to the use of improper surface boundary conditions*".

4.4.3 Study of the consistency: unstable case

Figure 4.15 shows the differences found between a high resolution simulation and a low resolution simulation in an unstable situation.

Description of the test case To design a test case with an unstable stratification the sea surface temperature is forced to follow a daily oscillation between 279 K and 281 K. The initial profiles of temperature and wind are set to constant values of respectively 280 K and 8 m.s^{-1}. As in the stable case the geostrophic wind is $u_G = 8$ m.s^{-1} and the time step is $\Delta t = 30$ s. The "low resolution" is composed of 50 grid levels of 10 m each; 15 additional stretched levels between 500 m and 1080 m make sure that the upper boundary condition

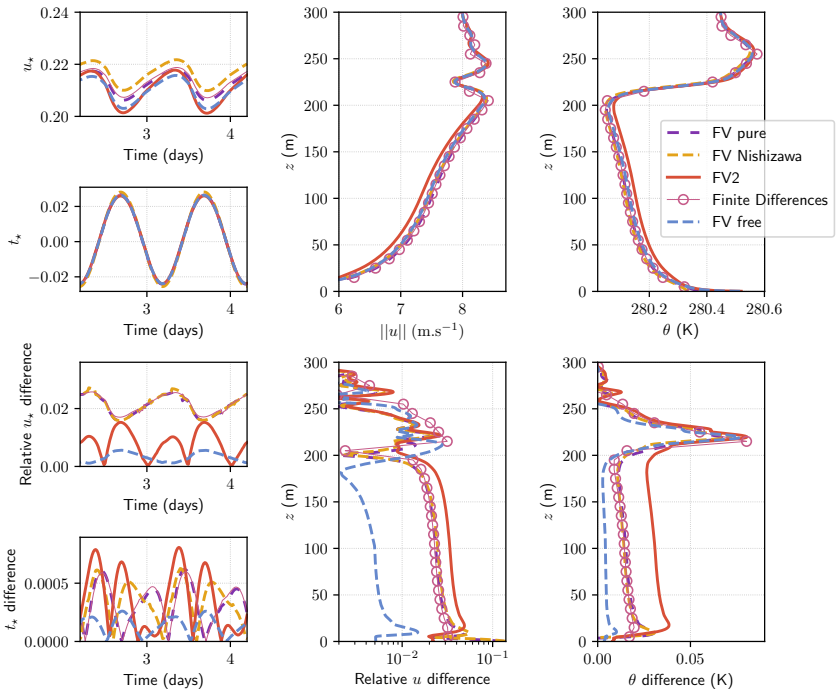

Figure 4.15: Differences (bottom) in $u_\star, t_\star, ||u||$ and θ between a high resolution and a low resolution of the surface flux schemes presented in an unstable stratification. The corresponding profiles with the low resolution simulations are shown in the top panels.

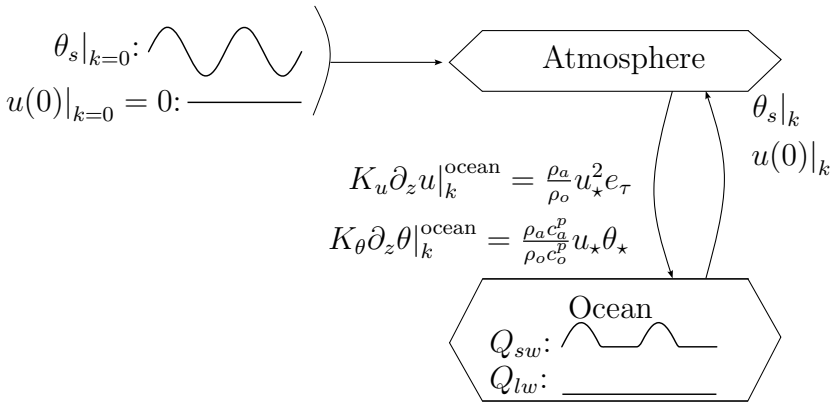

Figure 4.16: Schwarz algorithm applied to ocean-atmosphere coupling

is not involved in the results. The "high resolution" divides every space levels into 3 space levels of equal size.

Results Figure 4.15 shows that the "FV2" scheme is also less consistent in the unstable case. This time in the first 200 meters the scheme "FV free" seems a lot more robust than the other schemes. However, above this height the differences between the high resolution and the low resolution simulations oscillate and there is no clear conclusion that can be made. As in the stable case, the schemes that assume an evolution equation inside the surface layer are not very sensitive to the choice of the height of the surface layer. The main conclusion is hence that **if Monin-Obukhov profiles are enforced in the surface layer the importance of the choice of δ_a increases.** In both cases, the different profiles are very similar. A ocean-atmosphere coupled case is presented in Section 4.4.4, where the surface scheme may be of a greater importance.

4.4.4 Study of the consistency: coupled case

We now introduce an oceanic column model below the atmospheric model. Figure 4.17 shows the differences found between a high resolution simulation and a low resolution simulation in an unstable situation of this coupled system.

Description of the test case In this test case everything is identical to the unstable case except for the sea surface temperature θ_s and the surface current $u(0)$. Instead of prescribing these values directly, a Schwarz algorithm is used: the first iteration begins with the atmosphere and corresponds to the unstable test case. The atmosphere is integrated in time and sends its turbulent fluxes $u_\star^2$ and $u_\star \theta_\star$ to the ocean model, which returns the surface values $u(0)$, θ_s. This process is iterated (see Figure 4.16) and Figure 4.17 shows the state of the atmospheric model after 3 iterations.

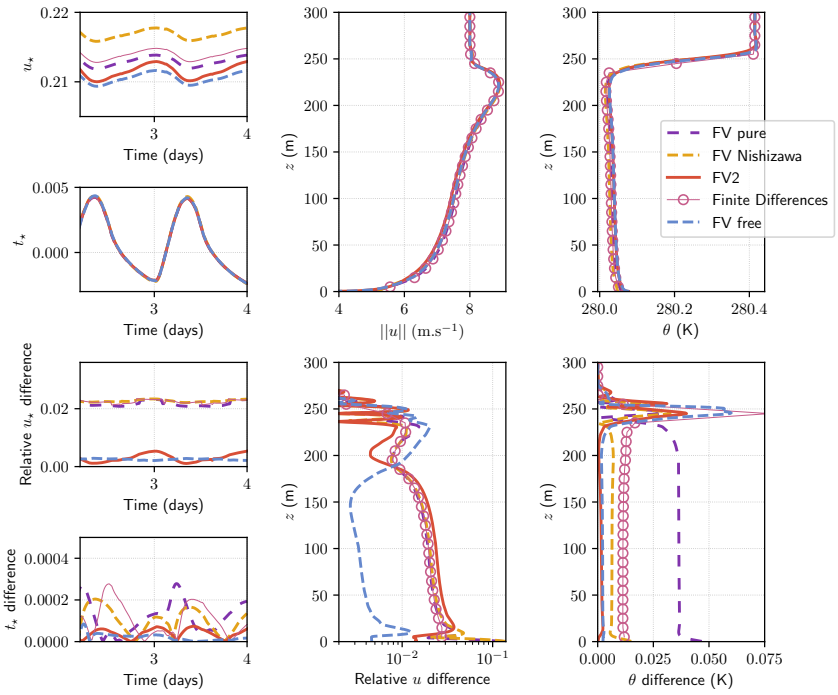

Figure 4.17: Same as Figure 4.15 but the sea surface temperature θ_s and surface currents $u(0)$ are obtained with a coupled ocean column model.

The ocean model will be described in Chapter 5 (Finite Differences, $\delta_o = 0$). It is forced with radiative fluxes to model a diurnal cycle:

- a shortwave (positive downward) heat flux
$$Q_{sw} = \max(0, Q_{\max} \cos(2\pi d)) \tag{4.71}$$
penetrates in the first few levels of the ocean (d is the time in days and $Q_{\max} = 500\mathrm{W.m}^{-2}$);
- a longwave (positive downward) heat flux $Q_{lw} = -\frac{Q_{\max}}{\pi}$ is applied at the surface. Its value corresponds to the daily-averaged Q_{sw}.

Results Figure 4.17 shows in its top panels $u_\star$, $\theta_\star$ and the vertical profiles of $||u||$, θ in the atmosphere after 3 Schwarz iterations with the ocean model. First, note that the oscillations of $u_\star$ and $\theta_\star$ are of a smaller amplitude than in the unstable experiment. Then, in the bottom panel, one can see that the difference in $u_\star$ and u between high and low resolutions when using the "FV free" scheme is smaller than with the other schemes. Unlike the previous cases, the "FV2" scheme do not show a lot of differences between its high and low resolutions. Finally, the dependency of $t_\star$ and θ on the resolution was attenuated by the coupling with the ocean column.

4.5 Partial conclusion

In fluid dynamics, having a rough surface requires to exclude from the computational domain a surface layer. A vast majority of models use Monin-Obukhov Similarity Theory (MOST) to avoid solving the small scales of motion inside the surface layer. We compared several strategies for the treatment of the surface layer and proposed one ("FV free") with two main assets:

- one can choose freely the height δ_a of the surface layer;
- MOST is enforced in the surface layer which avoids a contradiction between the evolution equation and MOST (that is quasi-stationary).

We compared the strategies by verifying that a high-resolution discretisation would be close to the low-resolution one. The strategy "FV free" shows less differences between high- and low-resolution simulations than the other strategies, especially for the wind speed and in unstable situations.

In the comparison, we used a Finite Volume method based on spline reconstruction. This method encourages us to be clean in the derivation of the discretisation: using the wall law for the surface viscosity together with the quadratic spline reconstruction in the surface layer led to an unphysical behaviour. On the other hand, this method also allows to choose the reconstruction to follow the wall law.

Chapter 5

Discretization of the oceanic surface layer

Table of contents

In this Chapter, we focus on the ocean part of the coupled turbulent Ekman problem (defined in Chapter 1) and in particular to the oceanic surface layer. [Pelletier et al., 2021] introduced a *two-sided* bulk method which does not only take as input the "relative" (w.r.t. surface currents) wind but also takes into account the depth δ_o at which the surface current is evaluated. This *two-sided* bulk is detailed in Section 5.1. We call the region between $z = 0$

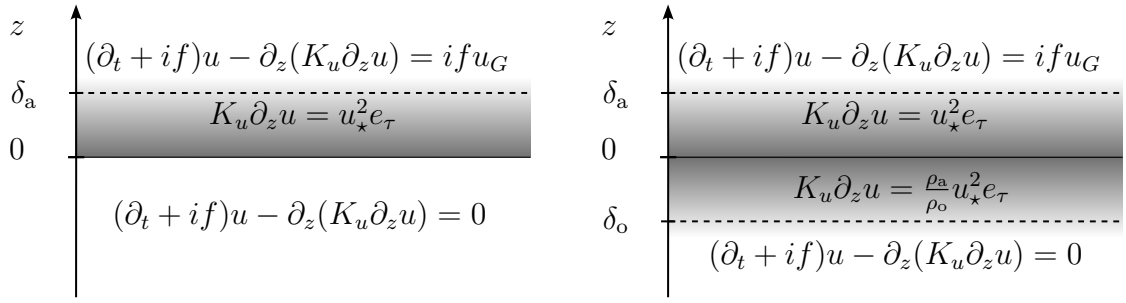

Figure 5.1: *one-sided* surface layer (left) and *two-sided* surface layer (right).

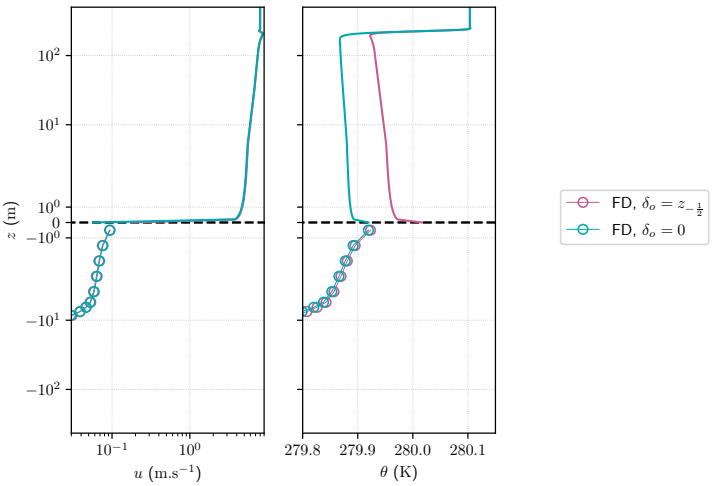

Figure 5.2: Comparison between two-sided bulk ($\delta_o = z_{-\frac{1}{2}}$) and one-sided bulk ($\delta_o = 0$) in a coupled situation after one day of integration. The parameters of this experiment are the same as in Section 4.4.4.

and $z = \delta_o$ the Oceanic Surface Layer (OSL). The two-sided bulk method relies on MOST profiles in the OSL. The idea of the previous chapter is used again to derive a discretization based on spline reconstruction in Section 5.2. In all this chapter, the atmosphere surface flux scheme chosen is "FV free".

5.1 A two-sided bulk for the ocean-atmosphere interface

As it is explained in [Pelletier et al., 2021], it is now recognized that the wind-stress depends strongly on surface currents. However in actual coupled ocean-atmosphere simulation, the surface currents are evaluated below the surface at $z = \delta_o$: this amounts to assume that the currents are constant in the oceanic surface layer.

The new idea introduced by [Pelletier et al., 2021] is to consider that there is a Monin-Obukhov boundary layer below the ocean surface when calculating friction scales with the BULK algorithm. The method of assuming a boundary layer on either side of the interface is called *two-sided* bulk (see Figure 5.1).

Figure 5.2 shows the difference between the use of a two-sided bulk and a one-sided bulk in a coupled situation. The atmosphere model "FV free" (described in Chapter 4) is coupled with a Finite Difference discretization of the ocean column. This corresponds to comparing $\delta_o < 0$ and $\delta_o = 0$. We find that using a surface layer in the ocean changes the sea surface

temperature and leads to a difference in temperature in the atmosphere column.

By applying bulk methods on the outputs of realistic models, [Pelletier et al., 2021] found that the near-surface velocity profiles are more affected by the use of a two-sided bulk than the surface temperature. We find different results here with idealized models but including the two-sided bulk method inside the coupling. Other experiments are needed to evaluate the consequences of using a two-sided bulk method.

5.2 Oceanic surface layer

This section focuses on the discretization of an ocean column and its surface layer. Indeed, we consider from now on that the bulk formulation takes into account the surface layer of the ocean and that this surface layer is based on

$$\forall z \in [\delta_o, 0], \begin{cases} |K_u \partial_z u| & = \frac{\rho_a}{\rho_o} u_\star^2 \\ K_\theta \partial_z \theta & = \frac{\rho_a c_a^p}{\rho_o c_o^p} \theta_\star u_\star - \frac{Q_{lw}+Q_{sw}(z)}{\rho_o c_o^p} \end{cases} \tag{5.1}$$

where c_a^p, c_o^p are the heat capacities of air and water and Q_{lw}, Q_{sw} are radiative fluxes defined in Section 5.2.2.

As it was discussed in Chapter 4, it can be important to take into account the hypotheses of the surface layer within the discretization. The first part of this section is dedicated to the extention of the surface flux scheme of Chapter 4 for the oceanic surface layer.

The second part of this section focuses on a specificity of the oceanic surface layer: the radiative fluxes. The latter penetrate in the first few meters of the ocean, creating an external forcing which affects the surface layer. In particular, the flux $\langle w'\theta' \rangle = -K_\theta \partial_z \theta$ is no more constant along the vertical when considering the radiative fluxes.

As a first step towards a discretization including the radiative fluxes, we will derive in Section 5.2.2 a discretization based on an approximative reconstruction of the potential temperature.

We first (§5.2.1) specify the differences between the ocean and atmosphere models in use, then focus on the radiative fluxes in §5.2.2. Finally, Section 5.2.3 presents the sensitivity to the discretization obtained of the surface layer in a forced setting and in a coupled setting.

5.2.1 Differences with the atmosphere and derivation of a symmetric surface flux scheme

In this section, the numerical model of a stratified column of ocean is described. The objective is to obtain a model similar to the atmosphere while including the specificity of the ocean. In particular, the main changes compared to the atmosphere model are:

- the density which mainly affects the exchanges between ocean and atmosphere;

- the universal stability functions which are taken in [Large et al., 2019];
- the vertical coordinate z is negative;
- the time and space scales (the motion in the ocean is slower and smaller space steps are used with larger time steps).

5.2.1.1 The Ocean model

We describe here the continuous model in use for the ocean. The equations for momentum, potential temperature and turbulent kinetic energy in the inner domains are similar to those of the atmosphere except that the geostrophic momentum is not included in the ocean:

$$\begin{aligned}
&(\partial_t + if)u - \partial_z(K_u \partial_z u) = 0, && z \leq \delta_o \\
&\partial_t \theta - \partial_z(\partial_z K_\theta \theta) = F_\theta, && z \leq \delta_o \\
&\partial_t e = \underbrace{\partial_z\left(K_e \partial_z e\right)}_{\text{diffusion}} + \underbrace{K_u ||\partial_z u||^2}_{\text{shear}} - \underbrace{K_\theta N^2}_{\text{buoyancy}} - \underbrace{c_\epsilon \frac{e^{3/2}}{l_\epsilon(z)}}_{\text{dissipation}}
\end{aligned} \tag{5.2}$$

$F_\theta = -\frac{\partial_z Q_{sw}}{\rho_o C_p}$ is a forcing corresponding to the penetration of a shortwave radiadive flux coming from the sun in a diurnal cycle. As in the atmospheric case the buoyancy N^2 is given by a linear equation of state $N^2 = g\alpha\partial_z\theta$. The mixing lengths follow the description in 4.3.3 except that l_{up} and l_{down} are swapped and the shear is neglected in (4.53).

Initialization and boundary conditions. At initialization, the TKE is set to $e = e_{\min}$, the temperature is set to a constant $\theta = 280$ K and the initial momentum is set to $u = 0$ m.s^{-1}. At the bottom boundary, $\partial_z u = 0$, $\partial_z \theta = 0$ and $e = e_{\min}$.

5.2.1.2 The surface boundary condition

We derive here the discretization "FV free" applied to the oceanic column model. Let k be the space index such that $z_{k-1} < \delta_o \leq z_k$; in this chapter, we will assume that δ_o is inside the first cell under the surface as it was done in the beginning of Chapter 4. The index k hence corresponds to the surface index $z_k = 0$. we note $\widetilde{u}, \widetilde{\theta}$ the averaged variables over the interval (z_{k-1}, δ_o). In the case of the atmosphere column, equation (4.47) gives the relation between the averaged variables $\overline{u}, \overline{\theta}$ over the volume (z_{k-1}, z_k). The same relation can be written here:

$$\begin{aligned}
\alpha_{o,u}\widetilde{u} &= \overline{u}_{k-1/2} - \widetilde{h}\left(\frac{\phi_\delta}{3} + \frac{\phi_{k-1}}{6}\right)\left(\alpha_{o,u} - \frac{\widetilde{h}}{h_{k-1/2}}\right) - (1-\alpha_{o,u})u(0) \\
\alpha_{o,\theta}\widetilde{\theta} &= \overline{\theta}_{k-1/2} - \widetilde{h}\left(\frac{(\partial_z\theta)_\delta}{3} + \frac{(\partial_z\theta)_{k-1}}{6}\right)\left(\alpha_{o,\theta} - \frac{\widetilde{h}}{h_{k-1/2}}\right) - (1-\alpha_{o,\theta})\theta_s
\end{aligned} \tag{5.3}$$

with for $x = u, \theta$:

$$\alpha_{o,x} = \frac{\widetilde{h}}{h_{k-1/2}} + \frac{\frac{1}{h_{k-1/2}} \int_{\delta_o}^{z_k} x(0) - x(z) dz}{x(0) - x(\delta_o)} \tag{5.4}$$

Appendix 5.A details the derivation of the explicit formula of α_o with the oceanic universal stability functions. Finally, the scheme at the first grid level above the surface layer is:

$$(\partial_t + if)\widetilde{u} = \frac{K_{u,\delta_o}\phi_{\delta_o} - K_{u,k-1}\phi_{k-1}}{\widetilde{h}} \tag{5.5}$$

$$\partial_t \widetilde{\theta} = \frac{K_{\theta,\delta_o}(\partial_z\theta)_{\delta_o} - K_{\theta,k-1}(\partial_z\theta)_{k-1}}{\widetilde{h}} + \widetilde{F_\theta} \tag{5.6}$$

where for $x = u, \theta$:

$$\widetilde{x} = \frac{1}{\alpha_{\mathrm{o,x}}(t)} \left(\overline{x}_{k-1/2} - \widetilde{h}\left(\frac{(\partial_z x)_{\delta_o}}{3} + \frac{(\partial_z x)_{k-1}}{6}\right) \left(\alpha_{o,x} - \frac{\widetilde{h}}{h_{k-1/2}} \right) - (1 - \alpha_{o,x}) x(0) \right) \tag{5.7}$$

In the surface layer, the hypothesis that the potential temperature is quasi-stationary gives that $\forall z \in [\delta_o, 0], \quad \partial_z \left(K_\theta \partial_z \theta \right) = \frac{\partial_z Q_{sw}}{\rho_\mathrm{o} C_p}$. The scheme uses as boundary conditions at the surface layer:

$$\begin{aligned} K_{u,\delta_o}\phi_{\delta_o} &= \frac{\rho_\mathrm{a}}{\rho_\mathrm{o}} u_\star^2 e_\tau \\ K_{\theta,\delta_o}(\partial_z\theta)_{\delta_o} &= \frac{\rho_\mathrm{a} c_\mathrm{a}^p}{\rho_\mathrm{o} c_\mathrm{o}^p} \theta_\star u_\star - \frac{Q_{lw} + Q_{sw}(\delta_o)}{\rho_\mathrm{o} c_\mathrm{o}^p} \end{aligned} \tag{5.8}$$

The surface flux scheme is summarized in Figure 5.3. As it will be explained in Section 5.2.2 this surface flux scheme would require an integration of the radiative flux and we will instead use an evolution equation for θ together with an approximated reconstruction.

5.2.2 Radiative fluxes, another surface flux scheme

We note Q_{sw} and Q_{lw} the shortwave and longwave (positive downward) radiative fluxes. To include those fluxes in the bulk formula, [Pelletier et al., 2021] introduced a variable $\theta_\star^{\mathrm{rad}}$ that is similar to a friction scale but depends on z:

$$\theta_\star^{\mathrm{rad}}(z) = \theta_\star - \frac{Q_{sw}(z) + Q_{lw}}{u_\star \rho_\mathrm{a} c_\mathrm{a}^p} \tag{5.9}$$

This variable is used instead of $\theta_\star$ in the ocean part of the two-sided bulk procedure to include the radiative fluxes. To be fully consistent between the computational domain and the oceanic surface layer, the boundary condition for the temperature should take into account the radiative fluxes: in (5.8) the flux $K_\theta \partial_z \theta$ is exactly equal to $\frac{\rho_\mathrm{a} c_\mathrm{a}^p}{\rho_\mathrm{o} c_\mathrm{o}^p} \theta_\star^{\mathrm{rad}}(\delta_o) u_\star$.

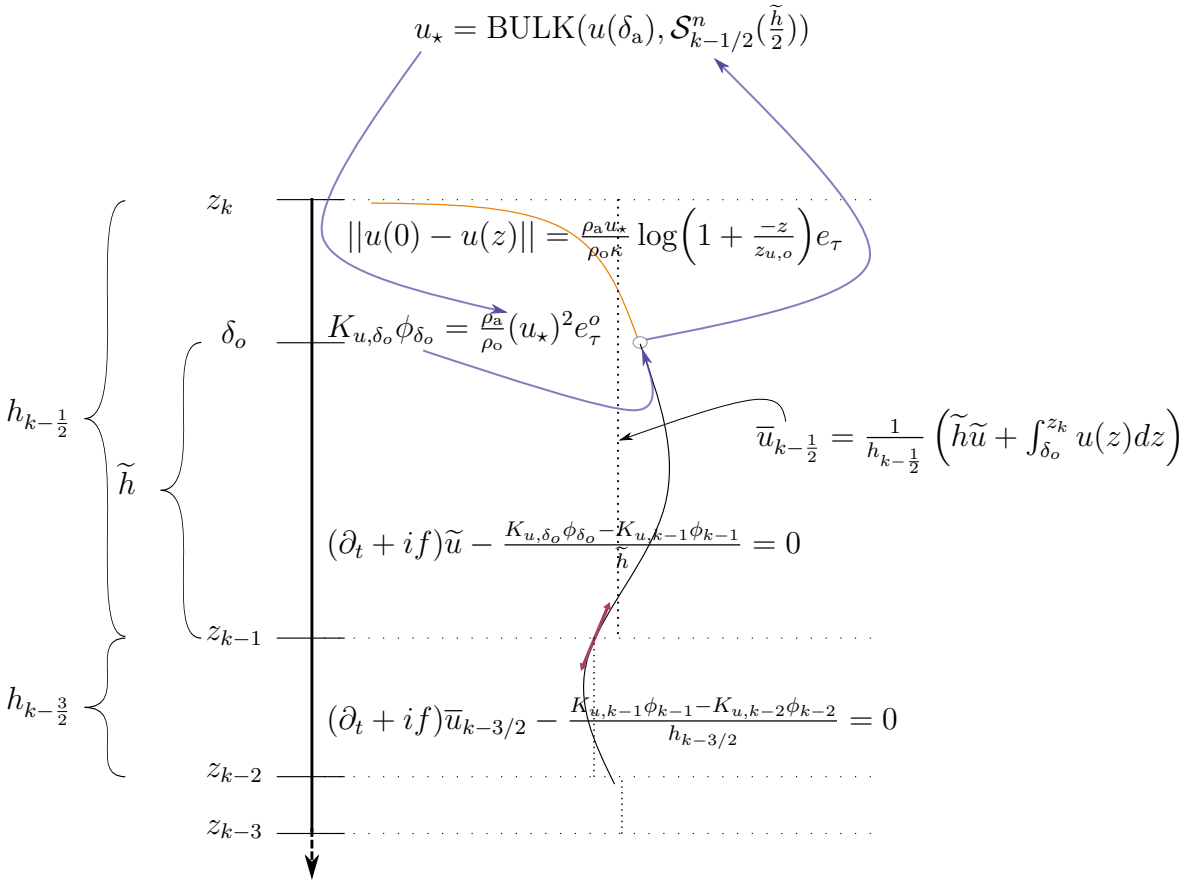

Figure 5.3: Surface layer scheme "FV free" in the ocean model

The reconstruction of θ requires an vertical integration of a combination of Q_{sw} and the stability functions of MOST. The integral involves a special functions (the exponential integral) and it would need to be integrated a second time for the Finite Volume representation. These difficulties are left for future work.

Instead, as an intermediate step to avoid the double integration of Q_{sw} in the Finite Volume discretization, we use an evolution equation inside the surface layer despite the contradiction with the quasi-stationarity. This intermediate discretization features a different reconstruction than outside the surface layer: it cannot be fully coherent with the surface layer hypotheses because of the quasi-stationarity but it might be more adapted than the quadratic spline reconstruction used outside the surface layer.

We neglect the molecular sub-layer and integrate between δ_o and 0: the flux at $z = 0$ is $K_\theta \partial_z \theta = \frac{Q_H - Q_{lw}}{\rho_o c_o^p}$ where $Q_H = \theta_\star u_\star \rho_a c_a^p$

$$h_{osl}\partial_t \overline{\theta}_{osl} = \frac{Q_H - Q_{lw}}{\rho_o c_o^p} - K_\theta \partial_z \theta|_{\delta_o} - h_{osl} \int_{\delta_o}^{0} \frac{\partial_z Q_{sw}}{\rho_o c_o^p} dz \tag{5.10}$$

where $h_{osl} = |\delta_o|$ is the size of the surface layer and $\overline{\theta}_{osl}$ is the average potential temperature in the surface layer.

Approximate reconstruction of $\theta(z)$

We will use the following reconstruction of θ inside the SL (taken from [Zeng and Beljaars, 2005] where the molecular surface layer was neglected to simplify the expressions):

$$\theta(z) = \theta_s - \left(\frac{z}{\delta_o}\right)^\nu (\theta_s - \theta_{\delta_o}) \tag{5.11}$$

where ν is a constant parameter that can be set to 1 to recover a linear reconstruction of $\theta(z)$. [Zeng and Beljaars, 2005] choose $\nu = 0.3$ and argue that the choice of ν is linked to the size of the molecular sub-layer. We formulate the reconstruction in terms of $\overline{\theta}_{osl}$ and $\partial_z \theta|_{\delta_o}$:

$$\overline{\theta}_{osl} = \frac{1}{\nu + 1}(\theta_{\delta_o} + \nu \theta_s), \quad \partial_z \theta|_{\delta_o} = \frac{\nu}{h_{osl}}(\theta_s - \theta_{\delta_o}) \tag{5.12}$$

We get that the surface temperature is $\theta_s = \overline{\theta}_{osl} + \frac{h_{osl}}{\nu(\nu+1)}\partial_z \theta$ and the difference of temperature between the surface and the bottom of the surface layer is $\theta_s - \theta_{\delta_o} = \frac{h_{osl}}{\nu}\partial_z \theta$:

$$\theta(z) = \overline{\theta}_{osl} + \frac{h_{osl}}{\nu}\partial_z \theta_{\delta_o} \left(\frac{1}{\nu + 1} - \left(\frac{z}{\delta_o}\right)^\nu\right) \tag{5.13}$$

Remark *It would be possible to consider that $\overline{\theta}_{osl}$ is the average in an interval (δ_o, z_k) with $z_k \neq 0$. However the radiative forcing would affect each individual cell inside the surface layer, leading to a contradiction with the simple reconstruction (5.11) of the surface layer. We instead assume here that $|\delta_o| < |z_{k-1}|$ and $z_k = 0$.*

Link with the quadratic spline

Let us assume now that $\theta(z)$ is a quadratic spline between z_{-1} and δ_o. Using the continuity at $z = \delta_o$ and Chasles' relation, we link the surface layer profile with the spline:

$$\underbrace{\overline{\theta}_{osl} - \frac{h_{osl}}{\nu+1}\,\partial_z\theta|_{\delta_o}}_{\theta(\delta_o^+)} = \underbrace{\widetilde{\theta} + \frac{\widetilde{h}}{3}\,\partial_z\theta|_{\delta_o} + \frac{\widetilde{h}}{6}\,\partial_z\theta|_{z_{-1}}}_{\theta(\delta_o^-)}, \qquad \underbrace{h_{-1/2}\overline{\theta} = h_{osl}\overline{\theta}_{osl} + \widetilde{h}\widetilde{\theta}}_{\int_{z_{-1}}^{0}\theta(z)dz} \tag{5.14}$$

The reconstruction for $|z| < |\delta_o|$ (inside the surface layer) is hence

$$\theta(z) = \overline{\theta}_{-\frac{1}{2}} + \left(\frac{h_{osl}\widetilde{h}}{-z_{-1}(\nu+1)} + \frac{\widetilde{h}^2}{-3z_{-1}} + \frac{h_{osl}}{\nu}\left(\frac{1}{\nu+1} + \left(\frac{z}{h_{osl}}\right)^{\nu}\right)\right)\partial_z\theta_{\delta_o} + \left(\frac{\widetilde{h}^2}{-6z_{-1}}\right)\partial_z\theta_{-1} \tag{5.15}$$

for $|\delta_o| < |z| < |z_{-1}|$ (in the quadratic region) we have

$$\theta(z) = \widetilde{\theta} + \left(z - \delta_o + \frac{(z-\delta_o)^2}{2\widetilde{h}} + \frac{\widetilde{h}}{3}\right)\partial_z\theta_{\delta_o} + \left(\frac{\widetilde{h}^2 - 3(z-\delta_o)^2}{6\widetilde{h}}\right)\partial_z\theta_{-1} \tag{5.16}$$

where $\widetilde{\theta}$ is computed with

$$\widetilde{\theta} = \overline{\theta}_{-1/2} - \frac{\delta_o}{z_{-1}}\left(\frac{h_{osl}}{\nu+1} + \frac{\widetilde{h}}{3}\right)\partial_z\theta_{\delta_o} - \frac{\widetilde{h}\delta_o}{6z_{-1}}\partial_z\theta_{-1} \tag{5.17}$$

Now that the reconstruction in all the first cell is known, the only thing left to do is to derive the evolution equations to integrate in time the potential temperature.

The discretization

The continuity equation at z_{-1} uses $\widetilde{h}$ as the space step:

$$\widetilde{\theta} - \frac{\widetilde{h}}{3}\partial_z\theta_{-1} - \frac{\widetilde{h}}{6}\partial_z\theta_{\delta_o} = \overline{\theta}_{-3/2} + \frac{\widetilde{h}}{3}\partial_z\theta_{-1} + \frac{\widetilde{h}}{6}\partial_z\theta_{-2} \tag{5.18}$$

The evolution equation of the first volume is:

$$h_{-\frac{1}{2}}\partial_t\overline{\theta}_{-\frac{1}{2}} = \frac{Q - Q_{lw}}{\rho_o c_o^p} - K_{\theta,-1}\partial_z\theta_{-1} - h_{-\frac{1}{2}}\int_{z_{-1}}^{0}\frac{\partial_z Q_{sw}}{\rho_o c_o^p}dz \tag{5.19}$$

We need a last equation to close the system. Starting from (5.17), we use the evolution equation $\widetilde{h}\partial_t\widetilde{\theta}K_\theta\partial_z\theta_{\delta_o} - K_\theta\partial_z\theta_{-1} - \widetilde{h}\int_{z_{-1}}^{\delta_o}\frac{\partial_z Q_{sw}}{\rho_o c_o^p}dz$ to obtain

$$\partial_t\left(\widetilde{h}\overline{\theta}_{-1/2} - \frac{\delta_o}{z_{-1}}\left(\frac{\widetilde{h}h_{osl}}{\nu+1} + \frac{\widetilde{h}^2}{3}\right)\partial_z\theta_{\delta_o} - \frac{\widetilde{h}^2\delta_o}{6z_{-1}}\partial_z\theta_{-1}\right) = K_\theta\partial_z\theta_{\delta_o} - K_\theta\partial_z\theta_{-1} - \widetilde{h}\int_{z_{-1}}^{\delta_o}\frac{\partial_z Q_{sw}}{\rho_o c_o^p}dz \tag{5.20}$$

Note that the reconstruction we are using is not differentiable in $z = 0$. If greater regularity is needed, it is possible to link the reconstruction with a proper modeling of the molecular sub-layer (e.g. $\rho_o c_o^p K_{mol} \partial_z \theta(z) = Q - Q_{lw} - \int_z^0 \partial_z Q_{sw}(z')dz'$ for $|z| \ll |\delta_o|$)

5.2.3 Sensitivity to the discretization of the surface layers

Figure 5.4 show the profiles obtained in wind and potential temperature with several discretisations. As in Chapter 4 a high resolution simulation where every cell is divided into three cells is also performed.

For the velocity, the differences between the different cases are located between $z = -1$ m and $z = 0$ m. For the temperature, significant differences are found down to the depth of 10 meters.

The output of the normal simulation is not extremely sensitive to the discretization (the continuous lines are close with each others); the Finite Difference and the Finite Volume discretizations give coherent results.

The size of the oceanic surface layer is $|\delta_o| = 0.17$. This choice actually corresponds to first grid level of the high resolution cutted in half. Indeed, the "FV free" discretization does not allow for inactive grid levels like in the atmosphere case.

The distance between the dashed line and the continuous line for the same color indicates how consistent is the surface layer discretization. Contrarily to the atmosphere case, the least consistent of the discretizations appears to be the "FV free".

Figure 5.5 is the same as Figure 5.4 except that the ocean column is coupled with the atmosphere column described in Chapter 4.

Similarly to the sensitivity to the use of a *two-sided* bulk (Figure 5.2), the difference in temperature is bigger than the difference in velocity. Moreover, as in Figure 5.4 the differences between the cases are in the direct neighborhood to the surface for u whereas they are also present further from the interface for θ.

The difference between the *one-sided* bulk ($\delta_o = 0$) and the *two-sided* bulk also appears in the potential temperature in the two "FV pure" cases.

The biggest difference between the normal simulation and the high-resolution simulation is again the scheme "FV free". A possible reason for this undesirable behavior is the lack of accuracy of the approximation of the profile of θ in the oceanic surface layer.

5.3 Partial conclusion

In this chapter, we extended the "FV free" discretization for the oceanic surface layer. The radiative fluxes inclusion was studied and we proposed a discretization to take them into account. They represent an instance of additional difficulties encountered when developping coherent numerical treatment of the surface layer.

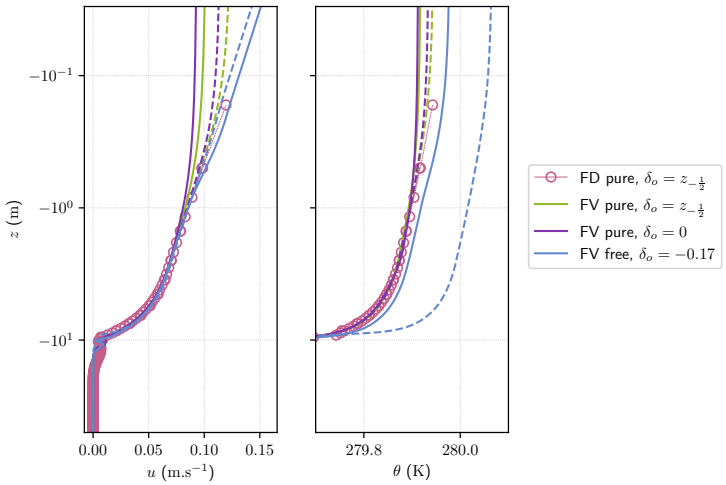

Figure 5.4: Forced case: dashed lines indicate a high resolution simulation and solid lines show the normal simulation. Numerical parameters are the same as in §4.4.4.

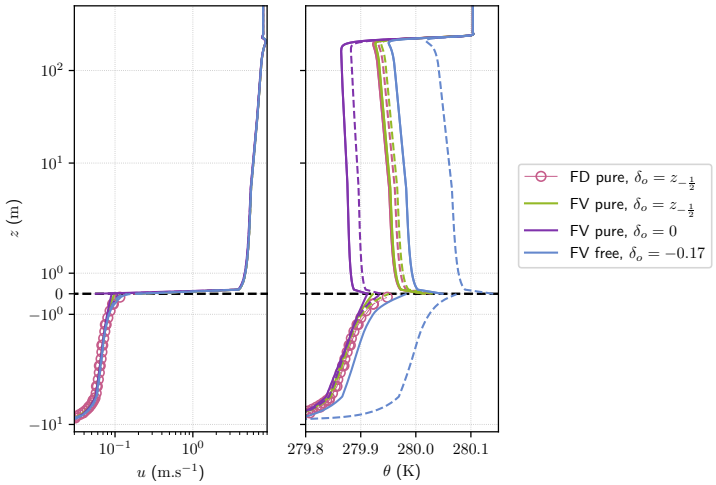

Figure 5.5: Coupled case. The observed convergence factor of the Schwarz method was around 10^{-2} (i.e. convergence in 2 or 3 iterations). Dashed lines indicate a high resolution simulation and solid lines show the normal simulation.

The discretization proposed in this chapter does not perform better than the other ones when comparing the consistencies in a coupled case and in a forced case.

No stability nor accuracy studies were conducted on the proposed discretisations. Although they seem to behave correctly in the experiments, further analyses of the "FV free" scheme are necessary before they can be used. In particular, the Finite Volume approximation between the first cell and the second corresponds to the use of a strongly unstructured grid, the second cell being typically twofold bigger than the explicit part of the first cell.

5.A Appendix: computing α_{sl}: stability function integration

In the ocean, we use the universal function of [Large et al., 2019] (as in [Pelletier et al., 2021])

$$\phi_m(\zeta) = \phi_h(\zeta) = 1 + 5\zeta, \quad \zeta \geq 0 \tag{5.21}$$

$$\phi_m(\zeta) = (1 - 14\zeta)^{-1/3}, \quad \zeta < 0 \tag{5.22}$$

$$\phi_h(\zeta) = (1 - 25\zeta)^{-1/3}, \quad \zeta < 0 \tag{5.23}$$

and the first integrated form, $\psi_{\{m,h\}}(\zeta) = \int_0^\zeta \frac{1-\phi_{\{m,h\}}(\zeta')}{\zeta'} d\zeta'$ is for $\zeta < 0$

$$\psi_{\{m,h\}}(\zeta) = \sqrt{3}\left[\arctan\left(\sqrt{3}\right) - \arctan\left(\frac{\sqrt{3}}{3}(2C_{\{m,h\}} + 1)\right)\right] + \frac{3}{2}\ln\left(\frac{(C_{\{m,h\}})^2 + C_{\{m,h\}} + 1}{3}\right) \tag{5.24}$$

and $\psi_{\{m,h\}}(\zeta) = -5\zeta$ for $\zeta \geq 0$ where $C_m = (1-14\zeta)^{1/3}$, $C_h = (1-25\zeta)^{1/3}$. We now compute its volume-averaged form $\Psi_{\{m,h\}}(\zeta) = \frac{1}{\zeta}\int_0^\zeta \psi_{\{m,h\}}(x)dx$.

First,

$$\int \ln\left(C_m^2 + C_m + 1\right)d\zeta = -2\frac{\zeta}{3} - \frac{1}{28}C_m^2 - \frac{1}{14}C_m + \zeta\ln\left(C_m^2 + C_m + 1\right) + \text{const} \tag{5.25}$$

and

$$\int \arctan\left(\frac{2C_m + 1}{\sqrt{3}}\right)d\zeta = \frac{\sqrt{3}}{56}C_m(C_m - 2) + \zeta\arctan\left(\frac{2C_m + 1}{\sqrt{3}}\right) + \text{const} \tag{5.26}$$

Putting them together, we get

$$\begin{aligned}\Psi_m(\zeta) = \sqrt{3}\arctan\left(\sqrt{3}\right) - \frac{3}{2}\ln(3) - \frac{3}{56\zeta}C_m(C_m - 2) - \sqrt{3}\arctan\left(\frac{2C_m + 1}{\sqrt{3}}\right) \\ -1 - \frac{3}{56\zeta}C_m^2 - \frac{3}{28\zeta}C_m + \frac{3}{2}\ln\left(C_m^2 + C_m + 1\right) + \frac{\text{const}}{\zeta}\end{aligned} \tag{5.27}$$

After simplification, using $\lim_{\zeta} \to 0 \int_0^{\zeta} \psi(x)dx = 0$:

$$\begin{aligned} \Psi_{\{m,h\}}(\zeta) &= -\frac{5}{2}\zeta, \qquad \zeta \geq 0 \\ \Psi_{\{m,h\}}(\zeta) &= \psi_{\{m,h\}}(\zeta) - \frac{(2C_{\{m,h\}}+1)(C_{\{m,h\}}-1)}{2\left((C_{\{m,h\}})^2 + C_{\{m,h\}} + 1\right)}, \qquad \zeta < 0 \end{aligned} \tag{5.28}$$

We finally get for u:

$$\alpha_{sl,u} = \frac{\widetilde{h}}{h_{k-1/2}} + \frac{\frac{1}{h_{k-1/2}}\left[(-z+z_{0m})\ln\left(1+\frac{-z}{z_{0m}}\right) + z - z\Psi_m(\frac{-z}{L_{MO}})\right]_{\delta_o}^{z_k}}{\ln\left(1+\frac{-\delta_o}{z_{0m}}\right) - \psi_u(\frac{-\delta_o}{L_{MO}})} \tag{5.29}$$

and for θ:

$$\alpha_{sl,\theta} = \frac{\widetilde{h}}{h_{k-1/2}} + \frac{1}{h_{k-1/2}} \frac{(Q_H - Q_{lw})\left[(-z+z_\theta)\ln\left(1+\frac{-z}{z_\theta}\right) + z - z\Psi_m(\frac{-z}{L_{MO}})\right]_{\delta_o}^{z_k} - Q_{sw}\int_{\delta_o}^{z_k} E(z)dz}{(Q_H - Q_{lw})\left(\ln\left(1+\frac{-\delta_o}{z_\theta}\right) - \psi_\theta(\frac{-\delta_o}{L_{MO}})\right) - Q_{sw}E(\delta_o)} \tag{5.30}$$

where $E(z) = \int_z^0 \frac{\phi_h(-x/L_o)\sum A_i \exp(k_i x)}{-x+z_u}dx$ and $Q_H = \theta_\star u_\star \rho_{\text{a}} c_{\text{a}}^p$. In practice, $\alpha_{sl,\theta}$ will not be used: in Section 5.2.2 we describe another way to include the radiative fluxes in the surface layer.

Chapter 6

Convergence of Schwarz methods applied to the discrete ocean-atmosphere coupling

Table of contents

We presented in Chapter 2 the discrete analysis of the convergence of Schwarz methods with Dirichlet-Neumann interface conditions; the implementation of the law of the wall was discussed in Chapter 4. We now aim to study the convergence properties of Schwarz methods when the law of the wall is used at the interface between ocean and atmosphere. In this

chapter, we study the Ekman problem with a simplified bulk condition at the surface such that it can be easily implemented to numerically validate the convergence results.

A part of this chapter was published in the proceedings of the 26th International Conference on Domain Decomposition Methods [Clement et al., 2021]. In addition to minor clarifications, Section 6.4 and Appendix 6.A were added, where the steady state and the well-posedness of the coupling problem considered are discussed. Moreover, a mistake in asymptotes computations has been noticed and corrected in Section 6.5. The convergence study of §6.5.2 was also further pursued, with the corresponding computations being presented in Appendix 6.B.

The full text of [Clement et al., 2021] is reported here and complemented: this chapter hence contains some redundancies with the previous ones (mainly in Sections 6.1 and 6.2).

6.1 Introduction

Schwarz-like domain decomposition methods are very popular in mathematics, computational sciences and engineering notably for the implementation of coupling strategies. Such an iterative method has been recently applied in a state-of-the-art Earth System Model (ESM) to evaluate the consequences of inaccuracies in the usual ad-hoc ocean-atmosphere coupling algorithms used in realistic models [Marti et al., 2021]. For such a complex application it is challenging to have an a priori knowledge of the convergence properties of the Schwarz method. Indeed coupled problems arising in ESMs often exhibit sharp turbulent boundary layers whose parameterizations lead to peculiar transmission conditions. The objective in this chapter is to study a model problem representative of the coupling between the ocean and the atmosphere, including discretization and so-called bulk interface conditions which are analogous to a quadratic friction law. Such a model is introduced in Section 6.2 and its discretization, as done in state-of-the-art ESMs, is described in Section 6.3. In the semi-discrete case in space we compute in Section 6.4 the steady state and discuss the well-posedness. A semi-discrete convergence analysis of the model problem is conducted in Section 6.5 first with a linear friction and then with a quadratic friction linearized around equilibrium solutions. Finally, in Section 6.6, numerical experiments in the linear and nonlinear case are performed to illustrate the relevance of our analysis.

6.2 Model problem for ocean-atmosphere coupling

We focus on the dynamical part of the oceanic and atmospheric primitive equations and neglect the horizontal variations of the velocity field, which leads to a model problem depending on the vertical direction only. This assumption, commonly made to study turbulent mixing in the boundary layers near the air-sea interface, is justified because of the large disparity between the vertical and the horizontal spatial scales in these layers. We consider

the following diffusion problem accounting for Earth's rotation (f is the Coriolis frequency and $\mathbf{k}$ a vertical unit vector):

$$\left\{\begin{array}{rcll} \partial_t \mathbf{u} + f\mathbf{k}\times\mathbf{u} - \partial_z\left(\nu(z,t)\partial_z\mathbf{u}\right) &=& \mathbf{g}, & \text{in } \Omega\times(0,T),\\ \mathbf{u}(z,0) &=& \mathbf{u}_0(z), & \forall z \text{ in } \Omega,\\ \mathbf{u}(H_o,t) &=& \mathbf{u}_o^\infty(t),\ \mathbf{u}(H_a,t)=\mathbf{u}_a^\infty(t), & t\in(0,T), \end{array}\right.$$

with $\mathbf{u}=(u,v)$ the horizontal velocity vector, $\nu(z,t)>0$ the turbulent viscosity and $\Omega=(H_o,H_a)$ a bounded open subset of $\mathbb{R}$ containing the air-sea interface $\Gamma=\{z=0\}$. In the ocean and the atmosphere, which are turbulent fluids, the velocity field varies considerably in the few meters close to the interface (in a region called *surface layer*, see Chapter 1). The cost of an explicit representation of the surface layer in numerical simulations being unaffordable, this region is numerically accounted for using wall laws [e.g. Mohammadi et al., 1998]. This approach, traditionally used to deal with solid walls, is also used in the ocean-atmosphere context, with additional complexity arising from the stratification effects [e.g. Pelletier et al., 2021]. In this context wall laws are referred to as *surface layer* parameterizations. The role of such parameterizations is to provide $\nu\partial_z\mathbf{u}$ on the upper and lower interfaces of the surface layer as a function of the difference of fluid velocities. Thus the coupling problem of interest should be understood as a domain decomposition with three non-overlapping subdomains. For the sake of convenience the velocity vector $\mathbf{u}=(u,v)$ is rewritten as a complex variable $U=u+iv$. Then the model problem reads

$$\left\{\begin{array}{rcll} \partial_t U_j + ifU_j - \partial_z\left(\nu_j(z,t)\partial_z U_j\right) &=& g_j, \quad (j=o,a) & \text{in } \Omega_j\times(0,T)\\ U_j(H_j,t) &=& U_j^\infty(t), & t\in(0,T),\\ U_j(z,0) &=& U_0(z), & \forall z \text{ in } \Omega_j,\\ \rho_o\nu_o\partial_z U_o(\delta_o,t) = \rho_a\nu_a\partial_z U_a(\delta_a,t) &=& \mathcal{F}_{\mathrm{sl}}(U_a(\delta_a,t)-U_o(\delta_o,t)), & t\in(0,T) \end{array}\right. \tag{6.1}$$

where $\rho_\mathrm{o},\rho_\mathrm{a}$ are the densities of water and air at the surface with $\frac{\rho_\mathrm{a}}{\rho_\mathrm{o}}\approx 10^{-3}$; the space domains are $\Omega_o=(H_o,\delta_o)$, $\Omega_a=(\delta_a,H_a)$, and $\mathcal{F}_{\mathrm{sl}}$ is a parameterization function for the surface layer extending over $\Omega_{\mathrm{sl}}=(\delta_o,\delta_a)$. A typical formulation for $\mathcal{F}_{\mathrm{sl}}$ is

$$\mathcal{F}_{\mathrm{sl}}(U_a(\delta_a,t)-U_o(\delta_o,t)) = \rho_a C_D|U_a(\delta_a,t)-U_o(\delta_o,t)|(U_a(\delta_a,t)-U_o(\delta_o,t))$$

which corresponds to a quadratic friction law with C_D a drag coefficient (assumed constant in the present study). Geostrophic winds and currents $u_G^a, u_G^o\in\mathbb{R}$ are used in this study as source terms and boundary conditions: $g_j=ifu_G^j$ and $U_j^\infty=u_G^j$. Geostrophic equilibrium is the steady state for which the Coriolis force compensates for the effects of gravity. It corresponds to the large scale dynamics of ocean and atmosphere, and leads to reasonable values of the solution U.

The well-posedness of (6.1) has been studied for a particular parameterization of ν_j in [Thery, 2021], where it is proved that its steady version admits a unique solution for realistic values of the parameters. The study of the nonstationary case is much more challenging:

numerical experiments tend to confirm this well-posedness and we give in Section 6.4.2 some elements for a theoretical proof. In the following, the viscosities ν_j are assumed to be constant.

6.3 Discretized coupled problem

6.3.1 Implementation of the surface layer

As described in Section 6.2, the full domain Ω is split into three parts: Ω_o in the ocean, Ω_a in the atmosphere and $\Omega_{\rm sl}$ a thin domain containing the interface (see Fig. 6.1). The role of $\Omega_{\rm sl}$ is to provide $\rho_j\nu_j\partial_z U_j$ at $z=\delta_j$ $(j=o,a)$ as a function of fluid velocities at the same locations. However, in state-of-the-art climate models, the discretization is based on an approximate form of the coupled problem (6.1). For practical reasons, the computational domains are $\widetilde{\Omega}_o = (H_o, 0) = \Omega_o \bigcup (\delta_o, 0)$ and $\widetilde{\Omega}_a = (0, H_a) = (0, \delta_a) \bigcup \Omega_a$, and the locations of the lower and upper boundaries of the surface layer $(z=\delta_j)$ are assimilated to the centers of the first grid cells (i.e. $\delta_o = -h_{\rm o}/2$ and $\delta_a = h_{\rm a}/2$ with $h_{\rm o}$ and $h_{\rm a}$ the thicknesses of the first grid cell in each subdomain), where the values of the velocity closest to the interface are available. Typical resolutions in the models are $\delta_a = h_{\rm a}/2 = 10$ m and $\delta_o = -h_{\rm o}/2 = -1$ m. At a discrete level, the transmission condition in (6.1) is replaced by

$$\rho_{\rm o}\nu_{\rm o}\partial_z U_{\rm o}(0,t) = \rho_{\rm a}\nu_{\rm a}\partial_z U_{\rm a}(0,t) = \rho_{\rm a}\alpha\left(U_{\rm a}\left(\frac{h_{\rm a}}{2},t\right) - U_{\rm o}\left(-\frac{h_{\rm o}}{2},t\right)\right) \tag{6.2}$$

where $\alpha = C_D\left|U_{\rm a}\left(\frac{h_{\rm a}}{2},t\right) - U_{\rm o}\left(-\frac{h_{\rm o}}{2},t\right)\right|$ for the *nonlinear* case. In the following, for the analysis in Section 6.5, we consider a *linear* friction where α is assumed constant and a quadratic friction *linearized* around equilibrium solutions. The coupled problem with this surface layer implementation reads:

$$\begin{array}{rcll} \partial_t U_j + if U_j - \partial_z\left(\nu_j(z,t)\partial_z U_j\right) &=& g_j, \quad (j=o,a) & \text{in } \widetilde{\Omega}_j \times (0,T) \\ U_j(H_j,t) &=& U_j^{\infty}(t), & t\in(0,T), \\ U_j(z,0) &=& U_0(z), & \forall z \text{ in } \widetilde{\Omega}_j, \\ \rho_j\nu_j\partial_z U_j(0,t) &=& \rho_{\rm a}\alpha\left(U_{\rm a}\left(\frac{h_{\rm a}}{2},t\right) - U_{\rm o}\left(-\frac{h_{\rm o}}{2},t\right)\right), & t\in(0,T) \end{array} \tag{6.3}$$

for which we will now define a Finite Difference discretization and a Schwarz Waveform Relaxation.

6.3.2 Schwarz Waveform Relaxation

As discussed for example in [Marti et al., 2021], current ocean-atmosphere coupling methods can actually be seen as a single iteration of a Schwarz Waveform Relaxation (SWR) algorithm. SWR applied to the coupling problem (6.3) with constant viscosity in each subdomain

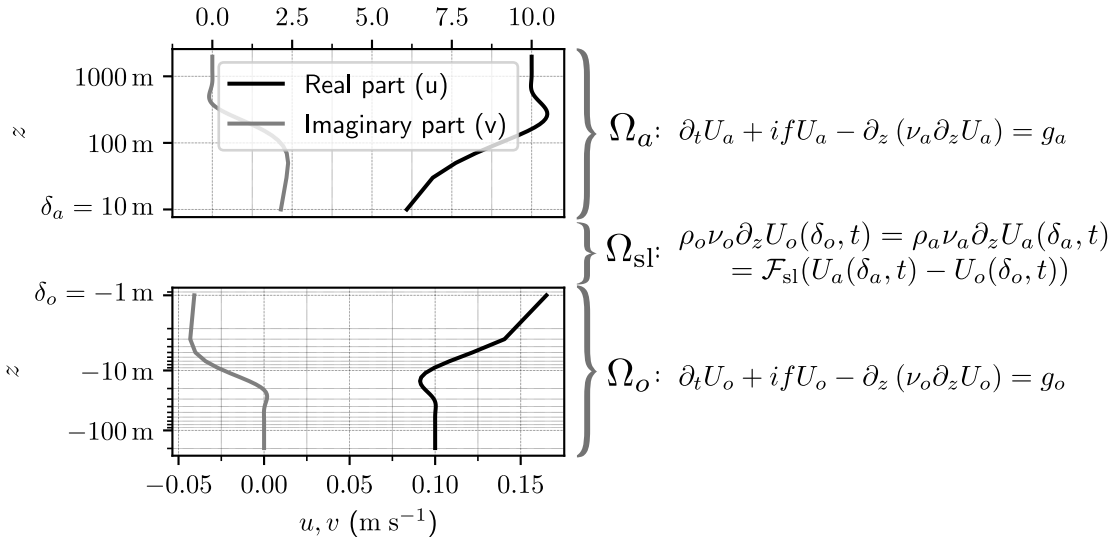

Figure 6.1: Discrete representation of the three domains $\Omega_a, \Omega_{\mathrm{sl}}, \Omega_o$ together with a typical steady state. Note the different scales for (u, v) in the ocean and in the atmosphere.

reads:

$$(\partial_t + if)U_j^k - \nu_j \partial_z \phi_j^k = g_j, \qquad \text{in } \widetilde{\Omega}_j \times (0,T) \tag{6.4a}$$

$$U_j^k(z,0) = U_0(z), \qquad \forall z \in \widetilde{\Omega}_j \tag{6.4b}$$

$$U_j^k(H_j,t) = U_j^\infty, \qquad t \in [0,T] \tag{6.4c}$$

$$\nu_{\mathrm{a}} \phi_{\mathrm{a}}^k(0,t) = \alpha^{k-1}\left(U_{\mathrm{a}}^{k-1+\theta}\left(\frac{h_{\mathrm{a}}}{2}, t\right) - U_{\mathrm{o}}^{k-1}\left(-\frac{h_{\mathrm{o}}}{2}, t\right)\right), \ t \in [0,T] \tag{6.4d}$$

$$\rho_{\mathrm{o}} \nu_{\mathrm{o}} \phi_{\mathrm{o}}^k(0,t) = \rho_{\mathrm{a}} \nu_{\mathrm{a}} \phi_{\mathrm{a}}^k(0,t), \qquad t \in [0,T] \tag{6.4e}$$

where $j = \mathrm{a}, \mathrm{o}$, $\phi_j = \partial_z U_j$, and $U_{\mathrm{a}}^{k-1+\theta} = \theta U_{\mathrm{a}}^k + (1-\theta) U_{\mathrm{a}}^{k-1}$ with θ a relaxation parameter (interpolation for $0 \leq \theta \leq 1$ or extrapolation for $\theta > 1$). At each iteration, (6.4e) ensures that the kinetic energy is conserved at the machine precision in the coupled system which is a major constraint for climate models. In (6.4d), the presence of the parameter θ makes it resemble to a Dirichlet-Neumann Waveform Relaxation algorithm. Indeed, if (6.4d) is replaced by $U_{\mathrm{a}}^k = \theta U_{\mathrm{o}}^{k-1} + (1-\theta) U_{\mathrm{a}}^{k-1}$ the DNWR algorithm is retrieved, as examined in the continuous case in [Gander et al., 2016] and in the discrete case in [Meisrimel et al., 2020]. However (6.4d) involves both ϕ_{a}^k and $U_{\mathrm{a}}^{k-1+\theta}$: the θ parameter appears thus here within a (close to Robin) condition $\nu_{\mathrm{a}} \phi_{\mathrm{a}}(0) - \alpha\theta U_{\mathrm{a}}(h_{\mathrm{a}}/2) = \ldots$, i.e. the relaxation is not performed directly on the converging variable which leads to convergence properties different from the DNWR case, as shown in Section 6.5. It is important to distinguish between the relaxation procedure described here and the choice of using an implicit or explicit interface condition discussed in Section 4.1.1. The latter refers to changing the time step t^n whereas the former

refers to choosing the iteration step k.

In the following, centered finite difference schemes in space are used with constant space steps h_j. Derivatives are approximated as $\phi_j(z,t) = \frac{U_j(z+h_j/2,t)-U_j(z-h_j/2,t)}{h_j}$ and the semi-discrete version of (6.4a) is

$$(\partial_t + if)U_{j,m+\frac{1}{2}}(t) = \nu_j \frac{\phi_{j,m+1}(t) - \phi_{j,m}(t)}{h_j} + g_j \tag{6.5}$$

6.4 Discrete steady state and well-posedness

In this section the focus is on the well-posedness of the semi-discrete coupled problem:

$$(\partial_t + if)U_{j,m+\frac{1}{2}} = \nu_j \frac{\phi_{j,m+1} - \phi_{j,m}}{h_j} + if u_G^j \tag{6.6a}$$

$$U_j|_{t=0} = U_0 \tag{6.6b}$$

$$U_j|_{z=H_j} = U_j^\infty \tag{6.6c}$$

$$\nu_{\mathrm{a}}\phi_{\mathrm{a},0} = C_D \left|U_{a,\frac{1}{2}} - U_{o,-\frac{1}{2}}\right| \left(U_{a,\frac{1}{2}} - U_{o,-\frac{1}{2}}\right) \tag{6.6d}$$

$$\rho_{\mathrm{o}}\nu_{\mathrm{o}}\phi_{\mathrm{o},0} = \rho_{\mathrm{a}}\nu_{\mathrm{a}}\phi_{\mathrm{a},0} \tag{6.6e}$$

[Lions et al., 1995] proved the existence at the continuous level of global-in-time weak solutions in two dimensions of the primitive equations with the nonlinearity of the advection inside the computational domains but with a linear interface condition. We focus here on showing the existence of strong unsteady solutions of the semi-discrete in space problem with a nonlinear interface condition. In [Chacon-Rebollo et al., 2014], the existence of unsteady solutions of nonlinear turbulent models for oceanic surface mixing layers is proven with the help of the inverse function theorem recalled here:

Inverse Function Theorem ([e.g. Hörmander, 2015]) *If a function* $\mathbf{\Phi}$ *is continuously differentiable and its derivative is invertible around some point* U^e *then* $\mathbf{\Phi}$ *is invertible in a neighborhood of* U^e.

We will follow their method which consists of three steps:

1. showing the existence of a steady state;
2. showing the well-posedness of the linearized problem around the steady state;
3. using of the inverse function theorem;

The previously cited studies use a continuous framework. Since we study here the semi-discrete in space well-posedness, the function spaces are not the same and some tools must be adapted (e.g. the variation of parameters in Appendix 6.A). However the steps of the proof remain the same.

6.4.1 Derivation of the steady state

The first step of the proof is the derivation of the steady state. The special case $f = 0$ is first set aside in §6.4.1.1; the steady states of the inner subdomains are then given in §6.4.1.2. Finally, the nonlinear boundary condition is treated in §6.4.1.3 and solutions are given in §6.4.1.4.

6.4.1.1 Special case $f = 0$

If we set to zero the Coriolis parameter, the steady state flux $\nu_j \phi_j$ is constant in each domain. If moreover $U_{\mathrm{a}}^{\infty} \neq U_{\mathrm{o}}^{\infty}$, because of the interface conditions, the derivatives ϕ_{a} and ϕ_{o} cannot be equal to zero and U_j are affine.

- With spatial domains of finite size: a steady state can be found following §6.4.1.3, except that U_j are affine.
- With spatial domains of infinite size: ϕ_j does not tend to zero for $z \to \pm\infty$ and we hence have that for $z \to \pm\infty$, $U_j \to \infty$. **There is no stationary solution with infinite domains for $f = 0$**[1]. Note that this is true for both semi-discrete and continuous cases.

In the remainder we consider $f \neq 0$ and we assume without loss of generality that the space domain is sufficiently large ($H_j \to \infty$): the results can be easily extended to domains of finite size.

6.4.1.2 Resolution in each subdomain

We note $U_j^e(z)$ the stationary solution (and ϕ_j^e its finite difference derivative) of (6.6). Computing U_j^e is similar to the discrete analysis of the finite difference scheme for Schwarz methods (see Chapter 2 or [Wu and Al-Khaleel, 2017]), except that:

- the frequency variable ω is not present;
- the transmission conditions are not required to be linear;
- since the source term does not vanish, the variable $U_o^e - u_G^o$ is considered to obtain the analytical expression of U_o^e.

We obtain $\phi_{\mathrm{o},-m}^e = A^e(\lambda_{\mathrm{o}} + 1)^m$ and $\phi_{\mathrm{a},m}^e = B^e(\lambda_{\mathrm{a}} + 1)^m$ with $\lambda_j = \frac{1}{2}\left(\chi_j - \sqrt{\chi_j}\sqrt{\chi_j + 4}\right)$, $\chi_j = \frac{ifh_j^2}{\nu_j}$ and m the space index.

[1] The existence of the stationary solution depends on the set of functions considered: there *exists* a stationary solution but it is not integrable or square-integrable.

Finally, the space discretization at the first grid level $\frac{h_j}{2}$ gives:

$$U_o^e|_{z=\delta_o} = u_G^o - \frac{\nu_o\lambda_o}{ifh_o}A^e, \qquad U_a^e|_{z=\delta_a} = u_G^a + \frac{\nu_a\lambda_a}{ifh_a}B^e \tag{6.7}$$

Remark ([Thery, 2021], §5.1.3, §5.1.4) *Similarly to the continuous case, the solution is of the form* $U_a^e|_{z=\delta_a} = u_G^a - u_\star^2 e_\tau \Psi_a$ *where* $u_\star^2 e_\tau = \nu_a \phi_a^e|_{z=\delta_a}$. *The difference stands in the discrete version of* $\Psi_j = -\frac{\lambda_j}{ifh_j}$ *which is simpler thanks to the hypotheses of constant diffusivities and infinite domains.*

6.4.1.3 The nonlinear transmission condition

The first condition of the bulk equation (6.6e) gives us $B^e = \frac{\rho_o\nu_o}{\rho_a\nu_a}A^e$ and the nonlinear condition (6.6d) gives

$$\frac{\rho_o\nu_o}{\rho_a C_D}A^e = \left|\left(\frac{\rho_o}{\rho_a}\frac{\nu_o\lambda_a}{ifh_a} + \frac{\nu_o\lambda_o}{ifh_o}\right)A^e + (u_G^a - u_G^o)\right|\left(\left(\frac{\rho_o}{\rho_a}\frac{\nu_o\lambda_a}{ifh_a} + \frac{\nu_o\lambda_o}{ifh_o}\right)A^e + (u_G^a - u_G^o)\right) \tag{6.8}$$

In order to lighten the notations we introduce $d = C_D\left(\frac{\lambda_a}{ifh_a} + \frac{\rho_a}{\rho_o}\frac{\lambda_o}{ifh_o}\right)$ and $\widetilde{x} = A^e\frac{\rho_o\nu_o}{\rho_a C_D}d + (u_G^a - u_G^o)$. $\widetilde{x}$ is the difference between the solutions U_j^e at interface and d is a quantity (in m^{-1}.s) that links $\widetilde{x}$ and $\rho_j\nu_j\phi_j^e(0)$. The problem is to find $\widetilde{x} \in \mathbb{C}$ such that

$$\widetilde{x} - (u_G^a - u_G^o) = d|\widetilde{x}|\widetilde{x} \tag{6.9}$$

Remark *If the infinite domains hypothesis is relaxed, equation (6.9) is retrieved with slightly different* $\widetilde{x}$ *and* d*; If* $f = 0$ *with finite domains we also obtain an equation of the form (6.9).*

Introducing the real and imaginary parts of $\widetilde{x} = \widetilde{x}_R + i\widetilde{x}_I$ and $d = d_R + id_I$, one gets:

$$\begin{aligned}\widetilde{x}_R &= |\widetilde{x}|(d_R\widetilde{x}_R - d_I\widetilde{x}_I) + u_G^a - u_G^o\\ \widetilde{x}_I &= |\widetilde{x}|(d_I\widetilde{x}_R + d_R\widetilde{x}_I)\end{aligned} \tag{6.10}$$

A combination (product with $\widetilde{x}_I, \widetilde{x}_R$) between those equations gives $d_I\,|\widetilde{x}|^3 = (u_G^a - u_G^o)\,\widetilde{x}_I$ which means that either $d_I = \widetilde{x}_I = 0$ or $d_I \neq 0$ and $\frac{u_G^a - u_G^o}{d_I}\widetilde{x}_I > 0$. From (6.9), $\widetilde{x}$ cannot be real because $u_G^a \neq u_G^o$ and d is not real. We get the equality $\widetilde{x}_I = \frac{d_I}{u_G^a - u_G^o}|\widetilde{x}|^3$. The system is hence equivalent to:

$$\begin{aligned}(1 - |\widetilde{x}|d_R)\,(u_G^a - u_G^o)\,\widetilde{x}_R &= -{d_I}^2|\widetilde{x}|^4 + (u_G^a - u_G^o)^2\\ |\widetilde{x}|^2 &= d_R|\widetilde{x}|^3 + (u_G^a - u_G^o)\,\widetilde{x}_R.\end{aligned} \tag{6.11}$$

$1 - |\widetilde{x}|d_R$ should not be zero as it would require that $u_G^a - u_G^o = \pm\frac{d_I}{d_R^2}$ (d does not depend on u_G^j and the latter values are arbitrarily chosen in this study: it is therefore unlikely that this equality holds). Eliminating $\widetilde{x}_R$ then leads to an equation on $|\widetilde{x}|$:

$$|\widetilde{x}|^2 - 2d_R|\widetilde{x}|^3 + |d|^2|\widetilde{x}|^4 = (u_G^a - u_G^o)^2 \tag{6.12}$$

A routine calculation finds 4 potential roots to this problem. Note that only the real positive roots are relevant. Typical values for our problem are $|d| \approx 10^{-1}$ m^{-1}.s and $d_R \approx -8 \times 10^{-2}$ m^{-1}.s. The solution is detailed below.

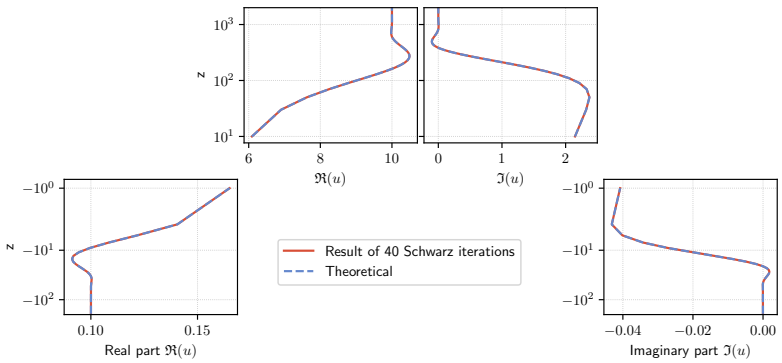

Figure 6.2: Stationary solution profile in ocean and atmosphere; the analysis exactly fits the result of Schwarz iterations. Notice that the surface layer is not explicitly computed. The profile is the same as in Figure 6.1.

6.4.1.4 Solutions

We define:

$$\begin{aligned} d &= C_D \left(\frac{\lambda_\mathrm{a}}{ifh_\mathrm{a}} + \frac{\rho_\mathrm{a}}{\rho_\mathrm{o}} \frac{\lambda_\mathrm{o}}{ifh_\mathrm{o}} \right), & d_R &= \mathfrak{R}(d), \\ s &= 2 + (u_G^\mathrm{a} - u_G^\mathrm{o})^2 \left(72|d|^2 - 108 d_R^2 \right), & \beta &= 1 - 12|d|^2 (u_G^\mathrm{a} - u_G^\mathrm{o})^2, \\ \gamma &= \frac{\sqrt[3]{s + \sqrt{s^2 - 4\beta^3}}}{3\sqrt[3]{2}|d|^2} + \frac{\sqrt[3]{2}\beta}{3|d|^2 \sqrt[3]{s + \sqrt{s^2 - 4\beta^3}}}, & \zeta &= -\frac{2}{3|d|^2} + \frac{{d_R}^2}{|d|^4} \end{aligned} \tag{6.13}$$

The steady state is given by a real, positive solution $|\widetilde{x}|$ of (6.12). Experimentally, it is seen that if it exists, it is the root of (6.12) corresponding to the three + operators in:

$$|\widetilde{x}| = \frac{d_R}{2|d|^2} \pm \frac{\sqrt{\zeta + \gamma}}{2} \pm \frac{1}{2} \sqrt{2\zeta - \gamma \pm \frac{2{d_R}^3 - 2d_R|d|^2}{|d|^6 \sqrt{\zeta + \gamma}}} \tag{6.14}$$

where the first $\pm$ and the third one are necessarily the same. For our parameters there is only one value of (6.14) that is real and non-negative. There is hence only one solution of (6.6).

Finally, we recover $\widetilde{x}$ from (6.9): $\widetilde{x} = \frac{u_G^{\mathrm{a}} - u_G^{\mathrm{o}}}{1 - d|\widetilde{x}|}$, then $A^e = \frac{C_D \rho_{\mathrm{a}}}{\rho_{\mathrm{o}} \nu_{\mathrm{o}} d} \left(\widetilde{x} - (u_G^{\mathrm{a}} - u_G^{\mathrm{o}})\right)$ and $B^e = \frac{\rho_{\mathrm{o}} \nu_{\mathrm{o}}}{\rho_{\mathrm{a}} \nu_{\mathrm{a}}} A^e$. The steady state U_j^e is given by

$$\begin{aligned} U^e_{\mathrm{o},-m-1/2} &= u_G^o - \frac{\nu_o \lambda_o}{if h_o}(1+\lambda_o)^m A^e \\ U^e_{\mathrm{a},m+1/2} &= u_G^a + \frac{\nu_a \lambda_a}{if h_a}(1+\lambda_a)^m B^e \end{aligned} \tag{6.15}$$

Figure 6.2 shows that this analysis exactly fits the result of Schwarz algorithm.

6.4.2 Existence of solutions of the nonlinear semi-discrete in space problem

The method used by [Chacon-Rebollo et al., 2014] to prove the existence and unicity of a solution in the neighborhood of a steady state can be used to deal with other types of nonlinearities. In particular, we can prove the existence and uniqueness of a solution to the problem (6.6) close to the steady state, thanks to the following steps:

1. The existence of a steady state U^e is discussed in §6.4.1.
2. The well-posedness of the linearized problem is discussed in Appendix 6.A.
3. The use of the inverse function theorem can be done in four steps:
   (a) concatenate the state vectors in a single vector $\mathbf{U} = \{U_a, U_o, \phi_a|_{z=0}\} \in \mathcal{U}$ where $\mathcal{U} = L^2([0,T])^{M_a+M_o+1}$. M_a, M_o are the number of grid levels in the subdomains. $\phi_a|_{z\neq 0}$ and ϕ_o are not in $\mathbf{U}$ because they can be expressed as linear combinations of elements of $\mathbf{U}$.
   (b) Define a mapping $\mathbf{\Phi} : \mathcal{U} \to \mathbf{Y}$ such that

$$\begin{aligned} \mathbf{\Phi}(\mathbf{U}) = \{&(\partial_t + if)U_a - \nu_a \partial_z \phi_a - g_a, \\ &(\partial_t + if)U_o - \nu_o \partial_z \phi_o - g_o, \\ &U_a(H_a, t) - U_a^\infty, \quad U_o(H_o, t) - U_o^\infty, \\ &\nu_{\mathrm{a}}\, \phi_{\mathrm{a}}|_{z=0} - \alpha \left(U_{\mathrm{a},\frac{1}{2}} - U_{\mathrm{o},-\frac{1}{2}}\right), \\ &U_a|_{t=0} - U_a^e, \quad U_o|_{t=0} - U_o^e\} \end{aligned} \tag{6.16}$$

   where $\phi_j|_{z\neq 0} = \partial_z U_j$ and ∂_z is to be understood as the finite difference operator which is applied only where it makes sense: for instance the first line of (6.16) is not applied for $z = H_a$. Let us draw some important remarks about $\mathbf{\Phi}$:
   - The equation $\phi_o = \frac{\rho_a \nu_a}{\rho_o \nu_o} \phi_a$ at interface is implicit: in (6.16), $\partial_z \phi_{\mathrm{o}}$ at the first grid level is $\frac{\rho_a \nu_a}{\rho_o \nu_o} \phi_{\mathrm{a}}\Big|_{z=0} - \frac{U_{\mathrm{o},-\frac{1}{2}} - U_{\mathrm{o},-\frac{3}{2}}}{h_{\mathrm{o}}}$.

- $\mathbf{\Phi}(\mathbf{U}^e) = 0$ where $\mathbf{U}^e$ is the steady state;
- The codomain $\mathbf{Y}$ is

$$\mathbf{Y} = L^2([0,T])^{M_a-1} \times L^2([0,T])^{M_o-1} \times L^2([0,T])^3 \times \mathbb{R}^{M_a+M_o} \tag{6.17}$$

- Finding $\mathbf{\Phi}^{-1}(y)$ is equivalent to solving the nonlinear semi-discrete problem (6.6) if the component of y corresponding to the interface condition is zero (the other components correspond to other forcing terms, boundary conditions and initial condition.). The idea of the proof is that if $\mathbf{\Phi}$ is invertible around $\mathbf{U}^e$ then the nonlinear semi-discrete problem (6.6) is invertible. Moreover, the inverse function theorem also tells us that $\mathbf{\Phi}^{-1}$ is continuous: this means that around the equilibrium state, the problem (6.6) is well-posed: it has a unique solution that depends continuously on the initial data.

(c) Prove that $\mathbf{\Phi}$ is C^1 in a neighborhood of $\mathbf{U}^e$. $\mathbf{\Phi}$ is linear except for the transmission condition. Besides, the nonlinearity in this transmission condition is the function $x \mapsto |x|x$, which is analytic in a ball that does not contain zero. It is then straightforward to show that $\mathbf{\Phi}$ is C^1 and that its differential $D\mathbf{\Phi}(\mathbf{U}^e)$ is given by the linearized problem (a rigourous proof that can be directly adapted here is given in [Chacon-Rebollo et al., 2014]).

(d) Prove that $D\mathbf{\Phi}(\mathbf{U}^e)$ is an isomorphism: $D\mathbf{\Phi}(\mathbf{U}^e)$ can be inverted by solving the linearized problem with additional input data. It is shown that it is well-posed in appendix 6.A.

6.5 Convergence analysis

In this section we conduct a convergence analysis of the SWR algorithm (6.4) first with α a constant and then in a more complicated case where the problem is linearized around its steady state. In the following we systematically make the assumption that the space domain is of infinite size (i.e. $H_j \to \infty$) for the sake of simplicity.

6.5.1 Linear friction case ($\alpha = \text{const}$)

We assume in this paragraph that $\alpha = \alpha_c$ with α_c a constant independent of U_j and we study the system satisfied by the errors (i.e. $g_j, U_0, U^\infty = 0$). The Fourier transform in time of the finite difference scheme (6.5), together with an analysis of the convergence as it was done in Chapters 2 and 3 (see Appendix 6.B for a detailed derivation in the linearized case) leads to $\widehat{u}^k_{\mathrm{o},-m-\frac{1}{2}} = A_k(\lambda_\mathrm{o}+1)^m$ and $\widehat{u}^k_{\mathrm{a},m+\frac{1}{2}} = B_k(\lambda_\mathrm{a}+1)^m$ with $\lambda_j = \frac{1}{2}\left(\chi_j - \sqrt{\chi_j}\sqrt{\chi_j+4}\right)$, $\chi_j = \frac{i(\omega+f)h_j^2}{\nu_j}$, and m the space index. The convergence factor of SWR is then the rate at which A_k or B_k tends to 0. The Fourier transform in time of the interface transmission

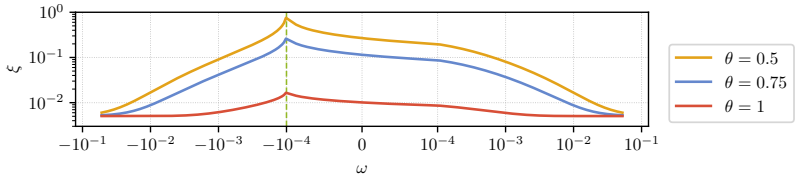

Figure 6.3: Convergence factor $\xi(\omega)$ in the linear case for $\theta = 0.5, 0.75, 1$. The vertical dashed line highlights the frequency for which $\omega + f \to 0$.

conditions gives the evolution of B_k which eventually leads to the following convergence factor:

$$\xi = \left| \frac{B_k}{B_{k-1}} \right| = \left| \frac{1 - \theta - \epsilon \frac{\lambda_a - \chi_a}{\lambda_o} \frac{\nu_a h_o}{\nu_o h_a}}{\frac{\nu_a}{\alpha_c h_a} (\lambda_a - \chi_a) - \theta} \right| \tag{6.18}$$

where $\epsilon = \frac{\rho_a}{\rho_o} \approx 10^{-3}$ in the ocean-atmosphere context. Note that the convergence factor (6.18) differs significantly from the semi-discrete convergence factor

$$\xi_{\text{DNWR}} = |1 - \theta_{\text{DNWR}} (1 - \epsilon h_a \lambda_o / (\lambda_a h_o))| \tag{6.19}$$

of the DNWR algorithm. Moreover, λ_j is equivalent to $-\sqrt{\chi_j}$ when $(\omega + f) \to 0$, and as $(\omega + f) \to \infty$ we have $\lambda_j \to -1$ and $|\lambda_a - \chi_a| \to \infty$. The asymptotes of ξ for$(\omega + f) \to 0$ and $(\omega + f) \to \infty$ are finally

$$\lim_{(\omega+f)\to 0} \xi = \frac{1}{\theta} \left| 1 - \theta - \epsilon \sqrt{\frac{\nu_a}{\nu_o}} \right| = \xi_0, \qquad \lim_{(\omega+f)\to\infty} \xi = \epsilon \frac{\nu_a h_o}{\nu_o h_a}.$$

As $\omega + f \to 0$ the asymptotic value ξ_0 depends on θ: it is $+\infty$ for $\theta = 0$ (i.e. a fast divergence), and $\xi_0 = \epsilon \sqrt{\frac{\nu_a}{\nu_o}}$ for $\theta = 1$. When $\omega \to \infty$, the convergence factor tends to a small value that does not depend on θ (i.e. the convergence is rather fast for high frequencies). Since we have $\epsilon \approx 10^{-3}$, the convergence is fast for $\theta = 1$. On the contrary, $\xi_0 \to \infty$ for $\theta = 0$ with almost all parameter values: the Schwarz method quickly diverges in this case. The optimal parameter θ_{opt} for low frequencies is $1 - \epsilon \sqrt{\frac{\nu_a}{\nu_o}}$ which is very close to 1.

Remark *The asymptotes are different in [Clement et al., 2021]. The mistake made in the authors' previous work is to consider for $\omega + f \to 0$ the convergence factor of $(\phi_k)_{k\in\mathbb{N}}$. Since $\phi_k \to 0$ as $\omega + f \to 0$ there is an underlying division by zero.*

Figure 6.3 shows that the asymptote $\omega + f \to 0$ is the upper bound of ξ for several values of θ. In this linear case, $\theta \approx 1$ is a good choice to reduce the convergence factor.

6.5.2 Linearized quadratic friction case

The analysis of the nonlinear quadratic friction case (i.e. with $\alpha = C_D \,|\, U_a (h_a/2, t) - U_o (-h_o/2, t) \,|$) cannot be directly pursued through a Fourier transform. We thus consider

the linearization of the problem around a steady state U_j^e, ϕ_j^e satisfying (6.6): assuming that $U_j^k(\pm h_j/2, t)$ is in a neighborhood of $U^e(\pm h_j/2)$, the modulus in α is non-zero and we can differentiate α. Differences with the steady state are noted $\delta\phi_j^k = \phi_j^k(0,t) - \phi_j^e(0)$ and $\delta U_j^k = U_j^k(\pm h_j/2, t) - U_j^e(\pm h_j/2)$.

Linearization of the transmission condition We will now linearize the transmission operator. First, $\alpha^{k-1}\left(\delta U_a^{k-1+\theta} - \delta U_o^{k-1}\right)$ is split into two parts in the nonlinear transmission condition:

$$\nu_a \phi_a^k = \underbrace{\alpha^{k-1}\left((U_{\mathrm{a}}^e - U_{\mathrm{o}}^e) + \left(\delta U_a^{k-1} - \delta U_o^{k-1}\right)\right)}_{C_D|\cdot|(\cdot)} + \theta\alpha^{k-1}\left(\delta U_a^k - \delta U_a^{k-1}\right) \tag{6.20}$$

The transmission condition is linearized as

$$\nu_a \delta\phi_a^k = \left\langle D_{(U_{\mathrm{a}}^e - U_{\mathrm{o}}^e)} C_D|\cdot|(\cdot), \left(\delta U_{\mathrm{a}}^{k-1} - \delta U_{\mathrm{o}}^{k-1}\right)\right\rangle + \theta\alpha^{k-1}\left(\delta U_a^k - \delta U_a^{k-1}\right) \tag{6.21}$$

where the linear map $\langle D_x\Upsilon, \cdot\rangle$ is the total derivative of the application Υ at x. Let us first compute the total derivative of $x \mapsto |x|x$. The total derivative of $|\cdot|^2$ is

$$\langle D_x|\cdot|^2, \mu\rangle = \overline{x}\mu + x\overline{\mu} \tag{6.22}$$

where $\overline{x}$ is the complex conjugate of x. We then use the chain rule to differentiate $|x| = \sqrt{|x|^2}$ and obtain

$$\langle D_x|\cdot|, \mu\rangle = \frac{1}{2}\frac{\overline{x}}{|x|}\mu + \frac{1}{2}\frac{x}{|x|}\overline{\mu} \tag{6.23}$$

Finally, the total derivative of the map $x \mapsto |x|x$ reads

$$\langle D_x|\cdot|(\cdot), \mu\rangle = \frac{1}{2}\underbrace{\frac{\overline{x}x}{|x|}}_{=|x|}\mu + \frac{1}{2}\underbrace{\frac{x^2}{|x|}}_{=|x|\frac{x}{\overline{x}}}\overline{\mu} + |x|\mu = |x|\left(\frac{3}{2}\mu + \frac{1}{2}\frac{x}{\overline{x}}\overline{\mu}\right) \tag{6.24}$$

and the linearized transmission operator reads

$$\nu_{\mathrm{a}}\delta\phi_{\mathrm{a}}^k = \alpha^e\left(\left(\frac{3}{2} - \theta\right)\delta U_{\mathrm{a}}^{k-1} + \theta\,\delta U_{\mathrm{a}}^k - \frac{3}{2}\delta U_{\mathrm{o}}^{k-1} + \frac{1}{2}\frac{U_{\mathrm{a}}^e - U_{\mathrm{o}}^e}{\overline{U_{\mathrm{a}}^e - U_{\mathrm{o}}^e}}\overline{\delta U_{\mathrm{a}}^{k-1} - \delta U_{\mathrm{o}}^{k-1}}\right) \tag{6.25}$$

with $\alpha^e = C_D\,|U_{\mathrm{a}}^e(h_{\mathrm{a}}/2) - U_{\mathrm{o}}^e(-h_{\mathrm{o}}/2)|$.

Convergence study with the linearized transmission condition Following the derivation in the previous paragraph (detailed in Appendix 6.B with space domains of finite size), we find that the evolution of B_k is:

$$B_{k+1}(\omega) = a_1(\omega)B_k(\omega) + a_2(\omega)\overline{B_k(-\omega)} \tag{6.26}$$

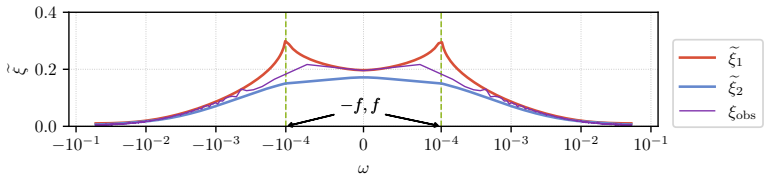

Figure 6.4: Singular values $\widetilde{\xi}_1(\omega)$, $\widetilde{\xi}_2(\omega)$ of the matrix $\begin{pmatrix} \frac{a_1(\omega)}{a_2(-\omega)} & \frac{a_2(\omega)}{a_1(-\omega)} \end{pmatrix}$. The observed "convergence factor" at the first iteration $\xi_{\text{obs}} = \sqrt{\frac{|B_2(\omega)|^2+|B_2(-\omega)|^2}{|B_1(\omega)|^2+|B_1(-\omega)|^2}}$ is in purple. The numerical validation ξ_{obs} fits the convergence analysis since $\widetilde{\xi}_2 \leq \xi_{\text{obs}} \leq \widetilde{\xi}_1$: Figure 6.5 explains that it is theoretically the case.

where $a_1, a_2 \in \mathbb{C}$ are defined in Appendix 6.B. Note that the variable $\overline{i\omega} = -i\omega$ appears when using the Fourier transform on $\overline{\delta U_a^{k-1} - \delta U_o^{k-1}}$. As a consequence, the convergence factor ξ^q in the linearized quadratic friction case differs from one iteration to another: it is a function of $\frac{\overline{B_{k-1}(-\omega)}}{B_{k-1}(\omega)}$. We need to look at both $B_{k+1}(\omega), \overline{B_{k+1}(-\omega)}$ at the same time:

$$\begin{aligned} B_{k+1}(\omega) &= a_1(\omega)B_k(\omega) + a_2\overline{B_k(-\omega)} \\ \overline{B_{k+1}(-\omega)} &= \overline{a_1(-\omega)B_k(-\omega) + a_2(-\omega)\overline{B_k(\omega)}} \end{aligned} \tag{6.27}$$

We examine the evolution of those two simultaneously evolving quantities:

$$\begin{pmatrix} B(\omega) \\ \overline{B(-\omega)} \end{pmatrix}_{k+1} = \begin{pmatrix} a_1(\omega) & a_2(\omega) \\ \overline{a_2(-\omega)} & \overline{a_1(-\omega)} \end{pmatrix} \begin{pmatrix} B(\omega) \\ \overline{B(-\omega)} \end{pmatrix}_k \tag{6.28}$$

The singular values (shown in Figure 6.4) of the 2×2 matrix in (6.28) can be studied instead of the convergence factor. One can see on Figure 6.4 that the two singular values are different for small frequencies, especially around the frequencies f and $-f$.

One can hence expect (see Figure 6.5) that for frequencies close to f and $-f$ the "convergence factor" $\sqrt{\frac{|B_k(\omega)|^2+|B_k(-\omega)|^2}{|B_{k-1}(\omega)|^2+|B_{k-1}(-\omega)|^2}}$ will be different from one iteration to another and will be between $\widetilde{\xi}_1$ and $\widetilde{\xi}_2$.

We optimize only the maximum over the frequencies of the largest singular value $\widetilde{\xi}_1$ (see Figure 6.6) and find that the optimal value of θ is slightly smaller than 1.5 (instead of an optimal value slightly larger than 1.5 for the asymptotic convergence for one iteration)

6.6 Numerical experiments

The aim of this section is to illustrate the influence of the parameter θ, in the linear and quadratic friction cases. The steady state U_j^e is used to compute $\alpha_c = \alpha^e = C_D|U_{\text{a}}^e(\frac{h_{\text{a}}}{2}) -$

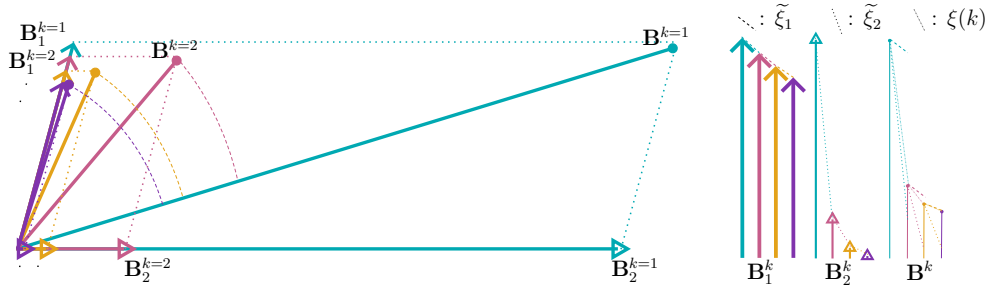

Figure 6.5: The vector $\mathbf{B}^k = \begin{pmatrix} B_k(\omega) \\ \overline{B_k(-\omega)} \end{pmatrix}$ can be decomposed into a basis[2] of eigenvectors $\mathbf{B}_i^k$ which converge linearly with convergence factors $\widetilde{\xi}_i$. 4 iterations are shematically represented in blue, pink, orange and purple. The "convergence factor" $\xi_{\text{obs}}(k) = \frac{||\mathbf{B}^{k+1}||}{||\mathbf{B}^k||}$ is such that $\widetilde{\xi}_2 \leq \xi_{\text{obs}} \leq \widetilde{\xi}_1$ and varies from one iteration to another. $\xi(k)$ gets closer to $\widetilde{\xi}_1$ when k increases as $\mathbf{B}^k$ gets closer to $\mathbf{B}_1^k$.

$U_{\text{o}}^e(\frac{h_{\text{o}}}{2})|$ in the linear case. Parameter values of the problem are taken as realistic: $C_D = 1.2 \times 10^{-3}$, the space steps are $\frac{h_{\text{a}}}{2} = 10$ m, $\frac{h_{\text{o}}}{2} = 1$ m, the time step is 60 s, the size of the time window T is 1 day ($1440\Delta t$) and the computational domains sizes are $H_o = H_a = 2000$ m (100 and 1000 nodes respectively in Ω_a and Ω_o). The Coriolis parameter is $f = 10^{-4}$ s^{-1} and the diffusivities are $\nu_{\text{a}} = 1$ m^2 s^{-1}, $\nu_{\text{o}} = 3 \times 10^{-3}$ m^2 s^{-1}. The geostrophic wind and current $u_G^j = U_j^\infty$ are set to constant values of 10 m s^{-1} in the atmosphere and 0.1 m s^{-1} in the ocean, while the forcing terms $g_j = ifu_G^j$ and the initial condition $U_0(z) = U_j^e(z)$. SWR is initialized at the interface with a white noise around the interface value of the initial condition. Figure 6.7 shows the evolution of the error for two choices of θ. The theoretical convergence according is also displayed: $\sup_\omega \xi$ is an upper bound of the L^2 convergence factor [Thery, 2021]. In the case $\alpha = \text{const}$ we use ξ_0 as an approximation of $\sup_\omega \xi$. The theoretical bounds $\max_\omega \widetilde{\xi}_1$ and ξ_0 fit rather accurately the convergence rate and one can see that those values are indeed greater than the observed convergence rate. Figure 6.7 confirms the results of Section 6.5: when considering $\alpha = \alpha_c$ constant, the fastest convergence is achieved when θ is close to 1, similarly to the DNWR algorithm. However this does not translate into the nonlinear case, which converges faster with $\theta = 1.5$. Figure 6.8 shows that the convergence behavior with the linearized transmission condition is similar to the nonlinear case. As expected the convergence is faster for $\theta = 1.5$ than for $\theta = 1$. We observed that those results are robust to changes in the values of the parameters in the range of interest. Linearized transmission conditions are hence relevant to study theoretically the convergence properties of our nonlinear problem.

[2] The matrix is indeed diagonalizable if $\widetilde{\xi}_1 \neq \widetilde{\xi}_2$; otherwise we have a simple convergence factor $\xi = \widetilde{\xi}_1 = \widetilde{\xi}_2$.

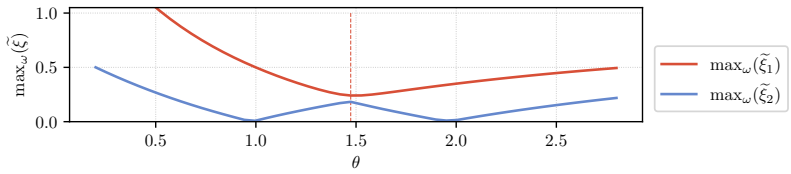

Figure 6.6: Singular values $\widetilde{\xi}_1, \widetilde{\xi}_2$ of $\begin{pmatrix} \dfrac{a_1(\omega)}{a_2(-\omega)} & \dfrac{a_2(\omega)}{a_1(-\omega)} \end{pmatrix}$ maximized over the set of discrete frequencies $\{-\frac{\pi}{\Delta t}, ..., \frac{\pi}{T}, 0, \frac{\pi}{T}, ..., \frac{\pi}{\Delta t}\}$. The vertical dashed line highlights the minimum of $\max \widetilde{\xi}_1$. The windows length T is one day and $\Delta t = 60$ s .

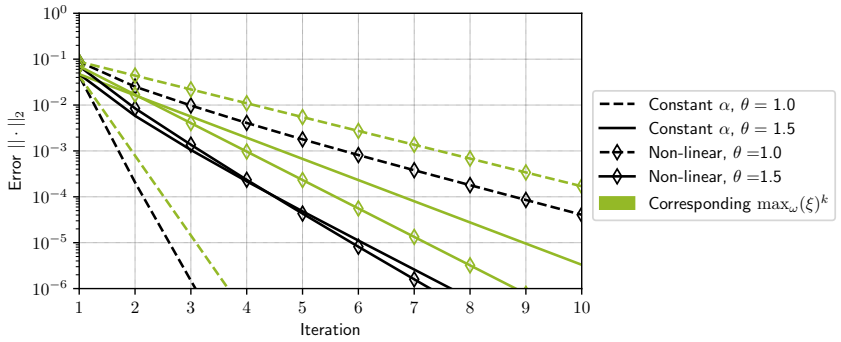

Figure 6.7: Evolution of the L^2 norm of the errors. Black lines represent the observed convergence; grey lines are the estimated convergence with slopes ξ_0 for linear cases and $\max_\omega \widetilde{\xi}_1$ for quadratic cases.

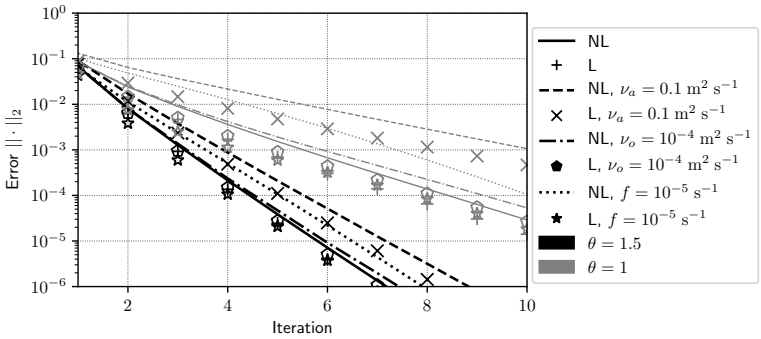

Figure 6.8: Evolution of the L^2 norm of the errors with linearized (L) and nonlinear (NL) transmission conditions. The legend indicates the changes in the parameters for each case.

6.7 Conclusion

In this chapter, we studied a SWR algorithm applied to a simplified ocean-atmosphere problem. This problem considers nonlinear transmission conditions arising from wall laws representative of the ones used in Earth-System Models and analogous to a quadratic friction law. We motivated the fact that the convergence analysis of such problems can only be done at a semi-discrete level in space due to the particular practical implementation of continuous interface conditions in actual climate models. The steady state of the coupled problem was derived analytically and it was proven that the unsteady problem is well-posed in a neighborhood of the steady state. Then we analytically studied the convergence properties in a case with linear friction and in a case with linearized quadratic friction. We formulated the problem with a relaxation parameter θ in the transmission conditions and systematically assessed its impact on the convergence speed. For the two cases of interest, the convergence factors were derived which allowed us to choose appropriate values for the parameter θ to guarantee fast convergence of the algorithm. The behavior of the algorithm for linear friction and linearized quadratic friction turns out to be different which leads to different "optimal" values of θ. Numerical experiments in the nonlinear case showed that the observed convergence behaves as predicted by the linearized quadratic friction case.

6.A Appendix: well-posedness of the linearized quadratic friction case

We look for the solutions of the Laplace transform (with the frequency variable $s = \sigma + i\omega, \sigma > 0$) of our coupled problem (the steady state has been subtracted from u):

$$(s+if)\widehat{u}_{m+\frac{1}{2}} - \nu_j \frac{\widehat{\phi}_{m+1} - \widehat{\phi}_m}{h_j} = U_0 \qquad \omega \in (\omega_{\min}, \omega_{\max}) \tag{6.29a}$$

$$u_m(t=0) = U_0(z_m), \qquad \forall m, M_o \leq m \leq M_a \tag{6.29b}$$

$$\widehat{u}(H_j, s) = 0, \qquad \omega \in (\omega_{\min}, \omega_{\max}) \tag{6.29c}$$

$$\frac{3\alpha^e}{2}\left(\widehat{u}_{1/2} - \widehat{u}_{-1/2} + \frac{\mathcal{O}}{3}\overline{\widehat{u}_{1/2}(\overline{s}) - \widehat{u}_{-1/2}(\overline{s})}\right) = \nu_{\mathrm{a}}\widehat{\phi}_{\mathrm{a},0}, \qquad \omega \in (\omega_{\min}, \omega_{\max}) \tag{6.29d}$$

$$\rho_{\mathrm{o}}\nu_{\mathrm{o}}\widehat{\phi}_{\mathrm{o},0} = \rho_{\mathrm{a}}\nu_{\mathrm{a}}\widehat{\phi}_{\mathrm{a},0}, \qquad \omega \in (\omega_{\min}, \omega_{\max}) \tag{6.29e}$$

where $\mathcal{O} = \frac{U^e_{\mathrm{a}} - U^e_{\mathrm{o}}}{U^e_{\mathrm{a}} - U^e_{\mathrm{o}}}$.

Remark *To show the well-posedness of the non-linear problem, it is necessary to add external data that does not depends on $\widehat{u}$ in (6.29c) and (6.29d). It only complicates the derivation and does not need any special treatment: we hence omit them.*

To show that there exists a unique solution to (6.29), we first compute the jump $\widehat{u}_{1/2} - \widehat{u}_{-1/2}$ then prove that the friction law always has a unique solution.

6.A.1 Jump of the solution $\widehat{u}_{1/2} - \widehat{u}_{-1/2}$

We first compute the jump of the solution $\widehat{u}_{1/2} - \widehat{u}_{-1/2}$.

Remark *If a Fourier transform was used (corresponding to $\sigma = 0$), the case $\omega = -f$ would require a particular attention as $\lambda_u^{-1} - \lambda_u$ would attain 0.*

We extend the well-known method of variation of parameters to the discrete case to compute a solution of (6.29a). Let B_m^1, B_m^2 and λ_u such that the solutions of (6.29a) are $\widehat{u}_{a,m+\frac{1}{2}} = B_m^1 \lambda_u^m + B_m^2 \lambda_u^{-m}$, where $\lambda_u = 1 + \frac{\chi_2}{2} - \frac{1}{2}\sqrt{\chi_2}\sqrt{\chi_2 + 4}$ and $\chi_j = h_j^2 \frac{s+if}{\nu_j}$. Note that it it similar to the solution of the homogeneous equation but B^1, B^2 now depend on m. Equation (6.29a) can be rewritten as

$$(\widehat{u}_{m+\frac{3}{2}} - \widehat{u}_{m+\frac{1}{2}}) - \chi_2 \widehat{u}_{m+\frac{1}{2}} - (\widehat{u}_{m+\frac{1}{2}} - \widehat{u}_{m-\frac{1}{2}}) = -\frac{h_2^2}{\nu_2} U_0 \tag{6.30}$$

Injecting $\widehat{u}_{m+\frac{1}{2}} = B_m^1 \lambda_u^m + B_m^2 \lambda_u^{-m}$ and rearranging terms gives

$$\begin{aligned} & B_m^1 \underbrace{\left(\lambda_u^{m+1} - \lambda_u^m - \chi_2 \lambda_u^m - (\lambda_u^m - \lambda_u^{m-1})\right)}_{=0} \qquad + B_m^2 \times 0 \\ & + \lambda_u^{m+1}(B_{m+1}^1 - B_m^1) - \lambda_u^m (B_m^1 - B_{m-1}^1) \quad + \lambda_u^{-m-1}(B_{m+1}^2 - B_m^2) - \lambda_u^{-m}(B_m^2 - B_{m-1}^2) \\ & + (\lambda_u^m - \lambda_u^{m-1})(B_m^1 - B_{m-1}^1) \qquad + (\lambda_u^{-m} - \lambda_u^{-m+1})(B_m^2 - B_{m-1}^2) \\ & \qquad = -\frac{h_2^2}{\nu_2} U_0 \end{aligned} \tag{6.31}$$

A particular solution of (6.29a) can be taken as

$$\begin{cases} \lambda_u^m (B_m^1 - B_{m-1}^1) + \lambda_u^{-m}(B_m^2 - B_{m-1}^2) & = 0 \\ (\lambda_u^m - \lambda_u^{m-1})(B_m^1 - B_{m-1}^1) + (\lambda_u^{-m} - \lambda_u^{-m+1})(B_m^2 - B_{m-1}^2) & = -\frac{h_2^2}{\nu_2} U_0 \end{cases} \tag{6.32}$$

which can be inverted:

$$\begin{pmatrix} B_m^1 - B_{m-1}^1 \\ B_m^2 - B_{m-1}^2 \end{pmatrix} = \begin{pmatrix} \lambda_u^m & \lambda_u^{-m} \\ (\lambda_u^m - \lambda_u^{m-1}) & (\lambda_u^{-m} - \lambda_u^{-m+1}) \end{pmatrix}^{-1} \begin{pmatrix} 0 \\ \frac{h_2^2}{\nu_2} - U_0 \end{pmatrix} \tag{6.33}$$

The determinant of the inverse matrix in (6.33) is $\lambda_u^{-1} - \lambda_u$ which is never zero because $\sigma > 0$.

Remark *A particular solution was chosen here: as in the continuous case of the variation of parameters, the difference between this solution and another one solves the homogeneous equation. The degrees of freedom B_0^1 and B_0^2 actually represent the whole space of solutions.*

The sum of (6.33) from 1 to m gives a relation between B_m^1, B_m^2 and B_0^1, B_0^2 with the parameters λ_u, $\frac{h_2^2}{\nu_2}U_0$ and m. Showing that B_0^1, B_0^2 are uniquely determined is hence sufficient to show that there is a unique solution $\widehat{u}$ in the atmosphere.

Let us note $\begin{pmatrix} B_m^1 \\ B_m^2 \end{pmatrix} := \begin{pmatrix} B_0^1 + S_m^1(U_0) \\ B_0^2 + S_m^2(U_0) \end{pmatrix}$. The vector $\begin{pmatrix} S_m^1(U_0) \\ S_m^2(U_0) \end{pmatrix}$ is the sum of the right hand side of (6.33) from 1 to m. It makes the link between B_0^1, B_0^2 and B_m^1, B_m^2 but will not affect the presence of a unique solution for B_0^1, B_0^2.

Remark *All the variables S in the following will not be used to determine the existence of a unique solution $\widehat{u}$.*

The Dirichlet boundary condition at $H_a = (M_a + \frac{1}{2})h_a$ is equivalent to $B_{M_a}^1(\lambda_u)^{2M_a} = -B_{M_a}^2$ which determines B_0^2:

$$-B_0^2 = \left(S_{M_a}^1(U_0) + B_0^1\right)(\lambda_u)^{2M_a} + S_{M_a}^2(U_0) \tag{6.34}$$

We hence only need the sole value of B_0^1 to characterize $\widehat{u}$. In particular, the variable $\widehat{u}_{\frac{1}{2}}$ used in the linearized transmission condition reads

$$\widehat{u}_{\frac{1}{2}} = B_0^1(1 - \lambda_u^{2M_a}) + \underbrace{S_0^1 + S_0^2 - S_{M_a}^1\lambda_u^{2M_a} - S_{M_a}^2}_{:=S_{u,a}^{m=1/2}(U_0)} \tag{6.35}$$

To obtain the derivative at interface $\widehat{\phi}_{a,0}$ (6.29a) is used at the first grid level:

$$\chi_a\widehat{u}_{\frac{1}{2}} = \widehat{u}_{\frac{3}{2}} - \widehat{u}_{\frac{1}{2}} - h_a\widehat{\phi}_{a,0} + \frac{h_a^2}{\nu_a}U_0 \tag{6.36}$$

Those equations give

$$\begin{aligned}\widehat{\phi}_{a,0} =& B_0^1 \underbrace{\frac{1}{h_a}\left(\lambda_u - \lambda_u^{2M_a-1} - (\chi_a+1)(1-\lambda_u^{2M_a})\right)}_{:=K_{1,a}} \\ &\underbrace{- \frac{1}{h_a}\left((\chi_a+1)S_{u,a}^{m=1/2} - S_{u,a}^{m=3/2} - \frac{h_a^2}{\nu_a}U_0\right)}_{:=S_{\phi,a}^{m=0}}\end{aligned} \tag{6.37}$$

We obtain similar equations in the ocean part:

$$\begin{aligned}&\widehat{u}_{-\frac{1}{2}} = A_0^1(1 - \lambda_{u_o}^{2M_o}) + S_{u,o}^{m=-1/2}(U_0) \\ &\widehat{\phi}_{o,0} = -A_0^1K_{1,o} - S_{\phi,o}^{m=0}, \qquad K_{1,o} = \frac{1}{h_o}\left(\lambda_{u_o} - \lambda_{u_o}^{2M_o-1} - (\chi_o+1)(1-\lambda_{u_o}^{2M_o})\right)\end{aligned} \tag{6.38}$$

The continuity of the flux at interface $\rho_o \nu_o \phi_o = \rho_a \nu_a \phi_a$ lets us rewrite

$$A_0^1 = -B_0^1 \times \epsilon \frac{\nu_a}{\nu_o} \frac{K_{1,a}}{K_{1,o}} - \frac{S^0_{\phi,o} - \epsilon \frac{\nu_a}{\nu_o} S^0_{\phi,a}}{K_{1,o}} \tag{6.39}$$

and the jump between the solutions is

$$\widehat{u}_{\frac{1}{2}} - \widehat{u}_{-\frac{1}{2}} = B_0^1 K_2 + \Delta S \tag{6.40}$$

where $K_2 = 1 - \lambda_{u_a}^{2M_a} + (1 - \lambda_{u_o}^{2M_o}) \epsilon \frac{\nu_a}{\nu_o} \frac{K_{1,a}}{K_{1,o}}$ and $\Delta S = S_{u,a}^{m=\frac{1}{2}} - S_{u,o}^{m=-\frac{1}{2}} + (1 - \lambda_{u_o}^{2M_o}) \frac{S^0_{\phi,o} - \epsilon \frac{\nu_a}{\nu_o} S^0_{\phi,a}}{K_{1,o}}$.

6.A.2 Inverting the friction law

After substitution of $\widehat{u}_{\frac{1}{2}} - \widehat{u}_{-\frac{1}{2}}$ and $\phi_{\mathrm{a},0}$ in the friction law (6.29d), we obtain a linear equation involving $B_0^1(s)$ and $\overline{B_0^1(\overline{s})}$:

$$\underbrace{(\nu_a K_{1,a} - \frac{3\alpha^e K_2}{2})}_{K_3(s)} B_0^1(s) - \underbrace{\alpha^e \frac{\mathcal{O}\overline{K_2}(\overline{s})}{2}}_{\overline{K_4(\overline{s})}} \times \overline{B_0^1(\overline{s})} = S_{\text{friction}} \tag{6.41}$$

where $S_{\text{friction}} = \frac{3\alpha^e}{2} \left(\Delta S + \frac{\mathcal{O}}{3} \overline{\Delta S(\overline{s})} \right) + \nu_a S_{\phi,a}^{m=0}$. The complex conjugate of (6.41) taken at $\overline{s}$ gives

$$-K_4(s) B_0^1(s) + \overline{K_3(\overline{s}) B_0^1(\overline{s})} = \overline{S_{\text{friction}}(\overline{s})} \tag{6.42}$$

Finally, B_0^1 (and $\widehat{u}_j$) can be uniquely determined if the system (6.41-6.42) has a unique solution, i.e. if the following matrix is invertible:

$$\begin{pmatrix} K_3(s) & -\overline{K_4(\overline{s})} \\ -K_4(s) & \overline{K_3(\overline{s})} \end{pmatrix} \tag{6.43}$$

Figure 6.9 shows that the determinant of this matrix is not zero for $\sigma > 0$. For the frequencies $\omega = f$ and $\omega = -f$ the determinant is close to zero, and it seems to be asymptotically proportional to $\sqrt{\sigma}$.

The Laplace transform can be uniquely inverted (e.g. [Cohen, 2007]) because $\widehat{u}_j(s)$ does not grow faster than exponentially for $|s| \to \infty$. Indeed, the asymptotic values of K_i for $|s| \to \infty$ are

$$K_{1,j} \sim -\frac{\chi_j}{h_j}, \qquad K_3 \sim -\frac{\nu_a \chi_a}{h_a}$$
$$K_2 \to 1 - \epsilon \frac{h_a}{h_o}, \qquad K_4 \to \alpha^e \frac{\mathcal{O}}{2} (1 - \epsilon \frac{h_a}{h_o})$$

One can see that $K_3 \to \infty$ whereas K_4 tends to a constant. Since $\widehat{u}$ is given by the inverse of (6.43), it tends to zero as $s \to \infty$. Figure 6.9 also shows that the determinant of (6.43) increases with ω^β (for some $\beta \approx 2$) for high $|s|$.

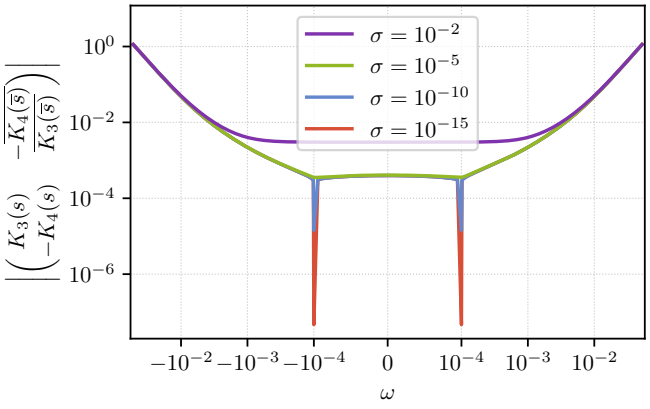

Figure 6.9: Absolute value of the determinant of (6.43) depending on the frequency variable. With our parameters, if $\sigma > 0$ the matrix is invertible $\forall \omega$.

6.B Appendix: detailed convergence study of the linearized case

We interest ourselves to the linearization of (6.4) around a stationary state U_j^e, ϕ_j^e.

$$\begin{aligned}
(\partial_t + if)u^k_{j,m+\frac{1}{2}} &= \nu_j \tfrac{\phi^k_{j,m+1} - \phi^k_{j,m}}{h} \\
u^k_j\big|_{t=0} &= 0 \\
u^k_j\big|_{z=H_j} &= 0 \\
\rho_{\mathrm{o}}\nu_{\mathrm{o}}\phi^k_{\mathrm{o},0} &= \rho_{\mathrm{a}}\nu_{\mathrm{a}}\phi^k_{\mathrm{a},0} \\
\nu_a\phi^k_{\mathrm{a},0} &= C_D\,|\Delta U^e|\left(\tfrac{3}{2}\Delta u^{k-1} + \tfrac{1}{2}\tfrac{\Delta U^e}{\overline{\Delta U^e}}\overline{\Delta u^{k-1}}\right) \\
&\quad -\theta\, C_D|\Delta U^e|\left(u^k_a - u^{k-1}_a\right)
\end{aligned}$$

The three first equations are used in a Fourier transform or z-transform to obtain

$$\begin{aligned}
(s + if)\widehat{u}^k_{j,m+\frac{1}{2}} &= \nu_j \tfrac{\widehat{\phi}^k_{j,m+1} - \widehat{\phi}^k_{j,m}}{h} \\
\widehat{u}^k_j\big|_{z=H_j} &= 0
\end{aligned} \tag{6.44}$$

where s is the frequency variable. Using the form of $\phi_{j,m\neq 0} = \frac{u_{j,m+1/2} - u_{j,m-1/2}}{h}$ we obtain for $m > 0$

$$(\chi_j + 2)\widehat{u}^k_{j,m+\frac{1}{2}} = \widehat{u}_{j,m+3/2} + \widehat{u}_{j,m-1/2}, \qquad \chi_j = h_j^2\frac{s + if}{\nu} \tag{6.45}$$

We use the ansatz

$$\widehat{u}_{a,m+1/2} = \sum_i B_k^i (1+\lambda_a^i)^m$$
$$\widehat{u}_{o,-m-1/2} = \sum_i A_k^i (1+\lambda_o^i)^m$$

where λ_j^i can be obtained by injecting the ansatz in (6.45):

$$(\chi_j + 2)(1+\lambda_j^i) = (1+\lambda_j^i)^2 + 1$$

The solutions of this equation are $\lambda_j = \lambda_j^1 = \frac{1}{2}\left(\chi_j - \sqrt{\chi_j}\sqrt{\chi_j+4}\right)$ and $\widetilde{\lambda}_j = \lambda_j^2 = \chi_j - \lambda_j$. One can prove that $(1+\lambda_j)(1+\widetilde{\lambda}_j) = 1$.

The boundary condition at $H_j = \pm(M_j + \frac{1}{2})h_j$ gives that $\{A_k^2, B_k^2\} = -\{A_k^1, B_k^1\}(1+\lambda_j)^{2M_j}$. Finally, the jump of the solution across the interface is

$$\widehat{u}_{a,1/2} - \widehat{u}_{o,-1/2} = B_k^1 - A_k^1 - B_k^1(1+\lambda_a)^{2M_a} + A_k^1(1+\lambda_o)^{2M_o} := B_k^1 I_a^- - A_k^1 I_o^-$$

and we also define $I_j^+ = 2 - I_j^-$. Note that all the variables $I_j^\pm \to 1$ with the infinite domain hypothesis, which is used in (6.18). The fluxes inside the domains are computed with the finite differences:

$$\phi_{a,m+1} = B_k^1 \frac{\lambda_a}{h_a}(1+\lambda_a)^m + B_k^2 \frac{\widetilde{\lambda}_a}{h_a}(1+\widetilde{\lambda}_a)^m \tag{6.46}$$

$$\phi_{o,-m-1} = -A_k^1 \frac{\widetilde{\lambda}_o}{h_o}(1+\lambda_o)^m - A_k^2 \frac{\lambda_o}{h_o}(1+\widetilde{\lambda}_o)^m \tag{6.47}$$

And the fluxes at the interface are obtained by using (6.44):

$$h_a\phi_{a,0} = h_a\phi_{a,1} - \chi_a\widehat{u}_{a,1/2} = B_k^1(\lambda_a - \chi_a) + B_k^2\left(\widetilde{\lambda}_a - \chi_j\right) = B_k^1(\lambda_a I_a^+ - \chi_a)$$
$$h_o\phi_{o,0} = h_o\phi_{o,-1} + \chi_o\widehat{u}_{o,-1/2} = A_k^1\left(-\widetilde{\lambda}_o + \chi_o\right) + A_k^2(-\lambda_o + \chi_o) = A_k^1((\lambda_o - \chi_o)I_o^+ + \chi_o)$$

A_k^2, B_k^2 will not intervene anymore and we now note $(A_k, B_k) = (A_k^1, B_k^1)$.

Remark *It can be checked that $\phi_{a,0}$ and $\phi_{o,0}$ correspond to the values obtained with $m = -1$ in (6.46) and (6.47). This was not obvious since they do not correspond to a finite difference approximation $\frac{u_{j,\frac{1}{2}} - u_{j,-\frac{1}{2}}}{h_j}$. It is hence correct if $\omega \neq -f$ to start from $\phi_j(\pm m h_j) = \phi_{j,0}(\lambda_j + 1)^m$ in Section 6.4 (where it is assumed that $H_j \to \infty$). However, the asymptotic analysis of the convergence factor for $\omega + f \to 0$ (as it was done in [Clement et al., 2021]) hides a division by zero when considering $\frac{\phi_{j,0}^k}{\phi_{j,0}^{k-1}}$.*

We are now ready to study the transmission conditions. The continuity of the flux leads to

$$h_o\widehat{\phi}_{o,0} = h_a\widehat{\phi}_{a,0}\epsilon\frac{\nu_a h_o}{\nu_o h_a} \Rightarrow A_k = B_k\frac{\lambda_a I_a^+ - \chi_a}{(\lambda_o - \chi_o)I_o^+ + \chi_o}\epsilon\frac{\nu_a h_o}{\nu_o h_a} \tag{6.48}$$

We inject this equality in the jump of the solution across the interface and obtain

$$\widehat{u}^k_{a,\frac{1}{2}} - \widehat{u}^k_{o,-\frac{1}{2}} = B_k\mu(s) \tag{6.49}$$

where

$$\mu(s) = I_a^- - I_o^-\frac{\lambda_a I_a^+ - \chi_a}{(\lambda_o - \chi_o)I_o^+ + \chi_o}\epsilon\frac{\nu_a h_o}{\nu_o h_a} \tag{6.50}$$

The second interface transmission condition which is linearized gives

$$\frac{\nu_{\mathrm{a}}}{h_a}B_k\left(\lambda_a I_a^+ - \chi_a\right) = \alpha^e\left(\frac{3}{2}B_{k-1}\mu(s) + \theta(\widehat{u}^k_{\mathrm{a}} - \widehat{u}^{k-1}_{\mathrm{a}}) + \frac{1}{2}\frac{\Delta U^e}{\overline{\Delta U^e}}\overline{B_{k-1}(\overline{s})\mu(\overline{s})}\right) \tag{6.51}$$

where

$$\widehat{u}^k_{\mathrm{a}} - \widehat{u}^{k-1}_{\mathrm{a}} = (B_k - B_{k-1})I_a^- \tag{6.52}$$

We finally obtain

$$B_k(s) = a_1 B_{k-1}(s) + a_2\overline{B_{k-1}(\overline{s})} \tag{6.53}$$

where

$$a_1 = \alpha^e\frac{\frac{3}{2}\mu(s) - \theta I_a^-}{\frac{\nu_a}{h_a}\left(\lambda_a I_a^+ - \chi_a\right) - \alpha^e\theta I_a^-}, \qquad a_2 = \alpha^e\frac{\frac{1}{2}\frac{\Delta U^e}{\overline{\Delta U^e}}\overline{\mu(\overline{s})}}{\frac{\nu_a}{h_a}\left(\lambda_a I_a^+ - \chi_a\right) - \alpha^e\theta I_a^-} \tag{6.54}$$

Remark *It is easy to obtain the convergence factor of the case* $\alpha = \text{const}$ *by removing the conjugate term and the factor* $\frac{3}{2}$ *in* (6.51)*. The convergence rate is then identical to* a_1*, without the* $\frac{3}{2}$ *factor.*

Conclusion and perspectives

This thesis focused on the numerical analysis of interactions between the ocean and atmosphere within their coupling. We proposed a new discretization of the surface layer which relies on hypotheses already in use in the computation of turbulent fluxes. Besides, the Schwarz methods were studied at discrete and semi-discrete levels and we have highlighted important features of their convergence. The analysis of convergence of Schwarz methods was finally pursued in the presence of a parameterized surface layer and we proved some convergence results on this simplified air-sea coupled problem.

Let us recall the three objectives of this thesis (a hierarchy of three models was used to achieve each of them):

- Improve our knowledge on how the discretization affects the convergence factor of Schwarz methods.
- Discuss the numerical treatment of the surface layer and propose improvements.
- Study the effect of the surface layer within the ocean-atmosphere coupling.

Chapter 2 discussed the convergence analysis of Schwarz methods at the semi-discrete and discrete levels. The goal was do develop a methodology to be used later on more sophisticated models. The effect of the discretization in both space and time was highlighted: we have notably identified the importance of the interface conditions, both in their interpolation within a multi-step time scheme and in their discretization in space. The interactions between space and time discretizations were also investigated: they are characterized by the parabolic Courant number. Finally, a Finite Volume discretization was derived based on a subgrid reconstruction with quadratic splines. The special attention on the subgrid reconstruction was later used for the discretization of the surface layer.

Chapter 3 introduced approximations that can be used to simplify the derivation of the theoretical semi-discrete and fully discrete convergence factors. Indeed, as the complexity of the discretizations increase the theoretical convergence factors become tedious to compute analytically. One method approximates the semi-discrete convergence factors relying on the modified equations technique and the other method combines the semi-discrete analyses to approximate the fully discrete one. The ideas of those methods are simple and we exposed some of their inherent strengths and weaknesses. For instance, the effect of the interpolation

of the interface conditions discussed in Chapter 2 is not present when using the modified equations technique. We found in which case those approximations could be useful and explained the reasons for which they can be inadequate in other cases.

In Chapter 4, the surface layer hypotheses were discussed: we proposed a discretization based on the Monin-Obukhov Similarity Theory. We used the solution profiles of this Similarity Theory as the subgrid reconstruction on which is based the Finite Volume discretization. This discretization is such that the computation of turbulent fluxes is coherent with the subgrid reconstruction of the solution. It was recently highlighted that the height of the surface layer should not (always) be limited to the first grid level. We hence allowed the size of the surface layer to be freely chosen independently from the grid levels: as a result, the consistency of the discretization was found to be better than the usual methods that constrain the surface layer height.

This discretization is applied to the oceanic part of the surface layer in Chapter 5, even though considering an oceanic surface layer is recent and still uncommon. We focused specifically on the handling of radiative fluxes which lead to particular difficulties in terms of subgrid reconstruction. The proposed discretization of the surface layer including radiative fluxes is a first step toward a well discretized oceanic surface layer. We have shown that this discretization does not perform well in terms of consistency and should be improved.

Finally, Chapter 6 studied at the semi-discrete-in-space level the effect of the surface layer on the ocean-atmosphere coupling. The methodology presented in Chapter 2 was used to treat a surface layer which was simplified compared to Chapters 4 and 5. The well-posedness of the coupled problem was discussed and the existence and unicity of a solution in the neighborhood of the steady state was proved using the inverse function theorem. We examined the convergence of Schwarz methods with a parameterized surface layer as a nonlinear transmission condition: interestingly, the convergence factor was found to change from one iteration to another. The convergence study was pursued by linearizing the transmission condition and we derived upper and lower bound of the convergence factor, corresponding to the singular values of a transition matrix between the iterations. We optimized numerically the convergence with respect to a relaxation parameter and compared the convergence of the nonlinear system with the one with a linearized transmission condition.

Perspectives

The ultimate goal of this thesis is to reduce the numerical errors linked to the ocean-atmosphere coupling in operational models. Two perspectives directly linked with this objective arise:

- Implement and evaluate the discretization of the surface layer introduced in Chapter 4 and 5 within more realistic simulations. The order of accuracy would need to be improved in the process: in particular, splitting a cell in two parts breaks the possible structured grid properties. Furthermore, the schemes should be analyzed in terms of

stability, monotonicity, and other mathematical or physical properties.

- Make sure that the convergence of Schwarz methods is attained in one or two iterations: iterative coupling is otherwise unaffordable in this ocean-atmosphere context. This can be done by choosing better transmission conditions and/or by improving the first guess. This first guess could be obtained either with a well-chosen extrapolation of other time windows (the latter option is presently studied in the AIRSEA team in collaboration with O. Marti for the model IPSL-CM) or with Schwarz iterations on a simplified internal subproblem (e.g. similar to the ones studied in this thesis).

Besides those direct applications, the theoretical aspects also need to be consolidated in terms of well-posedness and in terms of convergence of Schwarz methods. It seems that this mathematical knowledge is not going to catch up soon with the increasing complexity of the operational models. However, the former could provide guidelines to wisely parameterize and discretize the latter while keeping good mathematical properties.

Several steps forward can be pursued as the following of the present thesis which used the simplification that the viscosity is constant. Convergence studies of Schwarz methods were conducted with variable viscosities but never to our knowledge at the semi-discrete-in-space level. Two perspectives arise from the objective of taking the varying viscosities into account:

- Developing mathematical tools so that the semi-discrete-in-space convergence factor could be studied with varying viscosities (as it was done in the continuous case in [Thery, 2021]) or varying space steps. A first step toward this convergence factor would be to use the idea of the *combined* convergence factor in Chapter 3: instead of combining the contribution of the space scheme and of the time scheme, it could be relevant to combine the contribution of the space scheme and of the varying viscosities.

- Extending the proof of well-posedness of Chapter 6 to varying viscosities that depend on the surface layer parameterization. The atmosphere and ocean models were developed separately and are coupled through a surface layer whose parameterization contains additional hypotheses. The compatibility between all the components of the ocean-atmosphere coupling is not guaranteed and the well-posedness study of simplified models could teach us a lot.

The coherence between the surface layer parameterization and the discretization is a small aspect within the much wider problem of articulating a dynamical core with a physical parameterization. Incoherence may appear in this conception because of the huge complexity of the numerical models: the development and the implementation of parameterizations need a numerical analysis to ensure a global harmony.

Bibliography

Adam, Y. (1977). Highly accurate compact implicit methods and boundary conditions. *Journal of Computational Physics*, 24(1):10–22. (Cited on page 81.)

Arnoult, A., Japhet, C., and Omnes, P. (2022). Discrete-time analysis of Schwarz waveform relaxation convergence. ⟨hal-03746438⟩. (Cited on page 3.)

Basu, S. and Lacser, A. (2017). A cautionary note on the use of Monin–Obukhov similarity theory in very high-resolution large-eddy simulations. *Boundary-Layer Meteorology*, 163(2):351–355. (Cited on pages 13, 78, and 84.)

Bougeault, P. and Lacarrere, P. (1989). Parameterization of orography-induced turbulence in a mesobeta–scale model. *Monthly Weather Review*, 117(8):1872–1890. (Cited on page 96.)

Boussinesq, J. (1897). *Théorie de l'écoulement tourbillonnant et tumultueux des liquides dans les lits rectilignes a grande section*, volume 1. Gauthier-Villars. (Cited on page 9.)

Boussinesq, J. (1903). *Théorie analytique de la chaleur*, volume 2. Gauthier-Villars. (Cited on page 7.)

Burchard, H. (2002). Energy-conserving discretisation of turbulent shear and buoyancy production. *Ocean Modelling*, 4(3-4):347–361. (Cited on page 10.)

Caetano, F., Gander, M. J., Halpern, L., and Szeftel, J. (2011). Schwarz waveform relaxation algorithms with nonlinear transmission conditions for reaction-diffusion equations. In *Domain Decomposition Methods in Science and Engineering XIX*, pages 245–252. Springer. (Cited on page 4.)

Chacon-Rebollo, T., Gomez-Marmol, M., and Rubino, S. (2014). On the existence and asymptotic stability of solutions for unsteady mixing-layer models. *Discrete and Continuous Dynamical Systems*, 34(2):421–436. (Cited on pages 3, 127, 131, and 132.)

Clement, S. (2022). Code for PhD thesis: Numerical analysis for the reconciliation in space and time of the discretizations of the air-sea exchanges and their parameterization. (Cited on page 23.)

Clement, S., Lemarié, F., and Blayo, E. (2021). Discrete analysis of Schwarz waveform relaxation for a simplified air-sea coupling problem with nonlinear transmission conditions. In *Domain Decomposition Methods in Science and Engineering XXVI*, pages 189–196. Springer. (Cited on pages 123, 133, and 143.)

Clement, S., Lemarié, F., and Blayo, E. (2022). Discrete analysis of Schwarz waveform relaxation for a diffusion reaction problem with discontinuous coefficients. *SMAI journal of computational mathematics*, 8:99–124. (Cited on pages III, 4, and 23.)

Cohen, A. M. (2007). Inversion formulae and practical results. In *Numerical Methods for Laplace Transform Inversion*, pages 23–44. Springer. (Cited on page 141.)

Connors, J. M., Howell, J. S., and Layton, W. J. (2012). Decoupled time stepping methods for fluid-fluid interaction. *SIAM Journal on Numerical Analysis*, 50(3):1297–1319. (Cited on page 77.)

Donlon, C. J., Minnett, P. J., Gentemann, C., Nightingale, T. J., Barton, I. J., Ward, B., and Murray, M. J. (2002). Toward improved validation of satellite sea surface skin temperature measurements for climate research. *Journal of Climate*, 15(4):353–369. (Cited on page 14.)

ECMWF (2020). *IFS Documentation CY47R1*. IFS Documentation. ECMWF. (Cited on page 77.)

Fairall, C. W., Bradley, E. F., Hare, J. E., Grachev, A. A., and Edson, J. B. (2003). Bulk Parameterization of air–sea fluxes: updates and verification for the COARE algorithm. *Journal of Climate*, 16(4):571–591. (Cited on page 77.)

Gander, M. J. (2006). Optimized Schwarz methods. *SIAM Journal on Numerical Analysis*, 44(2):699–731. (Cited on page 3.)

Gander, M. J., Kumbhar, P. M., and Ruehli, A. E. (2018). Analysis of Overlap in Waveform Relaxation Methods for RC Circuits. In *Domain Decomposition Methods in Science and Engineering XXIV*, pages 281–289. Springer. (Cited on page 3.)

Gander, M. J., Kwok, F., and Mandal, B. C. (2016). Dirichlet-Neumann and Neumann-Neumann waveform relaxation algorithms for parabolic problems. *Electronic transactions on numerical analysis*, 45:424–456. (Cited on page 126.)

Gerardo-Giorda, L. and Nataf, F. (2005). Optimized Schwarz methods for unsymmetric layered problems with strongly discontinuous and anisotropic coefficients. *Journal of Numerical Mathematics*, 13(4):265–294. (Cited on page 4.)

Haynes, R. D. and Mohammad, K. (2020). Fully discrete Schwarz waveform relaxation on two bounded overlapping subdomains. In *Domain Decomposition Methods in Science and Engineering XXV*, pages 159–166. Springer. (Cited on page 4.)

Häberlein, F. and Halpern, L. (2014). Optimized Schwarz waveform relaxation for nonlinear systems of parabolic type. In *Domain Decomposition Methods in Science and Engineering XXI*, pages 29–42. Springer. (Cited on page 4.)

Hörmander, L. (2015). *The Analysis of Linear Partial Differential Operators I: Distribution Theory and Fourier Analysis*. Springer. (Cited on page 127.)

Kawai, S. and Larsson, J. (2012). Wall-modeling in large eddy simulation: length scales, grid resolution, and accuracy. *Physics of Fluids*, 24(015105). (Cited on pages 11, 77, and 83.)

Kármán, T. v. (1930). Mechanische aenlichkeit und turbulenz. *Nachrichten von der Gesellschaft der Wissenschaften zu Göttingen, Mathematisch-Physikalische Klasse*, 1930:58–76. (Cited on page 11.)

Large, W. G., Patton, E. G., DuVivier, A. K., Sullivan, P. P., and Romero, L. (2019). Similarity theory in the surface layer of large-eddy simulations of the wind-, wave-, and buoyancy-forced southern ocean. *Journal of Physical Oceanography*, 49(8):2165–2187. (Cited on pages 113 and 120.)

Larsson, J., Kawai, S., Bodart, J., and Bermejo-Moreno, I. (2016). Large eddy simulation with modeled wall-stress: recent progress and future directions. *Mechanical Engineering Reviews*, 3:15–00418. (Cited on page 2.)

Lemarié, F., Blayo, E., and Debreu, L. (2015a). Analysis of ocean-atmosphere coupling algorithms: consistency and stability. *Procedia Computer Science*, 51:2066–2075. (Cited on page 1.)

Lemarié, F., Debreu, L., Madec, G., Demange, J., Molines, J., and Honnorat, M. (2015b). Stability constraints for oceanic numerical models: implications for the formulation of time and space discretizations. *Ocean Modelling*, 92:124–148. (Cited on page 77.)

Lemarié, F., Samson, G., Redelsperger, J.-L., Giordani, H., Brivoal, T., and Madec, G. (2021). A simplified atmospheric boundary layer model for an improved representation of air–sea interactions in eddying oceanic models: implementation and first evaluation in NEMO (4.0). *Geoscientific Model Development*, 14(1):543–572. (Cited on pages 96 and 98.)

LeMone, M. A., Angevine, W. M., Bretherton, C. S., Chen, F., Dudhia, J., Fedorovich, E., Katsaros, K. B., Lenschow, D. H., Mahrt, L., Patton, E. G., Sun, J., Tjernström, M., and Weil, J. (2019). 100 years of progress in boundary layer meteorology. *Meteorological Monographs*, 59:9.1 – 9.85. (Cited on page 75.)

Lions, J. L., Temam, R., and Wang, S. (1995). Mathematical theory for the coupled atmosphere-ocean models (CAO III). *Journal de Mathematiques Pures et Appliquees*, 74. (Cited on pages 3 and 127.)

Maronga, B., Knigge, C., and Raasch, S. (2020). An improved surface boundary condition for large-eddy simulations based on Monin–Obukhov similarity theory: evaluation and consequences for grid convergence in neutral and stable conditions. *Boundary-Layer Meteorology*, 174(2):297–325. (Cited on pages 77 and 105.)

Marti, O., Braconnot, P., Dufresne, J.-L., Bellier, J., Benshila, R., Bony, S., Brockmann, P., Cadule, P., Caubel, A., Codron, F., de Noblet, N., Denvil, S., Fairhead, L., Fichefet, T., Foujols, M.-A., Friedlingstein, P., Goosse, H., Grandpeix, J.-Y., Guilyardi, E., Hourdin, F., Idelkadi, A., Kageyama, M., Krinner, G., Lévy, C., Madec, G., Mignot, J., Musat, I., Swingedouw, D., and Talandier, C. (2010). Key features of the IPSL ocean atmosphere model and its sensitivity to atmospheric resolution. *Climate Dynamics*, 34(1):1–26. (Cited on page 19.)

Marti, O., Nguyen, S., Braconnot, P., Valcke, S., Lemarié, F., and Blayo, E. (2021). A Schwarz iterative method to evaluate ocean–atmosphere coupling schemes: implementation and diagnostics in IPSL-CM6-SW-VLR. *Geoscientific Model Development*, 14(5):2959–2975. (Cited on pages 2, 19, 123, and 125.)

Meisrimel, P., Monge, A., and Birken, P. (2020). A time adaptive multirate Dirichlet-Neumann waveform relaxation method for heterogeneous coupled heat equations. (Cited on page 126.)

Mogensen, K., Keeley, S., and Towers, P. (2012). Coupling of the NEMO and IFS models in a single executable. ECMWF. (Cited on page 19.)

Mohammadi, B., Pironneau, O., and Valentin, F. (1998). Rough boundaries and wall laws. *International Journal for Numerical Methods in Fluids*, 27(1-4):169–177. (Cited on pages 75 and 124.)

Nishizawa, S. and Kitamura, Y. (2018). A surface flux scheme based on the Monin–Obukhov similarity for finite volume models. *Journal of Advances in Modeling Earth Systems*, 10:3159–3175. (Cited on pages VII, 3, 78, 81, 82, 83, 94, and 95.)

Obukhov, A. (1946). Turbulence in thermally inhomogeneous atmosphere. *Trudy Inst. Teor. Geofiz. Akad. Nauk SSSR*, 1:95–115. (Cited on page 13.)

Optis, M., Monahan, A., and Bosveld, F. C. (2014). Moving beyond Monin–Obukhov similarity theory in modelling wind-speed profiles in the lower atmospheric boundary layer under stable stratification. *Boundary-Layer Meteorology*, 153(3):497–514. (Cited on page 13.)

Pelletier, C., Lemarié, F., Blayo, E., Bouin, M.-N., and Redelsperger, J.-L. (2021). Two-sided turbulent surface-layer parameterizations for computing air–sea fluxes. *Quarterly Journal of the Royal Meteorological Society*, 147(736):1726–1751. (Cited on pages VIII, 2, 12, 14, 15, 110, 111, 112, 114, 120, and 124.)

Piller, M. and Stalio, E. (2004). Finite-volume compact schemes on staggered grids. *Journal of Computational Physics*, 197(1):299–340. (Cited on pages 80 and 81.)

Redelsperger, J. L., Mahé, F., and Carlotti, P. (2001). A simple and general subgrid model suitable both for surface layer and free-stream turbulence. *Boundary-Layer Meteorology*, 101(3):375–408. (Cited on page 98.)

Renault, L., Lemarié, F., and Arsouze, T. (2019). On the implementation and consequences of the oceanic currents feedback in ocean–atmosphere coupled models. *Ocean Modelling*, 141:101423. (Cited on page 76.)

Schlichting, H. (1960). *Boundary layer theory*. McGraw-Hill, 4th edition. (Cited on page 12.)

Thery, S. (2021). *Etude numérique des algorithmes de couplage océan-atmosphère avec prise en compte des paramétrisations physiques des couches limites*. PhD Thesis, Université Grenoble Alpes. (Cited on pages 14, 124, 129, 136, and 147.)

Thery, S., Pelletier, C., Lemarié, F., and Blayo, E. (2021). Analysis of Schwarz waveform relaxation for the coupled Ekman boundary layer problem with continuously variable coefficients. *Numerical Algorithms*, 89:1145–1181. (Cited on page 4.)

Voldoire, A., Sanchez-Gomez, E., Salas y Mélia, D., Decharme, B., Cassou, C., Sénési, S., Valcke, S., Beau, I., Alias, A., Chevallier, M., Déqué, M., Deshayes, J., Douville, H., Fernandez, E., Madec, G., Maisonnave, E., Moine, M.-P., Planton, S., Saint-Martin, D., Szopa, S., Tyteca, S., Alkama, R., Belamari, S., Braun, A., Coquart, L., and Chauvin, F. (2013). The CNRM-CM5.1 global climate model: description and basic evaluation. *Climate Dynamics*, 40(9):2091–2121. (Cited on page 19.)

Ward, B. (2006). Near-surface ocean temperature. *Journal of Geophysical Research: Oceans*, 111(C2). (Cited on page 14.)

Wu, S.-L. and Al-Khaleel, M. (2017). Optimized waveform relaxation methods for RC circuits: discrete case. *ESAIM Mathematical Modelling and Numerical Analysis*, 51:209–223. (Cited on pages 3 and 128.)

Wu, S.-L. and Al-Khaleel, M. D. (2014). Semi-discrete Schwarz waveform relaxation algorithms for reaction diffusion equations. *BIT Numerical Mathematics*, 54(3):831–866. (Cited on page 3.)

Zeng, X. and Beljaars, A. (2005). A prognostic scheme of sea surface skin temperature for modeling and data assimilation. *Geophysical Research Letters*, 32(14):L14605. (Cited on page 116.)

Zisowsky, A. and Ehrhardt, M. (2006). Discrete transparent boundary conditions for parabolic systems. *Mathematical and Computer Modelling*, 43(3):294–309. (Cited on page 3.)

Les modèles numériques de prévision de l'océan et de l'atmosphère sont essentiels pour la compréhension des phénomènes géophysiques qui y sont liés. Le couplage de ces modèles dans les simulations joue un rôle clé pour une large gamme d'échelles temporelles (cycle diurne, cyclone tropicaux, climat...) où il est nécessaire de représenter les interactions entre l'océan et l'atmosphère.

L'implémentation du couplage est généralement réalisée de manière partielle et introduit une erreur numérique qu'il convient de minimiser. Dans ce but, des méthodes de couplage itératives et leur vitesse de convergence sont considérées ici, les pratiques actuelles étant souvent équivalentes à une seule itération.

Une difficulté dans l'analyse mathématique de la convergence des méthodes de couplage est la présence d'une couche limite de surface entre l'océan et l'atmosphère. Cette spécificité justifie d'étudier la convergence au niveau discret (c'est-à-dire en prenant en compte certains choix d'implémentation) plutôt que continu.

Par ailleurs, les paramétrisations de la couche limite de surface s'appuient sur des hypothèses qui ne sont pas mathématiquement imposées au sein des modèles. Cette thèse propose de renforcer la cohérence entre le calcul des flux turbulents intervenant dans la couche limite et les discrétisations des équations décrivant l'océan et l'atmosphère.

L'analyse de la couche limite de surface au sein du couplage océan-atmosphère est réalisée ici en utilisant une hiérarchie de modèles permettant à la fois d'obtenir des résultats mathématiques et de reproduire des comportements numériques d'intérêt.

Numerical models of the ocean and atmosphere are essential for the understanding of the associated geophysical phenomena. The coupling of these models plays a key role for a wide range of time scales (diurnal cycle, tropical cyclone, global climate...) where it is necessary to represent the interactions between the ocean and the atmosphere.

The implementation of the coupling is generally done only partially and introduces a numerical error that should be minimized. For this purpose, iterative coupling methods and their convergence speed are considered here, the current practices being often equivalent to a single iteration.

A difficulty in the mathematical convergence analysis of coupling methods is the presence of a surface layer between the ocean and the atmosphere. This specificity justifies studying the convergence at the discrete level (i.e. taking into account some implementation choices) rather than at the continuous level.

Moreover, the parameterizations of the surface layer are based on assumptions which are not mathematically enforced within the models. This thesis proposes to consolidate the coherence between the computation of turbulent flows in the surface layer and the discretizations of the equations describing the ocean and the atmosphere.

The analysis of the surface boundary layer within the ocean-atmosphere coupling is carried out here using a hierarchy of models allowing to obtain both mathematical results and the replication of numerical behaviors of interest.